

**From Darkness to Light: Signatures of the Universe's First Galaxies  
in the Cosmic 21-cm Background**

by

**Jordan Mirocha**

B.S., Physics, Drake University, 2009

M.S., Astrophysics, University of Colorado, 2011

A thesis submitted to the  
Faculty of the Graduate School of the  
University of Colorado in partial fulfillment  
of the requirements for the degree of  
Doctor of Philosophy  
Department of Astrophysical & Planetary Science

2015

This thesis entitled:  
From Darkness to Light: Signatures of the Universe's First Galaxies in the Cosmic 21-cm Background  
written by Jordan Mirocha  
has been approved for the Department of Astrophysical & Planetary Science

---

Prof. Jack Burns

---

Prof. Jeremy Darling

---

Prof. J. Michael Shull

Date \_\_\_\_\_

The final copy of this thesis has been examined by the signatories, and we find that both the content and the form meet acceptable presentation standards of scholarly work in the above mentioned discipline.

Mirocha, Jordan (Ph.D., Astrophysics)

From Darkness to Light: Signatures of the Universe’s First Galaxies in the Cosmic 21-cm Background

Thesis directed by Prof. Jack Burns

Within the first billion years after the Big Bang, the intergalactic medium (IGM) underwent a remarkable transformation, from a uniform sea of cold neutral hydrogen gas to a fully ionized, metal-enriched plasma. Three milestones during this Epoch of Reionization – the emergence of the first stars, black holes, and full-fledged galaxies – are expected to manifest as spectral “turning points” in the sky-averaged (“global”) 21-cm background. However, interpreting these measurements will be complicated by the presence of strong foregrounds and non-trivialities in the radiative transfer (RT) required to model the signal.

In this thesis, I make the first attempt to build the final piece of a global 21-cm data analysis pipeline: an inference tool capable of extracting the properties of the IGM and the Universe’s first galaxies from the recovered signal. Such a framework is valuable even prior to a detection of the global 21-cm signal as it enables end-to-end simulations of 21-cm observations that can be used to optimize the design of upcoming instruments, their observing strategies, and their signal extraction algorithms.

En route to a complete pipeline, I found that (1) robust limits on the physical properties of the IGM, such as its temperature and ionization state, can be derived analytically from the 21-cm turning points within two-zone models for the IGM, (2) improved constraints on the IGM properties can be obtained through simultaneous fitting of the global 21-cm signal and foregrounds, though biases can emerge depending on the parameterized form of the signal one adopts, (3) a simple four-parameter galaxy formation model can be constrained in only 100 hours of integration provided a stable instrumental response over a broad frequency range ( $\sim 80$  MHz), and (4) frequency-dependent RT solutions in physical models for the global 21-cm signal will be required to properly interpret the 21-cm absorption minimum, as the IGM thermal history is highly sensitive to the spectral energy distribution of the first galaxies. These results highlight the need for continued development of theoretical models that can incorporate constraints from current and near-future observatories, and the implementation of statistical algorithms capable of distinguishing competing models.

## **Dedication**

To my family.

## Acknowledgements

I am very fortunate to have been surrounded by so many great mentors, educators, collaborators, and friends in my six years in Boulder, without whom I would have undoubtedly struggled, both academically and in my personal life.

The first few weeks of graduate school were (perhaps unsurprisingly) some of the most frustrating, trying to juggle classes and research and build some semblance of a social life. Research was especially stressful given that I couldn't seem to install the software packages needed to do any of the simulations we had planned! Luckily, rescue came swiftly from Britton, Sam, and Eric, who spent many hours of their lives helping me with the tedium of software installations and guiding me through the deep recesses of a code in which I'd have otherwise been lost. I am so thankful to have had you guys around – I truly don't know if I'd have made it past the first semester without your help.

In the years that followed, I had the pleasure of working closely with many more students, postdocs, and faculty on a variety of projects unrelated to my thesis. Most notably, I must thank the Department of Astrophysical and Planetary Science and Jason Glenn for giving me the opportunity to help develop content for a new class and eventually teach it as instructor of record, and to Jeremy Darling for his supervision on my comps II project. Teaching was one of the most rewarding experiences of my grad school career, being able to see a course through from its humble beginnings as an outline and a textbook, to a full set of lectures, tutorials, and assignments, to the feedback from students after the first iteration of the course. Jason: I could not have had a better mentor through this process – I strive to emulate you everyday I stand up in front of a class. To Jeremy: our weekly meetings were some of my favorite times in grad school, speculating wildly about black holes and their role in galaxy evolution. Your patience with me in the years since seems to know

no bounds – I can't thank you enough for this. This project *will* get done!

My thesis work was enabled by funding from various sources, including the NASA Lunar Science Institute, the NASA Earth and Space Science Fellowship program, the director's office at NASA Ames Research Center, and the Graduate School at the University of Colorado, to whom I am extremely grateful. I also must thank my committee members, Mike Shull, Vanja Dukic, Steve Furlanetto, Jeremy Darling, and Jack Burns for their guidance throughout this process and regular feedback on my work. In particular, my advisor, Jack Burns, has gone to great lengths to insure my continued progress, including the initiation of collaborations with members of the community beyond Boulder. These efforts, as well as your support in all endeavors outside the immediate realm of my thesis work has made your interest in my long-term success as a well-rounded academic, rather than my short-term productivity as a student, abundantly clear. For that, I will forever be grateful. This was a bonus, on top of the constant support and guidance over the years as we navigated this new field together. Thank you! I look forward to collaborating for many years to come.

Lastly, I must thank the people who are responsible for boosting my morale on a regular basis. My family and friends in Minnesota, who have always supported me from afar via texts, emails, and phone calls, and somehow haven't given up on calling me despite my terseness over the phone. I'm not the chattiest person on Earth, I know, I just hope you never mistake my silence for apathy! To Greg, Julia, Devin, Sam, Gins, Addie, Kyle, Eric, and Grant: the afternoon trips to Pekoe, Laughing Goat, and Folsom, kept me going on days when I couldn't seem to do anything right. I'll forever be strangely nostalgic while waiting in line for coffee, because for years that's been when I got to spend time with you. To Marek, Anthony, and Grant: I never thought it would be possible to have so much fun in the final year of grad school while so busy writing proposals and worrying about where I'd be moving next. I know sometimes I was difficult, being especially resistant to excursions beyond the South Boulder bubble, but it's only because the most fun nights of my life were spent just sitting around the table at the Armer house with you guys.

## Contents

### Chapter

|          |   |           |
|----------|---|-----------|
| <b>1</b> | <b>Introduction</b>   | <b>1</b>  |
| 1.1      | The High- $z$ Universe . . . . .  | 1         |
| 1.1.1    | First Stars . . . . .   | 3         |
| 1.1.2    | Black Holes . . . . .   | 7         |
| 1.1.3    | Galaxies & the Epoch of Reionization . . . . .  | 12        |
| 1.2      | Established Probes of High- $z$ Galaxies and Reionization . . . . .                           | 16        |
| 1.2.1    | The Galaxy Luminosity Function . . . . .  | 16        |
| 1.2.2    | The Ly- $\alpha$ Forest, Gunn-Peterson Troughs, and the Meta-Galactic UV Background . . . . . | 19        |
| 1.2.3    | Thomson Optical Depth to the Cosmic Microwave Background . . . . .                            | 22        |
| 1.3      | The 21-cm Background . . . . .  | 24        |
| 1.3.1    | Basic Physics . . . . .   | 25        |
| 1.3.2    | The Global 21-cm Signal . . . . .   | 27        |
| 1.4      | Motivation and Outline for Subsequent Chapters . . . . .                                      | 32        |
| <br>     |   |           |
| <b>2</b> | <b>Model-Independent Constraints from the Sky-Averaged Global 21-cm Signal</b>                | <b>35</b> |
| 2.1      | Context . . . . .   | 35        |
| 2.2      | Introduction . . . . .  | 36        |
| 2.3      | Evolution of the Global 21-cm Signal . . . . .  | 36        |
| 2.4      | Critical Points in the 21-cm History . . . . .  | 39        |

|          |   |           |
|----------|---|-----------|
| 2.4.1    | Turning Point B: End of the Dark Ages . . . . .   | 40        |
| 2.4.2    | Turning Point C: Heating Epoch . . . . .  | 41        |
| 2.4.3    | Turning Point D: Reionization . . . . .   | 49        |
| 2.5      | Discussion . . . . .  | 49        |
| 2.5.1    | A Shift in Methodology . . . . .  | 49        |
| 2.5.2    | An Example History . . . . .  | 50        |
| 2.5.3    | Synergies with Upcoming Facilities . . . . .  | 54        |
| 2.5.4    | Caveats . . . . .   | 54        |
| 2.6      | Conclusions . . . . .   | 55        |
| <b>3</b> | <b>Signal Extraction for All-Sky 21-cm Experiments: Dependence on the Assumed Parameterization of the Global 21-cm Signal</b> | <b>57</b> |
| 3.1      | Context . . . . .   | 57        |
| 3.2      | Introduction . . . . .  | 58        |
| 3.3      | Signal Extraction Methodology . . . . .   | 59        |
| 3.4      | Results . . . . .   | 63        |
| 3.5      | Discussion & Conclusions . . . . .  | 70        |
| <b>4</b> | <b>Parameter Estimation for Global 21-cm Experiments: Prospects for Constraining Simple Galaxy Formation Models</b>           | <b>75</b> |
| 4.1      | Context . . . . .   | 75        |
| 4.2      | Introduction . . . . .  | 76        |
| 4.3      | Numerical Methods . . . . .   | 77        |
| 4.3.1    | Physical Model for the Global 21-cm Signal . . . . .  | 77        |
| 4.3.2    | Signal Extraction . . . . .   | 82        |
| 4.3.3    | Parameter Estimation . . . . .  | 85        |
| 4.4      | Results . . . . .   | 88        |
| 4.4.1    | Constraints on the Intergalactic Medium . . . . .   | 88        |

|          |  |            |
|----------|--|------------|
| 4.4.2    | Constraints on the Physical Model . . . . .                                | 94         |
| 4.5      | Discussion . . . . .   | 98         |
| 4.5.1    | Are all three points necessary? . . . . .                                  | 98         |
| 4.5.2    | Assumptions Underlying the Physical Model . . . . .                        | 100        |
| 4.5.3    | Priors and the Prospects for Model Selection . . . . .                     | 103        |
| 4.6      | Conclusions . . . . .  | 105        |
| <b>5</b> | <b>Signatures of Accreting Black Holes at Redshifted 21-cm Wavelengths</b> | <b>110</b> |
| 5.1      | Context . . . . .  | 110        |
| 5.2      | Introduction . . . . .   | 111        |
| 5.3      | Theoretical Framework . . . . .  | 113        |
| 5.3.1    | Astrophysical Models . . . . .   | 114        |
| 5.3.2    | Cosmological Radiative Transfer . . . . .                                  | 115        |
| 5.3.3    | Ionization & Heating Rates . . . . .                                       | 116        |
| 5.3.4    | Global 21-cm Signal . . . . .  | 117        |
| 5.4      | The Code . . . . .   | 118        |
| 5.4.1    | Discretizing the Radiative Transfer Equation . . . . .                     | 119        |
| 5.4.2    | Accuracy & Expense . . . . .   | 123        |
| 5.5      | Accreting Black Holes in the Early Universe . . . . .                      | 126        |
| 5.6      | Discussion . . . . .   | 131        |
| 5.6.1    | An Evolving IGM Optical Depth . . . . .                                    | 133        |
| 5.6.2    | Neutral Absorption . . . . .   | 133        |
| 5.6.3    | Accretion Physics . . . . .  | 136        |
| 5.6.4    | Choosing Representative Parameter Values . . . . .                         | 137        |
| 5.6.5    | Helium Effects . . . . .   | 138        |
| 5.7      | Conclusions . . . . .  | 139        |

|          |   |            |
|----------|---|------------|
| <b>6</b> | <b>Optimized Multi-Frequency Spectra for Applications in Radiative Feedback and Cosmological Reionization</b> | <b>140</b> |
| 6.1      | Context . . . . .   | 140        |
| 6.2      | Introduction . . . . .  | 141        |
| 6.3      | Radiative Transfer Framework . . . . .  | 144        |
| 6.4      | Assessing the Consequences of Discrete Radiation Fields . . . . .   | 149        |
| 6.4.1    | 10 <sup>5</sup> K Blackbody . . . . .   | 149        |
| 6.4.2    | Power-Law X-Ray Source . . . . .  | 152        |
| 6.5      | Optimization Strategy . . . . .   | 155        |
| 6.6      | Results . . . . .   | 157        |
| 6.6.1    | Optimal Discrete SEDs . . . . .   | 157        |
| 6.6.2    | Confirmation with One-dimensional Calculations . . . . .  | 160        |
| 6.6.3    | Three-dimensional Radiation-hydrodynamic Simulations with <i>Enzo</i> . . . . .                               | 161        |
| 6.7      | Discussion . . . . .  | 163        |
| 6.8      | Conclusions . . . . .   | 165        |
| <b>7</b> | <b>Conclusions and Future Work</b>  | <b>172</b> |
|          | <b>Bibliography</b>   | <b>177</b> |
|          | <b>Appendix</b>   |            |
| <b>A</b> | <b>The Differential Brightness Temperature</b>  | <b>196</b> |
| <b>B</b> | <b>Non-Equilibrium Chemistry in a Gas of Primordial Composition</b>   | <b>201</b> |
| <b>C</b> | <b>Cosmological Radiative Transfer: Test Problem</b>  | <b>203</b> |
| <b>D</b> | <b>1-D Radiative Transfer: Test Problems</b>  | <b>206</b> |

|          |  |            |
|----------|--|------------|
| <b>E</b> | <b>Secondary Ionization &amp; Heating</b>          | <b>210</b> |
| <b>F</b> | <b>Multi-Frequency vs. Multi-Group Transfer</b>    | <b>211</b> |
| F.1      | 'Multi-Group' Methods . . . . .                    | 211        |
| F.2      | Analytic Limits . . . . .                          | 211        |
| F.2.1    | Perfectly Optically Thin . . . . .                 | 211        |
| F.2.2    | Optically Thin Cells, Arbitrary $\tau_v$ . . . . . | 212        |
| F.2.3    | Small Optical Depth . . . . .                      | 212        |
| F.2.4    | General Case . . . . .                             | 216        |
| <b>G</b> | <b>Simulated Annealing</b>                         | <b>217</b> |

## Tables

### Table

|     |   |     |
|-----|---|-----|
| 1.1 | History of $\tau_e$ . . . . .                                     | 24  |
| 2.1 | Features of the global 21-cm signal . . . . .                     | 51  |
| 4.1 | Reference Model Properties and Simulated Constraints . . . . .    | 81  |
| 4.2 | Parameter Space Explored . . . . .                                | 87  |
| 5.1 | Parameter Space Explored . . . . .                                | 132 |
| 6.1 | Optimal SEDs for $10^5$ K Blackbody Sources . . . . .             | 158 |
| 6.2 | Optimal SEDs for $\alpha = 1.5$ Power-Law X-ray Sources . . . . . | 158 |
| B.1 | Description of terms in above equations. . . . .                  | 202 |

## Figures

### Figure

- 1.1 All-sky map of the cosmic microwave background radiation from *Planck*. Contrast between blue and red regions corresponds to temperature fluctuations of order  $10^{-5}$ . . . . . 3
- 1.2 Cooling curves for primordial gas at the  $z \sim 10$  cosmic mean density,  $n_{\text{H}} = 0.045 \text{ cm}^{-3}$ . Solid red line shows that of a purely atomic hydrogen and helium gas, with peaks corresponding to temperatures at which collisional excitation cooling of H I and He II becomes efficient. Dashed blue curve shows the same quantity for a pure  $\text{H}_2$  gas. From (Barkana and Loeb, 2001). . . . . 6
- 1.3 Model spectral energy distributions from metal-poor ( $Z = 0.001 Z_{\odot}$ ) and metal-enriched ( $Z = 0.04 Z_{\odot}$ ) stellar populations with Salpeter a Salpeter initial mass function. The solid lines show the SED 1 Myr after a  $10^6 M_{\odot}$  burst of star formation, while the dashed lines show the SEDs 10 Myr after the initial burst. Dotted vertical lines denote the He II ionization threshold and H I ionization threshold from left to right. Adapted from (Leitherer et al., 1999). . . . . 8
- 1.4 *Left*: X-ray Luminosity star-formation rate ( $L_X$ -SFR) relation from (Mineo et al., 2012b). *Right*: X-ray SED of star-forming galaxy (per unit star-formation), assuming XRBs have  $\alpha = 1.5$  power-law spectra. The solid green line shows the  $L_X$ -SFR of Mineo et al. (2012b), while dashed and dotted lines show factor of 5 and 10 amplification of the Mineo et al. (2012b) relation. Black and blue curves are the same as those in Figure 1.3. . . . . 11

- 1.5 Cartoon showing a plausible guess for the formation of the first galaxies. **(1)** The first stars form in small halos via  $H_2$  cooling. **(2)** These stars empty evacuate their host halos of gas via photoevaporation and supernova blast-waves, changing the mode of star formation. **(3)** The IR and UV radiation from low- and high-mass stars suppresses star formation throughout the universe, gradually increasing the characteristic mass of star-forming halos. **(4)** The first self-sustaining galaxies eventually form in massive halos, as accreting stellar remnants of the first stars in binary systems give rise to a relatively uniform X-ray background. **(5)** X-rays cause large-scale heating, which increases the characteristic mass of star-forming halos even further. The Epoch of Reionization has begun, and PopIII stars have likely become extinct. . . . . 13
- 1.6 Artists depiction of the evolution of structure in the Universe, from the CMB (far left), to reionization (middle), to the present-day (far right). . . . . 14
- 1.7 Empirical fit to the rest-frame  $1500\text{\AA}$  galaxy luminosity function at  $z \sim 6$  (Oesch et al., 2012). Top panel shows the galaxy luminosity function itself, while the bottom panel shows the cumulative luminosity emitted by galaxies fainter than the corresponding value of  $L$ . Clearly, faint galaxies (i.e., those fainter than  $L_*$ ), are expected to dominate the volume-averaged luminosity, though exactly how much they dominate depends on the faintest galaxy,  $L_{\min}$  (dotted, solid, dashed, and dash-dotted lines). . . . . 18
- 1.8 Dark matter halo mass function at  $z = 6, 8$  and  $10$ . Assumes the Sheth and Tormen (2002) form of the mass function and *Planck* cosmological parameters. Computed using the HMF code (Murray et al., 2013b). . . . . 20
- 1.9 Spectra of 19 quasars at  $5.764 < z < 6.42$  from (Fan et al., 2006) showing the emergence of the Gunn-Peterson trough at  $z \sim 6$ . . . . . 21

1.10 *Left:* Early models for the global 21-cm signal from Shaver et al. (1999), including a toy “step” model of reionization (a) and two models from the numerical simulations of Gnedin and Ostriker (1997) and Baltz et al. (1998) (b and c, respectively). *Right:* Re-produced step model of Shaver et al. (1999) (black) compared with more recent physically motivated models, including a tanh model of reionization with  $z_{\text{rei}} = 8$  and  $\Delta z_{\text{rei}} = 1$  (blue), and an empirically constrained model of reionization from Robertson et al. (2015) (red). The physical models assume  $T_S \gg T_\gamma$ , i.e., they use Equation 1.27. Note that the y-axis in the right panel has been re-normalized relative to the CMB, and re-expressed in units of mK, rather than K. The dotted black line shows the maximum allowed amplitude of the signal, i.e., the saturated limit with  $\bar{x}_i = 0$ . . . . . 28

1.11 Maps of the galactic foreground at 40 MHz (top), 80 MHz (middle), and 120 MHz (bottom) computed using the de Oliveira-Costa et al. (2008) sky model. . . . . 30

1.12 The evolution of a slice of the Universe (upper panel; compare to Figure 1.6), from early times at left to late times at right as well as the corresponding sky-averaged 21-cm signal relative to the CMB (lower panel). The first stars form at  $z \sim 30$  in the fiducial model simulation (labeled B on black curve) and “turn on” the 21-cm signal in absorption against the CMB (light blue in top panel). The fiducial model assumes the first sources are similar to those in nearby galaxies. At  $z \sim 20$  (Turning Point C), accreting black holes heat the gas, transforming the signal from absorption to emission ( $z \sim 12$ ; Turning Point D, red in top panel). At later times, ionized bubbles (black, upper panel) grow to fill the universe by  $z \sim 8$ . The bottom panel illustrates the current theoretical uncertainties in first star and black hole parameters. Blue curves vary the UV flux from the first stars by a factor of 100 while green curves vary the X-ray heating rate by a factor of 100. Figure adapted from Pritchard and Loeb (2010) using the new reference model from Mirocha et al. (2015). . . . . 31

- 2.1 Example global 21-cm spectrum (top), its derivative (middle), and corresponding thermal evolution (bottom) for a model in which reionization is driven by PopII stars, and the X-ray emissivity of the universe is dominated by high-mass X-ray binaries. . . . . 38
- 2.2 Values  $J_\alpha = h\nu_\alpha \widehat{J}_\alpha$  and  $d \log J_\alpha / d \log t$  that give rise to turning point B at position  $(z_B, \delta T_b(z_B))$ . The color scale shows the value of  $J_\alpha$  (top panel, in units of  $J_{21} = 10^{-21} \text{ erg s}^{-1} \text{ cm}^{-2} \text{ Hz}^{-1} \text{ sr}^{-1}$ ), and  $d \log J_\alpha / d \log t$  (bottom panel) required for turning point B to appear at the corresponding position in the  $(z_B, \delta T_b(z_B))$  plane, under the assumptions given in Section 3.1. The gray shaded region is excluded unless heating occurs in the dark ages. For reference, the highlighted black contours represent Ly- $\alpha$  fluxes (assuming a flat spectral energy distribution at energies between Ly- $\alpha$  and the Lyman-limit,  $h\nu_\alpha \leq h\nu \leq h\nu_{\text{LL}}$ ), corresponding to Lyman-Werner band fluxes of  $J_{\text{LW}}/J_{21} = \{10^{-2}, 10^{-1}, 2 \times 10^{-1}\}$  (from top to bottom), which roughly bracket the range of fluxes expected to induce negative feedback in minihalos at  $z \sim 30$  (Haiman et al., 2000). . . . . 42
- 2.3 Cooling rate of the universe under different assumptions. The black line is an approximate analytic solution (Peebles, 1993), while the blue and green lines are numerical solutions. The blue curve considers cooling via radiative recombination, collisional excitation and ionization, and the Hubble expansion, and heating via Compton scattering. The green line is an even more detailed numerical solution obtained with the COSMOREC code (Chluba and Thomas, 2011), which includes a multi-level atom treatment and many radiative transfer effects. . . . . 43

- 2.4 *Top:* constraints on the cumulative energy deposition as a function of the redshift and brightness temperature of turning point C. The gray region is disallowed because it requires cooling to be more rapid than Hubble (adiabatic) cooling. *Bottom:* Constraints on the co-moving heating rate density ( $\text{cMpc}^{-3}$  means co-moving  $\text{Mpc}^{-3}$ ) as a function of  $z_C$  alone. The blue region includes heating rate densities insufficient to overcome the Hubble cooling, while the red region is inconsistent with the existence of an absorption feature at  $z_C$  because such heating rates would instantaneously heat  $T_K$  above  $T_\gamma$ . The triangles, plotted in increments of 50 mK between  $\delta T_b = \{-250, -50\}$  mK show how a measurement of  $\delta T_b(z_C)$ , as opposed to  $z_C$  alone, enables more stringent upper limits on the heating rate density. . . . . 45
- 2.5 Constraints on the co-moving heating rate density (once again  $\text{cMpc}^{-3}$  means co-moving  $\text{Mpc}^{-3}$ ) as a function of the absorption-emission transition redshift,  $z_{\text{trans}}$ , and the slope of the 21-cm signal at that redshift. As in Figure 2.4, the blue region indicates heating rates insufficient to overcome the Hubble cooling, while the red region denotes heating rates that would instantaneously heat  $T_K$  above  $T_\gamma$ . The triangles show how measuring the slope of the signal at  $z_{\text{trans}}$  can provide a lower limit on  $\epsilon_{\text{heat}}$ . . . . . 47

- 2.6 Plausibility of an ionization-driven absorption feature assuming *tanh* models of reionization with  $z_{\text{rei}} = 8, 10, \text{ and } 12$  from left to right. The filled contours denote measures of  $\delta T_b(z)$  (and thus  $\bar{x}_i$  assuming an adiabatically-cooling universe) which correspond to ionization histories consistent with WMAP 9 values of  $\tau_e$  (Bennett et al., 2012) at the 1, 2, and 3- $\sigma$  level (green, blue, and red, respectively). However, while the filled contours denote plausible reionization scenarios, not all of them would induce a turning point in the global 21-cm signal. The white contour denotes  $(z, \delta T_b)$  pairs where Equation (2.4) is satisfied exactly, meaning  $(z, \delta T_b)$  points lying within the filled contours *and* along the white contour mark locations where turning point C would be a produced by ionization and also be consistent with the CMB constraint. The symbols denote *tanh* models with  $\Delta z_{\text{rei}} = 1, 2, 4, 6, 8$  (diamond, upward/rightward/downward/leftward-facing triangles, respectively). The values of  $\Delta z_{\text{rei}} \leq 7.9$  are consistent with the most conservative (model-dependent) constraints from South Pole Telescope (via the kinetic Sunyaev-Zeldovich (SZ) effect; Zahn et al., 2012), which assume no prior knowledge of angular correlations in the cosmic infrared background and thermal SZ power. . . . . 48
- 3.1 Structure in the de Oliveira-Costa et al. (2008) global sky model, shown via the residual between the spectrum in a single (representative) pixel in the de Oliveira-Costa et al. (2008) map and a  $\log \nu$ - $\log T$  polynomial fit to that spectrum. The dotted horizontal marks a residual of 10 mK. . . . . 61

- 3.2 The ability of different parameterizations to fit the input global 21-cm signal, which was generated with ARES. The solid black line shows the input model, which also assumes foregrounds modelled as third-order polynomials in  $\log\nu$ - $\log T$ , an idealized instrument model in which the antenna has flat 85% sensitivity between 35 and 120 MHz, and an experiment which observes four independent sky regions for 250 hours each. The recovered signal using the turning points parametrization is shown in the solid blue line; if we shift this down so that the temperature of turning point C agrees with the input signal, we have the dashed red line. If we use the actual positions of the maxima and minima of the ARES signal as the parameter values in our turning points model, we produce the magenta dot-dashed curve. Finally, if the synthetic dataset is fit using the tanh model, the signal we recover is shown as the cyan, dotted curve. . . . . 64
- 3.3 We show how the constraints on the  $\delta T_b$  history from the tanh fit translate into constraints on the turning points. In each panel, the dotted lines show the input parameter value. The dashed vertical line in panel (e) shows the upper end of the frequency range, while the nearly horizontal line shows the path the signal would follow in a hot, completely neutral Universe for which the emission signal saturates. The dark blue and green contours show 1- and 2- $\sigma$  confidence regions. . . . . 65
- 3.4 A comparison of the 68% confidence regions for constraints on the positions of the turning points for three different datasets: the same as that used in Fig. 3.3 (black); a dataset where the upper limit of the frequency range is set to 100 MHz instead of 120 MHz (blue); and a dataset where the foregrounds are fourth-order polynomials in  $\log\nu$ - $\log T$  rather than third-order (green). . . . . 66

- 3.5 The constraints on the IGM parameters for which the constraining power comes mainly from turning point C. These parameters are the kinetic temperature of the gas (colder than the CMB at this point), the heating rate density, and the Ly- $\alpha$  flux. The dataset assumes 1000 hrs of data split between four sky regions, though the results are qualitatively similar for fewer sky regions and for shorter integrations. The black lines show constraints (1D posterior distributions and 1- $\sigma$  contours) coming directly from the tanh fit to the dataset, while the blue lines show the results obtained with a more complex foreground model. The green lines assume that only the positions of the turning points and the covariances between the turning points are known, whereas the red lines assume that only the turning point positions are known (nothing about the shape of the signal in between) and that the errors on the turning points are independent and Gaussian, with the positions and the size of the errors coming from the tanh fit. Dotted vertical and horizontal lines show the true values. . . . . 68
- 3.6 The constraints on the IGM parameters for which the constraining power comes mainly from turning point D. These parameters are the kinetic temperature of the gas (hotter than the CMB at this point), the heating rate density, the volume filling factor of H II regions,  $Q_{\text{HII}}$ , and the volume-averaged ionization rate,  $\Gamma_{\text{HI}}$ . The colors have the same meaning as those shown in Figure 3.5. . . . . 69
- 3.7 Constraints on the curvature, indicated by  $\delta''$  (in units of  $\text{mK MHz}^{-1}$ ), of the signal at the turning points. Blue and green regions are 68% and 95% confidence regions, respectively. . . 71
- 3.8 Constraints on the turning point positions as a function of the number of sky regions and integration time. Green, black, and blue points correspond to constraints on turning points B, C, and D, respectively, and are slightly offset in the x-direction for clarity. The top row shows errors in the frequency of the turning points, relative to their input values, while the bottom row shows errors in the amplitude of each turning point. All error-bars shown are 68 per cent credible intervals. Note that the y range for the panels on the right has been zoomed in. . . . . 72

- 4.1 Illustration of the basic dependencies of the global 21-cm signal. The black line is the same in each panel, representing our reference model (see Table 4.1), while all solid green (blue) lines correspond to a factor of 2 increase (decrease) in the parameter noted in the upper left corner, and dashed lines are factor of 10 changes above and below the reference value. The right half of the figure is qualitatively similar to Figure 2 of Pritchard and Loeb (2010), though our reference values for the  $\xi$  parameters are different, as are our cosmological parameters, leading to quantitative differences. The dotted lines show the maximum allowed amplitude of the signal (i.e., the amplitude of the signal when  $\bar{x}_i = 0$  and  $T_S \gg T_\gamma$ ), and the minimum allowed amplitude of the signal (set by assuming  $T_S = T_K = T_{\text{ad}}(z)$ , where  $T_{\text{ad}}$  is the gas temperature in an adiabatically-cooling Universe). Because we refer to the spectral features as turning points B, C, and D throughout the paper, we annotate them in the lower left panel for reference. . . . . 80
- 4.2 *Bottom:* Rate of collapse onto halos above a given virial temperature threshold,  $T_{\text{min}}$ , scaled to the Hubble time. *Top:* Effective power-law index (Eq. 4.11) as a function of redshift for each  $df_{\text{coll}}/dt$  model. Empirical power-laws from Oesch et al. (2012) are overlaid for comparison, as well as the best-fit 4-parameter SFRD model used in Robertson et al. (2015). 83
- 4.3 Comparison of EM1 and EM2 for turning point D, the point at which they differ most substantially (see Table 4.1). In blue and red, solid (dashed) contours denote 68% (95%) confidence regions for EM1 and EM2, respectively. The dotted black line shows the saturated limit, in which  $\bar{x}_i = 0$  and  $T_S \approx T_K \gg T_\gamma$ , while the dashed vertical line denotes the position of turning point D in our reference model (solid black curve). Note that the EM1 error ellipse for turning point D extends to  $\sim 130$  MHz, beyond the edge of the bandpass considered in Harker et al. (2015), though the  $2 - \sigma$  upper limit for EM2 is within the assumed band, at  $\nu_D \sim 117$  MHz. . . . . 86

- 4.4 Constraints on the background Ly- $\alpha$  intensity at the redshift of turning point B, in units of  $J_{21} = 10^{-21} \text{erg s}^{-1} \text{cm}^{-2} \text{Hz}^{-1} \text{sr}^{-1}$ . Dotted vertical line shows the input value, which occurs at  $z = 29$  in our reference model. The black histogram is the constraint obtained if using EM1, while the analogous constraint for EM2 is shown in green. . . . . 89
- 4.5 Constraints on the IGM temperature, heating rate density, and Ly- $\alpha$  background intensity at the redshift of turning point C. The heating rate density,  $\epsilon_X$ , is expressed in units of  $\text{erg s}^{-1} \text{cMpc}^{-3}$ , while  $J_\alpha$  is once again expressed in units of  $J_{21} = 10^{-21} \text{erg s}^{-1} \text{cm}^{-2} \text{Hz}^{-1} \text{sr}^{-1}$ . Dotted vertical lines show the input values, which occur at  $z = 19$  in the reference model. Open contours are those obtained with EM1 (68% and 95% confidence regions in solid and dashed curves, respectively), while filled contours are the constraints obtained by EM2 (68% and 95% confidence regions in blue and green, respectively). The color-scheme along the diagonal is the same as in Figure 4.4, with EM1 (EM2) curves in black (green). . . . . 91
- 4.6 Constraints on the IGM temperature, volume-filling factor of ionized gas,  $Q_{\text{HII}}$ , heating rate density, and volume-averaged ionization rate,  $\Gamma$ , at the redshift of turning point D, which occurs at  $z = 11.75$  in our reference model. Open contours are 68% (solid) and 95% (dashed) confidence regions for EM1, while filled contours show the results from EM2, with 68% and 95% confidence regions shown in blue and green, respectively. Input values are denoted by black dotted lines in each panel. . . . . 93
- 4.7 Constraints on our 4-parameter reference model. Filled contours in the interior panels are 2-D marginalized posterior PDFs with 68% confidence intervals shaded blue and 95% confidence regions in green. Panels along the diagonal are 1-D marginalized posterior PDFs for each input parameter, with  $1-\sigma$  asymmetric error-bars quoted, as computed via the marginalized cumulative distribution functions. Dotted lines denote the input values of our reference model (Table 4.1). Bins of width 0.05 dex are used in each panel. Annotated best-fit values and error bars along the diagonal are those associated with EM2. . . . . 95

- 4.8 *Left:* Ratio of yields in the ionizing ( $h\nu > 13.6$  eV) and LW ( $10.2 \leq h\nu/\text{eV} \leq 13.6$ ) bands per stellar baryon as a function of metallicity and stellar IMF. Symbols represent model SEDs generated with STARBURST99 (those shown in Figures 1, 3, and 5 of Leitherer et al., 1999), while the horizontal lines show the values one obtains for pure blackbodies at 10,000, 30,000, and 50,000 K from bottom to top. The filled symbols are investigated in more detail in the right panel. *Right:* Constraints on the stellar population and the escape fraction of ionizing radiation. The solid contour is the  $2\text{-}\sigma$  constraint on our reference model, i.e., identical to the green area of panel (e) in Figure 4.7, while dashed contours correspond to turning point constraints from EM2 (see Table 4.1), which has a tighter constraint on the emission maximum (turning point D). The blue, green, and red bands have the same value of  $N_{\text{ion}}/N_{\text{LW}}$  as the filled plot symbols in the left-hand panel, while the cross-hatched band instead adopts a pure 50,000 K blackbody spectrum for the stellar population. The width of each band corresponds to a factor of 2 change in the escape fraction,  $0.1 \leq f_{\text{esc}} \leq 0.2$ . . . . . 107
- 4.9 Constraints on sources of X-rays. The solid and dashed histograms are identical to the black and green PDFs shown in panel (i) of Figure 4.7, respectively, while dotted vertical lines denote values representative of 2x and 4x enhancements to the  $L_X$ -SFR relation, holding the star-formation efficiency constant at  $f_* = 0.1$ . For reference, we show the  $3\text{-}\sigma$  upper limit from extraction EM2 in red. Even if  $f_* = 0.01$ , we limit  $f_X < 20$ . . . . . 107
- 4.10 Constraints on the 4-parameter model, assuming the emission maximum is not detected. Solid black contours are the 95% confidence intervals of our reference fit to all three features. Blue contours are 95% confidence regions obtained when only turning points B and C are used in the fit, while the green hatched regions show areas of parameter space excluded at 95% confidence if only turning point C used in the fit. When only upper or lower limits are available, we denote them with arrows in the marginalized 1-D PDFs. . . . . 108

- 4.11 Constraints on the 4-parameter model, assuming turning point B is not detected. Solid black contours are the 95% confidence intervals of our reference fit to all three features. Blue contours are 95% confidence regions obtained when only turning points C and D are used in the fit, while the green hatched regions show areas of parameter space excluded at 95% confidence if only turning point D used in the fit. When only upper or lower limits are available, we denote them with arrows in the marginalized 1-D PDFs. . . . . 109
- 5.1 X-ray background intensity,  $J_\nu$ , at  $z = 20$  assuming a population of  $10 M_\odot$  BHs. The IGM optical depth,  $\bar{\tau}_\nu$ , is sampled at 128 logarithmically spaced frequencies between 0.2 and 30 keV, and linearly in redshift by  $\Delta z = 0.4$  (red), 0.2 (green), 0.1 (blue), and 0.05 (cyan). Poor redshift resolution always leads to overestimates of the background intensity at soft X-ray energies ( $h\nu \lesssim 0.5$  keV) since the integrand is a rapidly evolving function of redshift. The solid black line is the full numerical solution obtained by integrating Equation 5.4 with a Gaussian quadrature technique, and the dashed black line is the same calculation assuming the optically thin  $\bar{x}_i(z) = \text{constant} = 1$  limit as opposed to  $\bar{x}_i(z) = \text{constant} = 0$ . In order to prevent errors in  $J_\nu$  at all energies  $h\nu \geq 0.2$  keV, the redshift dimensions of  $\bar{\tau}_\nu$  must be sampled at better than  $\Delta z = 0.05$  resolution. . . . . 120
- 5.2 Accuracy of presented algorithm. *Top*: Relative error in the heating rate density,  $\epsilon_X$ , as a function of the number of redshift points,  $n_z$ , used to sample  $\bar{\tau}_\nu$ , as compared to a brute-force solution to Equation 5.11 using a double Gaussian quadrature integration scheme. *Middle*: Relative error in the cumulative heating as a function of  $n_z$ . *Bottom*: Relative error in the position of the 21-cm minimum, in redshift (black crosses) and amplitude (blue crosses). Dotted and dashed lines indicate 0.1% and 1% errors, respectively. . . . . 124

- 5.3 Testing the approximation of Equations 5.24 and 5.25. Dashed lines represent the approximate solutions, while solid lines represent the full solution for the global 21-cm signal using the procedure outlined in Section 5.4. *Left:* X-ray sources are assumed to have power-law (PL) SEDs with spectral index  $\alpha$ , extending from 0.2 to 30 keV. *Right:* X-ray sources are assumed to have multi-color disk (MCD) SEDs (Mitsuda et al., 1984). All sources have been normalized to have the same luminosity density above 0.2 keV ( $3.4 \times 10^{40} \text{erg s}^{-1} (M_{\odot} \text{yr}^{-1})^{-1}$ ), and all calculations are terminated once the emission peak ( $12 \lesssim z \lesssim 14$ ) has been reached. For the hardest sources of X-rays considered (left:  $\alpha = -0.5$ , right:  $M_{\bullet} = 10 M_{\odot}$ ), the global 21-cm minimum is in error by up to  $\sim 15$  mK in amplitude and  $\Delta z \simeq 0.5$  in position when Equation 5.24 is used to compute  $\epsilon_X$ . . . . . 125
- 5.4 Subset of SEDs used in this work. *Top panel:* Assuming  $M_{\bullet} = 10 M_{\odot}$ , varying the fraction of disk photons scattered into the high energy power-law tail,  $f_{\text{sc}}$ , and the spectral index of the resulting high energy emission,  $\alpha$ , using the SIMPL model (Steiner et al., 2009). Solid, dashed, dotted, and dash-dotted black lines represent neutral absorption corresponding to  $N_{\text{HI}}/\text{cm}^{-2} = 0, 10^{20}, 10^{21},$  and  $10^{22}$ , respectively. Solid and dashed lines of different colors correspond to high energy emission with power-law indices of  $\alpha = -2.5$  and  $\alpha = -1.5$ , respectively, with the color indicating  $f_{\text{sc}}$  as shown in the legend. *Bottom panel:* Pure MCD SEDs for  $M_{\bullet} = 10 - 10^4 M_{\odot}$ , with no intrinsic absorption or Comptonization of the disk spectrum. The solid black line is our reference model, and is the same in both panels. . . . . 128

- 5.5 Evolution of the 21-cm brightness temperature for different BH SED models. *Left:* Effects of coronal physics, parameterized by the fraction of disk photons up-scattered by a hot electron corona,  $f_{\text{sc}}$ , and the resulting spectral index of up-scattered emission,  $\alpha$ , using the SIMPL Comptonization model of Steiner et al. (2009). The colors correspond to different values of  $f_{\text{sc}}$ , while the width of each band represents models with  $-2.5 \leq \alpha \leq -0.5$  (the upper edge of each band corresponds to the softest SED at fixed  $f_{\text{sc}}$ , in this case  $\alpha = -2.5$ ). *Right:* Effects of BH mass and neutral absorbing column. Colors correspond to  $N_{\text{H I}}$ , while the width of each band represents models with  $10 \leq M_{\bullet}/M_{\odot} \leq 10^3$  (the upper edge of each band corresponds to the softest SED at fixed  $N_{\text{H I}}$ , in this case  $M_{\bullet} = 10^3 M_{\odot}$ ). The dashed black line is our reference “pure MCD” model with  $M_{\bullet} = 10 M_{\odot}$ . The black and blue regions overlap considerably, indicating that absorbing columns of  $N_{\text{H I}} \gtrsim 10^{20} \text{ cm}^2$  are required to harden the spectrum enough to modify the thermal history. Every realization of the signal here has the exact same ionization history, Ly- $\alpha$  background history, and BH accretion history. As in Figure 5.3, all calculations are terminated once the peak in emission is reached. Coronal physics influences the global 21-cm minimum at the  $\lesssim 10$  mK level, while  $M_{\bullet}$  is a 10-20 mK effect and  $N_{\text{H I}}$  is potentially a  $\sim 50$  mK effect. . . . . 130
- 5.6 Consequences of the  $\bar{x}_i = \text{constant} = 0$  approximation on the background radiation field for our reference model (see Table 5.1). *Top:*  $\tanh$  ionization histories considered, i.e.,  $\bar{x}_i(z) \propto \tanh((z - z_r)/\Delta z)$ . *Bottom:* Angle-averaged background intensity,  $J_{\nu}$ , at  $z = 10, 12$  and  $14$  (black, blue, green) assuming a neutral IGM for all  $z$  (solid), compared to increasingly early and extended reionization scenarios (dotted and dashed). Errors in the background intensity due to the  $\bar{x}_i = \text{constant} = 0$  could be important at  $z \lesssim 14$ , assuming early and extended reionization scenarios (e.g.,  $z_r = 12, \Delta z = 4$ ), though by this time the global 21-cm signal is likely insensitive to the thermal history. . . . . 134

|      |   |     |
|------|---|-----|
| 6.1  | Comparison of ionization (top) and temperature (bottom) profiles around a $10^5$ K blackbody source after 10 Myr (left) and 100 Myr (right) using continuous (black) and monochromatic (red) SEDs. Solid lines in the top panels correspond to the neutral fraction ( $x_{\text{H I}}$ ), while dashed lines correspond to the ionized fraction ( $x_{\text{H II}}$ ). We apply these line color and line style conventions for all radial profiles presented in this paper. . . . .  | 150 |
| 6.2  | Comparison of hydrogen (top) and helium (bottom) ionization profiles around an $\alpha = 1.5$ power-law X-ray source after 45 Myr using continuous (black) and monochromatic (red) SEDs. . . . .  | 154 |
| 6.3  | Comparison of temperature profiles around an $\alpha = 1.5$ power-law X-ray source after 45 Myr using continuous (black) and monochromatic (red) SEDs. . . . .  | 154 |
| 6.8  | Comparison of ionization (top) and temperature (bottom) profiles around a $10^5$ K blackbody source after 100 Myr showing the solutions obtained using continuous (black), monochromatic (red), and optimal four-bin discrete (blue circles/squares) SEDs. . . . .  | 169 |
| 6.10 | Comparison of the four-bin solutions of Wise and Abel (2011) (black) and our own (blue crosses) in a radiation-hydrodynamic simulation using the <i>Enzo</i> code. The setup is the same as in RT06 Test Problem 2, except hydrodynamics is included. . . . .   | 170 |
| A.1  | Cartoon of the radiative transfer problem of the 21-cm signal. . . . .  | 197 |
| C.1  | Cosmic X-ray background spectrum at $z = 20$ for $\alpha = -1.5$ and $\beta = -3$ . Normalization of the y-axis can be scaled arbitrarily depending on the normalization of the emissivity. The deviation at high energies is due to the fact that the analytic solution is not truncated by $z_f$ or $E_{\text{max}}$ , meaning there are always higher energy photons redshifting to energies $h\nu \leq h\nu_{\text{max}}$ . The numerical solutions are computed with finite integration limits and truncated at $E_{\text{max}}$ , such that the emissivity at $h\nu > h\nu_{\text{max}}$ is zero, resulting in no flux at $h\nu \geq h\nu_{\text{max}}$ . Elsewhere, the agreement is very good, with discrepancies arising solely due to the use of approximate bound-free photo-ionization cross sections in the analytic solution. . . . . | 205 |

# Chapter 1

## Introduction

In this chapter, I will focus on the broader context of this thesis and defer most technical details to later chapters and appendices. In Section 1.1, I will introduce the high- $z$  Universe<sup>1</sup> as the sub-field in astronomy & astrophysics it has become. Why is it difficult to study, and why is it worth pursuing? Then, in Section 1.2, I will turn to current observational diagnostics of the high- $z$  Universe that are beginning to test theoretical models. This will set the stage for a discussion of the 21-cm background to follow in (§1.3), including the basic physics involved and early predictions for the spectral structure of the global 21-cm signal. I will close this chapter by motivating my thesis work within the context of Sections 1.1-1.3, and provide an outline for chapters to follow.

### 1.1 The High- $z$ Universe

Observations of the cosmic microwave background (CMB) reveal a universe of great simplicity just 400,000 years after the Big Bang (BB), varying in density and temperature on average by a factor of only  $10^{-5}$  across the cosmos. Yet, from this homogeneous state emerged a landscape teeming with stars, galaxies, and super-massive black holes (BHs) – all in less than one billion years. This brief window in time is bracketed by observations of the CMB at redshift  $z \approx 1100$ , and quasars at redshift  $z \approx 6$ , but the intervening  $\sim$  billion years remain virtually unexplored.

This may not seem like great cause for concern given that the Universe is  $\sim 13.7$  Giga-years (Gyr)

---

<sup>1</sup> The “high- $z$  Universe” is a vague term, whose meaning has evolved considerably over the last few decades. For example, in the early 1960s the most distant objects known were at  $z \sim 0.4$ , and it wasn’t until the late 1980s that objects at  $z > 4$  had been found. For the remainder of this document, the phrase “high- $z$ ” loosely corresponds to  $z \gtrsim 6$ , i.e., the time from the Big Bang until the end of the Epoch of Reionization.

old, meaning the entire  $z > 6$  epoch constitutes less than 10% of the current age of the Universe. However, the first stars are thought to be exotic, massive  $\sim 100 M_{\odot}$  stars that transform their environs in life through intense ionizing radiation fields and in death via mechanical heating and chemical enrichment of nearby clouds – the raw material from which the next generation of stars may form. The formation mechanism of the first BHs is as intriguing as that of the first stars. If the first BHs were the remnants of the first stars, and thus likely 10's of solar masses initially, they would need to grow in mass by a factor of  $\sim 10^7$  or  $10^8$  in less than a Gyr in order to become the engines powering  $z \sim 6$  quasars. A tempting short-cut in mass is available if, for some reason, black holes can form via the direct collapse of massive proto-galactic clouds.

Part of the allure of the high- $z$  Universe are these puzzles, interesting in their own right, but also in the broader context of galaxy formation. How did the first stars and BHs – exotic or not – sculpt the first galaxies? When did galaxies begin to resemble objects not too dissimilar from those we see in the local Universe?

There are three main reasons that answers to these questions remain elusive:

- (1) The first galaxies lie at great cosmological distances and are thus difficult to observe directly simply because they are faint.
- (2) The luminosity of galaxies is dominated by their most massive stars, whose spectra peak at ultraviolet (UV) wavelengths. This means that observers detect  $z > 6$  sources at IR wavelengths, which are absorbed readily by molecules in the Earth's atmosphere.
- (3) The IGM is increasingly neutral at  $z > 6$ , which makes UV sources even more difficult to observe since neutral hydrogen atoms readily absorb UV photons with energies above 13.6 eV (wavelengths  $\leq 912 \text{ \AA}$ ).

The first two difficulties can be overcome to some degree by a large, space-based, optical/infrared telescope, such as NASA's *Hubble Space Telescope*, or better yet, the *James Webb Space Telescope* (JWST). However, point #3 implies that there exists a redshift beyond which rest frame emission from galaxies at wavelengths below  $912 \text{ \AA}$  cannot be seen at all, owing to a fully neutral, and thus opaque IGM.

Given the dearth of observational constraints on high- $z$  galaxies, we will focus in the next three subsections on a plausible theoretical picture pieced together over the last few decades that describes the emergence of galaxies in the early Universe and their impact on the IGM. A discussion of observational tests of this picture will follow in Section 1.2.

### 1.1.1 First Stars

For a few hundred thousand years after the Big Bang, the entire Universe was a (nearly) perfectly uniform medium composed of hydrogen and helium, hot enough to keep protons and electrons from binding to form neutral atoms. As cosmic expansion continued the gas cooled, eventually falling below  $\sim 10^4$  K at which point protons and electrons could combine to form neutral hydrogen atoms. The rapid disappearance of free electrons meant most photons had scattered for the last time, streaming freely through the Universe from that moment onward. This “surface of last scattering” is now visible as the cosmic microwave background (CMB), most recently mapped by the *Planck* satellite (see Figure 1.1).

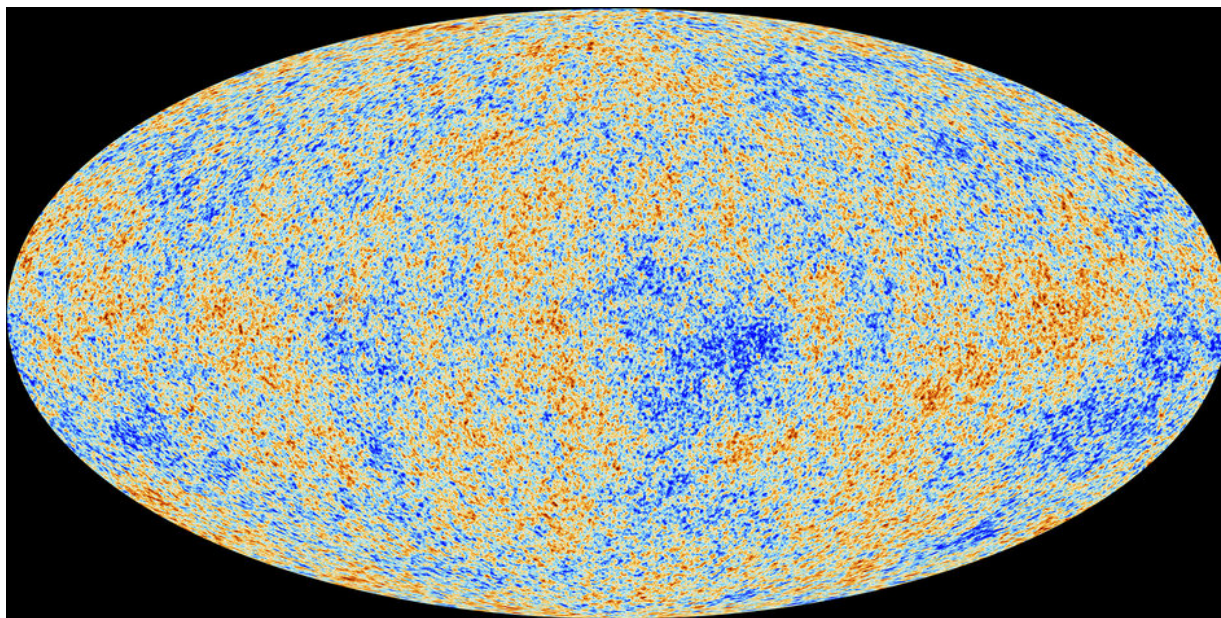


Figure 1.1 All-sky map of the cosmic microwave background radiation from *Planck*. Contrast between blue and red regions corresponds to temperature fluctuations of order  $10^{-5}$ .

In the darkness following cosmological recombination, tiny density perturbations grew under the

influence of gravity until eventually the central regions of collapsing clouds reached densities and temperatures great enough to ignite nuclear fusion. A critical milestone in the evolution of any proto-stellar cloud – whether it resides in the Milky Way or a tiny dark matter halo just a few Myr after the Big Bang – is the moment at which thermal pressure can no longer withstand the inward pull of gravity.

The first stars to form in the Universe, though we have yet to detect them directly, are sure to have been unique relative to stars today for one simple reason: by definition, as the *first* stars they formed out of chemically pristine gas clouds, since massive stars capable of forging heavy elements had yet to exist. Without heavy elements, the first proto-stellar clouds would have had difficulty cooling efficiently, thus allowing thermal pressure to stall otherwise near-certain gravitational collapse.

One can predict the sense of this metallicity effect by considering an idealized spherical cloud. In order for it to collapse, the inward pull of gravity must exceed the outward push of gas pressure. To put it another way, collapse requires the sound-crossing time of a cloud to exceed its free-fall time, i.e.,

$$t_s > t_{\text{ff}}$$

$$\frac{r}{c_s} > \sqrt{\frac{3\pi}{32G\rho}} \quad (1.1)$$

where  $r$  is radius of the cloud,  $c_s$  is the speed of sound, and  $\rho$  is the density of the cloud. Assuming a monatomic ideal gas, we find that collapse can only proceed if a cloud exceeds a particular temperature- and density-dependent value, which scales as

$$M_J \propto T^{3/2} \rho^{-1/2}. \quad (1.2)$$

The  $T^{3/2}$  scaling of this “Jeans’ Mass” implies that a hot cloud, i.e., one which cannot cool, must be more massive than a cold cloud to collapse (at fixed density). However, in a purely atomic hydrogen gas, cooling does not become efficient until temperatures of  $T \sim 10^4$  K, at which time collisional excitation of Ly- $\alpha$  and subsequent radiative decay becomes effective. Without metals or nearby sources of radiation to heat the gas, early halos would have to wait to form stars until their temperatures were driven above the  $\sim 10^4$  K atomic cooling threshold by virialization.

The virial temperature of a halo is related to its mass via (e.g., Barkana and Loeb, 2001)

$$T_{\text{vir}} = 1.98 \times 10^4 \left( \frac{\mu}{0.6} \right) \left( \frac{M_{\text{halo}}}{10^8 M_{\odot}} \right)^{2/3} \left[ \frac{\Omega_m}{\Omega_m(z)} \frac{\Delta_c}{18\pi^2} \right]^{1/3} \left( \frac{1+z}{10} \right) \text{ K} \quad (1.3)$$

where  $\mu$  is the mean molecular weight of collapsing gas,  $M_{\text{halo}}$  is the halo mass,  $\Delta_c$  is the critical overdensity for collapse, and  $\Omega_m(z)$  is the matter density relative to the critical density. Without atomic cooling, halos less massive than  $\sim 10^8 M_{\odot}$  – which constitute 99% of the collapsed mass density of the Universe at  $z > 10$  – could not have formed stars. This is the irony of small halos in the early Universe: though they could have contained nearly  $\sim 10^8 M_{\odot}$  of raw star-forming material, *they would not have been hot enough to cool and form stars.*

The consideration of molecular hydrogen dramatically alters this simple prediction (Lepp and Shull, 1984). Unlike hydrogen atoms, whose lowest lying transition is 10.2 eV above the ground state, molecular hydrogen has a series of rho-vibrational transitions that can be excited at temperatures of only a few hundred Kelvin. This leads to efficient cooling, provided that there is no incident radiation field capable of dissociating  $\text{H}_2$  (see Figure 1.2). As a result, halos with masses on the order of  $\sim 10^5 M_{\odot}$  may have begun forming stars at  $z \sim 30$  (e.g., Haiman et al., 1996, Tegmark et al., 1997).

Early numerical calculations supported the massive first-star hypothesis. Though computational limitations prevent simulations from witnessing the moment of nuclear ignition, they were able to evolve clouds to extreme densities ( $n \gtrsim 10^{20} \text{ cm}^{-3}$ ) and compute their masses, which were  $M \gtrsim 100 - 10^3 M_{\odot}$  (e.g., Bromm et al., 1999, Abel et al., 2002). The implications for reionization and galaxy formation were immediately clear: the more massive a star, the more UV photons it emits. Not only will massive stars be brighter in the UV than typical O and B type stars, but their spectra will be harder as well (owing to surface temperatures of order  $10^5 \text{ K}$  Tumlinson and Shull, 2000, Bromm et al., 2001, Schaerer, 2002). That is, PopIII stars should emit a larger relative number of Lyman continuum photons (LyC;  $h\nu > 13.6 \text{ eV}$ ) than that of O and B stars, meaning they could ionize a substantial amount of intergalactic helium, in addition to hydrogen.

The epoch of PopIII star-formation was unlikely, however, to have been long-lived. Soft UV photons (i.e., those red-ward of the Lyman edge at 13.6 eV), though incapable of ionizing hydrogen, can still interact with gas in a very profound way. Most immediately, photons in the Lyman-Werner (LW) band ( $\sim 11.2 - 13.6$

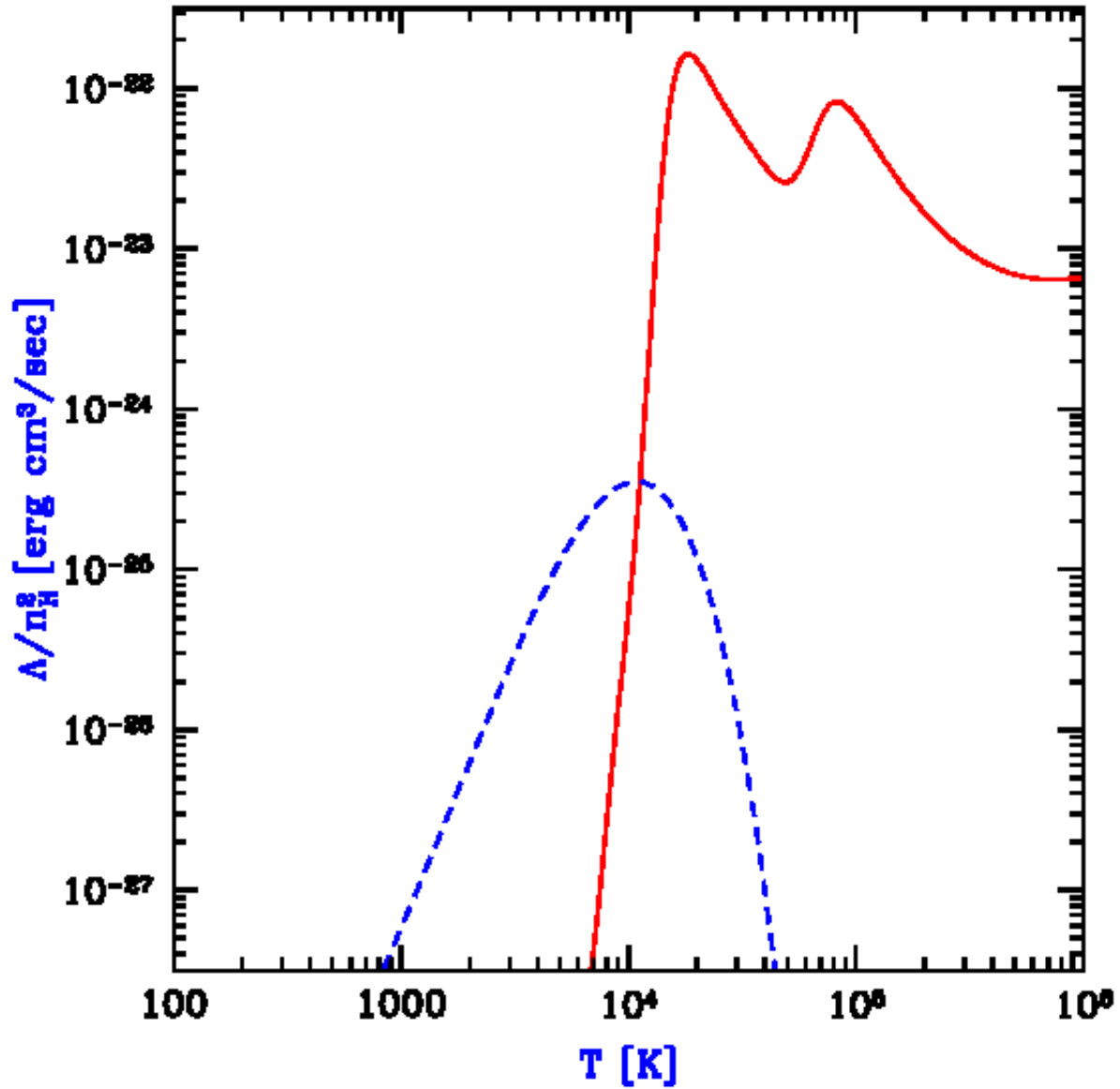


Figure 1.2 Cooling curves for primordial gas at the  $z \sim 10$  cosmic mean density,  $n_H = 0.045 \text{ cm}^{-3}$ . Solid red line shows that of a purely atomic hydrogen and helium gas, with peaks corresponding to temperatures at which collisional excitation cooling of H I and He II becomes efficient. Dashed blue curve shows the same quantity for a pure  $H_2$  gas. From (Barkana and Loeb, 2001).

eV) can dissociate molecular hydrogen – the very coolant that enables the  $H_2$  mode of star formation in the first place. On larger scales, in both time and space, LW photons redshift through Ly- $n$  resonances of atomic hydrogen, and ultimately contribute to the cosmic Ly- $\alpha$  background, either by redshifting into the blue wing of the Ly- $\alpha$  line itself or by cascading downwards through Ly- $n$  lines. We will find in Section 1.3 that the Ly- $\alpha$  background is responsible for first “activating” the 21-cm background at redshifts  $z \lesssim 40$ .

Even if one could artificially turn off the  $H_2$ -dissociating background, and thus stifle large-scale feedback, PopIII stars might still fundamentally alter the conditions for star-formation locally once they explode as supernovae. Blast-waves will mechanically heat the interstellar medium through shocks, and may sweep up and ultimately expel material from the galaxy entirely. In addition, once heavy elements are re-incorporated into the interstellar medium, cooling will be far more efficient than it was prior to first-light. The timing of this transition from PopIII to PopII star formation is highly uncertain.

Numerical simulations continue to grow in sophistication every year, and in many cases are revising the predicted mass scale for PopIII star formation downward with each improvement in resolution and the inclusion of each new physical process. For example, thermal pressure may be augmented by non-thermal processes, such as turbulence, magnetic fields, and radiation pressure (Hosokawa et al., 2011). In some cases, a halo’s first star may *not* form out of chemically pristine material, as nearby halos may have already seen a generation of star formation and polluted one or more of their neighbors (Smith et al., 2015).

Clearly, the formation of the first stars remains an area ripe for research. Their deaths also likely coincide with the birth of the Universe’s first compact objects, including neutron stars and black holes, which introduce an array of feedback processes unlike those brought about by their progenitors. These objects are the focus of the next subsection.

### 1.1.2 Black Holes

Black holes (BHs) are a common feature of all galaxies in today’s Universe. The Milky Way, for example, is likely to harbor  $\sim 10^7$ - $10^9$  stellar mass (with  $M_\bullet \sim 10 M_\odot$ ) black holes (van den Heuvel, 1992) – the survivors of the explosions of massive stars. In contrast, the Milky Way has just a single *super-massive* black hole (SMBH), which resides in the nucleus of the galaxy. This dichotomy seems to be the norm:

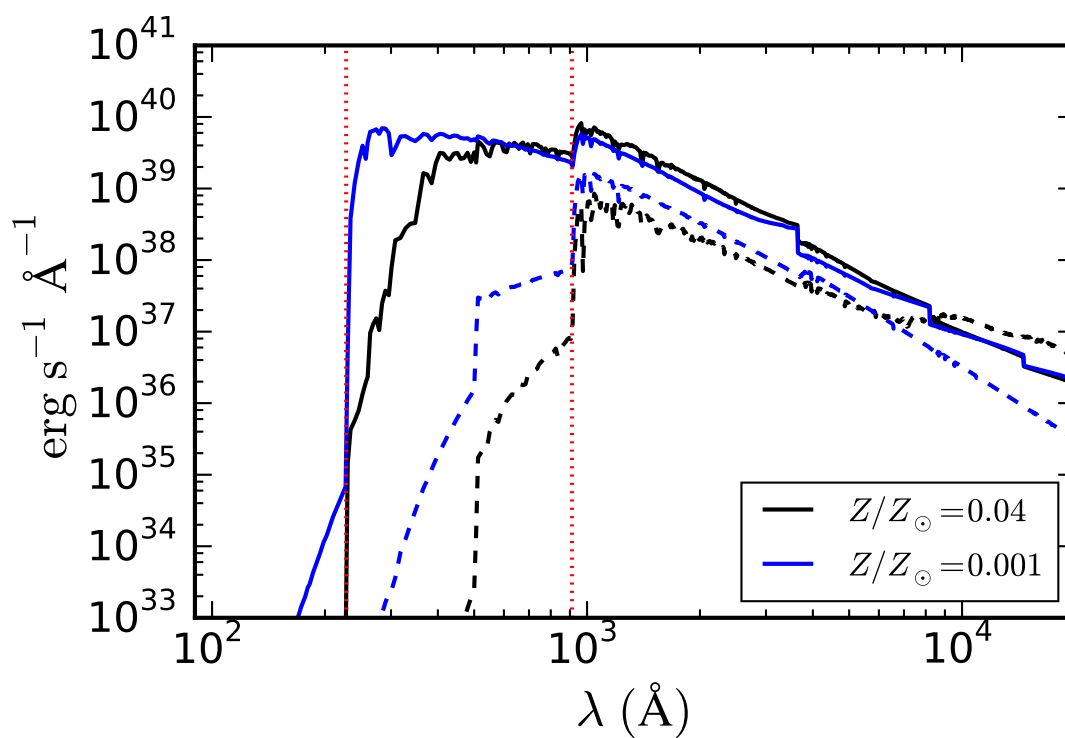


Figure 1.3 Model spectral energy distributions from metal-poor ( $Z = 0.001 Z_{\odot}$ ) and metal-enriched ( $Z = 0.04 Z_{\odot}$ ) stellar populations with Salpeter a Salpeter initial mass function. The solid lines show the SED 1 Myr after a  $10^6 M_{\odot}$  burst of star formation, while the dashed lines show the SEDs 10 Myr after the initial burst. Dotted vertical lines denote the He II ionization threshold and H I ionization threshold from left to right. Adapted from (Leitherer et al., 1999).

(nearly) all galaxies contain a nuclear SMBH with a mass of order  $10^6 \lesssim M_{\bullet}/M_{\odot} \lesssim 10^9$ , as well as an unknown (but likely large) number of stellar mass BHs ( $M_{\bullet} \sim 10 M_{\odot}$ ). The search for intermediate mass BHs ( $10^2 \lesssim M_{\bullet}/M_{\odot} \lesssim 10^5$ ) is an active area of research.

The sheer existence of  $10^9 M_{\odot}$  SMBHs, many of which were already in place at  $z > 6$  (Fan, 2006, Mortlock et al., 2011), is one of the biggest puzzles of the high- $z$  Universe. If the first stars are  $\sim 100 M_{\odot}$  and (optimistically) leave behind remnant black holes of comparable mass, they must accrete at the Eddington limit nearly continuously in order to reach  $\sim 10^9 M_{\odot}$  by  $z \sim 6$ . This challenge has inspired direct-collapse models (Begelman et al., 2006, 2008), which predict the formation of BHs with  $M_{\bullet} \gtrsim 10^3 M_{\odot}$  in massive, atomic-cooling dark matter halos via dynamical instabilities. These models alleviate the requirement of continual Eddington-limited accretion throughout the reionization epoch, but remain unconstrained.

Despite being some of the most enigmatic objects in the Universe, even the most massive SMBHs are dynamically irrelevant to their host galaxies, meaning the assembly of galaxies is unlikely to have been gravitationally affected by their presence. This is strange, given that there are strong correlations between the masses of SMBHs and the dynamics of their host galaxies (e.g., the BH mass - stellar velocity dispersion, or  $M$ - $\sigma$  relation; Gebhardt et al., 2000, Ferrarese and Merritt, 2000). However, if accompanied by a gas accretion disk, BHs can become prodigious sources of energetic photons and winds, and can thus potentially have a substantial effect on galactic and extragalactic gas nonetheless.

Though mysterious in origin and important in the context of galaxy-scale feedback, SMBHs seem to be less important in *hydrogen* reionization<sup>2</sup>, largely as a result of their rarity. Quasars are, however, thought to be the primary agents of helium reionization (at  $z \sim 3$ ) given that stellar sources emit few photons energetic enough ( $E > 54.4$  eV) to doubly ionize helium atoms. As a result, I will largely neglect quasars from here onward, instead devoting attention to their stellar mass cousins.

Stellar-mass black holes (in so-called X-ray binary systems; XRBs) are the dominant source of X-rays in nearby star-forming galaxies (Gilfanov et al., 2004, Mineo et al., 2012b). To gauge their role in reionization, consider a photon with rest-frame energy  $h\nu$ , traveling through a uniform medium. The mean

---

<sup>2</sup> They are, however, extremely *historically* important to studies of hydrogen reionization, as I will discuss briefly in §1.2.2.

free path of this photon is given by

$$l_\nu \equiv \left( \sum_j n_j \sigma_{j,\nu} \right)^{-1} \quad (1.4)$$

where  $n_j$  is the number density of absorbing species  $j$  and  $\sigma_{j,\nu}$  is the bound-free absorption cross section of species  $j$ . If we assume approximate cross sections,

$$\sigma_{j,\nu} \simeq \sigma_0 \left( \frac{\nu}{\nu_j} \right)^{-3} \quad (1.5)$$

where  $h\nu_j$  is the ionization threshold for species  $j$ ,  $\sigma_{0,j}$  is the cross-section at that energy, and a medium composed of hydrogen and helium, we find

$$\begin{aligned} l_\nu &= \nu^3 \left[ x_{\text{H I}} \bar{n}_{\text{H}}^0 (1+z)^2 \sigma_0 (\nu_{\text{H}}^3 + y \nu_{\text{He}}^3) \right]^{-1} \\ &\simeq 5.8 x_{\text{H I}}^{-1} \left( \frac{h\nu}{0.2 \text{ keV}} \right)^3 \left( \frac{1+z}{10} \right)^{-2} \text{ cMpc} \end{aligned} \quad (1.6)$$

where  $\bar{n}_{\text{H}}^0$  is the hydrogen number density today,  $y$  is the primordial helium abundance by number,  $x_i$  is the ionized fraction<sup>3</sup>, and “cMpc” is short for “co-moving Mega-parsecs.”

In contrast to stellar UV emission, which extends to at most a few tens of eV (see Figure 1.3) and is thus quickly absorbed in the IGM, Equation 1.6 shows that X-rays can travel great distances before being absorbed. X-ray sources like XRBs are probably only relevant to the thermal history of the IGM, since each X-ray ionization event produces photo-electrons that subsequently lose their energy to various processes, including collisional ionization of hydrogen (or helium), collisional excitation, and heat (Shull and van Steenberg, 1985, Ricotti et al., 2002, Furlanetto and Johnson Stoeber, 2010). Though in a neutral gas most of the photo-electron energy is deposited as further ionization, heating becomes the dominant channel once the ionized fraction reaches  $x_{\text{H II}} \gtrsim 10^{-2}$ .

Nearby star-forming galaxies exhibit a relationship between their X-ray luminosity and star-formation rate (the so-called  $L_X$ -SFR relation; Grimm et al., 2003, Gilfanov et al., 2004, Mineo et al., 2012b), that is well fit by

$$L_X = f_X c_X \left( \frac{\text{SFR}}{M_\odot/\text{yr}} \right) \quad (1.7)$$

---

<sup>3</sup> We assume the singly-ionized helium fraction is the same as the hydrogen ionized fraction,  $x_{\text{H II}} = x_{\text{He II}} = 0$ , and neglect doubly ionized helium, i.e.  $x_{\text{He III}} = 0$ .

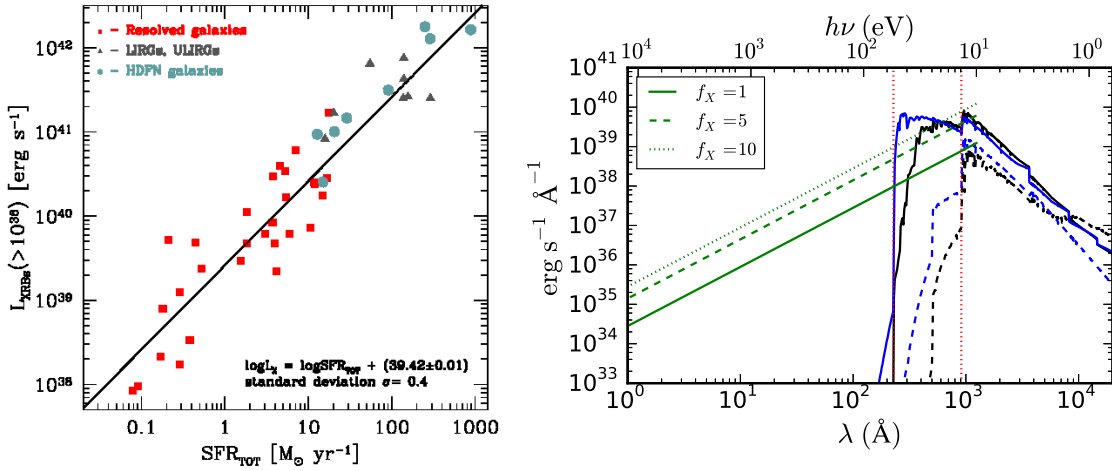


Figure 1.4 *Left*: X-ray Luminosity star-formation rate ( $L_X$ -SFR) relation from (Mineo et al., 2012b). *Right*: X-ray SED of star-forming galaxy (per unit star-formation), assuming XRBs have  $\alpha = 1.5$  power-law spectra. The solid green line shows the  $L_X$ -SFR of Mineo et al. (2012b), while dashed and dotted lines show factor of 5 and 10 amplification of the Mineo et al. (2012b) relation. Black and blue curves are the same as those in Figure 1.3.

where  $c_X = 2.6 \times 10^{39} \text{ erg s}^{-1}$  (measured in the 0.5 - 8 keV band, see Figure 1.4; Mineo et al., 2012b), and  $f_X$  is an unknown correction factor introduced to account for our ignorance of how this relationship extends to high- $z$ .

Assuming  $f_X = 1$  at all redshifts, the IGM should be heated to  $\sim 1.2 \times 10^4 \text{ K}$  in a Hubble time assuming a star formation efficiency of 10% in atomic cooling halos and a power-law XRB spectrum (Furlanetto, 2006). However, if the first stars are especially massive, we might expect their remnants to follow suit. Assuming Eddington-limited accretion,  $L_X \propto M_\bullet$ , this implies an amplification of the  $L_X$ -SFR relation at high- $z$ . As a result, any observations that can constrain the normalization of  $L_X$ -SFR (which we parameterize via  $f_X$ ) have the potential to constrain the first BHs to form in the Universe, and thus provide an indirect constraint on the first stars.

### 1.1.3 Galaxies & the Epoch of Reionization

The “galaxies” hosting the first generations of stars and BHs would have looked nothing like the spiral and elliptical galaxies that litter the cosmic landscape today<sup>4</sup>. In fact, the very first halos to experience star formation may have initially been home to just one massive metal-free star (or perhaps a few; Turk et al., 2009, panel 1 of Figure 1.5). A substantial fraction of halo gas would have been heated mechanically by the first supernovae, and may have required tens of Myr to subsequently cool and form stars once again. Accretion onto BH remnants of the first stars could lengthen a halo’s star-less period to  $\sim 100 \text{ Myr}$  through X-ray heating (Jeon et al., 2014). The fragility of the first halos and the array of potential feedback mechanisms support a “bursty” picture of star-formation at high- $z$ .

Second generation stars would almost certainly have formed from enriched material and thus have been less massive than the generation before them (panel 2 of Figure 1.5). With less intense ionizing radiation and less powerful supernovae than PopIII stars, their impact on the host galaxy would have been correspondingly weaker, meaning star-formation could have persisted rather steadily. With star and BH formation occurring in halos across the Universe, large-scale radiation backgrounds would have emerged,

---

<sup>4</sup> Despite bearing little resemblance to present-day galaxies, we will henceforth refer to all halos that have experienced star-formation as *galaxies*.

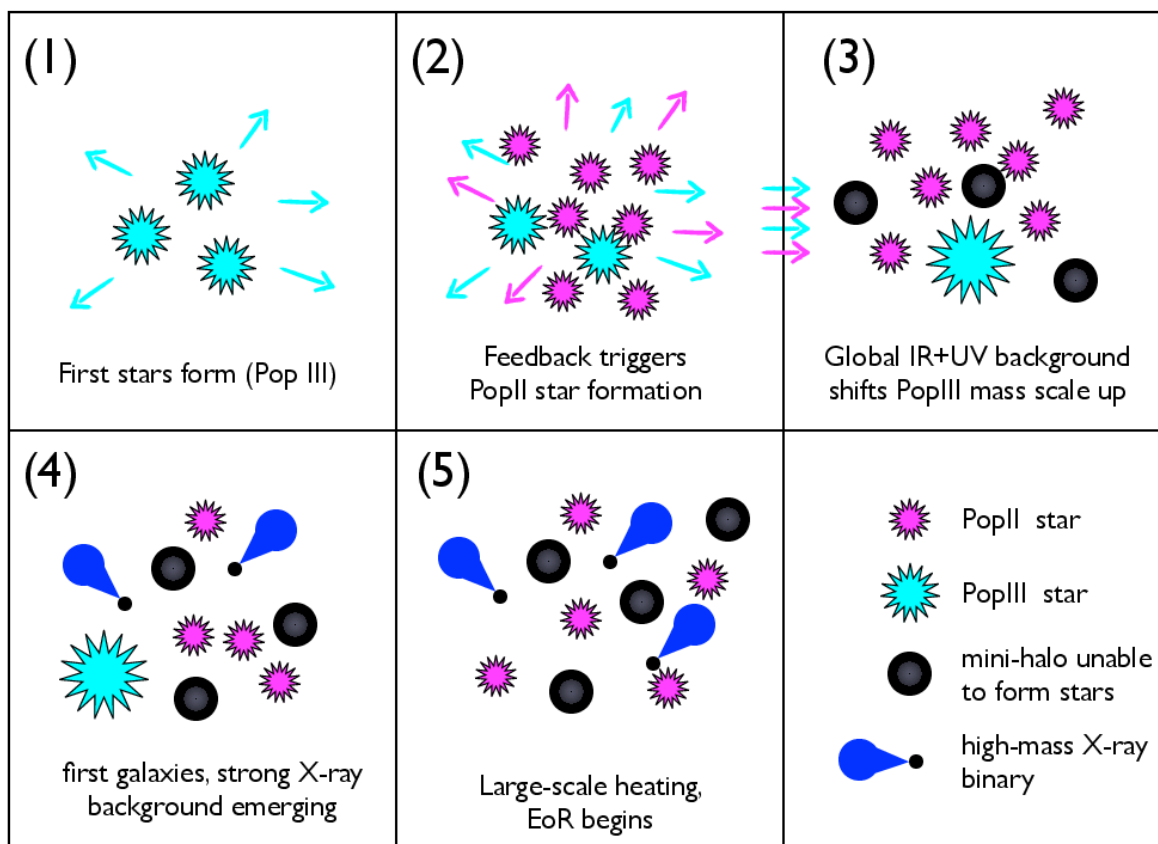


Figure 1.5 Cartoon showing a plausible guess for the formation of the first galaxies. **(1)** The first stars form in small halos via  $H_2$  cooling. **(2)** These stars empty evacuate their host halos of gas via photoevaporation and supernova blast-waves, changing the mode of star formation. **(3)** The IR and UV radiation from low- and high-mass stars suppresses star formation throughout the universe, gradually increasing the characteristic mass of star-forming halos. **(4)** The first self-sustaining galaxies eventually form in massive halos, as accreting stellar remnants of the first stars in binary systems give rise to a relatively uniform X-ray background. **(5)** X-rays cause large-scale heating, which increases the characteristic mass of star-forming halos even further. The Epoch of Reionization has begun, and PopIII stars have likely become extinct.

primarily in the Ly- $\alpha$ /LW ( $10.2 < h\nu < 13.6$  eV) and hard X-ray ( $h\nu \gtrsim 1$  keV) bands (following the mean-free-path arguments of the previous section), and introduced the possibility of *external* feedback. The LW background generally acts to suppress star formation in metal-free gases through dissociation of H<sub>2</sub>, meaning halos may have been “sterilized” before forming any stars at all (panel 3 of Figure 1.5). It is possible that an X-ray background could counteract H<sub>2</sub>-dissociative feedback by enhancing the free electron fraction and thus catalyzing H<sub>2</sub> formation (Kuhlen and Madau, 2005, Hummel et al., 2015). X-rays also heat the IGM on large-scales, i.e., the mostly neutral “bulk IGM” beyond the fully-ionized bubbles surrounding galaxies (panel 4 of Figure 1.5). Eventually, the LW background was likely strong enough to prevent the formation of metal-free stars in halos across the Universe, except those isolated enough to have remained metal-free. Galaxies, now composed primarily of PopII stars, could have sustained star formation at levels sufficient to grow large ionized bubbles around themselves. The Epoch of Reionization (EoR) had begun, likely by  $z \sim 10$  (panel 5 of Figure 1.5).

The persistence of star formation meant galactic HII regions would in time grow large enough to overlap with those associated with nearby galaxies, ultimately leading to the complete depletion of neutral intergalactic hydrogen. Figure 1.6 shows an artists rendition of this process, beginning with the CMB (at left) and ending with the present (at right).

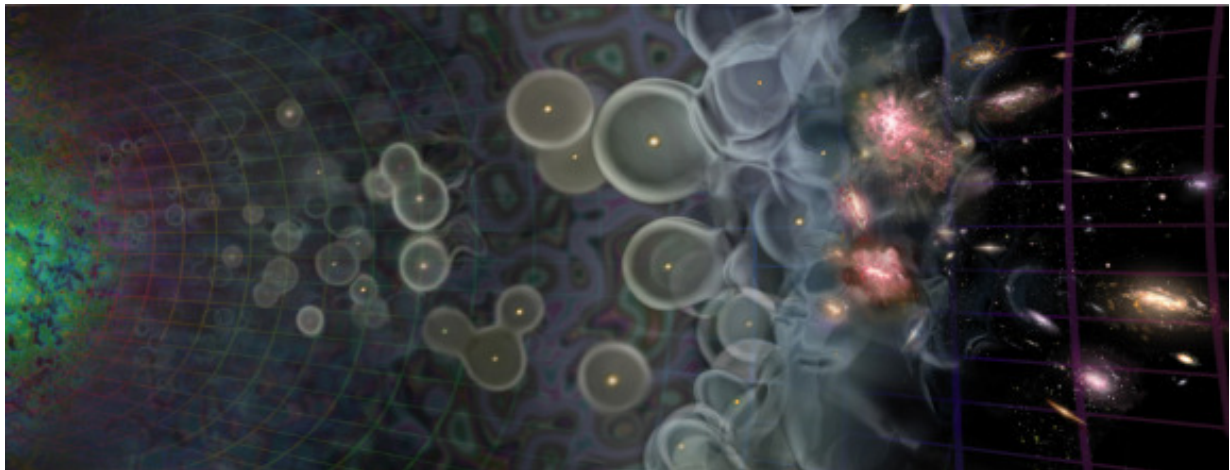


Figure 1.6 Artists depiction of the evolution of structure in the Universe, from the CMB (far left), to reionization (middle), to the present-day (far right).

The simplest model of this Reionization process tracks the balance between photo-ionizations and recombinations in a single volume element, i.e.,

$$\frac{dn_{\text{H II}}}{dt} = \Gamma_{\text{HI}} n_{\text{H I}} - \alpha_{\text{HII}}(T_{\text{K}}) n_e n_{\text{H II}} C(z) \quad (1.8)$$

where  $n_{\text{H}} = n_{\text{H I}} + n_{\text{H II}}$  is the number density of hydrogen atoms,  $\Gamma_{\text{HI}}$  is the rate coefficient for photo-ionization,  $\alpha(T_{\text{K}})$  is the rate coefficient for radiative recombination,  $n_e$  is the number density of free electrons, and  $C(z)$  is the ‘‘clumping factor.’’

Taking  $n_{\text{H I}} = x_{\text{H I}} n_{\text{H}}$ ,  $n_{\text{H II}} = x_{\text{H II}} n_{\text{H}}$ , and assuming that ionizing photons are distributed uniformly in space, we can write

$$\frac{dx_{\text{H II}}}{dt} = \dot{Q}_{\text{ion}} - \alpha_{\text{HII}}(T_{\text{K}}) n_e x_{\text{H II}} C(z) \quad (1.9)$$

where  $\dot{Q}_{\text{ion}}$  is the production rate of ionizing photons, i.e., the number ionizing photons produced by galaxies per second per unit volume.

This simple equation highlights several important factors that could influence how rapidly the Universe becomes ionized. Clearly, if we turn a knob in our model that makes galaxies brighter,  $\dot{Q}_{\text{ion}}$  will increase and bring Reionization to a close more rapidly (holding all other quantities fixed). Alternatively, in a clumpy medium (i.e., one with  $C > 1$ ), the recombination rate will be boosted and the progress of Reionization will be slowed. Simulations suggest that  $1 \lesssim C \lesssim 3$  (Shull et al., 2012). X-rays, while busy heating the IGM and thus reducing the recombination rate (through  $\alpha_{\text{HII}}$ ), can also modify the other parameters of this model. For example, even if the intrinsic UV luminosity of galaxies remains unchanged with time, X-rays may act to reduce the neutral hydrogen content of galaxies and thus enhance the number of UV photons which escape into the IGM (Benson et al., 2013). X-rays may also be responsible for raising the halo mass threshold required for star formation (Gnedin, 2000), and reducing clumping in the high- $z$  IGM.

The progression of events described in the previous three subsections is a plausible guess for how galaxy formation occurred at  $z \gtrsim 6$ , though it depends on many complex, inter-related, and difficult to observe processes and thus remains poorly constrained. The next section is dedicated to a discussion of current constraints on the EoR and high- $z$  galaxies, to be followed with a detailed introduction to the 21-cm background in §1.3.

## 1.2 Established Probes of High- $z$ Galaxies and Reionization

Though our focus will in large part remain on the global 21-cm signal throughout this thesis, it would be short-sighted to omit mention of other independent probes of the high- $z$  Universe. A discussion of observations at shorter wavelengths is warranted both for historical reasons, given that studies of the early Universe did not originate in the radio, and also so that the power of 21-cm observations becomes apparent in contrast. This is not to say, however, that 21-cm observations will eventually usurp all other techniques in the coming years. We will return to the possibility of bolstering the constraining power of 21-cm observations with current and near-future experiments in Chapter 7.

The following subsections are by no means a comprehensive census of all high- $z$  probes. Most notably, I will only focus on *contemporaneous* probes of high- $z$  galaxies, i.e., those which provide information coincident in time with the galaxies of interest. Observations of nearby galaxies (including our own) may provide important clues about star-formation at high- $z$ , e.g., via abundance patterns in low-mass stars (e.g., Salvadori et al., 2007, Rollinde et al., 2009) or the star-formation history of dwarf galaxies as inferred by their present-day stellar populations (Weisz et al., 2014, Boylan-Kolchin et al., 2015). However, the observational and theoretical methods of such “galactic archeology” have little in common with our own, so we neglect them in the interest of time and focus.

### 1.2.1 The Galaxy Luminosity Function

Perhaps the most intuitive approach to learn about the galaxy population is to simply count the number of galaxies in different luminosity bins. The resulting function, often denoted  $\phi(L, z)$ , is known as the galaxy luminosity function (LF), and describes the number density of galaxies as a function of both galaxy luminosity and redshift. For example, the total number density of galaxies at redshift  $z$  with luminosities greater than  $L$  is given by the integral

$$N_{\text{gal}}(L, z) = \int_L^{\infty} \phi(L', z) dL'. \quad (1.10)$$

Preliminary searches for high- $z$  galaxies have commenced, primarily with the *Hubble Space Telescope*, and have begun to reveal very bright galaxies at redshifts as high as  $z \sim 10$  (Zheng et al., 2012, Ellis et al., 2013,

Oesch et al., 2013). The galaxy LF is typically well-described by a Schechter function, i.e., a power-law with an exponential cutoff

$$\phi(L) = \phi(L_*) \left( \frac{L}{L_*} \right)^\alpha e^{-L/L_*}, \quad (1.11)$$

where  $\phi(L_*)$  is the number density of galaxies with the characteristic luminosity  $L_*$  and  $\alpha$  is the “faint-end slope” of the luminosity function.

The quantity most important for reionization is the luminosity *density* of high- $z$  galaxies, i.e., a weighted integral over  $\phi(L)$ ,

$$\rho_L(z, L_{\min}) = \int_{L_{\min}}^{\infty} \phi(L, z) L dL \quad (1.12)$$

where  $L_{\min}$  is the minimum galaxy luminosity. Figure 1.7 shows a recent fit to the  $z = 6$  LF, with the corresponding cumulative luminosity density on the bottom panel. The brightest galaxies are exceedingly rare, and thus contribute little to the total luminosity density. However, the individually faint but overwhelmingly numerous galaxies with  $L < L_*$  contribute a substantial fraction of the total luminosity density, and as a result are likely required to ensure that reionization ends by  $z \sim 6$  (e.g., Trenti et al., 2010, Wise et al., 2014).

Relating the galaxy LF to the dark matter halo mass function (HMF; see Figure 1.8) is one of the most powerful probes of feedback processes. Assuming a 1:1 corresponding between galaxies and DM halos, the abundance of galaxies should “match up” with the abundance of halos. For example,

$$\int_L^{\infty} \phi(L') dL' = \int_{m(L)}^{\infty} n(m') dm'. \quad (1.13)$$

where  $n(m)$  is the number density of halos of mass  $m$ . Note that this equality assumes independent knowledge of the conversion between mass and light,  $m(L)$ . If, for example, not all halos host galaxies, or if the luminous component of galaxies is time variable, the above equality will not hold even if  $m(L)$  is known exactly. To account for these possibilities, a correction factor is typically introduced,

$$\int_L^{\infty} \phi(L') dL' = \epsilon \int_{m(L)}^{\infty} n(m') dm'. \quad (1.14)$$

which can either be interpreted as an occupation fraction (of galaxies in halos) or as a duty cycle, i.e., fraction of the time galaxies are “on.” Numerous studies now indicate that  $\epsilon < 1$ , especially at the low-luminosity end of the galaxy LF (e.g., Trenti et al., 2010). We should expect feedback processes to be particularly strong in

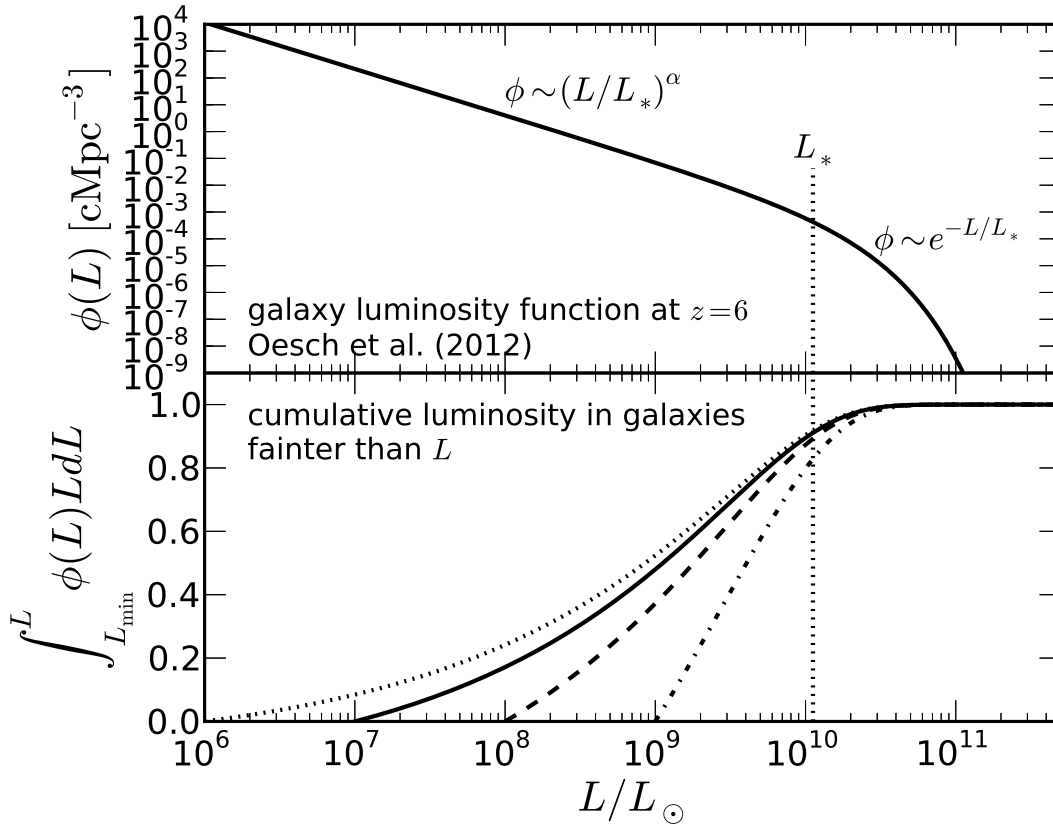


Figure 1.7 Empirical fit to the rest-frame 1500Å galaxy luminosity function at  $z \sim 6$  (Oesch et al., 2012). Top panel shows the galaxy luminosity function itself, while the bottom panel shows the cumulative luminosity emitted by galaxies fainter than the corresponding value of  $L$ . Clearly, faint galaxies (i.e., those fainter than  $L_*$ ), are expected to dominate the volume-averaged luminosity, though exactly how much they dominate depends on the faintest galaxy,  $L_{\min}$  (dotted, solid, dashed, and dash-dotted lines).

low-mass galaxies, since their shallow gravitational potential wells should have a harder time retaining gas than more massive galaxies. The properties of the faint galaxy population should thus contain a wealth of information about the processes shaping the first galaxies.

### 1.2.2 The Ly- $\alpha$ Forest, Gunn-Peterson Troughs, and the Meta-Galactic UV Background

Given the effect galaxies have on intergalactic gas, it would of course be advantageous to both search for galaxies directly (e.g., to determine the LF) and to measure properties of the IGM, which serve as an independent, albeit indirect, probe of galaxy properties. This has been done for years in studies of the  $z \lesssim 6$  Universe, providing constraints on the ionizing background (Weinberg et al., 1997) and the first evidence for a  $z \sim 6$  end to reionization (Fan et al., 2000, Becker et al., 2001).

Both of the aforementioned results are made possible by the absorption of Ly- $\alpha$  photons by neutral hydrogen atoms. The optical depth of a cloud as seen in absorption against bright background source (e.g., a quasar) is

$$d\tau_v = \sigma_v n_{\text{H I}} dl, \quad (1.15)$$

where  $\sigma_v$  is the frequency-dependent cross-section,  $n_{\text{H I}}$  is the number density of neutral hydrogen atoms, and  $dl$  is a differential line element. The measured flux in the vicinity of that absorption line (relative to the continuum flux  $F_0$ ) is

$$F_v = F_0 e^{-\tau_v}. \quad (1.16)$$

In practice, one is interested in the total optical depth of the line, since it encodes the column density of the absorber,  $dN = n_{\text{H I}} dl$ . Assuming absorption is sharply peaked near the Ly- $\alpha$  line center,

$$\sigma_v = \frac{\pi e^2}{m_e c} f_\alpha \phi_v = \frac{\pi e^2}{m_e c} f_\alpha \delta_D[v - v_\alpha] \quad (1.17)$$

where  $\delta_D$  is the Dirac delta function, and uniform absorbers,  $n_{\text{H I}} = \bar{n}_{\text{H}}^0 (1 + \delta)(1 + z)^3$ , we can write

$$\tau_\alpha = 2.6 \times 10^5 \times x_{\text{H I}} (1 + \delta) \left( \frac{1 - Y}{0.76} \right) \left( \frac{\Omega_{b,0}}{0.0486} \right) \left( \frac{\Omega_{m,0}}{0.3089} \right)^{-1/2} \left( \frac{h}{0.68} \right) \left( \frac{1 + z}{7} \right)^{3/2} \quad (1.18)$$

where  $Y$  is the primordial helium abundance by mass and  $H_0 = 100h \text{ km s}^{-1} \text{ Mpc}^{-1}$ .

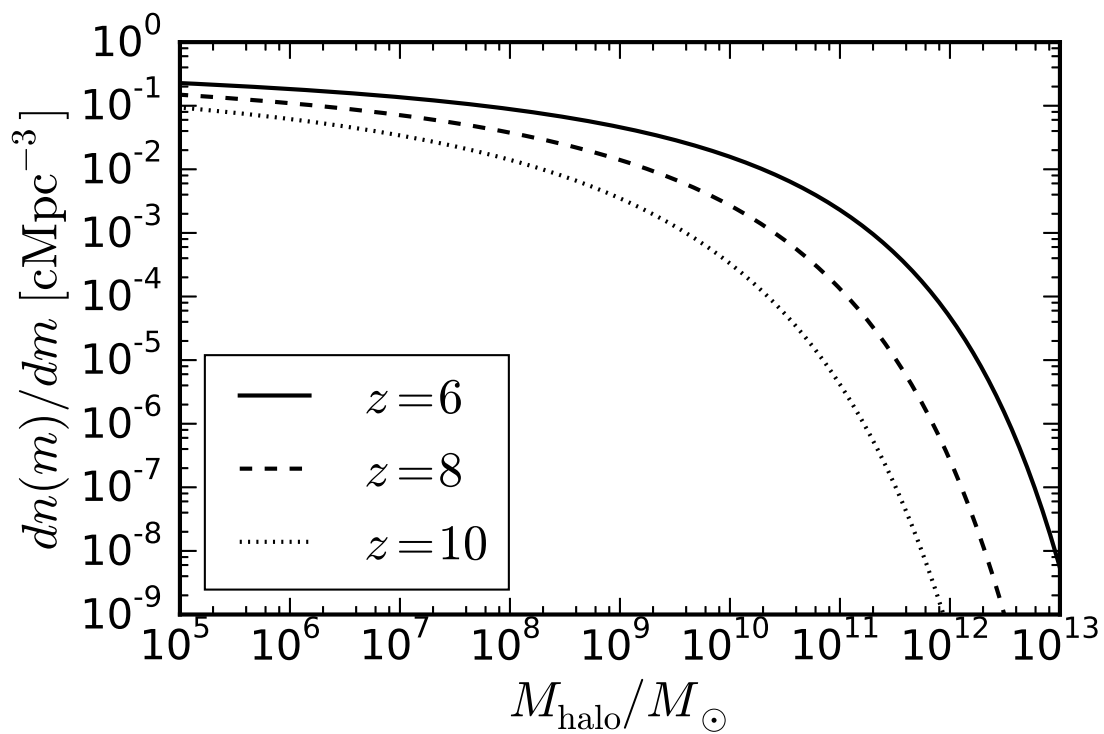


Figure 1.8 Dark matter halo mass function at  $z = 6, 8$  and  $10$ . Assumes the Sheth and Tormen (2002) form of the mass function and *Planck* cosmological parameters. Computed using the HMF code (Murray et al., 2013b).

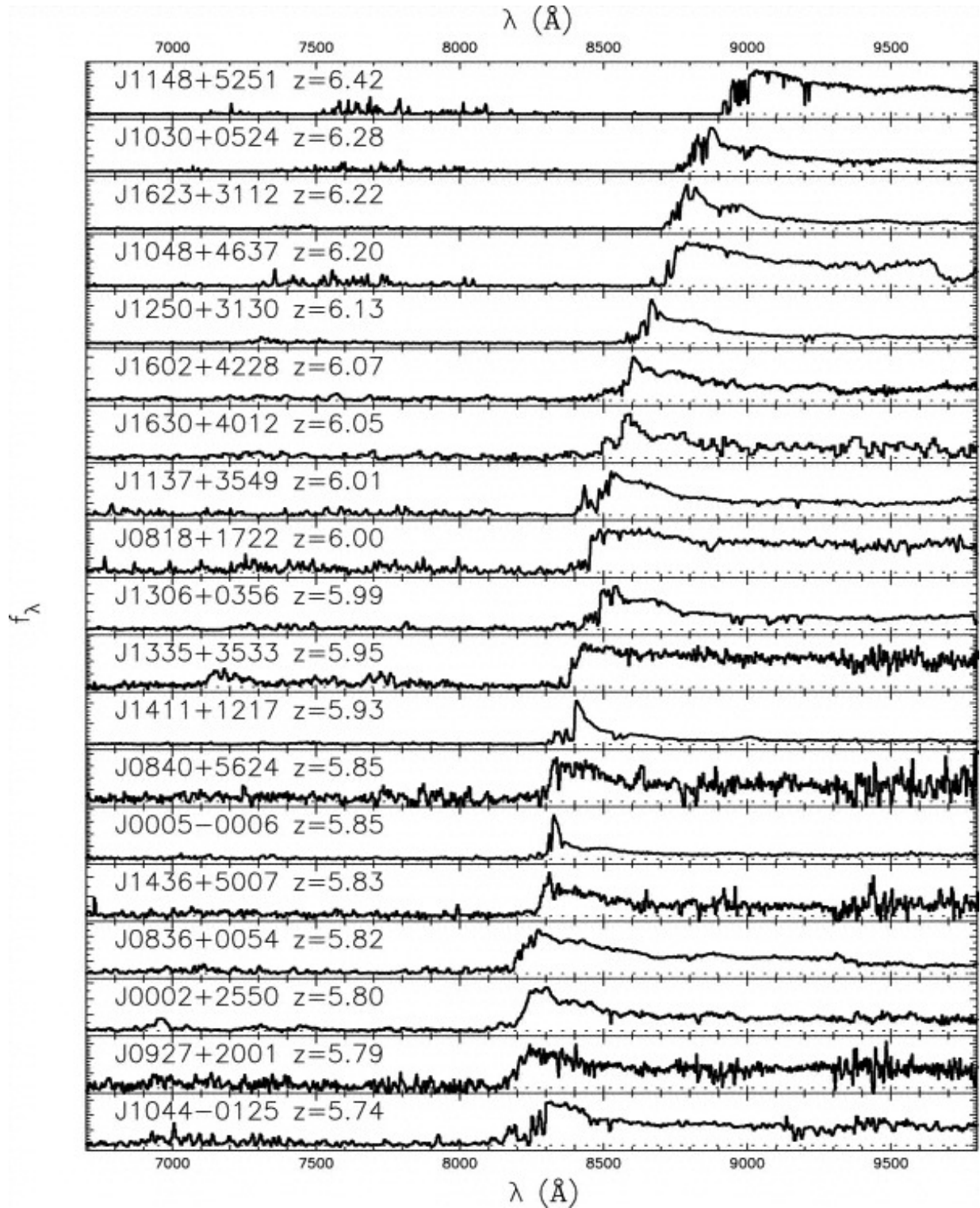


Figure 1.9 Spectra of 19 quasars at  $5.764 < z < 6.42$  from (Fan et al., 2006) showing the emergence of the Gunn-Peterson trough at  $z \sim 6$ .

Equation 1.18 shows that even gas at the cosmic mean density ( $\delta = 0$ ) with a very small neutral fraction can have a large optical depth. Because each observed frequency corresponds to a unique redshift,  $\nu = \nu_\alpha/(1+z)$ , in principle one could get a census of neutral hydrogen gas as a function of redshift by measuring the properties of each line in the “forest” of absorption lines in the spectrum of a distant quasar.

As the diffuse component of the IGM becomes increasingly neutral, individual absorbers will blend together into a “trough,” i.e., one would measure flux consistent with zero (see Figure 1.9). Given the high optical depth of Ly- $\alpha$ , *any* transmission at all implies a highly ionized medium with  $x_{\text{H I}} \lesssim 10^{-4}$ . Though this provides a powerful constraint on the end of Reionization, it of course means that Ly- $\alpha$  absorption is not a viable probe of the pre-Reionization IGM. This is one of the main reasons to seek out alternative probes of the IGM at higher redshifts, such as the 21-cm line, to be discussed in §1.3.

Despite the waning utility of Ly- $\alpha$  absorption at  $z \gtrsim 6$ , the Ly- $\alpha$  forest has provided a wealth of information about the ionizing background at  $z \lesssim 6$ . Assuming that the absorbing gas is in photo-ionization equilibrium, i.e.,

$$\frac{dx_{\text{H I}}}{dt} = \Gamma x_{\text{H I}} - \alpha_{\text{H II}}(T_{\text{K}})(1 - x_{\text{H I}})n_e = 0 \quad (1.19)$$

then one can relate the ionization state of absorbing gas ( $x_{\text{H I}}$  in Equation 1.18) to the ionization rate,  $\Gamma$ . The ionization rate is interesting as a probe of the meta-galactic background radiation,  $J_\nu$ ,

$$\Gamma = \int J_\nu \sigma_\nu d\nu \quad (1.20)$$

which is in turn related to the specific luminosity density of galaxies,  $\epsilon_\nu$ , diluted by the cosmic expansion and hardened by intergalactic absorption, i.e.,

$$J_\nu(z) \propto \int_z^\infty \frac{\epsilon_{\nu'}(z')}{H(z')} e^{-\tau_{\nu'}} dz'. \quad (1.21)$$

Following this line of reasoning, the Ly- $\alpha$  serves as a probe of the galaxy population. An analogous argument will resurface in Chapter 5 in the context of 21-cm measurements.

### 1.2.3 Thomson Optical Depth to the Cosmic Microwave Background

Though Ly- $\alpha$  absorption cannot probe redshifts far beyond  $z \sim 6$ , a crude measure of the duration of the EoR is accessible to CMB experiments. In §1.1.1 I was careful to say that the CMB represents the time

when *most* photons scattered for the last time. The probability of this occurring between recombination and present day is related to the optical depth to Thomson scattering between  $z \sim 1100$  and  $z = 0$ ,

$$\tau_e = \sigma_T N_e \quad (1.22)$$

where  $\sigma_T = 6.65 \times 10^{-25} \text{ cm}^{-2}$  is the Thomson cross-section, and  $N_e$  is the column density of electrons.

In an expanding Universe, the electron column is an integral of the electron density,  $n_e$ , along the cosmological line-element,  $dl/dz$ ,

$$\tau_e = \sigma_T \int_0^{z_{\text{rec}}} n_e \frac{dl}{dz} dz \quad (1.23)$$

where  $z_{\text{rec}}$  corresponds to the redshift of cosmological recombination. This electron optical depth enters as a damping term in the CMB power spectrum on small angular scales.

If we assume that all electrons were stripped from hydrogen atoms, such that  $n_e = n_{\text{H}}(z)x_i = \bar{n}_{\text{H}}^0(1+z)^3 x_i$ , and that the endpoint of Reionization,  $z_{\text{rei}}$ , is known, we can write

$$\tau_e = \sigma_T \bar{n}_{\text{H}}^0 \left\{ \int_0^{z_{\text{rei}}} (1+z)^3 \frac{dl}{dz} dz + \int_{z_{\text{rei}}}^{z_{\text{rec}}} x_i(z)(1+z)^3 \frac{dl}{dz} dz \right\} \quad (1.24)$$

since the ionized fraction is unity for all redshifts  $z < z_{\text{rei}}$ .

Assuming *Planck* cosmological parameters, the first term on the left hand side is  $\tau_e(z < z_{\text{rei}}) \simeq 0.04$ . The value of  $\tau_e$ , as inferred by CMB experiments has changed by a factor of  $\sim 3$  between the first release by the *Wilkinson Microwave Anisotropy Probe* (WMAP) in 2003 and *Planck* in 2015 (see Table 1.1). WMAP 9 results and *Planck* Year 1 results are borderline discrepant, likely due to foreground contamination in the WMAP maps. The recent *Planck* result ( $\tau_e = 0.066 \pm 0.012$ ) suggests that about 40% of  $\tau_e$  is due to free electrons at  $z > 6$ .

$\tau_e$  is a fairly crude measure of the EoR given that it is a line-of-sight-integrated measure of the electron content of the Universe. This means that any constraint it yields on the ionization history,  $x_i(z)$ , will be model-dependent. It is common to translate  $\tau_e$  into a ‘‘redshift of Reionization,’’  $z_{\text{rei}}$ , assuming the process is instantaneous. The *Planck* results find translate to  $z_{\text{rei}} \simeq 8.8$ , whereas previous constraints from WMAP supported  $z_{\text{rei}} \sim 10.1$ . This shift, to lower values of  $\tau_e$  and  $z_{\text{rei}}$ , has alleviated tensions between previous WMAP measurements of  $\tau_e$  and the ionizing emissivity of the high- $z$  galaxy population (Bouwens et al., 2015, Robertson et al., 2015).

Table 1.1. History of  $\tau_e$ 

| Value             | Experiment | Reference                   |
|-------------------|------------|-----------------------------|
| $0.170 \pm 0.04$  | WMAP-1     | Spergel et al. (2003)       |
| $0.089 \pm 0.030$ | WMAP-3     | Spergel et al. (2007)       |
| $0.084 \pm 0.016$ | WMAP-5     | Komatsu et al. (2009)       |
| $0.088 \pm 0.015$ | WMAP-7     | Komatsu et al. (2011)       |
| $0.089 \pm 0.014$ | WMAP-9     | Hinshaw et al. (2013)       |
| $0.066 \pm 0.012$ | Planck     | Collaboration et al. (2015) |

Note. — Constraints on  $\tau_e$ , as determined from several datasets over the last  $\sim 12$  years.

### 1.3 The 21-cm Background

In the early 1940s, H.C. Van de Hulst and Jan Oort realized that a hyperfine splitting in the ground state of the hydrogen atom should produce radiation at 21-cm wavelengths. Indeed, first detection of the 21-cm line occurred in 1951 (Ewen and Purcell, 1951, Muller and Oort, 1951), and has continued to be one of the most powerful tools in astronomy ever since. Given my focus on high- $z$  applications, I will neglect the overwhelming application at low- $z$  and from this point henceforth only consider the 21-cm line as a probe of galaxies in the early Universe, which was first considered by Sunyaev and Zeldovich (1972), and subsequently by Sunyaev and Zeldovich (1975), Hogan and Rees (1979), Oort (1984), Baldwin (1986), Swarup and Subrahmanyam (1987), Scott and Rees (1990).

The 21-cm line is an alluring probe of galaxy formation and cosmology for numerous reasons. For example, the 21-cm line provides a direct probe of the properties of intergalactic gas, meaning it holds the potential to map out the ionization history as a function of time. This is highly complementary to the integral constraints on reionization provided by CMB experiments, and also to high- $z$  galaxy surveys, which must model the ionization history based on the galaxy population they constrain. The 21-cm line also offers the ability to measure the thermal history of the IGM, as well as the emergence of the Ly- $\alpha$  background, neither of which are accessible to high- $z$  galaxy surveys or CMB experiments.

Additionally, campaigns to constrain the 21-cm background will improve the completeness of current and near-future galaxy surveys. For example, though *JWST* may be able to detect clusters of Population III

(PopIII) stars at  $2 \lesssim z \lesssim 7$  (Johnson, 2010), PopIII galaxies and proto-quasars at  $z \sim 10 - 15$  (Zackrisson et al., 2011, Johnson et al., 2012), and PopIII supernovae at  $z \sim 15 - 20$  (Whalen et al., 2013a,b), it will struggle to find *normal* galaxies, which are most important to reionization and in providing a statistical sample of objects. If the galaxy luminosity function flattens considerably at the low-luminosity end, as predicted by some recent models (O’Shea et al., 2015), or the formation efficiency of massive Population III stars is low, *JWST* may struggle to find faint galaxies beyond redshifts  $z \sim 10$  (Zackrisson et al., 2012).

A more thorough discussion of the synergies between 21-cm experiments and others will be presented in Chapter 7. For now, we turn to the basic physics of the 21-cm background and early predictions for the structure of the global 21-cm signal, in Sections 1.3.1 and 1.3.2, respectively.

### 1.3.1 Basic Physics

The 21-cm “spin flip” transition results from hyperfine splitting in the 1S ground state of the hydrogen atom when the magnetic moments of the proton and electron flip between aligned (triplet state) and anti-aligned (singlet state). The relative number of hydrogen atoms in each state depends sensitively on the temperature and ionization state of the gas, since it is the temperature and ionization state that determine the rate of hydrogen-hydrogen and hydrogen-electron collisions capable of inducing “spin exchange,” i.e., flipping from one hyperfine state to the other (Purcell and Field, 1956). Spin exchange can also be caused by more subtle radiative processes, depending on the abundance of Ly- $\alpha$  photons (Wouthuysen, 1952, Field, 1958). In principle, then, it probes the radiation fields generated by the first luminous sources, since the Ly- $\alpha$  and LW backgrounds are intimately related, heating is dominated by X-rays, and reionization is dominated by LyC photons.

Madau et al. (1997) were the first to realize that the 21-cm line could be used to study the diffuse IGM, deriving an equation for the brightness of intergalactic hydrogen relative to the CMB (their Equation 45). It is now often written as<sup>5</sup>

$$\delta T_b \simeq 27 x_{\text{HI}} (1 + \delta) \left( \frac{\Omega_{\text{b},0} h^2}{0.023} \right) \left( \frac{0.15}{\Omega_{\text{m},0} h^2} \frac{1+z}{10} \right)^{1/2} \left( 1 - \frac{T_{\text{Y}}}{T_{\text{S}}} \right) \left[ \frac{H(z)/(1+z)}{dv_{\parallel}/dr_{\perp}} \right] \text{ mK}, \quad (1.25)$$

---

<sup>5</sup> For a detailed derivation, see Appendix A.

In this equation,  $x_{\text{HI}}$  represents the hydrogen neutral fraction,  $\delta$  the gas density relative to the cosmic mean,  $T_\gamma$  the temperature of the CMB, and  $T_S$  the spin temperature, which describes the relative abundance of atoms in the hyperfine singlet and triplet states. The remaining quantities are cosmological parameters, including the energy density (relative to the critical density) in baryons ( $\Omega_{\text{b},0}$ ), all matter ( $\Omega_{\text{m},0}$ ), and the Hubble parameter  $H(z)$ . The final term describes the effect of line-of-sight velocities imparting an apparent shift in the 21-cm emission from one redshift to another, and is referred to as the “redshift-space distortions” term.

The dependence of the 21-cm brightness on  $x_{\text{HI}}$  is intuitive – there can be no 21-cm signal without neutral hydrogen, meaning  $\delta T_b$  approaches zero as reionization progresses, culminating in the complete depletion of neutral hydrogen in the IGM. However, prior to reionization (when  $x_{\text{HI}} \approx 1$ ), the behavior of  $\delta T_b$  is driven by evolution in  $T_S$ , which depends on the background intensity of Ly- $\alpha$  photons, predominantly produced by stars, and the IGM temperature, which is determined by X-ray sources like accreting BHs. Evolution in  $\delta T_b$  over cosmic time thus encodes the history of ionization (through  $x_{\text{HI}}$ ), the thermal history (through  $T_S$ ), and Ly- $\alpha$  emission (also through  $T_S$ ), which in principle means that the 21-cm signal probes the background radiation intensity at photon energies ranging from Ly- $\alpha$  to X-rays.

Early studies of HI signatures in the early Universe were exclusively geared toward spatially resolved studies. For example, Madau et al. (1997) focused on the immediate vicinity of quasars, and found that a non-zero HI signal should be visible within  $\sim 10$  Mpc of individual objects, and thus be potentially detectable with the Giant Metrowave Radio Telescope (GMRT) in India. Theirs was the first to consider structure in the HI emission arising due to spatial variations in the spin temperature and ionized fraction, rather than the density, as in previous studies (Hogan and Rees, 1979, Scott and Rees, 1990). Recently, it was realized that such measurements might actually reveal a wealth of information about the spectra of quasars and galaxies (Kramer and Haiman, 2008, Thomas and Zaroubi, 2008), in addition to providing strong evidence of a neutral IGM.

While the long term goal is to map the 21-cm fluctuations from the ground (a task on the horizon at  $z \lesssim 10$ ; via e.g., the Low Frequency Array (LOFAR), the Murchison Widefield Array (MWA), the Precision Array for Probing the Epoch of Reionization (PAPER), the Giant Metrowave Telescope (GMRT), and the

Square Kilometer Array(SKA); Harker et al., 2010, van Haarlem et al., 2013, Bowman et al., 2013, Parsons et al., 2010, Paciga et al., 2013, Carilli et al., 2004, Mellema et al., 2013)) or space (e.g., the Lunar Radio Array (LRA), the Radio Observatory on the Lunar Surface for Solar studies (ROLSS); Jester and Falcke, 2009, Lazio et al., 2011) using large interferometers, in the near term, the entire  $10 \lesssim z \lesssim 40$  window is likely to be accessible only to global 21-cm experiments.

### 1.3.2 The Global 21-cm Signal

The global 21-cm signal was first “discovered” by Shaver et al. (1999), who realized that deviations from  $T_S = T_\gamma$  in the diffuse IGM would manifest as a spectral signature on very large scales, and thus potentially be detected by modest radio telescopes with poor angular resolution. This was in stark contrast to prior studies, which focused on measuring HI from individual sources using resolved observations.

Considering HI only on very large scales, we can take  $\delta = 0$  (i.e., gas at the cosmic mean density), and assume the redshift-space distortions term in Equation 1.25 is unity (i.e., the line-of-sight velocities are simply the Hubble flow), leaving<sup>6</sup>

$$\delta T_b \simeq 27 x_{\text{HI}} \left( \frac{\Omega_{\text{b},0} h^2}{0.023} \right) \left( \frac{0.15}{\Omega_{\text{m},0} h^2} \frac{1+z}{10} \right)^{1/2} \left( 1 - \frac{T_\gamma}{T_S} \right) \text{ mK}. \quad (1.26)$$

Given that, at the time, Ly- $\alpha$  coupling was thought to be immediately followed by efficient heating (via resonant scattering of Ly- $\alpha$  photons; Madau et al., 1997), the initial focus was on the global 21-cm *emission* signature. With early and efficient heating,  $T_S \approx T_K \gg T_\gamma$  and Equation 4.8 becomes

$$\delta T_{b,\text{sat}} \simeq 27 x_{\text{HI}} \left( \frac{\Omega_{\text{b},0} h^2}{0.023} \right) \left( \frac{0.15}{\Omega_{\text{m},0} h^2} \frac{1+z}{10} \right)^{1/2} \text{ mK} \quad (1.27)$$

where we have added the subscript ‘sat’ to indicate that this is the differential brightness temperature in the saturated ( $T_S \gg T_\gamma$ ) limit. Clearly, in this limit, a measurement of the  $\delta T_b$  provides a direct measure of the volume-averaged neutral fraction,  $x_{\text{HI}}$ , and thus an important constraint on Reionization. However, note also that the emission signal has a known maximal amplitude (as a function of redshift) in the saturated regime.

Figure 1.10 shows the early models of the global 21-cm signal from Shaver et al. (1999), in addition to two more recent physically- and empirically- motivated models. While clearly these deviations are small

<sup>6</sup> Note that density fluctuations could in principle still affect the global 21-cm signal if there are strong correlations between  $\bar{x}_i$ ,  $T_S$ , and  $\delta$ . We neglect this complication for the duration of this work.

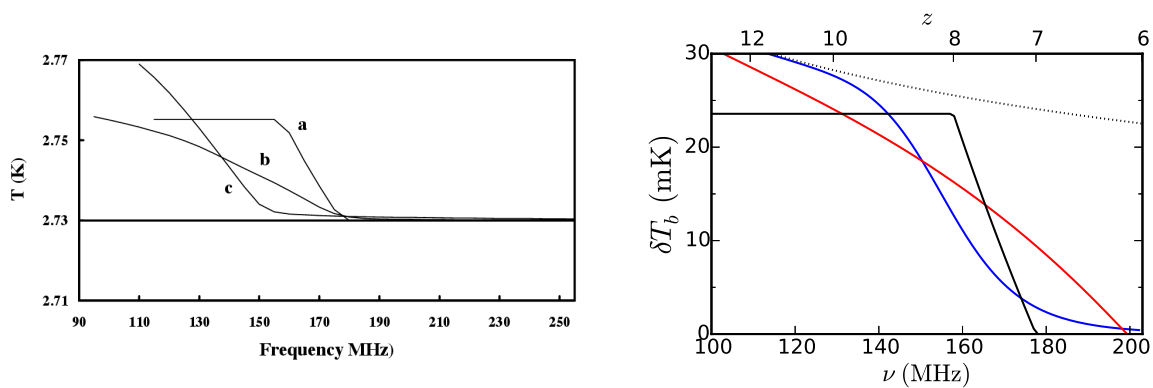


Figure 1.10 *Left*: Early models for the global 21-cm signal from Shaver et al. (1999), including a toy “step” model of reionization (a) and two models from the numerical simulations of Gnedin and Ostriker (1997) and Baltz et al. (1998) (b and c, respectively). *Right*: Re-produced step model of Shaver et al. (1999) (black) compared with more recent physically motivated models, including a tanh model of reionization with  $z_{\text{rei}} = 8$  and  $\Delta z_{\text{rei}} = 1$  (blue), and an empirically constrained model of reionization from Robertson et al. (2015) (red). The physical models assume  $T_S \gg T_\gamma$ , i.e., they use Equation 1.27. Note that the y-axis in the right panel has been re-normalized relative to the CMB, and re-expressed in units of mK, rather than K. The dotted black line shows the maximum allowed amplitude of the signal, i.e., the saturated limit with  $\bar{x}_i = 0$ .

relative the cosmic background, they are even smaller compared to the galactic foreground, which we show at 40, 80, and 120 MHz in Figure 1.11. Even in quiet patches of the sky, the brightness temperature exceeds  $\sim$  a few hundred Kelvin at the high frequencies (bottom panel), with the galactic plane typically exceeding  $\sim 10^3$  K in brightness temperature at all frequencies between 40 and 120 MHz.

We will soon see that the Shaver et al. (1999) models for the global 21-cm signal are only a small piece of most models in the literature today (e.g., Furlanetto, 2006, Pritchard and Loeb, 2010). Most notably, the Shaver et al. (1999) models were pure emission signals because at the time, heating by resonant scattering of Ly- $\alpha$  photons was thought to efficiently heat the IGM temperature above the CMB temperature almost immediately following the emergence of a Ly- $\alpha$  background. Many years later, several authors independently found (Chen and Miralda-Escudé, 2004, Hirata, 2006, Furlanetto and Pritchard, 2006, Chuzhoy et al., 2006) that the initial calculations (Madau et al., 1997) of Ly- $\alpha$  heating were too simplistic, and resulted in heating rates factors of  $\sim 10^3$  too high.

With the Ly- $\alpha$  heating issue resolved, and updated calculations for the rate of spin exchange at low temperatures (Zygelman, 2005), models for the global 21-cm signal began to resemble those common in the literature today. For example, the models of Furlanetto (2006) had rather deep absorption features whose depth and position varied with the efficiency of X-ray production in the first galaxies. Figure 1.12 shows a set of models that span a large range of currently viable parameter space.

Though the global 21-cm signal can in principle be studied with single-element receivers, several challenges in the field persist, in both observational and theoretical arenas. For example, the Earth is a sub-optimal platform for observations at the relevant frequencies ( $\nu \lesssim 200$  MHz) due to radio-frequency interference and ionospheric variability (Vedantham et al., 2013, Datta et al., 2014), making the lunar far-side<sup>7</sup> a particularly appealing destination for future observatories (e.g., LRA, ROLSS, the *Dark Ages Radio Explorer*; Burns et al., 2012). Some foregrounds, however, cannot be escaped even from the lunar farside. Synchrotron emission from our own galaxy is  $10^5$ - $10^6$  times stronger than the global 21-cm signal, while extragalactic point sources appear as another diffuse foreground to single-element receivers. Both must be

---

<sup>7</sup> The Moon is not completely devoid of an ionosphere – its atmosphere is characterized as a “surface-bounded exosphere,” whose constituents are primarily metal ions liberated by interactions with energetic particles and radiation from the Sun (e.g., Stern, 1999). However, it is tenuous enough to be neglected at frequencies  $\nu \gtrsim 1$  MHz.

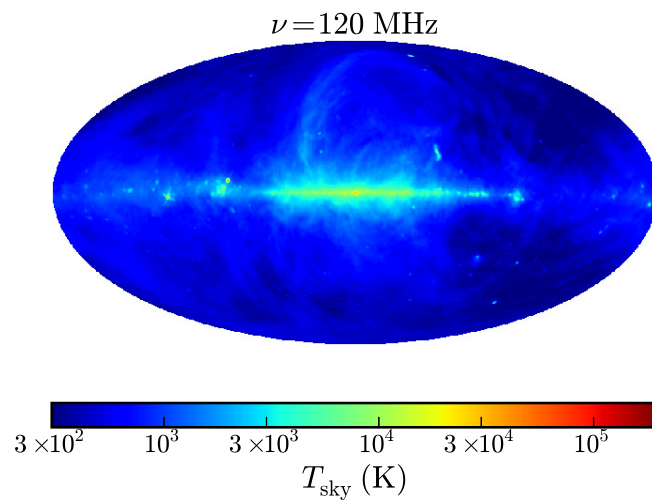
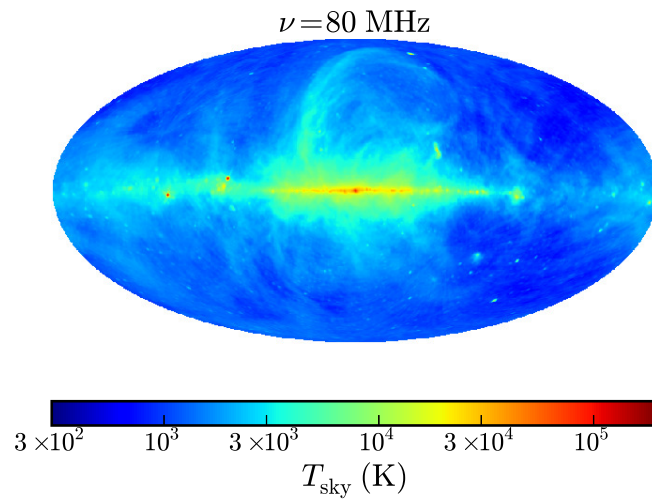
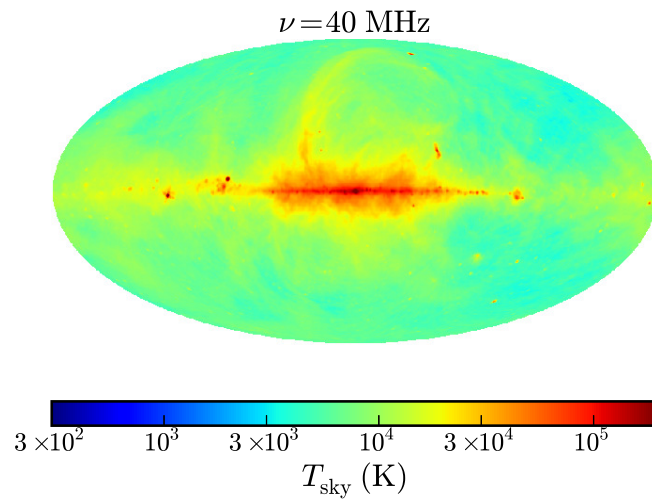


Figure 1.11 Maps of the galactic foreground at 40 MHz (top), 80 MHz (middle), and 120 MHz (bottom) computed using the de Oliveira-Costa et al. (2008) sky model.

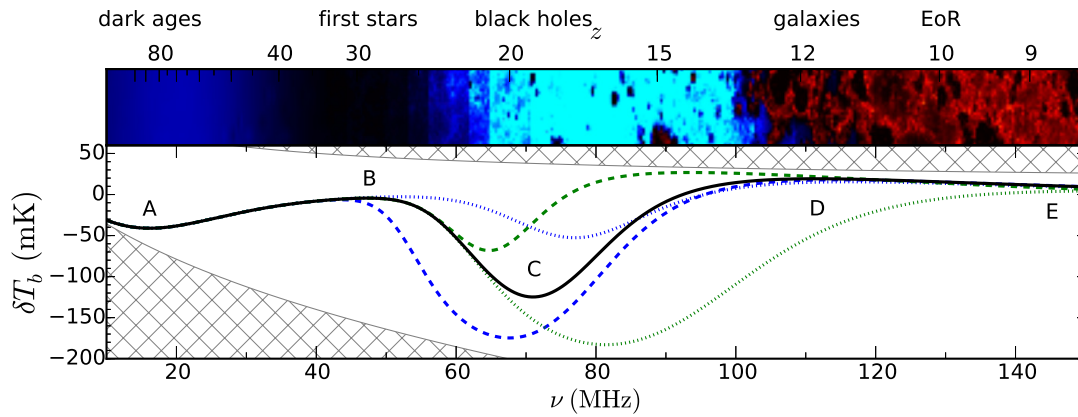


Figure 1.12 The evolution of a slice of the Universe (upper panel; compare to Figure 1.6), from early times at left to late times at right as well as the corresponding sky-averaged 21-cm signal relative to the CMB (lower panel). The first stars form at  $z \sim 30$  in the fiducial model simulation (labeled B on black curve) and “turn on” the 21-cm signal in absorption against the CMB (light blue in top panel). The fiducial model assumes the first sources are similar to those in nearby galaxies. At  $z \sim 20$  (Turning Point C), accreting black holes heat the gas, transforming the signal from absorption to emission ( $z \sim 12$ ; Turning Point D, red in top panel). At later times, ionized bubbles (black, upper panel) grow to fill the universe by  $z \sim 8$ . The bottom panel illustrates the current theoretical uncertainties in first star and black hole parameters. Blue curves vary the UV flux from the first stars by a factor of 100 while green curves vary the X-ray heating rate by a factor of 100. Figure adapted from Pritchard and Loeb (2010) using the new reference model from Mirocha et al. (2015).

removed in post-processing using sophisticated fitting algorithms (e.g., Harker et al., 2012, Liu et al., 2013). Because of these challenge, the only constraints obtained to date come from EDGES, which placed lower limits on the duration of reionization ( $\Delta z \gtrsim 0.06$ ; Bowman and Rogers, 2010).

On the theoretical side, though the global 21-cm signal is undoubtedly rich in the information it encodes, it has so far been unclear to what extent that information can be extracted reliably *even with a precision measurement*. This is largely due to computational restrictions that limit the accuracy of theoretical models, as well as strong degeneracies between model parameters of interest. Advancing theoretical models for the global 21-cm signal, and illuminating the degeneracies between their input parameters are among the chief goals of this thesis, among many, to be introduced in the next Section.

#### 1.4 Motivation and Outline for Subsequent Chapters

Given its sensitivity to the hydrogen ionized fraction, the gas kinetic temperature, and the Ly- $\alpha$  background intensity, the global 21-cm signal is in principle a powerful probe of the rest-frame UV and X-ray spectra of high- $z$  galaxies over time, as it is the LyC photons which ionize hydrogen, X-rays which heat the IGM, and soft UV photons which ultimately redshift or cascade through the Ly- $\alpha$  line and give rise to Wouthuysen-Field coupling. Though these dependencies have been explored on numerous occasions via forward modeling, i.e., models that predict that structure of the global 21-cm signal as a function of the star formation efficiency, mass of star-forming halos, etc., there has been little work dedicated to the prospects for inverting future 21-cm measurements. That is, given a measurement of the global 21-cm signal,  $\delta T_b(\nu)$ , what would we infer about the properties of the Universe's first galaxies, having taken into account degeneracies between the most fundamental parameters of interest and expectations for measurement uncertainty?

The goal of this thesis is to address the inversion problem through development of a framework for interpreting measurements of the global 21-cm signal. Such a tool will ultimately become the final stage of data analysis pipelines, but in the meantime, it will (i) uncover the mapping between features of the global 21-cm signal and properties of the high- $z$  IGM and high- $z$  galaxies, (ii) determine how simultaneous fits to the signal and foreground complicate this mapping, thus providing an important test of foreground removal algorithms, (iii) help optimize the design of next-generation facilities and their observing strate-

gies through parameter forecasting, and (iv) identify the most problematic uncertainties and persistent degeneracies among model parameters, which will help determine the independent measurements of highest degeneracy-breaking value, and also motivate efforts to both improve theoretical models and reduce uncertainty in the models themselves. Subsequent chapters will follow the basic progression outlined above.

In Chapter 2, we start with a simple analysis of an arbitrary realization of the global 21-cm signal characterized by the locations of its extrema (i.e., points B-D in Figure 1.12). This was motivated by the work of Furlanetto (2006) and Pritchard and Loeb (2010), who showed that while the range of expected realizations for the global 21-cm signal vary dramatically in structure, they consistently exhibit three main spectral features. What properties of the IGM do these features encode, and what assumptions must we make to draw robust inferences from the locations of these features?

Having laid the groundwork for interpreting a generic realization of the global 21-cm with a simple analytical model, we then shifted our attention to more concrete examples. How well can the features of the global 21-cm actually be extracted from the foregrounds? Much of this work, to be presented in Chapter 3, was conducted in a larger collaboration of which I was not the lead author, so I have extracted my contributions and those most pertinent for understanding subsequent material.

With reasonable estimates for errors on extrema in the global 21-cm signal yielded by near-future experiments, in Chapter 4 I turned to the prospects of constraining a physically-motivated galaxy formation model from measurements of the turning points of the global 21-cm signal. Can we expect to constrain, for example, the characteristic mass of star-forming halos at high- $z$ ? Could we rule out models for PopIII star formation or models for BH formation? Do we need to measure all three features of the signal, or should we expect narrow-band experiments to have success deciphering the epoch of the first stars and galaxies?

The next two chapters are focused on detailed frequency-dependent solutions to the radiative transfer equation, first on the large scales relevant to the global 21-cm signal (Chapter 5), and then on smaller scales relevant to numerical simulations of reionization and potentially models for the 21-cm power spectrum (Chapter 6).

In Chapter 7, I offer a general set of conclusions and a path for building upon this thesis in future work.

Chapters 2-6 closely mirror a series of published papers (Mirocha et al., 2012, 2013, Mirocha, 2014, Mirocha et al., 2015, Harker et al., 2015). An additional product of this thesis is a publicly available software package that can be used to model the global 21-cm signal, ionized bubbles around stars and BHs, and the meta-galactic radiation background generated by an entire population of such objects. Though over the years it has evolved considerably, through many organizational structures, user-interfaces, and names<sup>8</sup>, it now exists in its entirety in a single PYTHON package: the Accelerated Reionization Era Simulations (ARES) code<sup>9</sup>. Many of the results presented throughout can be reproduced in fairly short order using ARES.

---

<sup>8</sup> <https://bitbucket.org/mirochaj/rt1d>, <https://bitbucket.org/mirochaj/globb>

<sup>9</sup> <https://bitbucket.org/mirochaj/ares>

## Chapter 2

### Model-Independent Constraints from the Sky-Averaged Global 21-cm Signal

Reproduced with permission of the AAS.

Reference:

“Interpreting the Sky-Averaged 21-cm Signal from High Redshifts. I. Model Independent Constraints”

Mirocha, J., Harker, G. J. A., & Burns, J. O. 2013, ApJ, 777, 118

#### 2.1 Context

The sky-averaged (global) 21-cm signal is a powerful probe of the intergalactic medium (IGM) prior to the completion of reionization. However, so far it has been unclear whether, even in the best case scenario, in which the signal is accurately extracted from the foregrounds, it will provide more than crude estimates of when the universe’s first stars and black holes formed. In contrast to previous work, which has focused on predicting the 21-cm signatures of the first luminous objects, we investigate an arbitrary realization of the signal, and attempt to translate its features to the physical properties of the IGM. Within a simplified global framework, the 21-cm signal yields quantitative constraints on the Ly- $\alpha$  background intensity, net heat deposition, ionized fraction, and their time derivatives, without invoking models for the astrophysical sources themselves. The 21-cm absorption signal is most easily interpreted, setting strong limits on the heating rate density of the universe with a measurement of its redshift alone, independent of the ionization history or details of the Ly- $\alpha$  background evolution. In the next two chapters we extend these results, focusing first on the expected accuracy of signal extraction (Chapter 3) and subsequently, the constraints on the properties of the IGM and the first galaxies offered by near-future experiments (Chapter 4).

## 2.2 Introduction

Even if the astrophysical signal is perfectly extracted from the foregrounds, it is not clear that one could glean more than gross estimates of the timing of first star and black hole formation. While simply knowing the redshift at which the first stars and black holes form would be an enormous achievement, it is ultimately their properties that are of interest. Were the universe's first stars very massive? Did all SMBHs in the local universe form via direct collapse at high- $z$ ? Could the global 21-cm signal alone rule out models for the formation of the first stars and black holes? What if independent measurements from JWST and/or other facilities were available?

Motivated by such questions, we turn our attention in this chapter to the final stage of any 21-cm pipeline: interpreting the measurement. Rather than formulating astrophysical models and studying 21-cm realizations that result, we focus on an *arbitrary* realization of the signal, and attempt to recover the properties of the universe in which it was observed. We defer a detailed discussion of how these properties of the universe (e.g., the temperature, ionized fraction, etc.) relate to astrophysical sources to the next chapter.

The outline of this chapter is as follows. In Section 2, we introduce the physical processes that give rise to the 21-cm signal. In Section 3, we step through the three expected astrophysical features of the signal, focusing on how observational measures translate to physical properties of the universe. A discussion and conclusions are presented in Sections 4 and 5, respectively.

We adopt a cosmology with  $\Omega_{\text{m},0} = 0.272$ ,  $\Omega_{\text{b},0} = 0.044$ ,  $\Omega_{\Lambda,0} = 0.728$ , and  $H_0 = 70.2 \text{ km s}^{-1} \text{ Mpc}^{-3}$  throughout.

## 2.3 Evolution of the Global 21-cm Signal

As outlined in the introduction and Appendix A, the brightness temperature of HI gas relative to the CMB is given by

$$\delta T_b \simeq 27(1 - \bar{x}_i) \left( \frac{\Omega_{\text{b},0} h^2}{0.023} \right) \left( \frac{0.15}{\Omega_{\text{m},0} h^2} \frac{1+z}{10} \right)^{1/2} \left( 1 - \frac{T_Y}{T_S} \right), \quad (2.1)$$

where  $h$  is the Hubble parameter today in units of  $100 \text{ km s}^{-1} \text{ Mpc}^{-1}$ , and  $\Omega_{b,0}$  and  $\Omega_{m,0}$  are the fractional contributions of baryons and matter to the critical energy density, respectively. Whether the signal is seen in emission or absorption against the CMB depends entirely on the spin temperature, which is determined by the strength of collisional coupling and presence of background radiation fields,

$$T_S^{-1} \approx \frac{T_\gamma^{-1} + x_c T_K^{-1} + x_\alpha T_\alpha^{-1}}{1 + x_c + x_\alpha}, \quad (2.2)$$

where  $T_\gamma = T_{\gamma,0}(1+z)$  is the CMB temperature,  $T_K$  is the kinetic temperature, and  $T_\alpha \approx T_K$  is the UV color temperature. See Appendix A for a more thorough description of these equations.

Models for the global 21-cm signal generally result in a curve with five extrema<sup>1</sup>, three of which are labeled in Figure 2.1, roughly corresponding to the formation of the first stars (B), black holes (C), and beginning of the EoR (D). Due to the presence of strong (but spectrally smooth in principle; see Petrovic and Oh, 2011) foregrounds, the “turning points” are likely the only pieces of the signal that can be reliably extracted (e.g., Pritchard and Loeb, 2010, Harker et al., 2012). Our primary goal in Section 2.4 will be to determine the quantitative physical meaning of each feature in turn.

In preparation, we differentiate Equation (2.1),

$$\begin{aligned} \frac{d}{dv} [\delta T_b] \simeq 0.1 \left( \frac{1 - \bar{x}_i}{0.5} \right) \left( \frac{1+z}{10} \right)^{3/2} \left\{ \left( \frac{T_\gamma}{T_S} \right) \left[ 1 + \frac{3}{2} \frac{d \log T_S}{d \log t} \right] \right. \\ \left. - \frac{1}{2(1 - \bar{x}_i)} \left( 1 - \frac{T_\gamma}{T_S} \right) \left[ 1 - \bar{x}_i \left( 1 - 3 \frac{d \log \bar{x}_i}{d \log t} \right) \right] \right\} \text{mK MHz}^{-1}, \end{aligned} \quad (2.3)$$

making it clear that at an extremum, the following condition must be satisfied:

$$\frac{d \log T_S}{d \log t} = \frac{1}{3(1 - \bar{x}_i)} \left( \frac{T_S}{T_\gamma} - 1 \right) \left[ 1 - \bar{x}_i \left( 1 - 3 \frac{d \log \bar{x}_i}{d \log t} \right) \right] - \frac{2}{3}. \quad (2.4)$$

We can obtain a second independent equation for the spin-temperature rate of change by differentiating Equation (2.2),

$$\frac{d \log T_S}{d \log t} = \left[ 1 + x_{\text{tot}} \left( \frac{T_\gamma}{T_K} \right) \right]^{-1} \left\{ \frac{x_{\text{tot}}}{(1 + x_{\text{tot}})} \frac{d \log x_{\text{tot}}}{d \log t} \left[ 1 - \left( \frac{T_\gamma}{T_K} \right) \right] + x_{\text{tot}} \frac{d \log T_K}{d \log t} \left( \frac{T_\gamma}{T_K} \right) - \frac{2}{3} \right\}, \quad (2.5)$$

<sup>1</sup> We neglect the first and last features of the signal in this paper. The lowest redshift feature marks the end of reionization, and while its frequency derivative is zero, so is its amplitude, making its precise location difficult to pinpoint. The highest redshift feature is neglected because it is well understood theoretically and should occur well before the formation of the first luminous objects (though exotic physics such as dark-matter annihilation could complicate this, e.g., Furlanetto et al., 2006b).

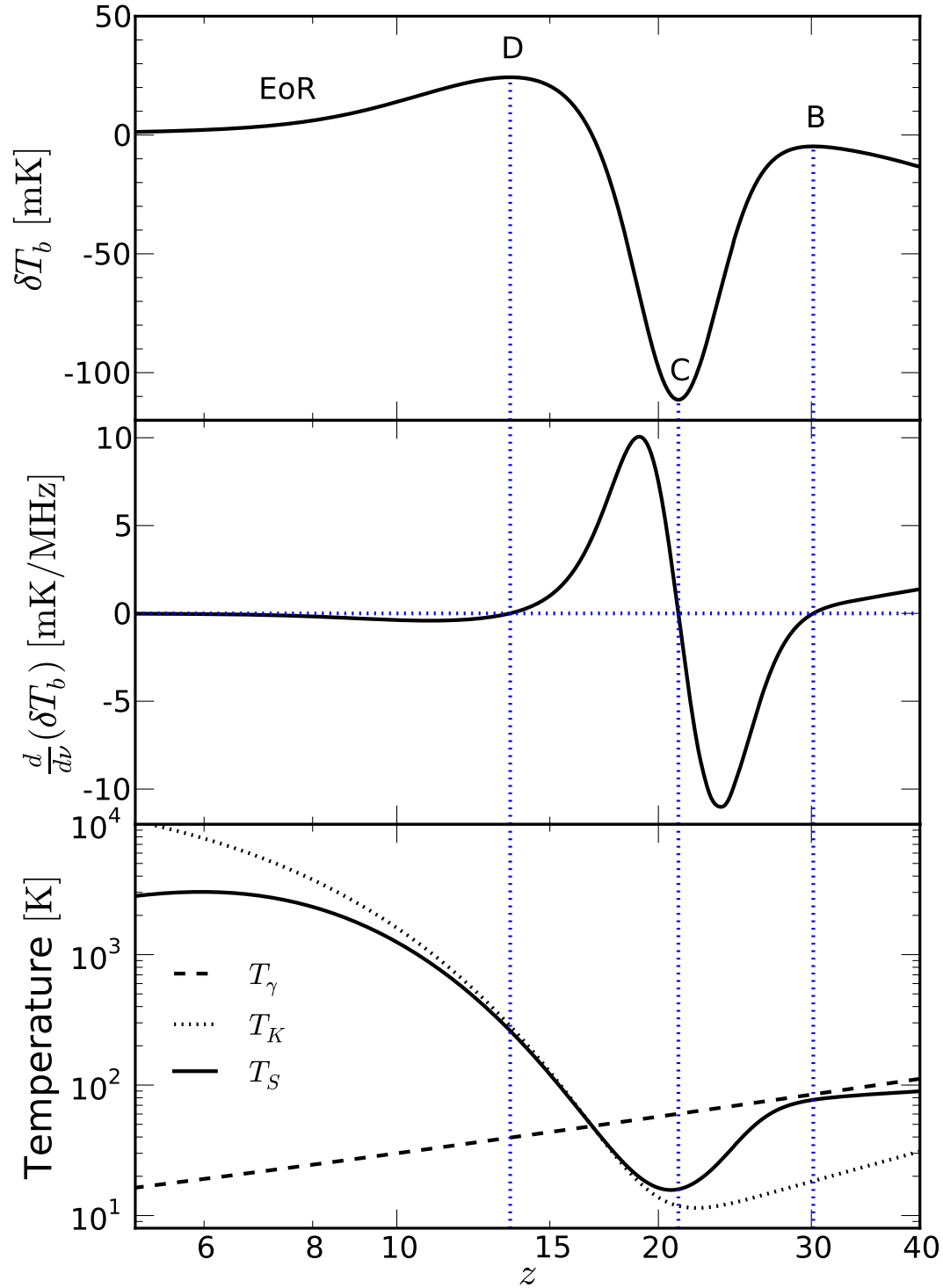


Figure 2.1 Example global 21-cm spectrum (top), its derivative (middle), and corresponding thermal evolution (bottom) for a model in which reionization is driven by PopII stars, and the X-ray emissivity of the universe is dominated by high-mass X-ray binaries.

where  $x_{\text{tot}} = x_c + x_\alpha$ , such that

$$\frac{d \log x_{\text{tot}}}{d \log t} = x_{\text{tot}}^{-1} \left[ \sum_i x_c^i \frac{d \log x_c^i}{d \log t} + x_\alpha \frac{d \log x_\alpha}{d \log t} \right]. \quad (2.6)$$

Expanding out the derivatives of the coupling terms, we have

$$\frac{d \log x_\alpha}{d \log t} = \frac{d \log \widehat{J}_\alpha}{d \log t} + \frac{d \log S_\alpha}{d \log T_K} \frac{d \log T_K}{d \log t} + \frac{2}{3} \quad (2.7)$$

and

$$\frac{d \log x_c^i}{d \log t} = \frac{d \log \kappa_{10}^i}{d \log T_K} \frac{d \log T_K}{d \log t} \pm \frac{d \log x_e}{d \log t} - \frac{4}{3}, \quad (2.8)$$

where the second to last term is positive for H-H collisions and negative for H- $e^-$  collisions.

As in Furlanetto (2006) and Pritchard and Furlanetto (2007), we adopt a two-zone model in which the volume filling fraction of HII regions,  $x_i$ , is treated separately from the ionization in the bulk IGM, parameterized by  $x_e$ . The mean ionized fraction is then  $\bar{x}_i = x_i + (1 - x_i)x_e$ . This treatment is motivated<sup>2</sup> by the fact that  $\delta T_b = 0$  in HII regions, thus eliminating the need for a detailed treatment of the temperature and ionization evolution, but beyond HII regions, the gas is warm and only partially ionized (at least at early times) so we must track both the kinetic temperature and electron density in order to compute the spin temperature.

## 2.4 Critical Points in the 21-cm History

From the equations of Section 2.3, it is clear that in general, turning points in the 21-cm signal probe a set of eight quantities,  $\theta = \{x_i, x_e, T_K, \widehat{J}_\alpha, x'_i, x'_e, T'_K, \widehat{J}'_\alpha\}$ , where primes represent logarithmic time derivatives. Given a perfect measurement of the redshift and brightness temperature,  $(z, \delta T_b)$ , at a turning point, the system is severely underdetermined with two equations (Equations (2.1) and (2.4)) and eight unknowns. Without independent measurements of the thermal and/or ionization history and/or Ly- $\alpha$  background intensity, no single element of  $\theta$  can be constrained unless one or more assumptions are made to reduce the dimensionality of the problem.

---

<sup>2</sup> Our motivation for the logarithmic derivative convention is primarily compactness, though the non-dimensionalization of derivatives is convenient for comparing the rate at which disparate quantities evolve. For reference, the logarithmic derivative of a generic function of redshift with respect to time,  $d \log w / d \log t = b$ , implies  $w(z) \propto (1+z)^{-3b/2}$  under the high- $z$  approximation,  $H(z) \approx H_0 \Omega_{m,0}^{1/2} (1+z)^{3/2}$ , which is accurate to better than  $\sim 0.5\%$  for all  $z > 6$ . For example, the CMB cools as  $d \log T_\gamma / d \log t = -2/3$ .

The most reasonable assumptions at our disposal are as follows.

- (1) The volume filling factor of the HII regions,  $x_i$ , and the ionized fraction in the bulk IGM,  $x_e$ , are both negligible, as are their time derivatives, such that  $\bar{x}_i = d \log \bar{x}_i / d \log t = 0$ .
- (2) There are no heat sources, such that the universe's temperature is governed by pure adiabatic cooling after decoupling at  $z_{\text{dec}} \simeq 150$  (Peebles, 1993), i.e.,  $d \log T_{\text{K}} / d \log t = -4/3$ .
- (3) Ly- $\alpha$  coupling is strong, i.e.,  $x_\alpha \gtrsim 1$ , such that  $T_{\text{S}} \rightarrow T_{\text{K}}$ , and the dependencies on  $\hat{J}_\alpha$  no longer need be considered.

These assumptions are expected to be valid at  $z \gtrsim 10$ ,  $z \gtrsim 20$ , and  $z \lesssim 10$ , respectively, according to typical models (e.g., Furlanetto, 2006, Pritchard and Loeb, 2010). However, since it may be impossible to verify their validity from the 21-cm signal alone, we will take care in the following sections to state explicitly how each assumption affects inferred values of  $\theta$ . We will now examine each feature of the signal in turn.

#### 2.4.1 Turning Point B: End of the Dark Ages

Prior to the formation of the first stars, the universe is neutral to a part in  $\sim 10^4$  (e.g., RECFAST, HYREC, COSMOREC; Seager et al., 1999, 2000, Ali-Haïmoud and Hirata, 2010, Chluba and Thomas, 2011), such that a measurement of  $\delta T_b$  probes  $T_{\text{S}}$  directly via Equation (2.1),

$$T_{\text{S}} \leq T_\gamma \left[ 1 - \frac{\delta T_b}{9 \text{ mK}} (1+z)^{-1/2} \right]^{-1} \quad (2.9)$$

where the  $\leq$  symbol accounts for the possibility that  $\bar{x}_i > 0$  (a non-zero ionized fraction always acts to reduce the amplitude of the signal). For the first generation of objects, we can safely assume  $\bar{x}_i \ll 1$ , and interpret a measurement of the brightness temperature as a proper constraint on  $T_{\text{S}}$  (rather than an upper limit). We will relax this requirement in Section 2.4.2.

If  $T_{\text{S}}$  and  $T_{\text{K}}$  are both known, Equation (2.2) yields the total coupling strength,  $x_{\text{tot}}$ . However, the contribution from collisional coupling is known as a function of redshift for a neutral adiabatically-cooling gas, and can simply be subtracted from  $x_{\text{tot}}$  to yield  $x_\alpha$ , and thus  $\hat{J}_\alpha$  (via Equation (A.14)). The top panel of Figure 2.2 shows lines of constant  $\log_{10}(J_\alpha/J_{21})$ , where  $J_\alpha = h\nu_\alpha \hat{J}_\alpha$  and  $J_{21} = 10^{-21} \text{ erg s}^{-1} \text{ cm}^{-2} \text{ Hz}^{-1} \text{ sr}^{-1}$ ,

given the redshift and brightness temperature of turning point B,  $\delta T_b(z_B)$ . From Equations (2.4) and (2.5), we can also constrain the rate of change in the background Ly- $\alpha$  intensity (Equation (2.7)), as shown in the bottom panel of Figure 2.2.

In the event that heating has already begun (rendering  $T_K(z)$  unknown), interpreting turning point B becomes more complicated.<sup>3</sup> Now,  $x_\alpha$  will be overestimated, given that a larger (unknown) fraction of  $x_{\text{tot}}$  is due to collisional coupling. Uncertainty in  $T_K$  propagates to  $S_\alpha$ , meaning  $x_\alpha$  can only be considered to provide an upper limit on the product  $S_\alpha \hat{J}_\alpha$ , rather than  $\hat{J}_\alpha$  alone. The interpretation of the turning point condition (Eq. 2.4) becomes similarly complicated if no knowledge of  $T_K(z)$  is assumed.

### 2.4.2 Turning Point C: Heating Epoch

In the general case where Hubble cooling and heating from astrophysical sources must both be considered, the temperature evolution can be written as

$$\frac{d \log T_K}{d \log t} = \frac{\tau_H}{\tau_X} - C \quad (2.10)$$

where we have defined a characteristic heating timescale  $\tau_X^{-1} \equiv \epsilon_{\text{heat}}/e_{\text{int}}$ , where  $e_{\text{int}}$  is the gas internal energy,  $\epsilon_{\text{heat}}$  and  $C$  are the heating and cooling rate densities, respectively, and  $\tau_H^{-1} = 3H(z)/2$  is a Hubble time at redshift  $z$  in a matter-dominated universe.

In a neutral medium, the solution to Equation (2.10) for an arbitrary  $\epsilon_{\text{heat}}$  is

$$T_K(z) = C_1^{-1} \int_z^\infty \epsilon_{\text{heat}}(z') \frac{dt}{dz'} dz' + T_{\gamma,0} \frac{(1+z)^2}{1+z_{\text{dec}}} \quad (2.11)$$

where  $C_1 \equiv 3\bar{n}_H^0(1+y)k_B/2$ ,  $k_B$  is Boltzmann's constant,  $\bar{n}_H^0$  is the hydrogen number density today,  $y$  is the primordial helium abundance (by number), and the second term represents the adiabatic cooling limit.

To move forward analytically, we again adopt the maximal cooling rate,  $C = 4/3$ . Detailed calculations with COSMOREC indicate that such a cooling rate is not achieved until  $z \lesssim 10$  in the absence of heat sources, which means we *overestimate* the cooling rate, and thus *underestimate*  $T_K$  at all redshifts. This

<sup>3</sup> We deem such a scenario “exotic” because it requires heat sources prior to the formation of the first stars. Heating via dark matter annihilation is one example of such a heating mechanism (Furlanetto et al., 2006b).

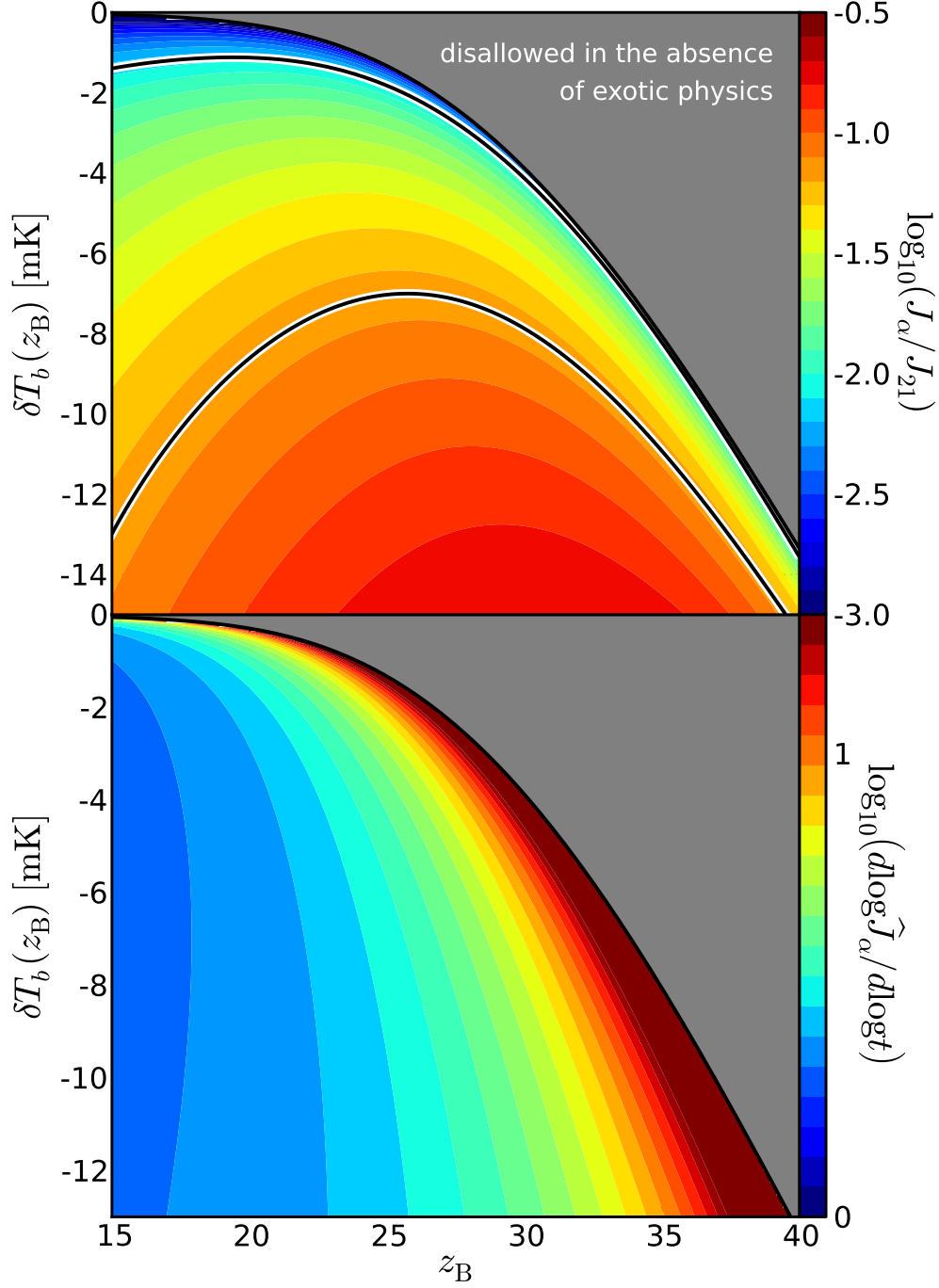


Figure 2.2 Values  $J_\alpha = h\nu_\alpha \hat{J}_\alpha$  and  $d \log J_\alpha / d \log t$  that give rise to turning point B at position  $(z_B, \delta T_b(z_B))$ . The color scale shows the value of  $J_\alpha$  (top panel, in units of  $J_{21} = 10^{-21} \text{ erg s}^{-1} \text{ cm}^{-2} \text{ Hz}^{-1} \text{ sr}^{-1}$ ), and  $d \log J_\alpha / d \log t$  (bottom panel) required for turning point B to appear at the corresponding position in the  $(z_B, \delta T_b(z_B))$  plane, under the assumptions given in Section 3.1. The gray shaded region is excluded unless heating occurs in the dark ages. For reference, the highlighted black contours represent Ly- $\alpha$  fluxes (assuming a flat spectral energy distribution at energies between Ly- $\alpha$  and the Lyman-limit,  $h\nu_\alpha \leq h\nu \leq h\nu_{\text{LL}}$ ), corresponding to Lyman-Werner band fluxes of  $J_{\text{LW}}/J_{21} = \{10^{-2}, 10^{-1}, 2 \times 10^{-1}\}$  (from top to bottom), which roughly bracket the range of fluxes expected to induce negative feedback in minihalos at  $z \sim 30$  (Haiman et al., 2000).

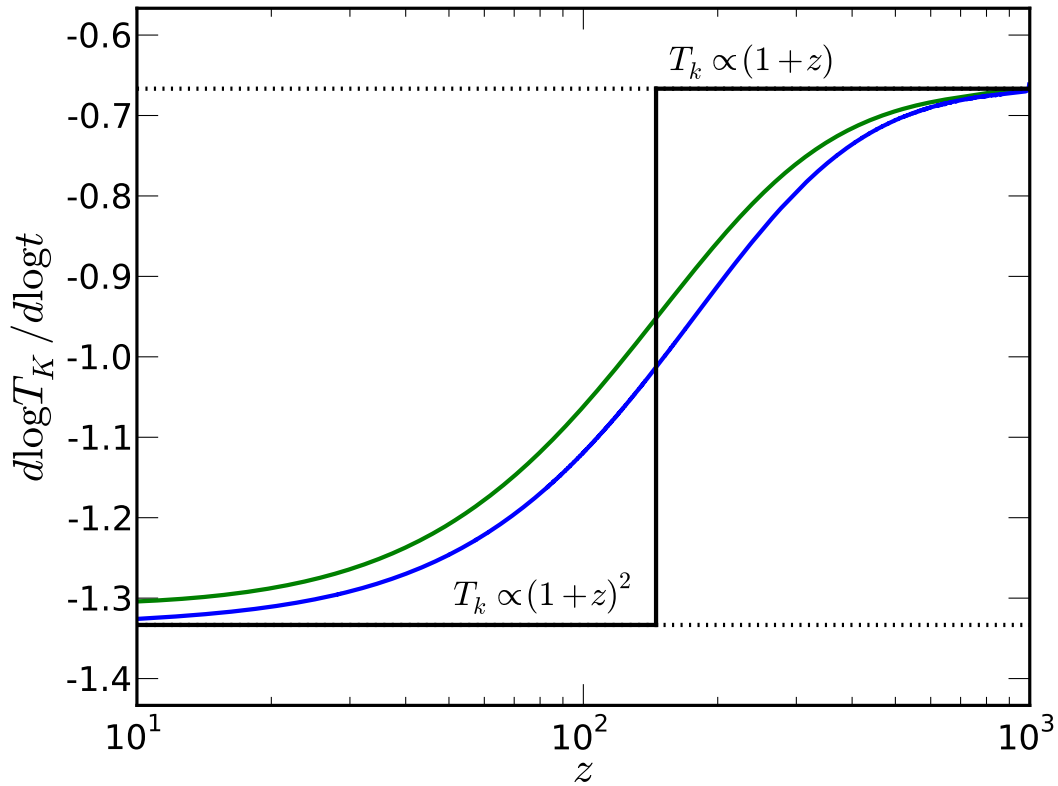


Figure 2.3 Cooling rate of the universe under different assumptions. The black line is an approximate analytic solution (Peebles, 1993), while the blue and green lines are numerical solutions. The blue curve considers cooling via radiative recombination, collisional excitation and ionization, and the Hubble expansion, and heating via Compton scattering. The green line is an even more detailed numerical solution obtained with the COSMOPHYSICS code (Chluba and Thomas, 2011), which includes a multi-level atom treatment and many radiative transfer effects.

lower bound on the temperature is verified in Figure 2.3, in which we compare three different solutions for the cooling rate density evolution.

In order for the 21-cm signal to approach emission, the temperature must be increasing relative to the CMB,<sup>4</sup> i.e.,  $\tau_H/\tau_X > 4/3$ , meaning the existence of turning point C, at redshift  $z_C$ , alone gives us a lower limit on  $\epsilon_{\text{heat}}(z_C)$ . The detection of the absorption signal (regardless of its amplitude) also requires the kinetic temperature to be cooler than the CMB temperature. If we assume a ‘burst’ of heating,  $\epsilon_{\text{heat}} \rightarrow \epsilon_{\text{heat}}\delta(z - z_C)$ , where  $\delta$  is the Dirac delta function, and require  $T_K < T_\gamma$ , we can solve Equation (2.10) and obtain an upper limit on the co-moving heating rate density. The bottom panel of Figure 2.4 shows the upper and lower limits on  $\epsilon_{\text{heat}}$  as a function of  $z_C$  alone.

A stronger upper limit on  $\epsilon_{\text{heat}}(z_C)$  is within reach, however, if we can accurately measure the brightness temperature of turning point C. Given that  $\delta T_b(z_C)$  provides an upper limit on  $T_S$  for all values of  $\bar{x}_i$  (Equation (2.9)), and an absorption signal requires  $T_K < T_S < T_\gamma$ , we can solve Equation (2.11) assuming  $T_K < T_S$ , and once again assume a burst of heating to get a revised upper limit on  $\epsilon_{\text{heat}}(z_C)$ .

In general, turning point C yields an upper limit (again because we have assumed  $C = 4/3$ ) on the *integral* of the heating rate density (Equation (2.11)), which is seen in the top panel of Figure 2.4.<sup>5</sup> This upper limit is independent of the ionization history, since any ionization reduces the amplitude of  $T_S$ , thus lessening the amount of heating required to explain an absorption feature of a given depth. The only observational constraints available to date are consistent with X-ray heating of the IGM at  $z \gtrsim 8$  (Parsons et al., 2013).

### 2.4.2.1 From Absorption to Emission

If heating persists, and the universe is not yet reionized, the 21-cm signal will eventually transition from absorption to emission. At this time, coupling is expected to be strong such that at the precise redshift of the transition,  $z_{\text{trans}}$ , Equation (2.3) takes special form since  $T_S \simeq T_K = T_\gamma$ ,

$$\frac{d}{dv} \left[ \delta T_b \right] \simeq 0.1 \left( \frac{1 - x_i}{0.5} \right) \left( \frac{1 + z_{\text{trans}}}{10} \right)^{3/2} \left[ 1 + \frac{3}{2} \frac{d \log T_K}{d \log t} \right] \text{mK MHz}^{-1}. \quad (2.12)$$

<sup>4</sup> Though see Section 2.4.2.2 for an alternative scenario.

<sup>5</sup> We express our results in units of  $\text{erg cMpc}^{-3}$  to ease the conversion between  $\epsilon_{\text{heat}}$  and the X-ray emissivity,  $\epsilon_X$  (see Section 2.5.2). For reference,  $10^{51} \text{ erg cMpc}^{-3} \simeq 10^{-4} \text{ eV baryon}^{-1}$ .

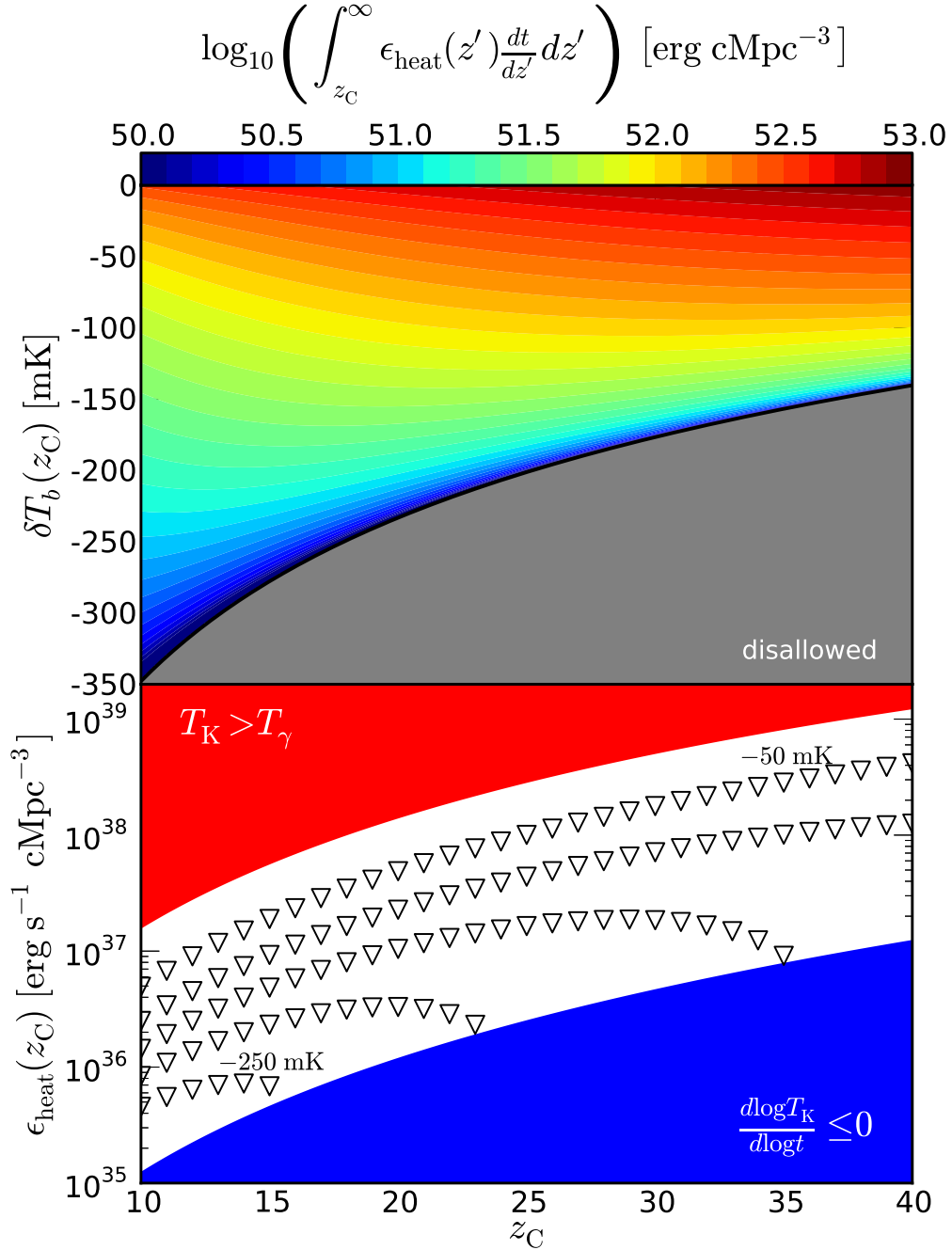


Figure 2.4 *Top*: constraints on the cumulative energy deposition as a function of the redshift and brightness temperature of turning point C. The gray region is disallowed because it requires cooling to be more rapid than Hubble (adiabatic) cooling. *Bottom*: Constraints on the co-moving heating rate density (cMpc<sup>-3</sup> means co-moving Mpc<sup>-3</sup>) as a function of  $z_C$  alone. The blue region includes heating rate densities insufficient to overcome the Hubble cooling, while the red region is inconsistent with the existence of an absorption feature at  $z_C$  because such heating rates would instantaneously heat  $T_K$  above  $T_\gamma$ . The triangles, plotted in increments of 50 mK between  $\delta T_b = \{-250, -50\}$  mK show how a measurement of  $\delta T_b(z_C)$ , as opposed to  $z_C$  alone, enables more stringent upper limits on the heating rate density.

That is, if we can measure the slope at the absorption-emission transition, we obtain a lower limit on the heating rate density. Our inferred heating rate density would be exact if  $\bar{x}_i$  were identically zero, but for  $\bar{x}_i > 0$ , the slope provides a lower limit. This is illustrated in the Figure 2.5.

#### 2.4.2.2 Could the Absorption Feature be Ionization-driven?

The absorption feature of the all-sky 21-cm signal is generally expected to occur when X-rays begin heating the IGM (e.g., Ricotti et al., 2005, Ciardi et al., 2010). However, this feature could also be produced given sufficient ionization, which similarly acts to drive the signal toward emission (albeit by reducing the absolute value of  $\delta T_b$  rather than increasing  $T_S$ ). We now assess whether or not such a scenario could produce turning point C while remaining consistent with current constraints from the Thomson optical depth to the CMB ( $\tau_e$ ; Dunkley et al., 2009, Larson et al., 2011, Bennett et al., 2012).

We assume that coupling is strong,  $T_S \simeq T_K$ , and that the universe cools adiabatically (i.e., the extreme case where turning point C is *entirely* due to ionization), so that a measurement of  $\delta T_b$  is a direct proxy for the ionization fraction (via Equation (2.1)). If we adopt a tanh model of reionization, parameterized by the midpoint of reionization,  $z_{\text{rei}}$ , and its duration,  $\Delta z_{\text{rei}}$ , we can solve Equation (2.1) at a given  $\delta T_b(z_C)$  for  $\bar{x}_i(z_C)$ . Then, we can determine the  $(z_{\text{rei}}, \Delta z_{\text{rei}})$  pair, and thus entire ionization history  $\bar{x}_i(z)$ , consistent with our measure of  $\bar{x}_i(z_C)$ . Computing the Thomson optical depth is straightforward once  $\bar{x}_i(z)$  is in hand – we assume HeIII reionization occurs at  $z = 3$ , and that HeII and hydrogen reionization occur simultaneously.

At a turning point, however, Equation (2.4) must also be satisfied. This results in a unique track through  $(z, \delta T_b)$  space corresponding to values of  $z_C$  and  $\delta T_b(z_C)$  that are consistent with both  $\bar{x}_i(z_C)$  and its time derivative for a given *tanh* model. Figure 2.6 shows the joint ionization and 21-cm histories consistent with WMAP 9 constraints on  $\tau_e$  (Bennett et al., 2012).

This technique is limited because it assumes a functional form for the ionization history that may be incorrect, in addition to the fact that we are only using two points in the fit – the first being  $z_{\text{rei}}$ , at which point  $\bar{x}_i = 0.5$  (by definition), and the second being  $\bar{x}_i(z_C)$  as inferred from  $\delta T_b(z_C)$ . However, it does show that reasonable reionization scenarios could produce turning point C, although at later times (lower redshifts) than typical models (where turning point C is a byproduct of heating) predict.

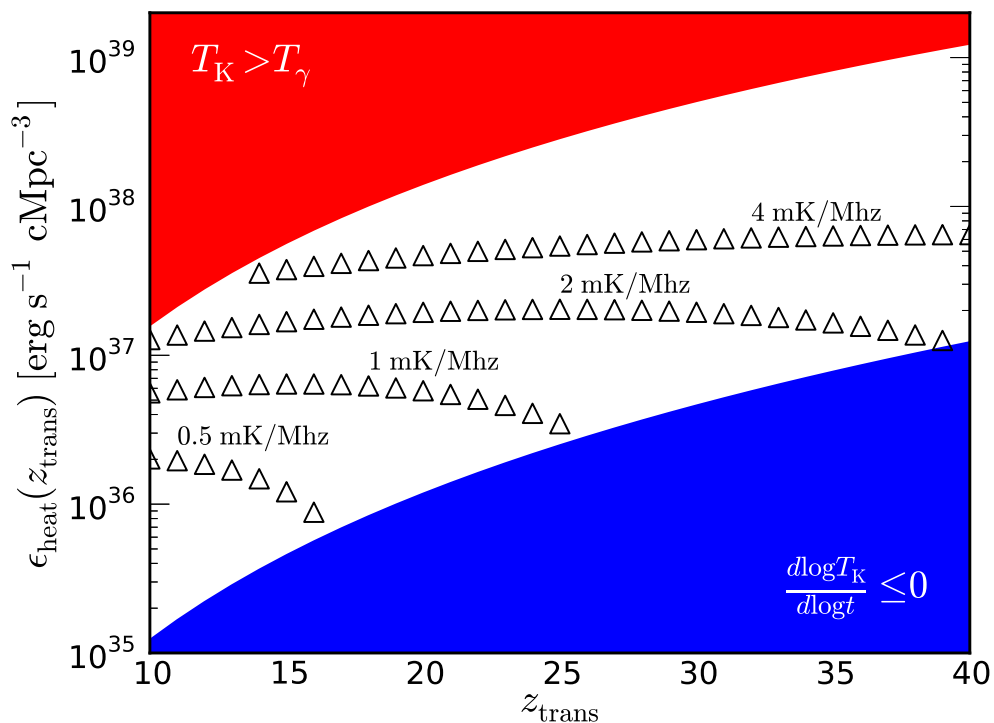


Figure 2.5 Constraints on the co-moving heating rate density (once again cMpc<sup>-3</sup> means co-moving Mpc<sup>-3</sup>) as a function of the absorption-emission transition redshift,  $z_{\text{trans}}$ , and the slope of the 21-cm signal at that redshift. As in Figure 2.4, the blue region indicates heating rates insufficient to overcome the Hubble cooling, while the red region denotes heating rates that would instantaneously heat  $T_K$  above  $T_\gamma$ . The triangles show how measuring the slope of the signal at  $z_{\text{trans}}$  can provide a lower limit on  $\epsilon_{\text{heat}}$ .

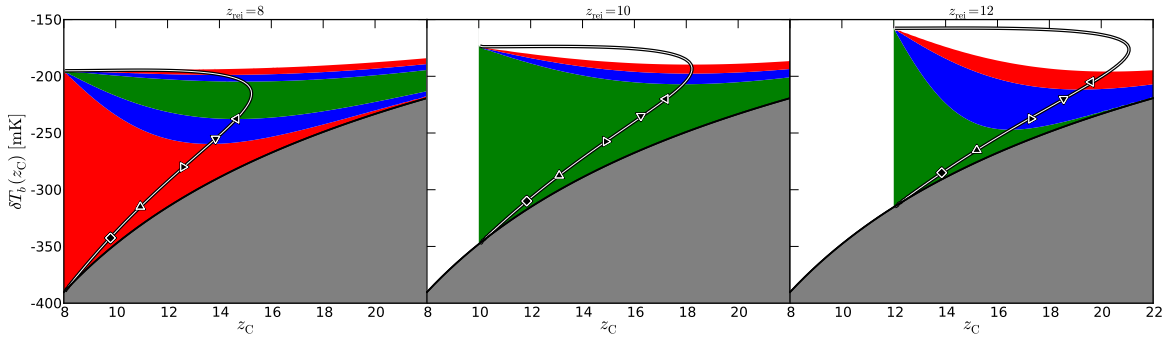


Figure 2.6 Plausibility of an ionization-driven absorption feature assuming *tanh* models of reionization with  $z_{\text{rei}} = 8, 10,$  and  $12$  from left to right. The filled contours denote measures of  $\delta T_b(z)$  (and thus  $\bar{x}_i$  assuming an adiabatically-cooling universe) which correspond to ionization histories consistent with WMAP 9 values of  $\tau_e$  (Bennett et al., 2012) at the 1, 2, and 3- $\sigma$  level (green, blue, and red, respectively). However, while the filled contours denote plausible reionization scenarios, not all of them would induce a turning point in the global 21-cm signal. The white contour denotes  $(z, \delta T_b)$  pairs where Equation (2.4) is satisfied exactly, meaning  $(z, \delta T_b)$  points lying within the filled contours *and* along the white contour mark locations where turning point C would be a produced by ionization and also be consistent with the CMB constraint. The symbols denote *tanh* models with  $\Delta z_{\text{rei}} = 1, 2, 4, 6, 8$  (diamond, upward/rightward/downward/leftward-facing triangles, respectively). The values of  $\Delta z_{\text{rei}} \leq 7.9$  are consistent with the most conservative (model-dependent) constraints from South Pole Telescope (via the kinetic Sunyaev-Zeldovich (SZ) effect; Zahn et al., 2012), which assume no prior knowledge of angular correlations in the cosmic infrared background and thermal SZ power.

### 2.4.3 Turning Point D: Reionization

In principle, turning point D could be due to a sudden decline in the Ly- $\alpha$  background intensity, which would cause  $T_S$  to decouple from  $T_K$  and re-couple to the CMB. Alternatively, turning point D could occur if heating subsided enough for the universe to cool back down to the CMB temperature. However, the more plausible scenario is that coupling continues between  $T_S$  and  $T_K$ , heating persists, and the signal “saturates,” i.e.,  $1 - T_\gamma/T_S \approx 1$ , in which case the brightness temperature is a direct proxy for the volume filling factor of HII regions<sup>6</sup>.

If saturated, Equation (2.4) becomes

$$\frac{\bar{x}_i}{1 - \bar{x}_i} \frac{d \log \bar{x}_i}{d \log t} \simeq \left( \frac{T_\gamma}{T_K} \right) \frac{d \log T_K}{d \log t} - \frac{1}{3}. \quad (2.13)$$

Even in the saturated regime, the first term on the right-hand side cannot be discarded since we have assumed nothing about  $d \log T_S/d \log t$ .

Many authors have highlighted the 21-cm emission signal as a probe of the ionization history during the EoR (e.g., Pritchard et al., 2010, Morandi and Barkana, 2012). Rather than dwell on it, we simply note that if 21-cm measurements of the EoR signal are accompanied by independent measures of  $\bar{x}_i$ , in principle one could glean insights into the thermal history from turning point D as well.

## 2.5 Discussion

### 2.5.1 A Shift in Methodology

The redshifted 21-cm signal has been studied by numerous authors in the last 10-15 years. Efforts have concentrated on identifying probable sources of Ly- $\alpha$ , Lyman-continuum, and X-ray photons at high- $z$ , and then solving for their combined influence on the thermal and ionization state of gas surrounding individual objects (e.g., Madau et al., 1997, Thomas and Zaroubi, 2008, Chen et al., 2008, Venkatesan and Benson, 2011), or the impact of populations of sources on the the global properties of the IGM (e.g., Choudhury and Ferrara, 2005, Furlanetto, 2006, Pritchard and Loeb, 2010). It has been cited as a probe of the first stars (Barkana and Loeb, 2005a), stellar-mass black holes and active galactic nuclei (e.g., Mirabel

---

<sup>6</sup> If the signal is not yet saturated, a measurement of turning point D instead yields an upper limit on  $\bar{x}_i$ .

et al., 2011, McQuinn, 2012, Tanaka et al., 2012, Fragos et al., 2013, Mesinger et al., 2013a), which primarily influence the thermal history through X-ray heating, but could contribute non-negligibly to reionization (e.g., Dijkstra et al., 2004, Pritchard et al., 2010, Morandi and Barkana, 2012). More recently, more subtle effects have come into focus, such as the relative velocity-difference between baryons and dark-matter, which delays the formation of the first luminous objects (Tsaliakhovich and Hirata, 2010, McQuinn and O’Leary, 2012, Fialkov et al., 2012).

Forward modeling of this sort, where the input is a set of astrophysical parameters and the output is a synthetic global 21-cm spectrum, is valuable because it (1) identifies the processes that most affect the signal, (2) has so far shown that a 21-cm signal should exist given reasonable models for early structure formation, and (3) that the signal exhibits the same qualitative features over a large subset of parameter space. However, this methodology yields no information about how unique a given model is.

We have taken the opposite approach. Rather than starting from an astrophysical model and computing the resulting 21-cm spectrum, we begin with an arbitrary signal characterized by its extrema, and identify the IGM properties that would be consistent with its observation. The advantage is that (1) we have a mathematical basis to accompany our intuition about which physical processes give rise to each feature of the signal, (2) we can see how reliably IGM properties can be constrained given a perfect measurement of the signal, and (3) we can predict which models will be degenerate without even computing a synthetic 21-cm spectrum.

### **2.5.2 An Example History**

In our analysis, we have found that the 21-cm signal provides more than coarse estimates of when the first stars and black holes form. Turning points B, C, and D constrain (quantitatively) the background Ly- $\alpha$  intensity, cumulative energy deposition, and mean ionized fraction, respectively, as well as their time derivatives, as summarized in Table 2.1. For concreteness, we will now revisit each feature of the signal for an assumed realization of the 21-cm spectrum, and demonstrate how each can be interpreted in terms of model-independent IGM properties.

We will assume the same realization of the signal as is shown in Figure 2.1, with turning points B, C,

Table 2.1. Features of the global 21-cm signal

| Feature    | Measurement                                   | Assumptions                              | Yield   | §       | Equations            | Figures  |
|------------|---|--|---|---------|----------------------|----------|
| B          | $z_B$   | ...                                      | lower limit on redshift of first star formation   | 2.4.1   | ...                  | ...      |
| B          | $\delta T_b(z_B)$                             | $\bar{x}_i = \epsilon_{\text{heat}} = 0$ | $\tilde{J}_\alpha(z_B), \tilde{J}'_\alpha(z_B)$   | 2.4.1   | 2.1-A.14, 2.4-2.8    | 2.2      |
| C          | $z_C$   | ...                                      | upper limit on $\epsilon_{\text{heat}}(z_C)$  | 2.4.2   | 2.11                 | 2.4      |
| C          | $z_C$   | $\bar{x}_i = 0$                          | lower limit on redshift of first X-ray source formation                                 | 2.4.2   | ...                  | ...      |
| C          | $z_C$   | $\bar{x}_i = 0$                          | lower limit on $\epsilon_{\text{heat}}(z_C)$  | 2.4.2   | 2.10                 | 2.3, 2.4 |
| C          | $\delta T_b(z_C)$                             | ...                                      | improved upper limit on $\epsilon_{\text{heat}}(z_C)$                                   | 2.4.2   | 2.1, 2.4, 2.10, 2.11 | 2.4      |
| C          | $\delta T_b(z_C)$                             | $\epsilon_{\text{heat}} = 0$             | rule out reionization scenario?   | 2.4.2.2 | 2.4                  | 2.6      |
| transition | $z_{\text{trans}}$                            | $T_S = T_K$                              | upper limit on $\int \epsilon_{\text{heat}} dt$   | 2.4.2.1 | 2.11                 | 2.5      |
| transition | $\frac{d}{dz} [\delta T_b](z_{\text{trans}})$ | $T_S = T_K$                              | lower limit on $\epsilon_{\text{heat}}(z_{\text{trans}})$                               | 2.4.2.1 | 2.12                 | 2.5      |
| D          | $z_D$   | ...                                      | start of EoR  | 2.4.3   | ...                  | ...      |
| D          | $\delta T_b(z_D)$                             | ...                                      | upper limit on $\bar{x}_i(z_D)$   | 2.4.3   | 2.1                  | ...      |
| D          | $\delta T_b(z_D)$                             | $T_S = T_K \gg T_\gamma$                 | $\bar{x}_i(z_D)$ , joint constraint on $\bar{x}'_i(z_D)$ , $T_K(z_D)$ , and $T'_K(z_D)$ | 2.4.3   | 2.1, 2.4, 2.13       | ...      |

Note. — Constraints on IGM properties from critical points in the global 21-cm signal. Each block focuses on a single feature of the signal (denoted in column #1) and from left to right reports how a given measurement (column #2; e.g., the feature's redshift,  $z$ ) under some set of assumptions (column #3) would be interpreted (column #4). The corresponding section of the text, as well as any equations and figures relevant to the given feature are listed in columns 5, 6, and 7, respectively. Within each block, elements appear in order of increasing complexity (in terms of the measurement difficulty and number of assumptions) from top to bottom.

and D at  $(z, \delta T_b/\text{mK})$  of  $(30.2, -4.8)$ ,  $(21.1, -112)$ , and  $(13.5, 24.5)$ , respectively, and absorption-emission transition at  $z_{\text{trans}} = 15$ ,  $d(\delta T_b)/dv = 4.3 \text{ mK MHz}^{-1}$ . At a glance, the 21-cm realization shown in Figure 2.1 indicates that the universe's first stars form at  $z \gtrsim 30$ , the first black holes form at  $z \gtrsim 21$ , and that reionization has begun by  $z \gtrsim 13.5$ . Global feedback models such as those presented in Tanaka et al. (2012) are inconsistent with this realization of the signal, as they predict  $T_K > T_\gamma$  at  $z \gtrsim 20$ .

More quantitatively, from Figure 2.2 we have an upper limit on the Ly- $\alpha$  background intensity of  $J_\alpha(z_B)/J_{21} \geq 10^{-1.8}$  and its time rate-of-change,  $d \log J_\alpha / d \log t \simeq 11.2$ . Moving on to turning point C (Figure 2.4), the kinetic temperature is constrained between  $9 \lesssim T_K/\text{K} \lesssim 16$ , meaning that the cumulative energy deposition must be  $\int \epsilon_{\text{heat}} dt \leq 10^{51.9} \text{ erg cMpc}^{-3}$ . In the absence of any ionization, a minimum heating rate density of  $\epsilon_{\text{heat}} \geq 10^{36.1} \text{ erg s}^{-1} \text{ cMpc}^{-3}$  is required to produce turning point C, and a maximum of  $\epsilon_{\text{heat}} \leq 10^{38.2} \text{ erg s}^{-1} \text{ cMpc}^{-3}$  is imposed given the existence of the absorption feature.

The slope of the signal as it crosses  $\delta T_b = 0$  is  $\delta T'_b = 4.3 \text{ mK MHz}^{-1}$ , corresponding to a lower limit on the heating rate density of  $\epsilon_{\text{heat}} \geq 10^{37.6} \text{ erg s}^{-1} \text{ cMpc}^{-3}$  (Figure 2.5). Finally, at turning point D, the ionized fraction must be  $\bar{x}_i \leq 0.24$  (Equation (2.1) when  $T_S \gg T_\gamma$ ). An ionization-driven turning point C can be ruled out by Figure 2.6, since the amount of ionization required to produce  $(z_C, \delta T_b(z_C)) = (21.1, -112)$  leads to  $\tau_e$  values inconsistent with *Wilkinson Microwave Anisotropy Probe* (s) at the  $> 3\sigma$  level, for *tanh* models with  $8 \leq z_{\text{rei}} \leq 12$ .

With limits on  $\hat{J}_\alpha$ ,  $\epsilon_{\text{heat}}$ ,  $\bar{x}_i$ , and their derivatives, the next step is to determine how each quantity relates to astrophysical quantities. Typically, models for the global 21-cm signal relate the emissivity of the universe to the cosmic star-formation rate density (SFRD) via simple scalings of the form  $\hat{\epsilon}_{i,v}(z) \propto f_i \hat{\rho}_*(z) I_v$  (e.g., Furlanetto, 2006, Pritchard and Loeb, 2010), in which case the parameters of interest are  $f_i$ , which converts a star formation rate into a bolometric energy output in band  $i$  (generally split between Ly- $\alpha$ , soft-UV, and X-ray photons), the SFRD itself,  $\hat{\rho}_*$ , and the spectral energy distribution (SED) of luminous sources being modeled,  $I_v$ .

Given that soft-UV photons have very short mean-free-paths in a neutral medium, a determination of  $d \log \bar{x}_i / d \log t$  is likely to be an accurate tracer of the soft-UV ionizing emissivity of the universe,  $\hat{\epsilon}_{\text{ion}}$ . However, the same is not true of photons emitted between Ly- $n$  resonances and hard X-ray photons, which

can travel large distances before being absorbed, where they predominantly contribute to Wouthuysen-Field coupling and heating, respectively. Because of this, translating  $\widehat{J}_\alpha$  and  $\epsilon_{\text{heat}}$  measurements to their corresponding emissivities,  $\widehat{\epsilon}_\alpha$  and  $\epsilon_X$ , is non-trivial. In general, the accuracy with which one can convert  $\widehat{J}_\alpha$  ( $\epsilon_{\text{heat}}$ ) to  $\widehat{\epsilon}_\alpha$  ( $\epsilon_X$ ) depends on the redshift-evolution of the co-moving bolometric luminosity and the SED of sources,  $I_\nu$ .

For a zeroth order estimate, we will assume that sources have a flat spectrum between the Ly- $\alpha$  resonance and the Lyman limit, and neglect “injected photons,” i.e., those that redshift into higher Ly- $n$  resonance and (possibly) cascade through the Ly- $\alpha$  resonance. If  $\widehat{\epsilon}_\alpha \propto N_\alpha \dot{\rho}_*$ , where  $N_\alpha$  is the number of photons emitted between  $\nu_\alpha \leq \nu \leq \nu_{\text{LL}}$  per baryon, then

$$\dot{\rho}_*(z) \approx 10^{-5} \left( \frac{9690}{N_\alpha} \right) \left( \frac{J_\alpha}{J_{21}} \right) \left( \frac{1+z}{30} \right)^{-1/2} M_\odot \text{ yr}^{-1} \text{ cMpc}^{-3} \quad (2.14)$$

where we have scaled  $N_\alpha$  to a value appropriate for low-mass PopII stars (Barkana and Loeb, 2005a).

Similarly, if we assume that a fraction  $f_{X,h} = 0.2$  of the X-ray emissivity is deposited as heat (appropriate for the  $E \gtrsim 0.1$  keV limit in a neutral medium; Shull and van Steenberg, 1985), and normalize by the local  $L_X$ -SFR relationship (e.g., Mineo et al., 2012a, who found  $L_{0.5-8\text{keV}} = 2.61 \times 10^{39} \text{ erg s}^{-1} (M_\odot \text{ yr}^{-1})$ ), we have

$$\dot{\rho}_*(z) \approx 2 \times 10^{-2} f_X^{-1} \left( \frac{0.2}{f_{X,h}} \right) \times \left( \frac{\epsilon_{\text{heat}}}{10^{37} \text{ erg s}^{-1} \text{ cMpc}^{-3}} \right) M_\odot \text{ yr}^{-1} \text{ cMpc}^{-3} \quad (2.15)$$

where we subsume all uncertainty in the normalization between  $L_X$  and  $\dot{\rho}_*$ , the SED of X-ray sources, and radiative transfer effects into the factor  $f_X$ .

If these approximate treatments are sufficient, then measures of  $J_\alpha$  provide two-dimensional constraints on  $\dot{\rho}_*$  and  $N_\alpha$ , and measures of  $\epsilon_{\text{heat}}$  constrain  $\dot{\rho}_*$  and  $f_X$ .<sup>7</sup> However, given the long mean free paths of X-rays and photons in the  $\nu_\alpha \leq \nu \leq \nu_{\text{LL}}$  band, the estimates above are likely to be inadequate. This is the subject of Mirocha (2014) (Chapter 5).

<sup>7</sup> Here we have assumed that high-mass X-ray binaries are the only source of X-rays, when in reality the heating may be induced by a variety of sources. Other candidates include X-rays from “miniquasars” (e.g., Kuhlen and Madau, 2005), inverse Compton scattered CMB photons off high energy electrons accelerated in supernovae remnants (Oh, 2001), or shock heating (e.g., Gnedin and Shaver, 2004, Furlanetto and Loeb, 2004).

### 2.5.3 Synergies with Upcoming Facilities

The prospects for synergies are most promising for turning point D, which is predicted to occur at  $z \lesssim 15$ , coinciding with the JWST window and current and upcoming campaigns to measure the 21-cm power spectrum. JWST will probe the high- $z$  galaxy population even more sensitively than HST (e.g., Robertson et al., 2013), which may allow degeneracies between the star-formation history and other parameters to be broken (e.g., the  $f_i$  normalization factors). However, our focus in this paper is on model-independent quantities – the issue of degeneracy among astrophysical parameters will be discussed in Paper II.

In terms of model-independent quantities, current and upcoming facilities will benefit global 21-cm measurements by constraining the ionization history. For example, one can constrain  $\bar{x}_i(z)$  via observations of Ly- $\alpha$ -emitters (LAEs; e.g., Malhotra and Rhoads, 2006, McQuinn et al., 2007, Mesinger and Furlanetto, 2008), the CMB through  $\tau_e$  and the kinetic Sunyaev-Zeldovich effect (Zahn et al., 2012), or via measurements of the 21-cm power spectrum, which reliably peaks when  $\bar{x}_i \simeq 0.5$  (Lidz et al., 2008). However, like the global signal, power spectrum measurements yield upper limits on  $\bar{x}_i$ , since they assume  $T_S \gg T_\gamma$ , which may not be the case. Constraints from LAEs require no such assumption, and instead set lower limits on  $\bar{x}_i$ , since our ability to see Ly- $\alpha$  emission from galaxies at high- $z$  depends on the *minimum* size of an HII region required for Ly- $\alpha$  photons to escape. Limits on  $\bar{x}_i(z)$  out to  $z \sim 10 - 15$  would yield a prediction for the amplitude of turning point D, which, in conjunction with a global 21-cm measurement could validate or invalidate the  $T_S \gg T_\gamma$  assumption often adopted for EoR work. In addition, one could determine if ionization-driven absorption features are even remotely feasible (Section 2.4.2.2).

### 2.5.4 Caveats

Simple models for the global 21-cm signal rely on the assumption that the IGM is well approximated as a two-phase medium, one phase representing HII regions, and the other representing the bulk IGM. As reionization progresses, the distinction between these two phases will become tenuous, owing to a warming and increasingly ionized IGM whose properties differ little from an HII region. Even prior to reionization the global approximation may be inadequate depending on the distribution of luminous sources. If exceed-

ingly rare sources dominate ionization and heating, we would require a more detailed treatment (a problem recently addressed in the context of helium reionization by Davies and Furlanetto, 2012).

Eventually, simple models must also be calibrated by more sophisticated simulations. This has been done to some extent already in the context of 21-cm fluctuations, with good agreement so far between semi-analytic and numerical models (Zahn et al., 2011). However, analogous comparisons for the global signal have yet to be performed rigorously. The limiting factor is that a large volume must be simulated in order to avoid cosmic variance, but the spatial resolution required to simultaneously resolve the first galaxies becomes computationally restrictive.

Finally, though we included an analysis of the absorption-emission transition point,  $z_{\text{trans}}$ , in truth, the slope measured from this feature will be correlated with the positions of the turning points. The most promising foreground removal studies rely on parameterizing the signal as a simple function (e.g., spline), meaning the slope at  $z_{\text{trans}}$  is completely determined by the positions of the turning points and the function used to represent the astrophysical signal.

## 2.6 Conclusions

In this paper we have addressed one tier of the 21-cm interpretation problem: identifying the physical properties of the IGM that can be constrained uniquely from a measurement of the all-sky 21-cm signal. Our main conclusions are as follows.

- The first feature of the global signal, turning point B, provides a lower limit on the redshift at which the universe's first stars formed. However, more quantitatively, its position in  $(z, \delta T_b)$  space measures the background Ly- $\alpha$  intensity,  $\hat{J}_\alpha$ , and its time derivative, respectively, assuming a neutral, adiabatically-cooling medium.
- The absorption feature, turning point C, is most likely a probe of accretion onto compact objects considering the  $\tau_e$  constraint from the CMB. As a result, it provides a lower limit on the redshift when the first X-ray emitting objects formed. Even if the magnitude of the absorption trough cannot be accurately measured, a determination of  $z_C$  alone sets strong upper and lower limits on

the heating rate density of the universe,  $\epsilon_{\text{heat}}(z_C)$ . If the absorption feature is deep ( $\delta T_b(z_C) \lesssim -200$  mK) and occurs late ( $z \lesssim 15$ ), it could be a byproduct of reionization.

- The final feature, turning point D, indicates the start of the EoR, and traces the mean ionized fraction of the universe and its time derivative. In general, it also depends on the spin-temperature evolution, though it is expected that at this stage the signal is fully saturated. Without independent constraints on the thermal history,  $\delta T_b(z_D)$  provides an upper limit on the mean ionized fraction,  $\bar{x}_i$ .

In general, the relationship between IGM diagnostics (such as  $\hat{J}_\alpha$  and  $\epsilon_{\text{heat}}$ ) and the properties of the astrophysical sources themselves (like  $\dot{\rho}_*$ ,  $N_\alpha$ , and  $f_X$ ) is expected to be complex. This will be the subject of Chapter 4.

## Chapter 3

### Signal Extraction for All-Sky 21-cm Experiments: Dependence on the Assumed Parameterization of the Global 21-cm Signal

Reproduced in part, with permission of the RAS and the authors.

Reference:

“Parametrizations of the Global 21-cm Signal”

Harker, G. J. A., Mirocha, J., Burns, J. O., & Pritchard, J.R., 2015, submitted to *MNRAS* (arXiv:1510.00271)

#### 3.1 Context

In the previous chapter, we found that model-independent constraints are within reach of 21-cm measurements, for example the temperature and ionization state of the IGM can be constrained quite well without invoking models for astrophysical sources at all. This conclusion requires only that the IGM is reasonably well-described as a two-phase medium. Before we proceed, and determine the model-*dependent* constraints offered by a detection of the global 21-cm signal, we need estimates for measurement errors given a particular instrument, observing strategy, and assumed model for the global 21-cm signal. In this chapter, we will detail this procedure using a new approach to extracting the signal, in which all contributions to the sky brightness are parameterized and their parameters simultaneously fit using a Markov Chain Monte Carlo scheme.

### 3.2 Introduction

Shaver et al. (1999) were the first to investigate both the expected strength of the global 21-cm signal and the prospects for extracting it from the galactic foreground. Considering a simple “step” 21-cm signal superposed on the galactic and extragalactic foreground, Shaver et al. (1999) presented several candidate techniques for detecting the global 21-cm signal, including: (1) a simple foreground subtraction procedure, in which one fits for all known foregrounds and subtracts them from the data, leaving the global 21-cm signal as a residual, (2) an analysis of variations in the spectral index, i.e.,

$$\alpha_S(\nu) \equiv \frac{d \log T}{d \log \nu}, \quad (3.1)$$

which should reveal any abrupt spectral signatures like a step, and (3) analyzing the “trend ratio,” which is the ratio of observations at  $\nu < 200$  MHz, over which the reionization step is expected to occur, to observations at  $\nu > 200$  MHz extrapolated *below* 200 MHz. In the latter cases, the authors showed that the global 21-cm emission signal was in principle detectable given the clear deviations from a smoothly varying  $\alpha_S(\nu)$  and trend ratio of unity, respectively.

The methods proposed by Shaver et al. (1999) are not too dissimilar from those employed more recently by Bowman and Rogers (2010), who set the first lower limit on the width of the Reionization “step” ( $\Delta z > 0.06$  at 95% confidence). Several authors have attacked the signal extraction problem more recently, performing Fisher matrix forecasting for the entire signal (i.e., not just the Reionization step; Pritchard et al., 2010, Liu et al., 2013, Presley et al., 2015), studies of how imperfections in 21-cm instruments affect the signal extraction process (Harker et al., 2012, Bernardi et al., 2015), and the implementation of Markov-Chain Monte Carlo algorithms (Harker et al., 2012, 2015) that can simultaneously fit an arbitrary set of contributions to the 21-cm sky brightness.

There are numerous shortcomings of the aforementioned work, including:

- (1) Use of simplified phenomenological form for the global 21-cm signal. For example, adoption of a Gaussian for the absorption trough (Liu et al., 2013, Bernardi et al., 2015), a tanh reionization model for  $\bar{x}_i(z)$  and assumption of a saturated signal at  $\nu \gtrsim 100$  MHz (Bowman and Rogers, 2010), or a cubic spline connecting the Turning Points (Pritchard and Loeb, 2010, Harker et al., 2012).

- (2) The assumption that the (phenomenological) functional form of  $\delta T_b(z)$  is known *a-priori*.
- (3) The traditional “foreground removal” techniques are most susceptible to biases. For example, if the foreground fit is imperfect, subtracting it from the data may remove part of the global 21-cm signal as well. MCMC methods allow one to simultaneously fit for the foreground and signal, and thus mitigate biasing effects to some degree.
- (4) MCMC is more general than the Fisher matrix analyses, which assume Gaussian likelihoods and perfect recovery of the maximum likelihood point.

To address these issues, we will here build on the work of Harker et al. (2012), who developed an MCMC approach to extracting the global 21-cm signal from the galactic foreground. In particular, we will focus on the assumed parameterization of the global 21-cm signal itself, and how it affects one’s ability to fit data and draw meaningful inferences about the properties of the IGM. Details of our implementation will be presented in the next section.

### 3.3 Signal Extraction Methodology

To put signal extraction algorithms to the test, we must first generate a synthetic database containing foregrounds and the global 21-cm signal. We use the global sky model (GSM) presented in de Oliveira-Costa et al. (2008) to determine model foreground spectra, as it was derived from datasets extending down to 10 MHz. It will also contain more spectral structure than the 408 MHz Haslam et al. (1982) GSM, since the Haslam et al. (1982) map would require extrapolation to lower frequencies. For a given pointing of the telescope, we convolve the GSM and beam power pattern to obtain a model spectrum for the galactic foreground. Because our focus is on the effects of global 21-cm signal parameterizations in this work, we assume for simplicity an idealized Gaussian antenna power pattern with full-width half-max of  $50^\circ$ . This has the additional benefit of enabling use of routines within the HEALPY<sup>1</sup> package, which is based on the

---

<sup>1</sup> <https://github.com/healpy/healpy>

HEALPix (Górski et al., 2005) package<sup>2</sup>. We add noise following the radiometer equation,

$$\sigma = T_{\text{sys}} / \sqrt{2t_{\text{obs}}\Delta\nu}. \quad (3.2)$$

We assume  $T_{\text{sys}} = 100$  K, though our results are insensitive to this choice, and spectral channels of width  $\Delta\nu = 1$  MHz. We will investigate  $t_{\text{obs}} = 100$  and 1000 hours.

It is very common to model the galactic foreground spectrum as a polynomial in  $\log\nu$ - $\log T$  space, i.e.,

$$\log T_{\text{fg}} = \sum_{i=0}^{N_{\text{poly}}} a_i \log \left( \frac{\nu}{\nu_0} \right)^i \quad (3.3)$$

where  $\nu_0$  is an arbitrary pivot point, and  $a_i$  are the polynomial coefficients. In general, however, the foreground spectra derived from the de Oliveira-Costa et al. (2008) sky model are *not* log polynomials. Several authors have attempted to determine the order of polynomial required to adequately subtract the foreground and recover the global 21-cm signal. Early studies suggested  $N_{\text{poly}} \geq 3$  (Pritchard and Loeb, 2010) for  $\nu > 100$  MHz, though recently Bernardi et al. (2015) found that  $N_{\text{poly}} = 5$  is required, even under idealized circumstances (i.e., perfect instrument). In a more general case, in which the antenna has significant angular and frequency structure,  $N_{\text{poly}} = 7$  is likely required to adequately remove the foreground. If one uses more sophisticated statistical approaches, one might actually be able to determine the appropriate value of  $N_{\text{poly}}$  from the data itself (Harker, 2015b).

Because our focus is not on the determining the optimal functional form of the galactic foreground, we make another simplifying assumption: rather than using the “raw” foreground spectrum derived by convolving an idealized beam with the de Oliveira-Costa et al. (2008) GSM, we use a  $\log\nu$ - $\log T$  fit to the GSM spectrum. Then, we take as free parameters in our model the  $\log\nu$ - $\log T$  polynomial coefficients, meaning in principle our foreground model could perfectly fit foreground spectra in our synthetic dataset.

We do not, however, make the analogous assumption for the global 21-cm signal. Physically-motivated models for the global 21-cm signal are not in general well-modeled as Gaussians, cubic splines, or Reionization step functions. As a result, we take the “true” global 21-cm signal to be the default model produced by the ARES code (i.e., the black curve in Figure 1.12, reproduced in Figure 3.2 below). We will test in the

---

<sup>2</sup> <http://healpix.sourceforge.net/>

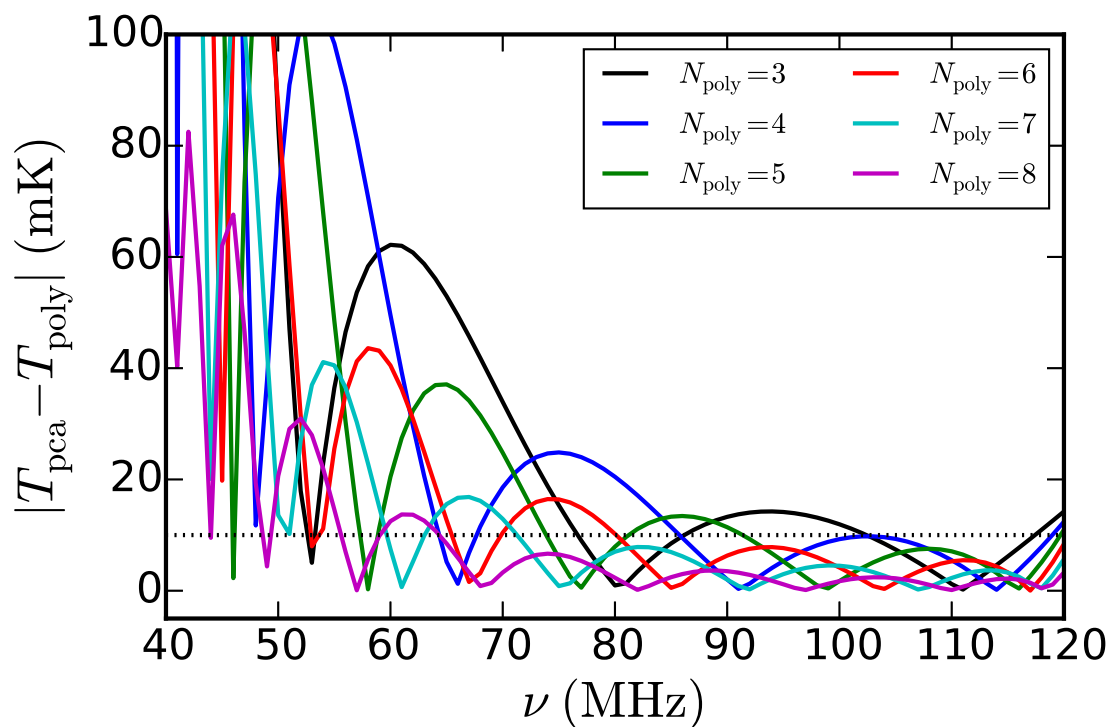


Figure 3.1 Structure in the de Oliveira-Costa et al. (2008) global sky model, shown via the residual between the spectrum in a single (representative) pixel in the de Oliveira-Costa et al. (2008) map and a  $\log \nu$ - $\log T$  polynomial fit to that spectrum. The dotted horizontal marks a residual of 10 mK.

§3.4 a few different parameterizations for the global 21-cm used in the actual fitting, to be introduced below.

The first studies to attempt broad-band extraction of the global 21-cm signal modeled the signal as a cubic spline passing through three extrema in the signal (turning points B, C, and D in Figure 1.12); Pritchard and Loeb, 2010, Harker et al., 2012). This model, being purely phenomenological, cannot be readily related to properties of the IGM. This precludes one from immediately interpreting constraints on the turning points and from incorporating priors on, e.g.  $\tau_e$ , since the cubic spline knows nothing of the ionization history.

Here, we use instead a series of tanh functions to model the Ly- $\alpha$  intensity, IGM temperature, and IGM ionization state as a function of time. That is, we model quantity  $A = J_\alpha, T_K, \bar{x}_i$  as

$$A(z) = \frac{A_{\text{ref}}}{2} \{1 + \tanh[(z_0 - z)/\Delta z]\}, \quad (3.4)$$

where  $A_{\text{ref}}$  is a normalization,  $z_0$  is the redshift at which Ly- $\alpha$  emission, heating, and ionization “turn on,” and  $\Delta z$  is the duration of each respective epoch. For physical histories, the normalization of  $\bar{x}_i$  is fixed to unity (i.e., Reionization is guaranteed to end), and the peak temperature is set to  $10^4$  K. This leaves 7 parameters to be fit in each MCMC calculation. Note that the thermal history actually contains a second term to account for the initial adiabatic cooling,  $T_K \propto (1+z)^2$ , of the IGM before heating begins.

In computing the likelihood, we assume all the frequency channels in all sky regions are independent, i.e. the probability density for obtaining the value  $T_{\text{meas}}^i(\mathbf{v}_j)$ , where  $i$  indexes the sky region, for a vector of parameters  $\theta$ , is

$$p_{ij} = \frac{1}{\sqrt{2\pi\sigma_i^2(\mathbf{v}_j|\theta)}} e^{-[T_{\text{meas}}^i(\mathbf{v}_j) - T_{\text{mod}}^i(\mathbf{v}_j|\theta)]^2 / 2\sigma_i^2(\mathbf{v}_j|\theta)}, \quad (3.5)$$

where  $\sigma_i(\mathbf{v}_j|\theta)$  is the rms noise in the channel, computed from  $T_{\text{mod}}^i(\mathbf{v}_j|\theta)$ , the bandwidth and the integration time using the radiometer equation, and the likelihood is just the product over all the channels,

$$L(T_{\text{meas}}|\theta) = \prod_{i=1}^{N_{\text{sky}}} \prod_{j=1}^{n_{\text{freq}}} p_{ij}. \quad (3.6)$$

In practice, we work with the log-likelihood, so this product is computed as a sum. We adopt broad, Gaussian priors for the foreground parameters, which have little impact since the data generally constrain them quite well. For the signal parameters we adopt broad uniform priors, which occasionally appear in constraints as

well-defined edges but for good reason: arbitrarily broad priors could lead to unphysical realizations of the signal, e.g., realizations with  $\bar{x}_i > 1$ .

### 3.4 Results

We first compare the recovered global 21-cm signal obtained assuming the turning points model to that recovered using the tanh approach. From Figure 3.2, it is clear that the tanh model provides a substantial improvement over the turning points parameterization. Most notably, there is a large systematic offset in the normalization of the recovered signal (solid blue curve) compared to the input signal (solid black curve). This is because the turning points parameterization has no knowledge of even simple physics, which in reality restrict both the minimum and maximum allowed amplitude of the signal (dashed lines in Figure 1.12). Without such prior knowledge, it is difficult to pinpoint the overall normalization of the signal, since constant offsets can be almost perfectly absorbed by the foreground (the zeroth order terms in the  $\log \nu$ - $\log T$  polynomial).

Though the global 21-cm signal recovered by the tanh model is a dramatic improvement over that yielded by the turning points model, there are still noticeable differences. For example, the shape of the recovered signal is offset from the input model at the highest frequencies (dotted cyan compared to solid black in Figure 3.2). In addition, the initial descent into absorption at  $\sim 50$  MHz is biased toward higher frequencies, and the absorption minimum is shallow relative to the input model. We will examine the significance of these biases momentarily.

Interestingly, the tanh model seems to do a better job constraining the turning points of the global 21-cm signal than a model whose free parameters are the turning points themselves! In Figure 3.3 we show a “triangle plot” of constraints on the frequencies and amplitudes of turning points B, C, and D. Though Figure 3.2 showed a bias in the depth of turning point C, panel (d) Figure 3.3 illustrates that this bias is of questionable statistical relevance, as the “true” value of  $\delta T_b(\nu_C)$  falls within  $1\sigma$  of the recovered value. Some biases, however, are more significant. For example, the recovered frequency of turning point C is discrepant at the  $\sim 2\sigma$  level.

Given the visually apparent discrepancy between the input signal and recovered signal at the highest

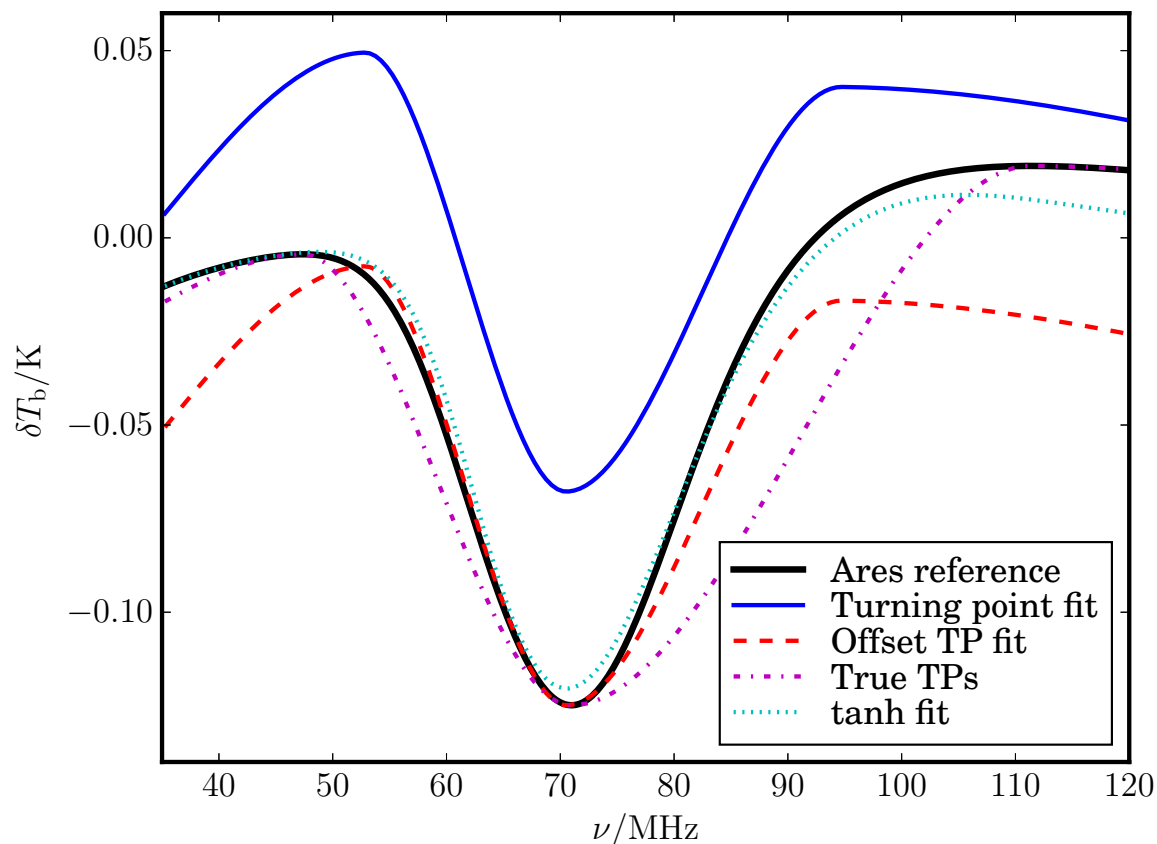


Figure 3.2 The ability of different parameterizations to fit the input global 21-cm signal, which was generated with ARES. The solid black line shows the input model, which also assumes foregrounds modelled as third-order polynomials in  $\log \nu$ - $\log T$ , an idealized instrument model in which the antenna has flat 85% sensitivity between 35 and 120 MHz, and an experiment which observes four independent sky regions for 250 hours each. The recovered signal using the turning points parametrization is shown in the solid blue line; if we shift this down so that the temperature of turning point C agrees with the input signal, we have the dashed red line. If we use the actual positions of the maxima and minima of the ARES signal as the parameter values in our turning points model, we produce the magenta dot-dashed curve. Finally, if the synthetic dataset is fit using the tanh model, the signal we recover is shown as the cyan, dotted curve.

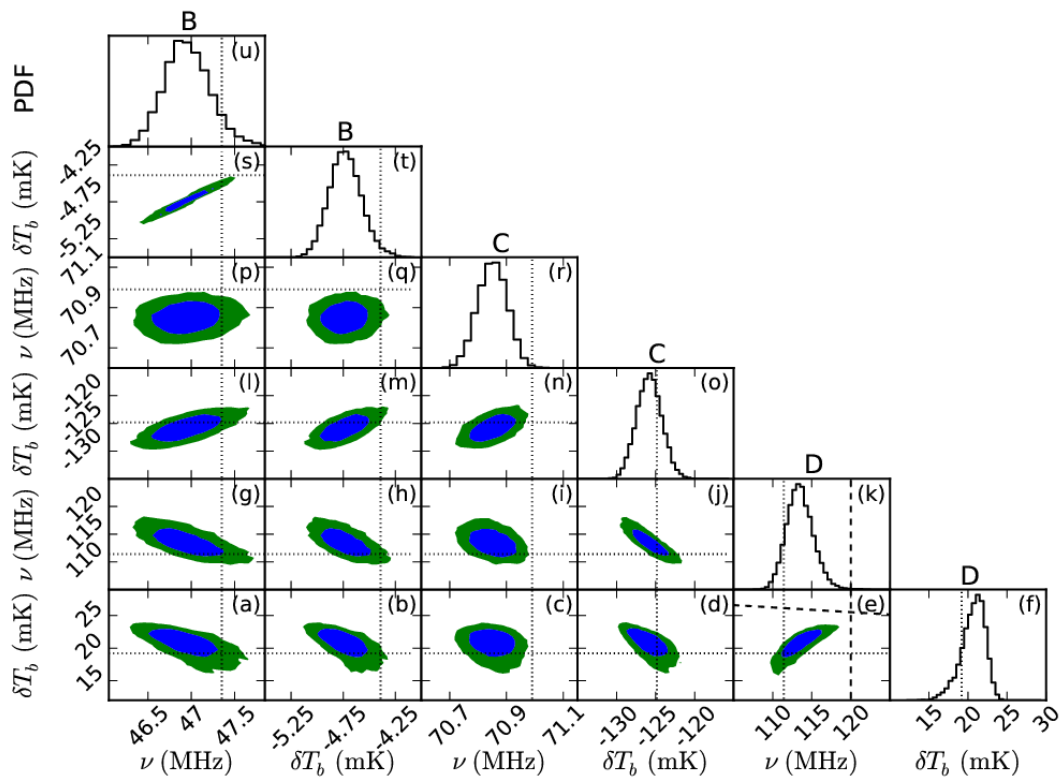


Figure 3.3 We show how the constraints on the  $\delta T_b$  history from the tanh fit translate into constraints on the turning points. In each panel, the dotted lines show the input parameter value. The dashed vertical line in panel (e) shows the upper end of the frequency range, while the nearly horizontal line shows the path the signal would follow in a hot, completely neutral Universe for which the emission signal saturates. The dark blue and green contours show 1- and 2- $\sigma$  confidence regions.

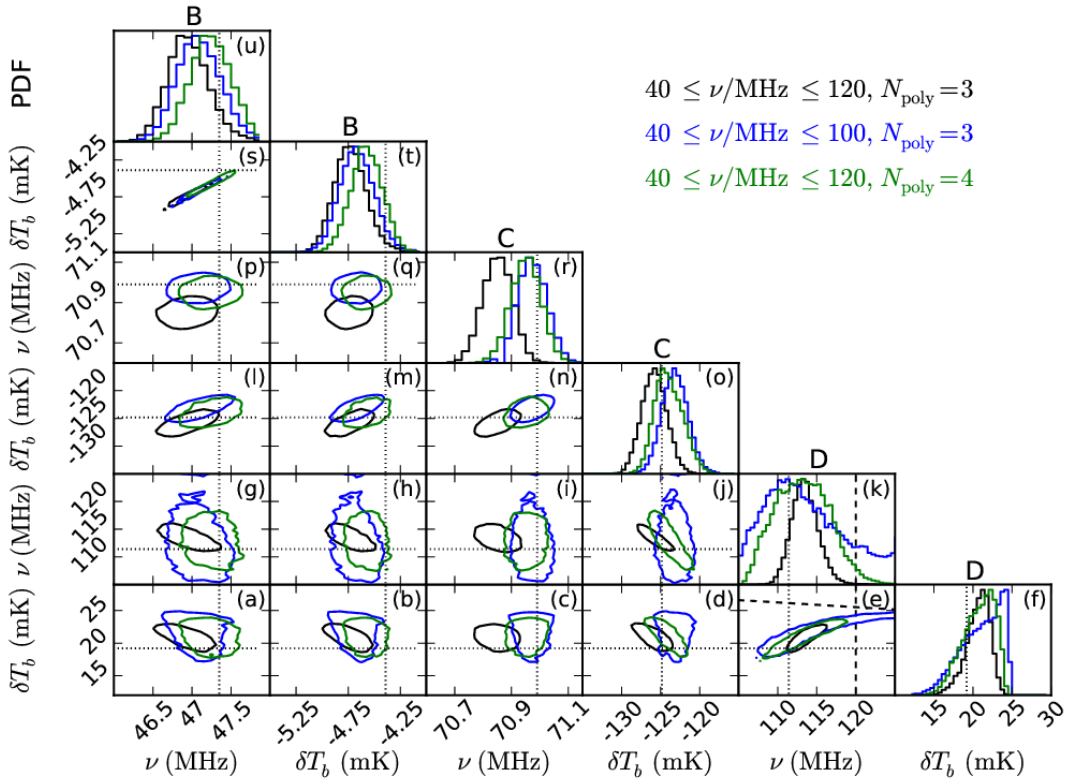


Figure 3.4 A comparison of the 68% confidence regions for constraints on the positions of the turning points for three different datasets: the same as that used in Fig. 3.3 (black); a dataset where the upper limit of the frequency range is set to 100 MHz instead of 120 MHz (blue); and a dataset where the foregrounds are fourth-order polynomials in  $\log \nu - \log T$  rather than third-order (green).

frequencies in Figure 3.2, we suspected that a shortcoming of our model at  $\nu \gtrsim 100$  MHz could be responsible for biases at lower frequencies. To test this hypothesis, we re-ran fits with (1) a bandpass truncated at 100 MHz, and (2) a foreground with  $N_{\text{poly}} = 4$ . The results are shown in Figure 3.4. Indeed, both techniques reduced the bias in the position of turning point C (see panel (n)). However, of course any constraints for turning point D are meaningless if one only includes  $\nu \leq 100$  MHz data in the fit. A more appealing option is the use of a 4<sup>th</sup> order polynomial for the foreground (green contours). In this case, the bias in turning point C is mitigated and the constraints on turning point D are still meaningful, though broader than those of the 3<sup>rd</sup> order foreground fit because we have made the model more complex.

Up until this point we have focused only on the accuracy with which the turning points can be extracted from the galactic foreground. In Figures 3.5 and 3.6, we move on to an issue that could not be addressed by the turning points model: how well are properties of the IGM constrained by measurements of the global 21-cm signal? In Figure 3.5 we focus only on IGM properties to which turning point C is most sensitive. To begin, address only the black contours, which correspond to our reference calculation with  $N_{\text{poly}} = 3$ . In this case, all constraints on IGM properties are biased relative to their input values, which we should expect given that our constraint on the position of turning point C in this case was also biased. Given that a more complex  $N_{\text{poly}} = 4$  foreground model unbiased the constraints on the position of turning point C, we might have expected to unbiased the IGM constraints in a similar fashion. However, the  $N_{\text{poly}} = 4$  (blue contours) constraints on the IGM properties remain biased.

The persistent biases in properties of the IGM in spite of accurate recovery of the turning points is an unexpected, but theoretically allowed, result. Because turning point C encodes both the IGM temperature and heating rate density, the solution for its position is not unique: one could imagine two subtly different thermal histories that both manage to arrive at the same combination of  $T_K, \epsilon_{\text{heat}}$  at the same redshift (in our case, that of turning point C), but whose evolution is distinct beforehand and afterward. This scenario is possible because the input global 21-cm signal being fit uses a different parameterization of the thermal history (one tied to the history of star formation, to be discussed in the next chapter) than the tanh model (which is phenomenological). Our first test of this hypothesis was to perform a “second stage fit,” in which we fit a tanh model directly to the recovered turning points, thus eliminating all possibility that shape information is

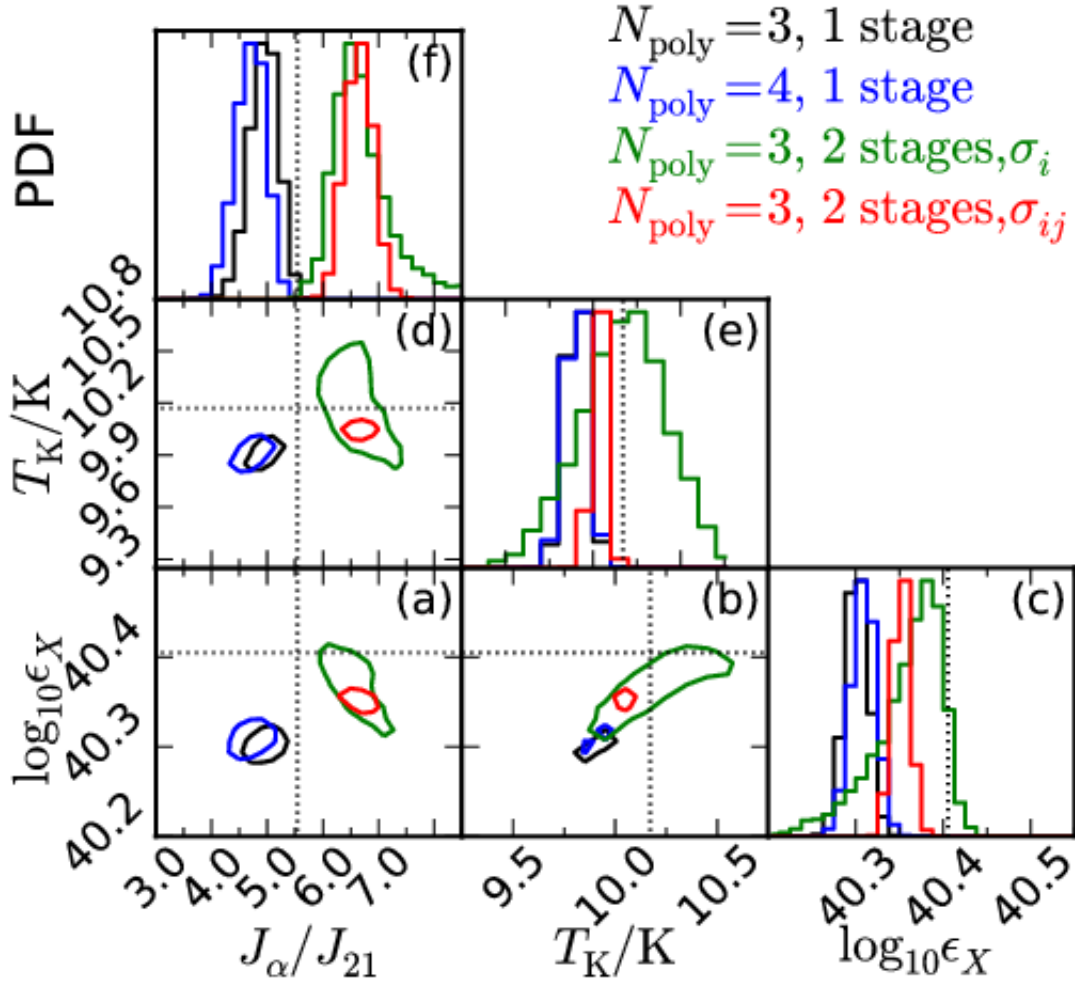


Figure 3.5 The constraints on the IGM parameters for which the constraining power comes mainly from turning point C. These parameters are the kinetic temperature of the gas (colder than the CMB at this point), the heating rate density, and the Ly- $\alpha$  flux. The dataset assumes 1000 hrs of data split between four sky regions, though the results are qualitatively similar for fewer sky regions and for shorter integrations. The black lines show constraints (1D posterior distributions and 1- $\sigma$  contours) coming directly from the tanh fit to the dataset, while the blue lines show the results obtained with a more complex foreground model. The green lines assume that only the positions of the turning points and the covariances between the turning points are known, whereas the red lines assume that only the turning point positions are known (nothing about the shape of the signal in between) and that the errors on the turning points are independent and Gaussian, with the positions and the size of the errors coming from the tanh fit. Dotted vertical and horizontal lines show the true values.

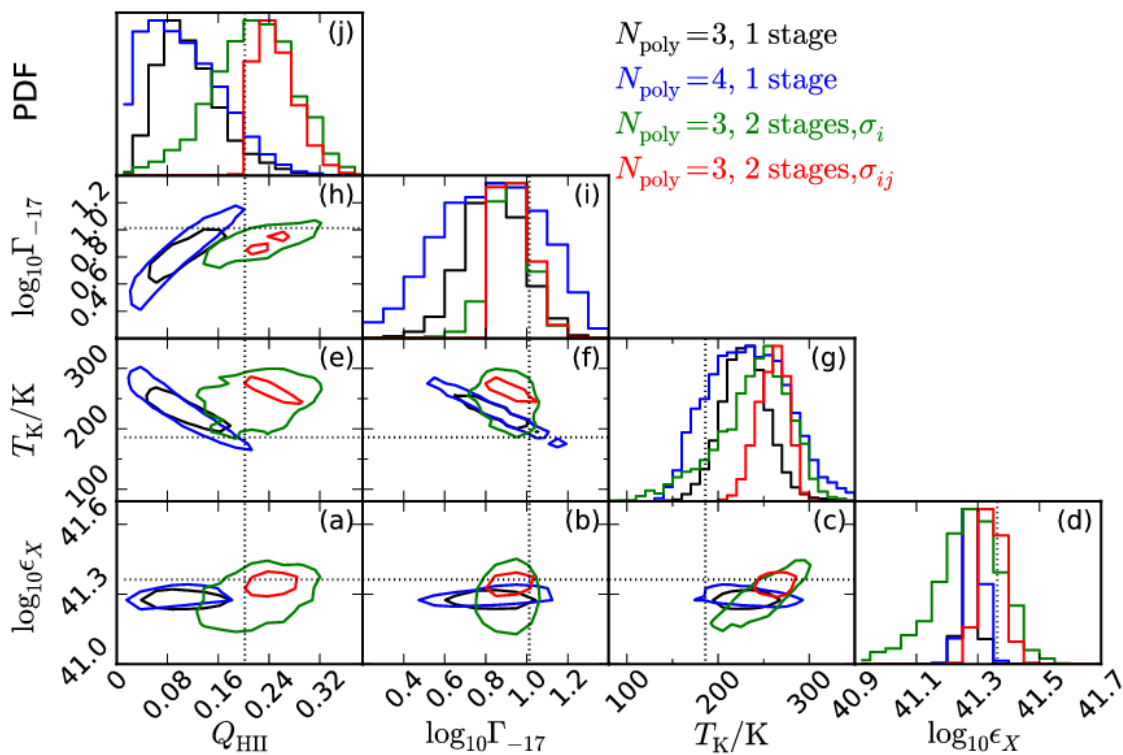


Figure 3.6 The constraints on the IGM parameters for which the constraining power comes mainly from turning point D. These parameters are the kinetic temperature of the gas (hotter than the CMB at this point), the heating rate density, the volume filling factor of H II regions,  $Q_{\text{HII}}$ , and the volume-averaged ionization rate,  $\Gamma_{\text{HI}}$ . The colors have the same meaning as those shown in Figure 3.5.

used to guide the fit.

This exercise is repeated in Figure 3.6 for turning point D, which now provides constraints on the ionization history as well as the thermal history. The same general behavior is seen here: constraints on the IGM are insensitive to the choice of  $N_{\text{poly}}$ . Interestingly, while the second stage fit reduces biases on  $Q_{\text{HII}}$ ,  $\Gamma_{\text{HI}}$ , and  $\epsilon_{\text{heat}}$ , the constraints on  $T_{\text{K}}$  are actually more biased than in the single-stage fit.

A final test of the shape-mismatch hypothesis is shown in Figure 3.7. Here, we extracted the recovered curvature of all turning points and compared them to the curvature of the input model at the turning points. The tanh model does indeed seem to prefer a signal with a slightly different shape than that of the ARES model: with turning points positions consistent with those of the ARES model, the tanh model seems to systematically produce turning points B and C that are less sharp (i.e., smaller curvature in absolute value) than those of our input ARES model. The curvature of turning point D is consistent with the input model. This seems to indicate that the tanh model is a better model for the ionization history than it is for the Ly- $\alpha$  or thermal histories.

The entire suite of calculations is shown in Figure 3.8. Clearly, the biases in the turning points persist in all cases (for  $N_{\text{poly}} = 3$ ), and increases in integration time have a stronger effect than viewing more sky areas. We have performed  $N_{\text{poly}} = 4$  fits for all combinations of  $\{N_{\text{sky}}, t_{\text{int}}\}$  and find comparable biases in the IGM quantities in all cases.

### 3.5 Discussion & Conclusions

In the previous section, we found that the tanh model outperforms the turning points model in extracting the positions of the turning points, despite the fact that the turning points are not parameters of the tanh model. We attribute this to two primary factors: (1) the tanh model is more flexible than the turning points model in the variety of shapes it can produce and as a result is more easily able to match the shape of a physically-motivated model, and (2) the tanh model has implicit knowledge of the maximum and minimum allowed amplitude of the signal, which allow it to more easily pinpoint the overall normalization of the global 21-cm signal. This second point may explain why the precision with which the turning points are extracted (Figure 3.8) depends mostly on the integration time and only weakly on the number of indepen-

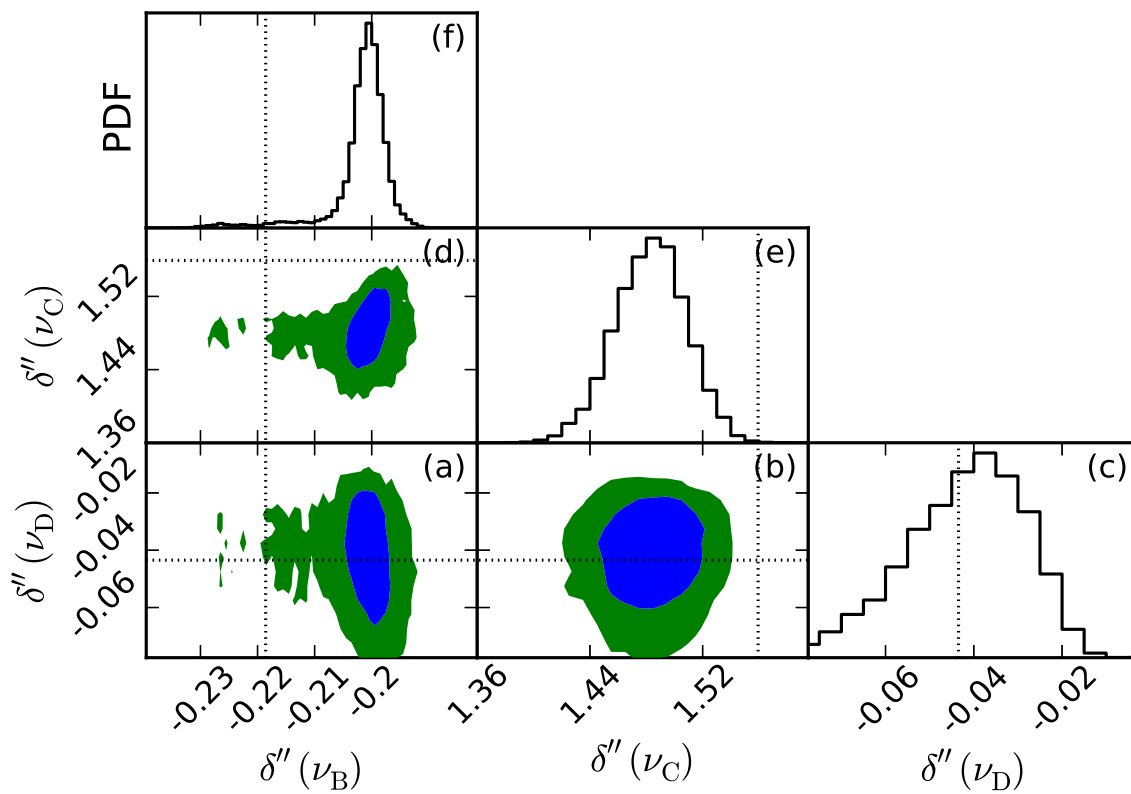


Figure 3.7 Constraints on the curvature, indicated by  $\delta''$  (in units of  $\text{mK MHz}^{-1}$ ), of the signal at the turning points. Blue and green regions are 68% and 95% confidence regions, respectively.

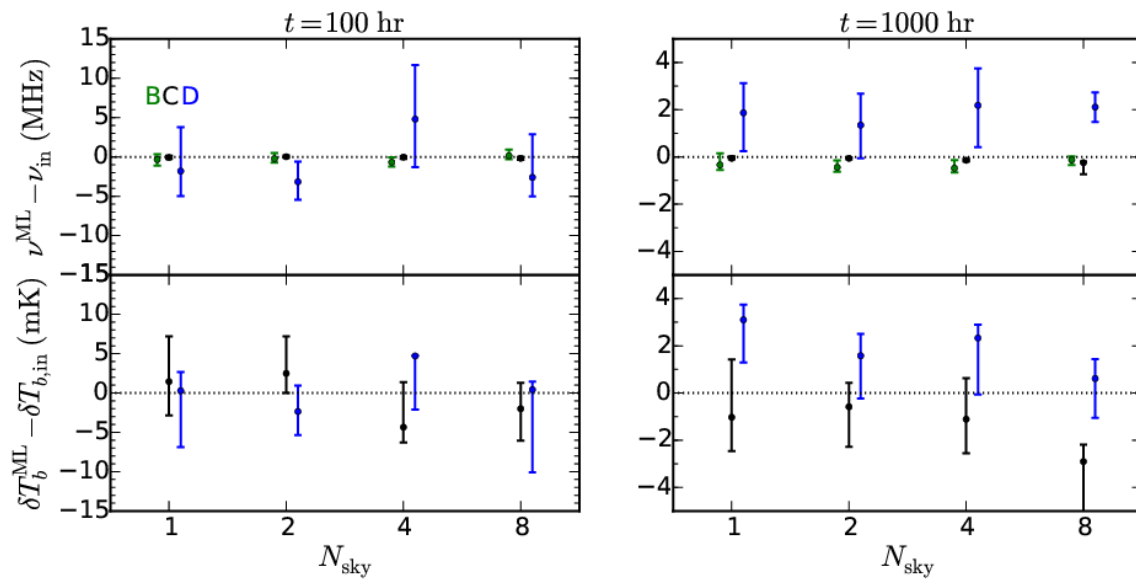


Figure 3.8 Constraints on the turning point positions as a function of the number of sky regions and integration time. Green, black, and blue points correspond to constraints on turning points B, C, and D, respectively, and are slightly offset in the x-direction for clarity. The top row shows errors in the frequency of the turning points, relative to their input values, while the bottom row shows errors in the amplitude of each turning point. All error-bars shown are 68 per cent credible intervals. Note that the y range for the panels on the right has been zoomed in.

dent sky regions observed. This has implications for the optimal 21-cm observing strategy, as it has been assumed for years that observations of many independent sky areas were needed primarily to help constrain the normalization of the global 21-cm signal.

Though at first glance the tanh model seems to provide a dramatic improvement in the ability to extract the global 21-cm signal from the galactic foreground, there are subtle issues that require further attention. For example, degeneracies between the global 21-cm signal and the foreground at frequencies  $\nu \gtrsim 100$  MHz bias constraints on features of the signal at low frequencies. One crude solution is to simply discard data at  $\nu > 100$  MHz, though of course in doing so, one removes all hope of constraining the position of turning point D, and the ionization and thermal state of the IGM it encodes. Alternatively, one might employ a more complex model for the galactic foreground spectrum, and thus increase its ability to cope with the spectrally smooth turn-over in the global 21-cm signal, which occurs at  $\sim 112$  MHz in our reference model.

Perhaps more interestingly, the physical ARES model seems to produce turning points that are slightly sharper than those of the tanh model. This led to biases in the tanh model’s inference of IGM properties at turning points C and D, despite the fact that the turning point positions of the best-fit recovered signal were consistent with the input model. Given the persistence of this finding independent of  $N_{\text{sky}}$  and  $t_{\text{int}}$ , it seems most likely that in fact we are seeing a mismatch in the shape between the tanh and ARES models.

These findings highlight the need for the development of a model selection pipeline, i.e., one that can derive quantitative evidence for one parameterization over another from the data itself. The obvious first test for any global 21-cm experiment is a null test, i.e., fit the data with signal-less model and then again with including a model for the global 21-cm signal. Is there quantitative evidence that the model including the global 21-cm signal is required by the data? The present work suggests a more advanced test that likely requires very accurate measurements: can we derive evidence that the data requires an ARES model instead of the tanh? Given that we have assumed an idealized instrument (with a flat response), it is possible that first-generation instruments will yield constraints on the turning points that are broader than those presented here, and thus may not need to grapple with this issue. It will of course be vital once global 21-cm measurements enter a “precision era,” an advance recently seen in the CMB community which led to the development of improved physical models (e.g., COSMOREC; Chluba and Thomas, 2011) and statistical

inference tools (e.g., POLYCHORD; Handley et al., 2015).

Both the null test and the tanh vs. ARES test are computationally prohibitive in the high-dimensional parameter spaces surveyed in most MCMC fits presented here. A direct fit of the ARES model is difficult, but not prohibitively so ( $\sim$  few seconds per likelihood evaluation). To date, the only study of model selection for the global 21-cm signal was performed for a single pointing, with an idealized instrument, foreground, and signal model (Harker, 2015b). Adoption of recent methods employed in the CMB community (e.g., POLYCHORD; Handley et al., 2015) will be required to scale to higher dimensional parameter spaces and more realistic signal models, but we will revisit such ideas in more detail in Chapter 7.

## Chapter 4

### Parameter Estimation for Global 21-cm Experiments: Prospects for Constraining Simple Galaxy Formation Models

Reproduced with permission of the AAS.

Reference:

“Interpreting the Sky-Averaged 21-cm Signal from High Redshifts. II. Parameter Estimation for Models of Galaxy Formation”

Mirocha, J., Harker, G. J. A., & Burns, J. O. 2015, accepted for publication in *ApJ* (arXiv:1509.07868)

#### 4.1 Context

Following our previous work, which focused on relating generic features in the sky-averaged (global) 21-cm signal to properties of the intergalactic medium, we now investigate the prospects for constraining a simple galaxy formation model with current and near-future experiments. This approach has yet to be employed in global 21-cm parameter estimation forecasts, which have instead attempted to constrain *phenomenological* models that can capture the basic structure of the signal at little computational cost, but cannot be readily related to *physical* models of galaxy formation. Markov-Chain Monte Carlo fits to our synthetic dataset, which includes a realistic galactic foreground and a plausible model for the signal, suggest that a simple four-parameter model that links the meta-galactic Lyman- $\alpha$ , Lyman-continuum, and X-ray backgrounds to the growth rate of dark matter halos, can be well-constrained (to  $\sim 0.1$  dex in each dimension) in only 100 hours so long as all three spectral features expected to occur between  $40 \lesssim \nu/\text{MHz} \lesssim 120$  are detected. Several important conclusions follow naturally from this basic numerical result, namely that

measurements of the global 21-cm signal can in principle (i) identify the characteristic mass threshold for star formation formation at all redshifts  $z \gtrsim 15$ , (ii) extend  $z \lesssim 4$  upper limits on the normalization of the X-ray luminosity star-formation rate ( $L_X$ -SFR) relation of  $f_X \sim$  a few out to  $z \sim 20$ , and (iii) provide the first constraints on stellar spectra and the escape fraction of ionizing radiation at  $z \gtrsim 10$ , degeneracies between which can be mitigated in 100 hours of integration split between two independent sky regions, and/or use of a more complex model for the galactic foreground. Though our approach is general, the power of a broad-band measurement renders our findings most relevant to the proposed *Dark Ages Radio Explorer*, which will have a clean view of the global 21-cm signal from  $\sim 40 - 120$  MHz from its vantage point above the radio-quiet, ionosphere-free lunar far-side.

## 4.2 Introduction

Given that the global 21-cm signal is an indirect probe of high- $z$  galaxies, some modeling is required to convert observational quantities to constraints on the properties of the Universe’s first galaxies. Though numerous studies have performed forward modeling to predict the strength of the global 21-cm signal (Furlanetto, 2006, Pritchard and Loeb, 2010), few have attempted to infer physical parameters of interest from synthetic datasets. Such forecasting exercises are incredibly useful tools for designing instruments and planning observing strategies, as they illuminate the mapping between constraints on observable quantities and model parameters of interest. Both Fisher matrix and Markov-Chain Monte Carlo (MCMC) approaches have been employed by the power spectrum community (e.g., Pober et al., 2014, Greig and Mesinger, 2015), the latter providing a powerful generalization that does not require the assumption of Gaussian errors or perfect recovery of the maximum likelihood point.

Most work to date has instead focused on forecasting constraints on *phenomenological* parameters of interest, e.g., the timing and duration of reionization (Liu et al., 2013), the depth and width of the deep minimum expected near  $\sim 70$  MHz prior to reionization (Bernardi et al., 2015), or all three spectral features predicted to occur between  $40 \lesssim \nu / \text{MHz} \lesssim 120$  (Pritchard and Loeb, 2010, Harker et al., 2012). These spectral “turning points” in the global 21-cm spectrum provide a natural basis for parameter forecasting, as they persist over large ranges of parameter space (Pritchard and Loeb, 2010), can be extracted from the

foreground with realistic instruments and integration times (at least under the assumption of a negligible ionosphere; Harker et al., 2012, Presley et al., 2015, Bernardi et al., 2015), and are relatively impervious to degeneracies between the cosmological signal and the galactic foreground (Harker et al., 2015). They can also be interpreted fairly robustly in terms of the physical properties of the IGM, at least in simple two-phase models (Mirocha et al., 2013, hereafter Paper I). Given the viability of the turning points as “products” of global 21-cm signal extraction pipelines, we will use them as a launching point in this paper from which to explore the prospects for constraining *astrophysical* parameters of interest with observations of the global 21-cm signal. Importantly, we will consider all three turning points simultaneously, rendering our findings particularly applicable to *DARE*, whose band extends from  $40 \leq \nu/\text{MHz} \leq 120$  in order to maximize the likelihood of detecting all three features at once.

This chapter is organized as follows. In Section 2 we outline our methods for modeling the global 21-cm signal and parameter estimation. Section 3 contains our main results, with a discussion to follow in Section 4. In Section 5, we summarize our results. We use the most up-to-date cosmological parameters from *Planck* throughout (last column in Table 4 of Planck Collaboration et al., 2015).

### 4.3 Numerical Methods

In order to forecast constraints on the properties of the first galaxies, we will need (1) a model for the global 21-cm signal, (2) estimates for the precision with which this signal can be extracted from the foregrounds, and (3) an algorithm capable of efficiently exploring a multi-dimensional parameter space to find the best-fit and uncertainties on the model parameters. The next three sub-sections are devoted to describing these three pieces of our pipeline in turn.

#### 4.3.1 Physical Model for the Global 21-cm Signal

Our approach to modeling the global 21-cm signal is similar to that presented in several other published works (e.g., Barkana and Loeb, 2005b, Furlanetto, 2006, Pritchard and Loeb, 2010, Mirocha, 2014), so we will only discuss it here briefly. The primary assumption of our model is that the radiation backgrounds probed by the turning points are generated by stars and their byproducts, which form at a rate

proportional to the rate of baryonic collapse into dark matter haloes. That is, we model the star-formation rate density (SFRD) as

$$\dot{\rho}_*(z) = f_* \bar{\rho}_b^0 \frac{df_{\text{coll}}}{dt}, \quad (4.1)$$

where  $f_{\text{coll}} = f_{\text{coll}}(T_{\text{min}})$  is the fraction of matter in collapsed halos with virial temperatures greater than  $T_{\text{min}}$ ,  $\bar{\rho}_b^0$  is the mean baryon density today, and  $f_*$  is the star formation efficiency. We use a fixed  $T_{\text{min}}$  rather than a fixed  $M_{\text{min}}$  because it provides physical insight into the processes governing star-formation, as one can easily identify the atomic and molecular cooling thresholds of  $\sim 500$  and  $\sim 10^4$  K. Note that a fixed value of  $T_{\text{min}}$  results in a time-dependent mass threshold,  $M_{\text{min}}$ .

In order to generate a model realization of the global 21-cm signal, we must convert star-formation to photon production. Given that the three spectral turning points probe the history of ionization, heating, and Ly- $\alpha$  emission, we will split the production of radiation into three separate bands: (1) from the Ly- $\alpha$  resonance to the Lyman-limit,  $h\nu_\alpha \leq h\nu/\text{eV} \leq h\nu_{\text{LL}}$ , which we refer to as the Lyman-Werner (LW) band despite its inclusion of photons below 11.2 eV, (2) hydrogen-ionizing photons, with energies  $h\nu_{\text{LL}} \leq h\nu/\text{eV} \leq 24.4$ , and (3) X-rays, with energies exceeding 0.1 keV. Each radiation background is linked to the SFRD, i.e.,

$$\dot{Q}_{\text{ion}} \propto \xi_{\text{ion}} \frac{df_{\text{coll}}}{dt} \quad (4.2)$$

$$\dot{Q}_{\text{LW}} \propto \xi_{\text{LW}} \frac{df_{\text{coll}}}{dt} \quad (4.3)$$

where the  $\xi$ 's have units of photons / baryon. The rate of X-ray production is more sensibly cast in terms of an energy per unit star-formation, i.e.,

$$L_X \propto c_X \xi_X \frac{df_{\text{coll}}}{dt} \quad (4.4)$$

where  $c_X$  is the normalization of the  $L_X$ -SFR relation, which we take to be  $c_X = 3.4 \times 10^{40} \text{ erg s}^{-1} (M_\odot \text{ yr})^{-1}$

following Furlanetto (2006)<sup>1</sup>. Note that we have absorbed  $f_*$  into the  $\xi$  parameters, i.e.

$$\xi_{\text{LW}} = N_{\text{LW}} f_* \quad (4.5)$$

$$\xi_{\text{ion}} = N_{\text{ion}} f_* f_{\text{esc}} \quad (4.6)$$

$$\xi_X = f_* f_X \quad (4.7)$$

$N_{\text{LW}}$  and  $N_{\text{ion}}$  are the number of LW and ionizing photons emitted per stellar baryon, and  $f_{\text{esc}}$  is the escape fraction of ionizing radiation.

Given  $L_X$ ,  $\dot{Q}_{\text{ion}}$ , and the Ly- $\alpha$  background intensity,  $\hat{J}_\alpha \propto Q_{\text{LW}}$ , we can evolve the ionization and thermal state of intergalactic gas in time, and compute the sky-averaged 21-cm signal via (e.g., Furlanetto, 2006)

$$\delta T_b \simeq 27(1 - \bar{x}_i) \left( \frac{\Omega_{\text{b},0} h^2}{0.023} \right) \left( \frac{0.15}{\Omega_{\text{m},0} h^2} \frac{1+z}{10} \right)^{1/2} \left( 1 - \frac{T_\gamma}{T_S} \right), \quad (4.8)$$

where  $\bar{x}_i$  is the volume-averaged ionization fraction,

$$\bar{x}_i = Q_{\text{HII}} + (1 - Q_{\text{HII}}) x_e \quad (4.9)$$

where  $Q_{\text{HII}}$  is the volume-filling factor of HII regions, and  $x_e$  is the ionized fraction in the bulk IGM.  $T_S$  is the excitation or “spin” temperature of neutral hydrogen, which quantifies the number of hydrogen atoms in the hyperfine triplet and singlet states,  $T_\alpha \simeq T_K$  (Field, 1958),

$$T_S^{-1} \approx \frac{T_\gamma^{-1} + x_c T_K^{-1} + x_\alpha T_\alpha^{-1}}{1 + x_c + x_\alpha} \quad (4.10)$$

where  $T_K$  is the gas kinetic temperature and  $h$  and the  $\Omega$ 's are take on their usual cosmological meaning. We compute the collisional coupling coefficient,  $x_c$ , by interpolating between the tabulated values in Zygelman (2005) with a cubic spline, and take  $x_\alpha = 1.81 \times 10^{11} \hat{J}_\alpha / (1+z)$ . We perform these calculations using the Accelerated Reionization Era Simulations (ARES) code<sup>2</sup>, which is the union of a 1-D radiative transfer code developed in Mirocha et al. (2012) and uniform radiation background code described in Mirocha (2014). See §2 of Mirocha (2014) for a more detailed description of the global 21-cm signal modeling procedure.

<sup>1</sup> Furlanetto (2006) computed this value by extrapolating the 2-10 keV  $L_X$ -SFR relation of Grimm et al. (2003) above 0.2 keV, assuming an unabsorbed  $\alpha = 1.5$  power-law spectrum. Our reference value of  $f_X = 0.2$  is chosen to match recent analyses in the 0.5-8 keV band, which find  $c_X = 2.6 \times 10^{39} \text{ erg s}^{-1} (M_\odot \text{ yr})^{-1}$  (Mineo et al., 2012b).

<sup>2</sup> <https://bitbucket.org/mirochaj/ares;revision7ba0d80>

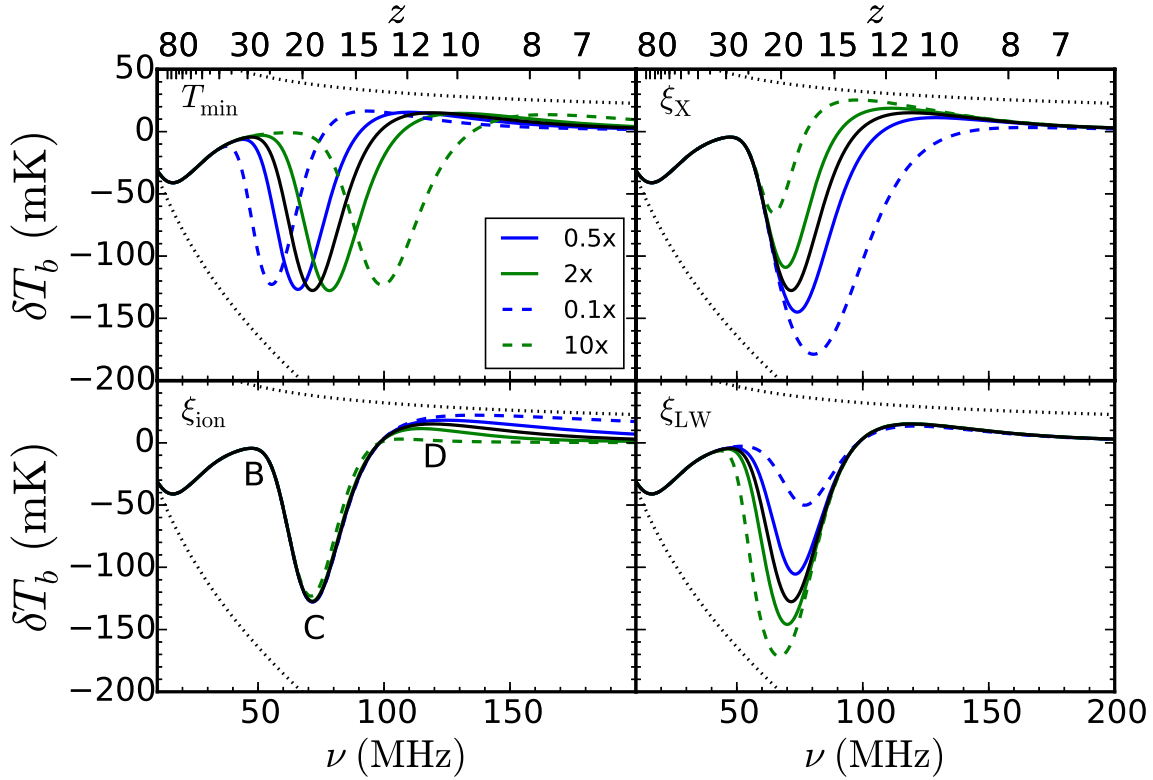


Figure 4.1 Illustration of the basic dependencies of the global 21-cm signal. The black line is the same in each panel, representing our reference model (see Table 4.1), while all solid green (blue) lines correspond to a factor of 2 increase (decrease) in the parameter noted in the upper left corner, and dashed lines are factor of 10 changes above and below the reference value. The right half of the figure is qualitatively similar to Figure 2 of Pritchard and Loeb (2010), though our reference values for the  $\xi$  parameters are different, as are our cosmological parameters, leading to quantitative differences. The dotted lines show the maximum allowed amplitude of the signal (i.e., the amplitude of the signal when  $\bar{x}_i = 0$  and  $T_S \gg T_\gamma$ ), and the minimum allowed amplitude of the signal (set by assuming  $T_S = T_K = T_{\text{ad}}(z)$ , where  $T_{\text{ad}}$  is the gas temperature in an adiabatically-cooling Universe). Because we refer to the spectral features as turning points B, C, and D throughout the paper, we annotate them in the lower left panel for reference.

Table 4.1. Reference Model Properties and Simulated Constraints

| Quantity                 | Reference Value | EM1              | EM2              | Description                             |
|--------------------------|-----------------|------------------|------------------|---|
| $\nu_B$ [MHz]            | 47.4            | $46.99 \pm 0.74$ | $47.08 \pm 0.60$ | Onset of Ly- $\alpha$ coupling          |
| $\nu_C$ [MHz]            | 71.0            | $70.95 \pm 0.20$ | $70.96 \pm 0.15$ | Onset of heating                        |
| $\nu_D$ [MHz]            | 111.4           | $110.9 \pm 5.0$  | $109.2 \pm 3.5$  | Beginning of reionization               |
| $\delta T_b(\nu_B)$ [mK] | -4.4            | n/a              | n/a              | Depth when Ly- $\alpha$ coupling begins |
| $\delta T_b(\nu_C)$ [mK] | -124.8          | $-122.6 \pm 5.0$ | $-121.7 \pm 3.7$ | Depth of absorption trough              |
| $\delta T_b(\nu_D)$ [mK] | 19.2            | $17.20 \pm 4.5$  | $19.88 \pm 1.7$  | Height of emission feature              |
| $z_{\text{rei}}$         | 9.25            | n/a              | n/a              | Midpoint of reionization                |
| $\tau_e$                 | 0.066           | n/a              | n/a              | CMB optical depth                       |

Note. — Observational properties of our reference model (solid black lines in Figure 4.1), and the best-fit and uncertainties for each extraction model (EM) we consider. Subscripts indicate different turning points, i.e., the cosmic dawn feature when the Wouthuysen-Field effect first drives  $T_S$  to  $T_K$  (B), the absorption trough, which indicates the onset of heating (C), and the beginning of reionization (D). EM1 and EM2 differ in the number of independent sky regions assumed (1 vs. 2), and in the complexity of the foreground model (3rd vs. 4th order polynomial), which leads primarily to a more robust detection of turning point D for EM2. All errors are  $1 - \sigma$ , and correspond directly to the diagonal elements of the turning point covariance matrix.

Figure 4.1 shows our reference model (properties of which are listed in Table 4.1), and the modulations in its structure that occur when varying  $T_{\min}$ ,  $\xi_X$ ,  $\xi_{\text{ion}}$ , and  $\xi_{\text{LW}}$ . It is immediately clear that  $T_{\min}$  affects the locations of all three turning points, whereas each  $\xi$  parameter affects at most two. We should therefore expect that in principle, an observation containing all three features will have the best chance to constrain  $T_{\min}$ , though this will be complicated at the lowest redshifts where  $df_{\text{coll}}/dt$  becomes a weaker function of  $T_{\min}$  (see bottom panel of Figure 4.2).

Figure 4.1 also shows that  $\xi_{\text{ion}}$  will be difficult to constrain using global signal data at these frequencies, as even factor of 10 changes lead only to small changes in the signal (at  $\nu \gtrsim 100$  MHz), whereas factor of 10 changes in  $\xi_X$  and  $\xi_{\text{LW}}$  are  $\sim 50$  mK effects. There are also clear degeneracies between  $T_{\min}$  and the  $\xi$  parameters. Exploring those degeneracies and determining the prospects for constraining each parameter independently are our primary goals in this work. The results will in large part depend on how accurately the signal can be recovered from the foregrounds, which we discuss in the next subsection.

Before moving on to signal extraction, it is worth reiterating that we do not model the normalization of the SFRD explicitly, instead absorbing the star-formation efficiency into the  $\xi$  parameters. However, we do treat the rate-of-change in the SFRD explicitly. It is illustrative to quantify this using an effective power-law index

$$\alpha_{\text{eff}}(z) \equiv \frac{d \log \dot{\rho}_*(z)}{d \log(1+z)}, \quad (4.11)$$

which enables a straightforward comparison with empirical models, which are often power-laws, i.e.,  $\dot{\rho}_*(z) \propto (1+z)^\alpha$ , in which case  $\alpha = \alpha_{\text{eff}} = \text{constant}$ . The  $\alpha_{\text{eff}}(z)$  values of our  $f_{\text{coll}}$  model are independent of  $f_*$  so long as  $df_*/dt = 0$ , and generally fall within the (broad) range of values permitted by observations of high- $z$  galaxies (Oesch et al., 2013, Robertson et al., 2015), as shown in the top panel of Figure 4.2.

### 4.3.2 Signal Extraction

In order to fit a physical model to the turning points of the global 21-cm signal, we require best-fit values for the turning point positions and estimates for uncertainties. To do this, we build on the work of Harker et al. (2012) and Harker et al. (2015), who introduced a Markov-Chain Monte Carlo (MCMC) technique for fitting global 21-cm signal data. The basic approach is to simultaneously fit a model for the

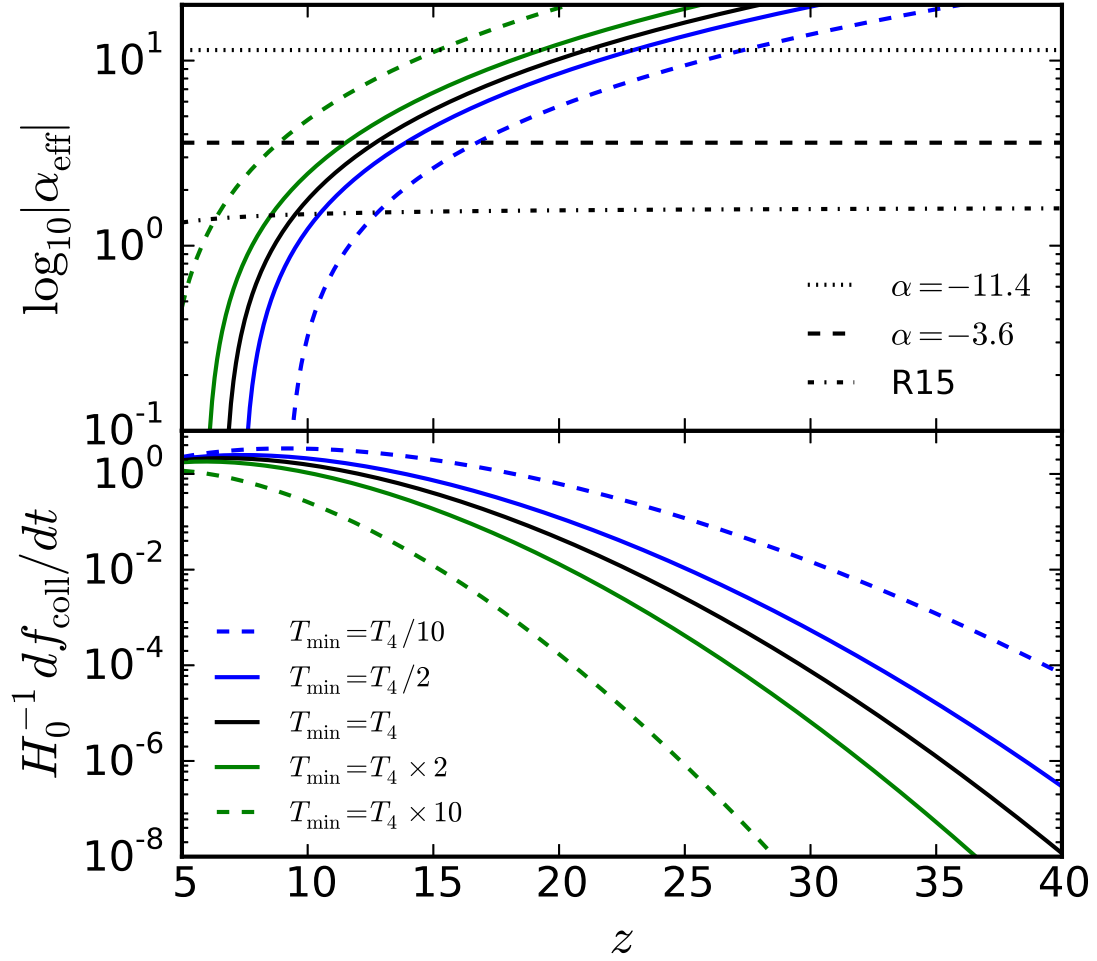


Figure 4.2 *Bottom*: Rate of collapse onto halos above a given virial temperature threshold,  $T_{\text{min}}$ , scaled to the Hubble time. *Top*: Effective power-law index (Eq. 4.11) as a function of redshift for each  $df_{\text{coll}}/dt$  model. Empirical power-laws from Oesch et al. (2012) are overlaid for comparison, as well as the best-fit 4-parameter SFRD model used in Robertson et al. (2015).

galactic foreground, the global 21-cm signal, and in general, parameters of the instrument (e.g., its response as a function of frequency), assuming some amount of integration time,  $t_{\text{int}}$ , and the number of independent sky regions observed,  $N_{\text{sky}}$ . The foreground is modeled as a polynomial in  $\log \nu - \log T$  space, while the astrophysical signal is modeled as either a spline (Harker et al., 2012) or series of tanh functions that represent  $J_{\alpha}(z)$ ,  $T_K(z)$ , and  $\bar{x}_i(z)$  (Harker et al., 2015).

The tanh approach to modeling the global 21-cm signal was chosen for numerous reasons. First and foremost, it was chosen as a computationally efficient substitute for more expensive, but physically-motivated models like those investigated in this paper. Some alternative intermediaries include the ‘turning points’ parameterization (Pritchard and Loeb, 2010, Harker et al., 2012) or models that treat the absorption feature as a Gaussian (Bernardi et al., 2015). Both are comparably cheap computationally, but cannot capture the detailed shape of physical models. Perhaps most importantly, the spline and Gaussian models are purely phenomenological, making them difficult to interpret in terms of IGM or galaxy properties and thus incapable of incorporating independent prior information on e.g., the ionization or thermal history. The tanh approach, on the other hand, can mimic the shape of typical global 21-cm signal models extremely well, and can be immediately related to physical properties of the IGM.

Harker et al. (2015) presented a suite of calculations spanning the 2-D parameter space defined by  $N_{\text{sky}} = \{1, 2, 4, 8\}$  and  $t_{\text{int}} = \{100, 1000\}$ . A small subset of the calculations were repeated with more complex foreground models or a bandpass limited to  $\nu \leq 100$  MHz rather than the standard 120 MHz upper cutoff. Limitations of the tanh model emerged in the  $t_{\text{int}} = 1000$  hr calculations, which narrowed confidence contours for the turning points well enough to reveal subtle biases in their positions, which led to biases in constraints on physical properties of the IGM as well. Harker et al. (2015) also found that biases in the turning point positions can be eliminated given a more sophisticated foreground model. Alternatively, if one is only interested in turning points B and C, truncation of the band at  $\nu \sim 100$  MHz also works since the biases arise primarily due to signal-foreground degeneracies at high frequencies. However, even with unbiased constraints on the turning point positions, biases in the IGM properties persist in the 1000 hr multiple sky region calculations because the tanh is not a perfect match in shape to the physical model injected into the synthetic dataset. To avoid such biases in the present work we focus on the  $t_{\text{int}} = 100$  hr cases, which

provide broader, but unbiased, constraints on the turning points. We also only analyze cases using one and two sky regions, for which model selection will be more immediately tractable computationally (Harker, 2015a).

Now, back to the simplest model of Harker et al. (2015) (EM1 in Table 4.1). This calculation assumed a single sky region, 100 hours of integration, and a third-order  $\log v - \log T$  polynomial for the galactic foreground. Harker et al. (2015) investigated the generic case of an idealized instrument (i.e., a flat 85% response function), though this could easily be modified to enable forecasting for non-ideal instruments. The foreground and astrophysical signal were simultaneously fit using the parallel-tempering sampler in the publicly available EMCEE code<sup>3</sup> (Foreman-Mackey et al., 2013), a PYTHON implementation of the affine-invariant Markov Chain Monte Carlo sampler of Goodman and Weare (2010), from which constraints on the positions of the turning points followed straightforwardly. The errors are in general not Gaussian, though for the purposes of our fitting, we approximate the errors as 1-D independent Gaussians, since covariances carry shape information and are thus known to induce biases in inferences of IGM properties (Harker et al., 2015). Table 4.1 summarizes the different signal extraction models, which are shown graphically in Figure 4.3.

### 4.3.3 Parameter Estimation

With a physical model for the global 21-cm signal (§4.3.1) and a set of constraints on the turning point positions (§4.3.2), we then explore the posterior probability distribution function (PDF) for the model parameters,  $\theta$ , given the data,  $\mathcal{D}$ . That is, we evaluate Bayes' theorem,

$$P(\theta|\mathcal{D}) \propto \mathcal{L}(\mathcal{D}|\theta)\mathcal{P}(\theta). \quad (4.12)$$

The log-likelihood is given by

$$\log \mathcal{L}(D|\theta) \propto - \sum_i \frac{[x(\theta) - \mu_i]^2}{2\sigma_i^2} \quad (4.13)$$

where  $\mu_i$  is the “measurement” with errors  $\sigma_i$  (i.e., the values listed in columns 3 and 4 of Table 4.1), and  $x(\theta)$  represents a vector of turning point positions extracted from the model global 21-cm signal generated

---

<sup>3</sup> <http://dan.iel.fm/emcee/current/>

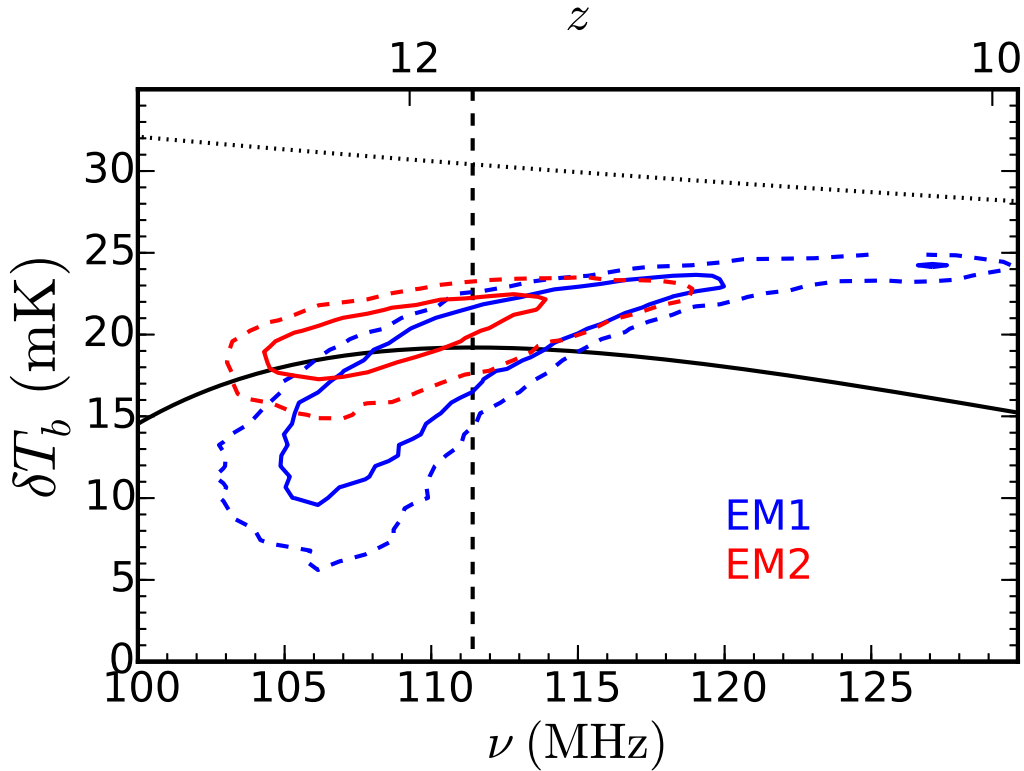


Figure 4.3 Comparison of EM1 and EM2 for turning point D, the point at which they differ most substantially (see Table 4.1). In blue and red, solid (dashed) contours denote 68% (95%) confidence regions for EM1 and EM2, respectively. The dotted black line shows the saturated limit, in which  $\bar{x}_i = 0$  and  $T_S \approx T_K \gg T_\gamma$ , while the dashed vertical line denotes the position of turning point D in our reference model (solid black curve). Note that the EM1 error ellipse for turning point D extends to  $\sim 130$  MHz, beyond the edge of the bandpass considered in Harker et al. (2015), though the  $2 - \sigma$  upper limit for EM2 is within the assumed band, at  $\nu_D \sim 117$  MHz.

Table 4.2. Parameter Space Explored

| Parameter          | Description                              | Input  | Min       | Max        |
|--------------------|--|--------|-----------|------------|
| $T_{\min}$ (K)     | Min. virial temp. of star-forming haloes | $10^4$ | 100       | $10^{5.7}$ |
| $\xi_{\text{LW}}$  | Ly- $\alpha$ efficiency                  | 969    | 10        | $10^6$     |
| $\xi_X$            | X-ray efficiency                         | 0.02   | $10^{-4}$ | $10^6$     |
| $\xi_{\text{ion}}$ | Ionizing efficiency                      | 40     | $10^{-4}$ | $10^5$     |

Note. — Parameter space explored for results presented in §4.4. The first two columns indicate the parameter name and a brief description, the third column is the “true value” of the parameter in our reference model, while the last two columns indicate the bounds of the priors for each parameter, all of which are assumed to be uninformative, i.e., modeled as uniform distributions between the minimum and maximum allowed values.

with parameters  $\theta$ . This “two-stage approach” to fitting the global 21-cm signal – the first stage having been conducted by Harker et al. (2015) – is much more tractable computationally than a direct “one-stage” fit to a mock dataset using a physical model. Note that the brightness temperature of turning point B,  $\delta T_b(\nu_B)$ , is tightly coupled to its frequency, so we are effectively only using 5 independent data points in our fits.

To explore this four-dimensional space, we use EMCEE. We assume broad, uninformative priors on all parameters (listed in Table 4.2), but note that our physical model implicitly imposes three additional priors on the astrophysical signal:

- (1) We neglect exotic heat sources at high- $z$ , which confines turning point B to a narrow “track” at  $\nu \lesssim 50$  MHz.
- (2) We assume that the Universe cannot cool faster than the Hubble expansion, which sets a redshift-dependent lower limit on the strength of the absorption signal (lower dotted curve in all panels of Figure 4.1).
- (3) We assume the mean density of the IGM we observe is the universal mean density, i.e., it has  $\delta = 0$ , which prevents the signal from exceeding the “saturated limit,” in which  $T_S \gg T_\gamma$  and  $x_i = 0$  (upper dotted curve in all panels of Figure 4.1).

Our code could be generalized to accommodate exotic heating models, though this is beyond the scope of this paper. Bullets 2 and 3 above are manifestly true for gas at the cosmic mean density (via Equation

4.8), though imaging campaigns will likely see patches of IGM whose brightness temperatures exceed (in absolute value) these limits, owing to over-densities  $\delta > 0$ .

For all calculations presented in this work, we use 384 *walkers*, each of which take a 150 step burn-in, at which point they are re-initialized in a tight ball centered on the region of highest likelihood identified during the burn-in. We then run for 150 steps more (per walker), resulting in MCMC chains with 57,600 links. The mean acceptance fraction, i.e., the number of proposed steps that are actually taken during our MCMC runs, is  $\sim 0.3$ . The runs are well-converged, as we see no qualitative differences in the posterior distributions when we compare the last two 10,000 element subsets of the full chain.

## 4.4 Results

Each MCMC fit yields 57,600 samples of the posterior distribution, which is a 4-dimensional distribution in  $\{T_{\min}, \xi_{\text{LW}}, \xi_X, \xi_{\text{ion}}\}$  space. However, we also analyze each realization of the global 21-cm signal on-the-fly as the MCMC runs, saving IGM quantities of interest every  $\Delta z = 0.1$  between  $5 \leq z \leq 35$ , as well as at the turning points. To build upon the analytical arguments presented in Paper I, which provided a basis for interpreting the turning points in terms of IGM properties, we start with an analysis of the inferred IGM properties at the turning points in §4.4.1, deferring a full analysis of the IGM history to future work. Readers interested only in the constraints on our four-parameter model can proceed directly to §4.4.2.

### 4.4.1 Constraints on the Intergalactic Medium

We begin by showing our mock constraints on properties of the IGM at the redshifts of turning points B, C, and D in Figures 4.4, 4.5, and 4.6, respectively.

Because turning point B primarily probes the Ly- $\alpha$  background, we focus only on its ability to constrain  $J_\alpha$  in Figure 4.4. The input value is recovered to  $1 - \sigma$ , with relatively tight error-bars limiting  $J_\alpha$  to within a factor of 2. Use of EM2 has little effect on this constraint as its main improvement over EM1 is at frequencies  $\nu \gtrsim 100$  MHz.

Figure 4.5 shows constraints on the Ly- $\alpha$  background and thermal history at the redshift of turning point C. In the  $\sim 90$  Myr separating turning points B and C, the Ly- $\alpha$  background intensity,  $J_\alpha$ , has risen by

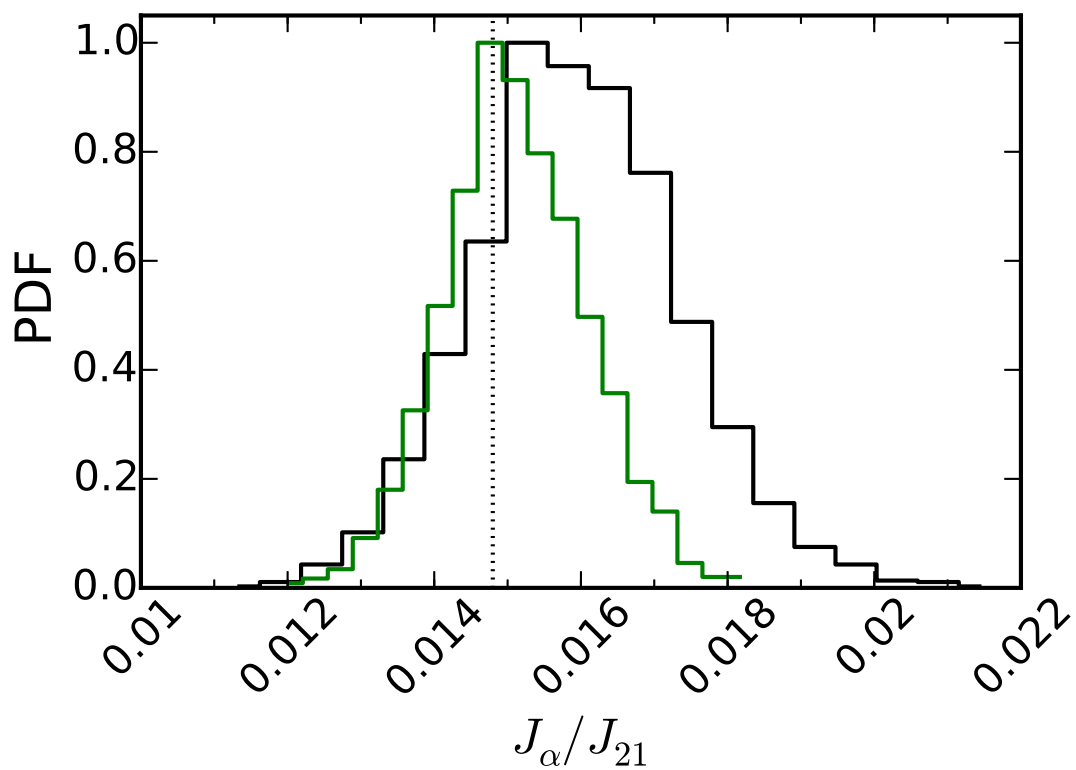


Figure 4.4 Constraints on the background Ly- $\alpha$  intensity at the redshift of turning point B, in units of  $J_{21} = 10^{-21} \text{erg s}^{-1} \text{cm}^{-2} \text{Hz}^{-1} \text{sr}^{-1}$ . Dotted vertical line shows the input value, which occurs at  $z = 29$  in our reference model. The black histogram is the constraint obtained if using EM1, while the analogous constraint for EM2 is shown in green.

a factor of  $\sim 350$ , though we still constrain its value to within a factor of  $\sim 2$  (panel f). The IGM temperature is limited to  $9 \lesssim T_K/\text{K} \lesssim 11$ , and would otherwise be  $\sim 7.4$  K at this redshift in the absence of heat sources. There are noticeable degeneracies in the 2-D PDFs, which are not necessarily obvious intuitively.

Let us first focus on the anti-correlations in the  $J_\alpha$ - $\epsilon_X$  and  $J_\alpha - T_K$  planes (panels a and d in Figure 4.5). For this exercise – and those that follow – it will be useful to consider slight excursions away from our reference model. We can see from the lower right panel of Figure 4.1 that a small increase in  $\xi_{\text{LW}}$  will shift turning point B to slightly higher redshifts (lower frequencies) holding all other parameters fixed. Turning point C will also occur earlier than in our reference model (since a stronger Ly- $\alpha$  background can couple  $T_S$  to  $T_K$  more rapidly) and be deeper, since there has been less time for X-rays to heat the IGM, leading to increased contrast between the IGM and the CMB. Panels (a) and (d) in Figure 4.5 now make sense: the anti-correlations in the  $J_\alpha$ - $\epsilon_X$  and  $J_\alpha - T_K$  planes arise because measurement errors permit slight excursions away from the reference model, which if achieved through enhancements to  $\xi_{\text{LW}}$ , shift turning points B and C to slightly earlier – and thus cooler – times.

One could also counteract a mild increase in  $\xi_{\text{LW}}$  with a corresponding increase in  $\xi_X$ , which enhances heating and thus leads to shallower absorption troughs. However, increasing  $\xi_X$  shifts turning point C to shallower depths *and* lower frequencies, thus exacerbating the leftward shift caused by larger values of  $\xi_{\text{LW}}$ . As a result,  $T_{\text{min}}$  would also need to be increased in order to delay the onset of Wouthuysen-Field coupling and heating. Indeed, we will find this series of positive correlations among the physical parameters of our model in the §4.4.2.

Before moving on to the IGM constraints associated with turning point D, we note that the correlation between  $T_K$  and  $\epsilon_X$  (panel b) is simply because  $T_K \propto \int \epsilon_X dz$ , and  $\epsilon_X$  is monotonic. Also, apparently the improvement at the highest frequencies offered by EM2 also acts to slightly bias constraints on  $J_\alpha$  and  $\epsilon_X$  relative to their input values. Referring back to Figure 4.3, we do see a slight bias in the EM2 PDF for turning point D toward larger amplitude, which would require more rapid heating at earlier times. In fact, this is precisely the sense of the bias we see in Figure 4.5: slightly larger values of  $\epsilon_X$  at turning point C, and a corresponding downward shift in  $J_\alpha$  as described above.

And finally, Figure 4.6 shows constraints on the ionization and thermal histories at the redshift of

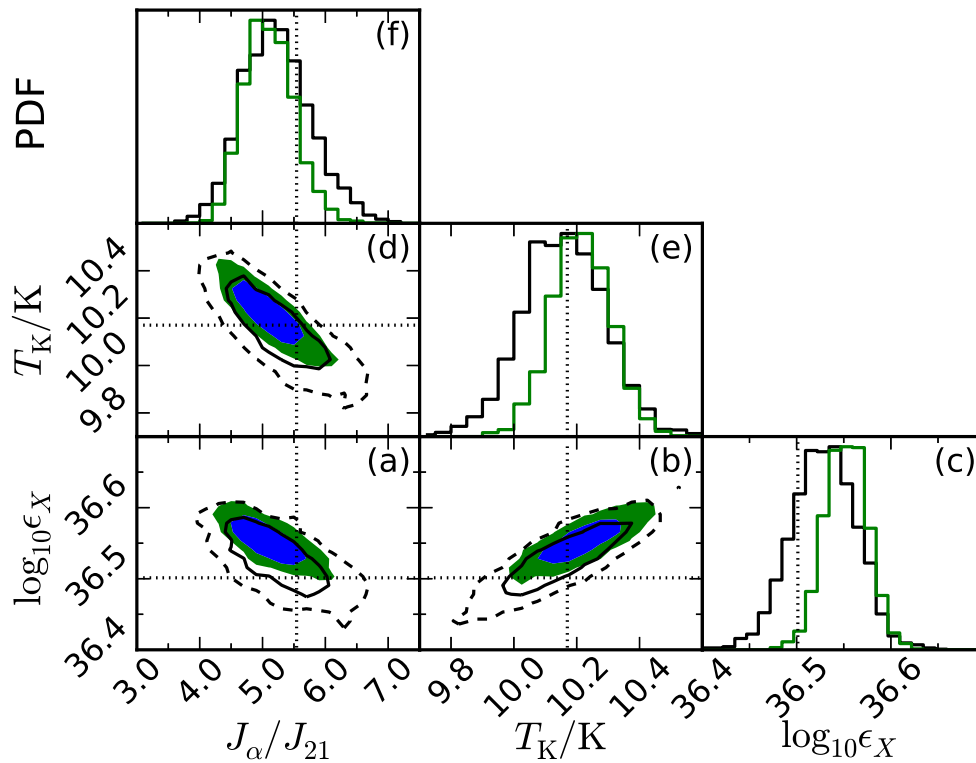


Figure 4.5 Constraints on the IGM temperature, heating rate density, and Ly- $\alpha$  background intensity at the redshift of turning point C. The heating rate density,  $\epsilon_X$ , is expressed in units of  $\text{erg s}^{-1} \text{cMpc}^{-3}$ , while  $J_\alpha$  is once again expressed in units of  $J_{21} = 10^{-21} \text{erg s}^{-1} \text{cm}^{-2} \text{Hz}^{-1} \text{sr}^{-1}$ . Dotted vertical lines show the input values, which occur at  $z = 19$  in the reference model. Open contours are those obtained with EM1 (68% and 95% confidence regions in solid and dashed curves, respectively), while filled contours are the constraints obtained by EM2 (68% and 95% confidence regions in blue and green, respectively). The color-scheme along the diagonal is the same as in Figure 4.4, with EM1 (EM2) curves in black (green).

turning point D, which occurs at  $z = 11.75$  in our input model. The behavior here is complex, as the signal is not yet saturated (i.e.,  $T_S \gg T_\gamma$  is a poor approximation) and the mean ionized fraction is non-zero (i.e.,  $Q_{\text{HII}} \sim 0.2$ ). This means the global 21-cm signal depends on both the ionization history and the thermal history, which we may parameterize in terms of the volume filling factor of ionized gas,  $Q_{\text{HII}}$ , the IGM temperature,  $T_K$ , and their time-derivatives<sup>4</sup>  $\Gamma_{\text{HI}}$  and  $\epsilon_X$ . We may, however, neglect the Ly- $\alpha$  history at this stage, since  $T_S \approx T_K$  is accurate to high precision, rendering any constraints on  $J_\alpha$  completely parameterization-dependent (i.e.,  $J_\alpha$  can be anything, so long as it is large enough to drive  $T_S \rightarrow T_K$ ).

It is once again useful to consider excursions away from the reference model. At fixed thermal history, a slight increase in  $\xi_{\text{ion}}$  will act to decrease the amplitude of turning point D and shift it to slightly higher redshift. With less time to heat the IGM between turning points C and D, the IGM is cooler at the redshift of turning point D in this scenario and as a result, the emission signal is weaker than that of our reference model. This line of reasoning explains the anti-correlations between the ionization and thermal history parameters in Figure 4.6. As in Figure 4.5, positive correlations occur by construction, since state quantities like  $Q_{\text{HII}}$  and  $T_K$  are just integrals of  $\Gamma_{\text{HI}}$  and  $\epsilon_X$ , which are both monotonically increasing with decreasing redshift.

The advantages of EM2 over EM1 are also clear in Figure 4.6. This improvement occurs because EM1 does not detect turning point D with significance away from the saturated limit or within the assumed band ( $\nu \leq 120$  MHz), whereas the EM2 fit does both at the  $> 2 - \sigma$  level. Perhaps most notably, this leads to a strong detection of the early stages of reionization ( $0.12 \leq Q_{\text{HII}} \leq 0.29$  at  $2 - \sigma$ ; green PDF in panel j).

Lastly, we note that although the amplitude of the signal is set by  $\bar{x}_i$ , a volume-averaged ionized fraction, we only show constraints on  $Q_{\text{HII}}$ , as  $x_e$  never reaches values above  $\sim 10^{-2}$  at  $z \gtrsim 10$  in any of our calculations. As a result, it has a negligible direct effect on  $\delta T_b$ . However, even mild ionization of the bulk IGM enhances the efficiency of heating rather substantially, as the fraction of photo-electron energy deposited as heat (as opposed to ionization or excitation) is a strong function of the electron density (e.g.

---

<sup>4</sup> Although we use the symbol  $\Gamma$ , we caution that our values should not be compared to extrapolations of constraints on  $\Gamma_{\text{HI}}$  from the Ly- $\alpha$  forest at  $z \lesssim 6$ . The latter is a probe of the meta-galactic ionizing background (i.e., large-scale backgrounds), whereas our values of  $\Gamma$  probe the growth rate of ionized regions, and thus should be considered a probe of radiation fields *near* galaxies. A more detailed cosmological radiative transfer treatment could in principle reconcile the two tracers of ionizing sources.

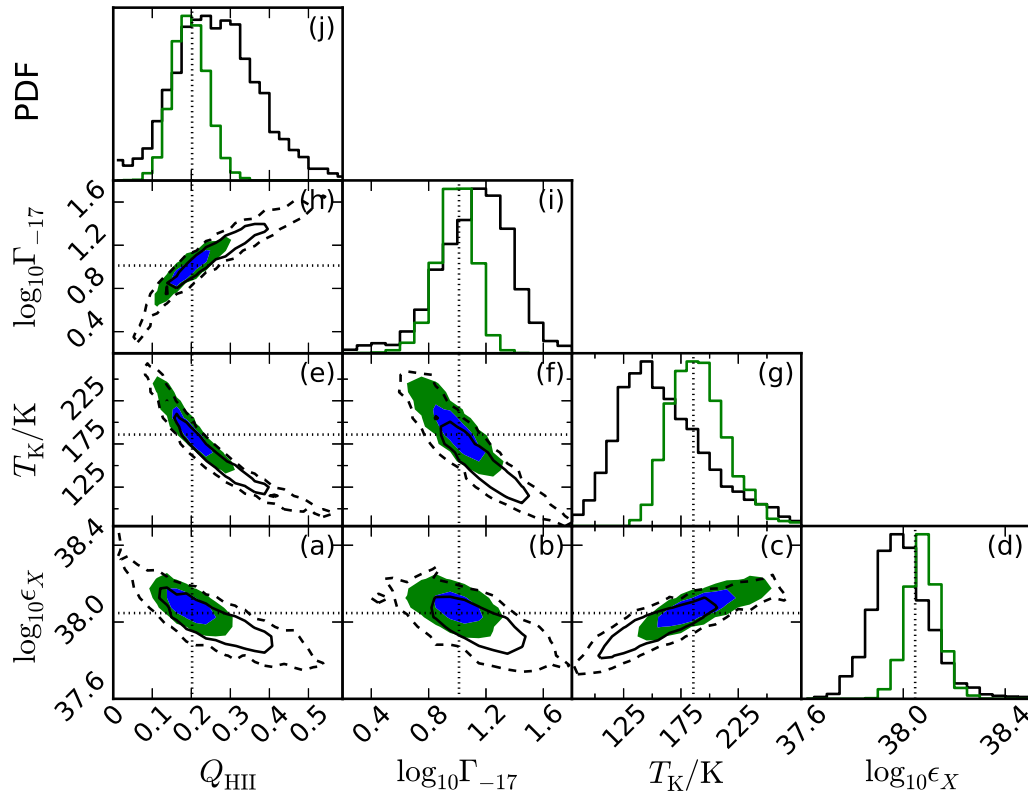


Figure 4.6 Constraints on the IGM temperature, volume-filling factor of ionized gas,  $Q_{\text{HII}}$ , heating rate density, and volume-averaged ionization rate,  $\Gamma$ , at the redshift of turning point D, which occurs at  $z = 11.75$  in our reference model. Open contours are 68% (solid) and 95% (dashed) confidence regions for EM1, while filled contours show the results from EM2, with 68% and 95% confidence regions shown in blue and green, respectively. Input values are denoted by black dotted lines in each panel.

Shull and van Steenberg, 1985, Furlanetto and Johnson Stoeber, 2010). Our choice of a mean X-ray photon energy of  $h\nu_X = 0.5$  keV, in lieu of a detailed solution to the radiative transfer equation, drives this result. More expensive calculations that solve the RTE in detail (e.g. Mirocha, 2014) could enable scenarios in which the bulk IGM is ionized substantially prior to the overlap phase of reionization, which could have interesting observational signatures. We defer a more detailed treatment of this effect and others associated with proper solutions to the RTE to future work.

#### 4.4.2 Constraints on the Physical Model

Our main results are illustrated in Figures 4.7, 4.8, and 4.9, which analyze the full 4-D constraints on our reference model and the implications for UV and X-ray sources, respectively. In this section, we'll examine each in turn.

It is perhaps most intuitive to begin with the panels along the diagonal of Figure 4.7, which show the marginalized 1-D constraints on the parameters of our reference model. As predicted, given its broad-band influence on the signal,  $T_{\min}$  (panel d) is most tightly constrained, with  $1\sigma$  error bars of order  $\sim 0.05$  dex. Therefore, an idealized instrument observing a single sky region for 100 hours can rule out star-formation in molecular halos (onto which gas collapses more slowly; see Figure 4.2), at least at levels sufficient to affect all three turning points. Errors on  $\xi_X$  and  $\xi_{\text{LW}}$  are comparable (panels i and j), though the positive error-bars are larger at  $\sim 0.1$  dex. The errors on  $\xi_{\text{ion}}$  are more asymmetric, at  $+0.1/-0.2$  dex (panel g).

Strong degeneracies are also apparent, particularly in panels (a), (b), and (h), which show 2-D constraints in the  $T_{\min}$ - $\xi_{\text{LW}}$ ,  $T_{\min}$ - $\xi_X$ , and  $\xi_{\text{LW}}$ - $\xi_X$  planes, respectively. The first two are straightforward to understand. An increase in  $\xi_{\text{LW}}$  means an enhancement in Ly- $\alpha$  production *per unit star-formation*, so to keep turning point B fixed, a reduction in the star-formation rate *density* is required. In our modeling framework, a reduction in the SFRD is achieved by increasing  $T_{\min}$ , confining star formation to more massive and thus more rare halos. If  $f_*$  were allowed to vary, it too could limit the SFRD, though the change would be systematic, whereas varying  $T_{\min}$  affects the normalization and the redshift evolution. The same line of reasoning explains the relationship between  $T_{\min}$  and  $\xi_X$ .

The  $\xi_{\text{LW}}$ - $\xi_X$  degeneracy is slightly more complex. An increase in  $\xi_{\text{LW}}$  seeds a stronger Ly- $\alpha$  back-

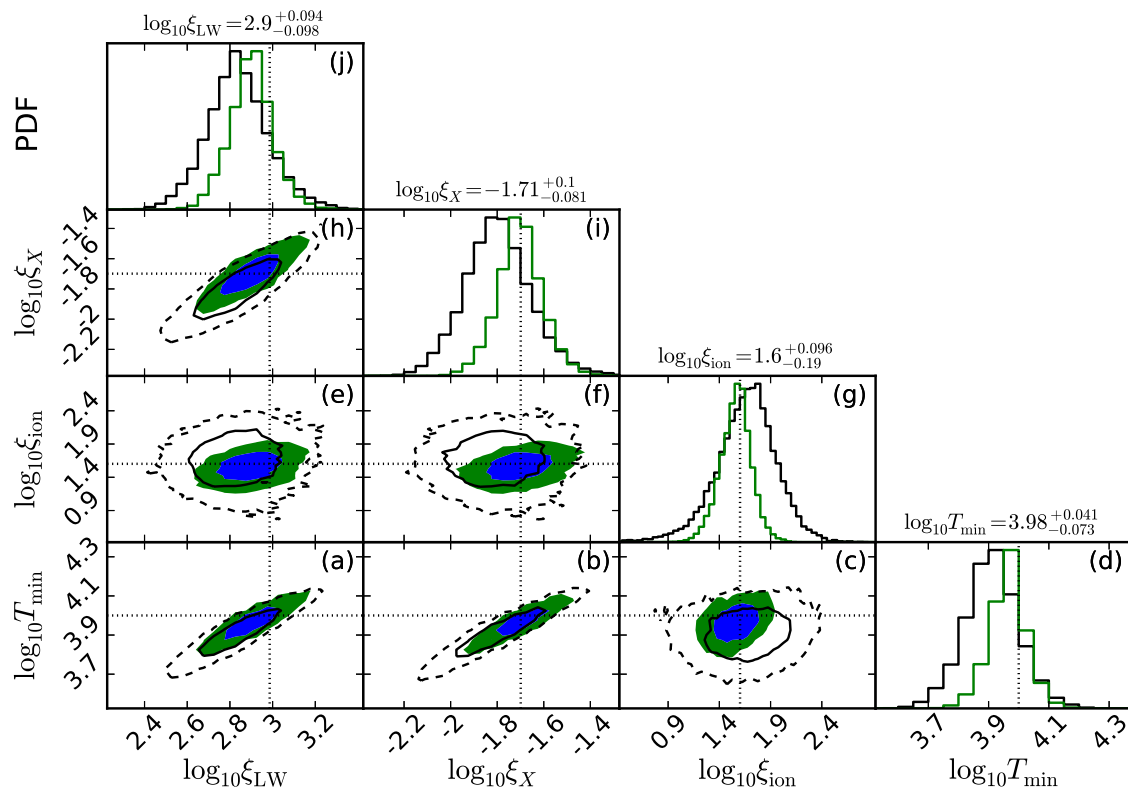


Figure 4.7 Constraints on our 4-parameter reference model. Filled contours in the interior panels are 2-D marginalized posterior PDFs with 68% confidence intervals shaded blue and 95% confidence regions in green. Panels along the diagonal are 1-D marginalized posterior PDFs for each input parameter, with 1- $\sigma$  asymmetric error-bars quoted, as computed via the marginalized cumulative distribution functions. Dotted lines denote the input values of our reference model (Table 4.1). Bins of width 0.05 dex are used in each panel. Annotated best-fit values and error bars along the diagonal are those associated with EM2.

ground (holding  $T_{\min}$  fixed), which in turn shifts turning point B to lower frequencies (see the lower right panel of Figure 4.1), which measurement error permits to some degree. This will result in a deeper (and earlier) absorption trough *unless*  $\xi_X$  is increased, causing a shallower trough (see upper right panel of Figure 4.1). Once again, measurement error sets the degree to which an increase in  $\xi_X$  can compensate for an increase in  $\xi_{\text{LW}}$ . In the limit of very large error-bars, these contours would not close, and instead we would have large “bands” through parameter space, signifying an insurmountable degeneracy between two parameters. Our results indicate that observations of a single sky region for 100 hours, albeit with an idealized instrument, are precise enough to close these contours, and recover all input values to within  $1 - \sigma$  confidence. We will revisit this claim in §4.5.

At this stage it may seem like we have just traded constraints on one set of phenomenological parameters (the tanh parameters) for another ( $T_{\min}$  and the  $\xi$ 's). However, if we assume that  $\xi_{\text{LW}}$  and  $\xi_{\text{ion}}$  probe the same stellar population, their ratio is independent of the star-formation history, and thus constrains the spectral energy distribution (SED) of galaxies modulo a factor of the escape fraction<sup>5</sup>, i.e.,

$$\frac{\xi_{\text{ion}}}{\xi_{\text{LW}}} = \frac{N_{\text{ion}}}{N_{\text{LW}}} f_{\text{esc}}. \quad (4.14)$$

To compute  $N_{\text{ion}}/N_{\text{LW}}$ , we take model spectral energy distributions directly from Leitherer et al. (1999). We focus on those assuming an instantaneous burst of star-formation with nebular emission included (their Figures 1, 3, and 5). We find the cumulative number of photons emitted in the LW and hydrogen-ionizing bands, which typically reaches its maximum around  $\sim 20$  Myr after the initial burst. The results, as a function of metallicity and stellar initial mass function (IMF), are shown in the left panel of Figure 4.8. While the values of  $N_{\text{ion}}$  and  $N_{\text{LW}}$  vary by factors of  $\sim 2$  over the metallicity range  $0.001 \leq Z/Z_{\odot} \leq 0.04$ , their *ratio* changes by only  $\sim 5\%$  over this same interval in metallicity. The more important dependence is on the stellar IMF: a standard Salpeter IMF, with  $\alpha_{\text{IMF}} = 2.35$  and an upper mass cutoff of  $M_{\text{cut}} = 100 M_{\odot}$ , yields  $0.25 \lesssim N_{\text{ion}}/N_{\text{LW}} \lesssim 0.3$  for all  $10^{-3} \leq Z/Z_{\odot} \leq 0.04$  (blue circles in the left panel of Figure 4.8), whereas mass functions with fewer massive stars, whether that be achieved with steeper power-law indices ( $\alpha_{\text{IMF}} = 3.3$ ; green squares in Figure 4.8) or by reducing the upper cutoff ( $M_{\text{cut}} = 30 M_{\odot}$ ; red triangles in

<sup>5</sup> We assume the escape fraction of LW photons is 100%, though in reality this is only likely to be true in the smallest halos (e.g., Kitayama et al., 2004). For simplicity, we neglect this complication and defer a more thorough treatment to future work.

Figure 4.8), yield  $0.07 \lesssim N_{\text{ion}}/N_{\text{LW}} \lesssim 0.12$ .

In the right panel of Figure 4.8, we compare our constraints in the  $\xi_{\text{LW}} - \xi_{\text{ion}}$  plane with the  $Z = 0.04 Z_{\odot}$  stellar population models described above. The red, green, and blue bands in the right panel correspond to the stellar population models denoted by filled points of the same color in the left panel. We also show the case of a pure 50,000 K blackbody spectrum in the cross-hatched region. The width of each band corresponds to a factor of two change in the escape fraction,  $0.1 \leq f_{\text{esc}} \leq 0.2$ .

Our mock constraints on  $\xi_{\text{LW}}/\xi_{\text{ion}}$  given 100 hours of integration on a single sky region (EM1) can only rule out rather extreme cases. For example, this scenario rules out the 50,000 K toy stellar population with  $f_{\text{esc}} \gtrsim 0.2$  at one extreme, and bottom-heavy IMFs with escape fractions below  $f_{\text{esc}} \lesssim 0.1$  at the other extreme. A stronger detection of turning point D, achieved by EM2, tightens these constraints considerably. The pure 50,000 K stellar population would require  $f_{\text{esc}} \lesssim 0.01$ , while a stellar population with a prevalence of lower mass stars would require  $f_{\text{esc}} \gtrsim 0.2$ . Note that the surface temperatures of PopIII stars are expected to be  $\sim 10^5$  K, which only strengthens our limits quoted for the 50,000 K population. Our reference model assumes a typical PopII stellar population, so it is reassuring to see that our constraints coincide with the blue diagonal band, which represents a standard Salpeter IMF.

Synthesis models for black hole populations are growing in maturity, though still only loosely constrained by observations, especially at low metallicities (e.g., Belczynski et al., 2008). An immediate interpretation of a measurement of  $\xi_X$  *apart from the star-formation history*, as we have done above for constraints on the stellar IMF and  $f_{\text{esc}}$ , will thus be very challenging barring progress on this front in the coming years. For simplicity, we assume an  $\alpha = 1.5$  power-law spectrum above 0.2 keV consistent with the findings of Mineo et al. (2012b), and  $f_* = 0.1$ . The 1-D marginalized PDF for  $\xi_X$  for EM's 1 and 2 are shown in Figure 4.9. Such enhancements are allowed out to  $z \lesssim 4$  (Dijkstra et al., 2012, Basu-Zych et al., 2013), though the redshifts probed by the global 21-cm signal are far beyond the reach of the techniques used to establish such limits (the cosmic X-ray background and image stacking, respectively). All signal extraction models considered here rule out factor of 2 enhancements to  $f_X$  at the  $\sim 3\sigma$  level assuming  $f_* = 0.1$ . We will revisit this type of constraint in §4.5.

Our reference model is seemingly inconsistent with star formation in molecular halos and a stellar

IMF that yields more high-mass X-ray binaries than average (per unit star formation). This does not rule out star formation in molecular halos or a top-heavy IMF, *it just rules out such sources as important drivers of the turning points*. If we assume that PopIII stars have  $N_{\text{LW}} = 4800$ , a SFRD of  $\approx 3 \times 10^{-7} M_{\odot} \text{ yr}^{-1} \text{ cMpc}^{-3}$  would be required to match the constraint on  $J_{\alpha}$  provided by turning point B (following Eq. 17 of Mirocha et al., 2013), which corresponds to  $f_{*} \approx 0.1$  in  $T_{\text{min}} = 300 \text{ K}$  halos. Such a population would have to die out rapidly in order for turning point C to be unaffected. Put another way, if PopIII stars do form relatively efficiently at  $z \sim 30$ , and continue to do so for more than  $\sim 100 \text{ Myr}$ , we should expect the position of turning point C to change (relative to our reference model) due to a stronger Ly- $\alpha$  background and potentially a stronger X-ray background, depending on the properties of PopIII remnants.

## 4.5 Discussion

Our results suggest that simultaneous fits to the three spectral turning points of the global 21-cm signal can yield powerful constraints on the properties of the Universe’s first galaxies. A simple 4-parameter model can be constrained quite well in only 100 hours of integration on a single sky region, provided an idealized instrumental response function. The  $\xi$  parameters place interesting constraints on the properties of the first generations of stars and black holes, while constraints on the characteristic redshift-dependent mass of star-forming galaxies follows immediately from constraints on  $T_{\text{min}}$ . In this section, we discuss these findings within a broader context, focusing in particular on how our results depend on the assumed measurement (§4.5.1) and model (§4.5.2), and how improvements to our fitting procedure might be improved to maximize the return from ongoing and near-future observing campaigns (§4.5.3).

### 4.5.1 Are all three points necessary?

Our forecasts have so far assumed that all three spectral features in the  $40 \lesssim \nu / \text{MHz} \lesssim 120$  window are detected and characterized reasonably well, apart from the EM1 detection of turning point D which was only marginal. Given practical limitations in constructing an instrument with a broad-band response, the ionospheric challenges at low frequencies, and a weak emission feature potentially plagued by terrestrial radio frequency interference (RFI), it is worth asking: must we detect all three features at once to constrain

even the simplest of galaxy formation models?

Figures 4.10 and 4.11 show the constraints on our 4-parameter model assuming only a subset of the turning points are detected. We consider all possible cases, except a scenario in which only turning point B is detected, as it seems unlikely that one could recover this feature from the foreground without help from neighboring spectral structure, given its amplitude of  $\lesssim 5$  mK. Note that the black contours in each plot are identical to the 95% confidence regions in Figure 4.7, though the x and y scales of each individual panel here are much broader than those in Figure 4.7 due to worsening constraints. Blue contours denote fits including two turning points, while green cross-hatched regions correspond to fits including only a single turning point. Because the PDFs for the one- and two-point fits are broad, they tend to become noisy. This behavior is expected: by design, walkers spend less time in low-likelihood regions. If those regions of parameter space are large (which they are for the one- and two-point fits), it will take a long time to properly explore them.

In Figure 4.10, we focus on the case in which the emission maximum, turning point D, is not used in the fit. In the most optimistic case, both turning points B and C are still detected, and give rise to the constraints shown in blue. As expected, constraints on  $\xi_{\text{ion}}$  are virtually nil except for a weak upper limit (panel g). However, constraints on  $\xi_{\text{LW}}$ ,  $\xi_X$ , and  $T_{\text{min}}$  remain largely intact. The subtle excursion away from the black contours in panels b, h, and f toward small values of  $\xi_X$  are real: they indicate scenarios in which heating is negligible and turning point C is induced by ionization (see §3.2.2 in Paper I). Such models would likely lead to an early end to the EoR, and a large value of the Thomson optical depth,  $\tau_e$ , though without a detection of turning point D or a prior on  $\tau_e$  such scenarios remain allowed. In a more pessimistic scenario in which only the absorption minimum, turning point C, is detected,  $2 - \sigma$  constraints span  $\sim 3$  orders of magnitude (green contours and cross-hatched regions), though still rule-out large regions of currently permitted parameter space.

In the event that the lowest frequency feature, turning point B, is not detected, we instead arrive at the constraints shown in Figure 4.11. Provided that turning points C and D are still detected, we obtain the blue contours, which are broader by  $\sim 1$  order of magnitude in each dimension except for  $\xi_{\text{ion}}$ , though they still close within the broad space defined by our priors. If only the emission maximum is detected, we instead

derive the contours in green.  $T_{\min}$  is unconstrained in this scenario, and only limits are available for each parameter when marginalizing over the others.

The results shown in Figures 4.10 and 4.11 are almost certainly optimistic, since it is the spectral structure which makes signal extraction possible in the first place. With a narrow-band measurement of the global 21-cm signal that only includes two features, we should then expect the errors on the positions of those turning points to be *larger* than those quoted in Table 4.1. Even so, such constraints would still be a big step forward, ruling out large regions of currently permitted parameter space and providing priors for next-generation experiments.

#### 4.5.2 Assumptions Underlying the Physical Model

Our constraints on the four-parameter model of course assume that this model is “correct,” i.e., its parameters are assumed to be physically meaningful. In this section, we describe the assumptions and approximations at the heart of this model and the circumstances in which they may deteriorate. This will provide a basis for our final discussion section, regarding the use of independent constraints and model selection techniques in §4.5.3.

##### 4.5.2.1 The Star Formation History

Our  $f_{\text{coll}}$ -based recipe for the global 21-cm signal is certainly not unique in its ability to model the first galaxies and the high- $z$  IGM. For example, it would not be unreasonable to employ a more flexible “multi-population” model (e.g., Furlanetto, 2006) in which the Ly- $\alpha$ , soft UV, and X-ray backgrounds are produced by distinct sources, whose redshift evolution, photon production rates, and/or spectral energy distributions are allowed to be different. This approach may be warranted, given that the radiative properties and formation efficiencies (with time) of PopII and PopIII stars are expected to be different.

Some recent work has instead used empirical constraints on the SFRD at high- $z$  to model the global 21-cm signal (Yajima and Khochfar, 2015). While in principle such models are capable of more varied star-formation histories than our own, and can more seamlessly be compared to pre-existing empirical constraints on the SFRD in the post-EoR Universe (from which such SFRD models were first born), they have

more free parameters and potentially obfuscate the dominant mode of star formation, which is of primary interest in this study. It would be straightforward to generalize our code to test empirically-calibrated parameterizations, which have the greatest strength at the lowest redshifts ( $z \lesssim 10$ ), thus complementing the  $f_{\text{coll}}$  approach, which is likely most accurate at the highest redshifts.

Such changes to the underlying model would prevent some of the analysis so far presented. For example, our constraints on the stellar IMF and escape fraction relied on the assumption of a single population well-described by time-independent values of  $f_*$ , the IMF (which we model implicitly through  $N_{\text{LW}}$  and  $N_{\text{ion}}$ ), and  $f_{\text{esc}}$ . Such analyses could still be applied for a single-population model with an empirical SFRD, but for any kind of multi-population model, Equation 4.14 no longer applies. In addition, the value of  $N_{\text{ion}}/N_{\text{LW}}$  may take on a new meaning, since it could probe  $N_{\text{LW}}$  of PopIII stars that induce turning point B, and the  $N_{\text{ion}}$  of more ordinary PopII star-forming galaxies responsible for driving turning point D.

#### 4.5.2.2 Stellar Population Models

Even with perfect knowledge of the SFRD, properly interpreting  $N_{\text{ion}}/N_{\text{LW}}$  in terms of the stellar population requires robust predictions from synthesis codes, which aim to generate a model SEDs as a function of time. Despite a long history (Leitherer et al., 1999) and plenty of observational datasets to compare against, such codes are still being revised to account for updates in e.g., stellar atmosphere models, evolutionary tracks (Leitherer et al., 2014), stellar rotation (Leitherer et al., 2014, Topping and Shull, 2015), and nebular emission (Zackrisson et al., 2011).

#### 4.5.2.3 Stellar Remnants and X-ray Emission

A “complete” stellar synthesis code would model the remnants of stars, in addition to stars themselves, if a comparison to datasets in the X-ray band were desired. This is because neutron stars and black holes, when in binary systems, are known to dominate the X-ray luminosity of star-forming galaxies (without active nuclei; Grimm et al., 2003, Gilfanov et al., 2004, Mineo et al., 2012b), while supernovae can provide yet another source of X-rays, either via inverse Compton scattering off hot electrons in the remnant (Oh, 2001), or indirectly by heating the interstellar medium (ISM) which then emits thermal bremsstrahlung

radiation (Mineo et al., 2012). While we are not in the business of comparing model and measured X-ray spectra, we are concerned with modeling the X-ray SED of galaxies insofar as it affects the thermal history of the IGM.

The modeling compact object populations has become a larger industry in recent years, motivated in large part by the development of gravitational wave observatories, continued interest in ultra-luminous X-ray sources (Belczynski et al., 2002, Belczynski et al., 2008), and the likely importance of compact objects in reheating of the high- $z$  IGM (Power et al., 2013, Fragos et al., 2013). As in the case of pure stellar population modeling, the number of compact objects and their mass distribution is expected to depend strongly on the metallicity. Unfortunately, the observational data is sparse, especially at low metallicities, making it difficult to calibrate the models to local analogs of high- $z$  galaxies.

Whereas our forecast for the stellar IMF and escape fraction relied on the assumption of time-independent (but free to vary) values for  $f_*$  and  $T_{\min}$ , our ability to constrain  $f_X$  was intimately linked to the precise value of  $f_*$ . Without more robust predictions for the X-ray yields of stellar populations, interpretation of  $f_X$  will hinge on assumptions, or hopefully independent constraints, on the efficiency of star formation in high- $z$  galaxies. Even if  $L_X$ -SFR does not evolve much with redshift, spectral evolution will affect the global 21-cm considerably (Mirocha, 2014), likely requiring independent measurements of the 21-cm power spectrum to disentangle constraints on the normalization and spectral shape of the X-ray background (Pritchard and Furlanetto, 2007, Pacucci et al., 2014).

#### 4.5.2.4 Cosmology and the Mass Function of Dark Matter Halos

We have fixed cosmological parameters as well as parameters governing the halo mass function, adopting the most up-to-date values from *Planck* and the Sheth-Tormen form of the mass function throughout. Variations in the cosmological parameters alone should be a secondary effect to all astrophysical processes we consider, but potentially discernible with observations of dark ages ( $\nu \sim 20$  MHz), prior to first-light. Variations in the cosmological parameters will also influence the abundance of halos, though discrepancies in halo abundances in the literature are known to be primarily due to differences in calibration of the fitting functions rather than uncertainties in cosmological parameters (Murray et al., 2013a), at least

at low redshifts ( $z \lesssim 2$ ). Calibration of the mass function at high redshifts and for low-mass halos in which the first objects form is limited, given the dynamic range needed to resolve small halos in large volumes. If the mass function at  $z \gtrsim 20$  deviates significantly from the Sheth-Tormen form, it would certainly affect the way we interpret  $T_{\min}$ , and thus should be considered an important avenue for future work.

#### 4.5.2.5 The Two-Zone IGM Formalism

Our entire procedure hinges on the ability to rapidly generate model realizations of the global 21-cm signal, which has led us to a simple two-phase IGM formalism rather than more detailed (and expensive) numerical or semi-numerical simulations. Whereas simple models have been compared to numerical simulations in the context of the 21-cm power spectrum (Zahn et al., 2011), and found to agree quite well, no such comparison has been conducted for global models. As far as we can tell, this is because there has yet to be a single numerical simulation capable of self-consistently generating a synthetic global 21-cm signal. Doing so will require high dynamic range, capable of resolving the first star-forming halos, the radiation backgrounds they seed, in a volume large enough to be considered a global volume element.

Without a suite of numerical simulations to calibrate against, we have not attempted to attach any intrinsic uncertainty associated with our model, as was done recently by Greig and Mesinger (2015) in the context of the 21-cm power spectrum. However, we do expect this formalism to be accurate over nearly the entire redshift range covered by our calculations (i.e., we do not use it solely out of computational necessity). The two-zone formalism operates best when HII regions are distinct and have sharp edges, and the heating and Ly- $\alpha$  is well-modeled by a uniform background. At turning point D, overlap between bubbles is likely minimal given that the volume filling factor of HII regions is small ( $Q \sim 0.2$ ). In addition, their edges are likely sharp since  $f_X$  is at most  $\sim$  a few. As a result, we do not have reason to suspect a breakdown in the formalism, at least for the reference model we have chosen.

#### 4.5.3 Priors and the Prospects for Model Selection

Changes to the physical model, like those discussed in the previous section, generally fall into two categories: they either (1) change how we interpret the constraints on model parameters of interest, or (2)

fundamentally change the characteristics of the modeled signal. For example, improvements to synthesis models of stars and black holes will change how the  $\xi$  parameters relate to the stellar IMF and properties of stellar remnants, but so long as we still employ the four-parameter model, our constraints on the values of  $\xi$  will *not* change. If instead we introduced new parameters that allowed  $\xi$  or  $T_{\min}$  to evolve with redshift, we have then enhanced the flexibility of the model enough that we may now be capable of generating realizations of the global 21-cm that our previous approach simply could not have.

A “double reionization” scenario, which could lead to two emission features rather than our single “turning point D,” is an unrealistic (Furlanetto, 2006) but illustrative example of a model with enhanced flexibility. Our four-parameter model simply could not produce two emission features. One could imagine less drastic changes that might still have new and potentially discernible effects on the signal through modulations of its shape, such as redshift-dependent  $\xi$  and  $T_{\min}$ , feedback, and/or multiple distinct source populations.

We should expect that more complex model parameterizations will only have an easier time fitting the turning points, and thus a fit to the turning points alone may not enable one to constrain additional parameters. Use of a more complex parameterization may still be warranted, however, provided independent constraints on one or more of the model parameters, to be used as priors in the fit. However, if we do a “single-stage” fit, in which we fit a physical model directly to the data rather than using a computationally inexpensive intermediary to extract the turning points, we may find that a more complex model is required by the data. In order to justify the additional parameters rigorously, more advanced inference tools are required (e.g., MULTINEST, POLYCHORD; Feroz et al., 2009, Handley et al., 2015) to compute the Bayesian evidence.

To date, there has only been one paper on model selection for global 21-cm datasets (Harker, 2015a). This work investigated performed a simple null test, as well as a more complex fit testing the necessity of an emission signal. Computing the evidence is expensive enough that Harker (2015a) was limited to relatively low-dimensional spaces and simplistic signal models. In the future, such tests will be required in order to test whether or not more complex models are required by the data. This presents a unique and challenging problem for ongoing and upcoming experiments and their associated signal extraction pipelines.

## 4.6 Conclusions

This work represents the first attempt to forecast constraints on astrophysical parameters of interest from mock observations of the global 21-cm signal. There is clearly much still to be learned, even from synthetic datasets, about how observations in  $(\nu, \delta T_b)$  space translate to constraints on the properties of the IGM and/or the properties of high- $z$  galaxies. Assuming an idealized instrument, signal recovery consistent with the numbers quoted in Table 4.1, and the validity of our four-parameter model for the global 21-cm signal, we find that:

- (1) Constraints on the turning points constrain the parameters of a simple 4 parameter model well (to  $\sim 0.2$  dex each, on average), with factor of  $\sim 2$  improvements within reach of experiments viewing multiple sky regions and employing more complex foreground parameterizations (Figure 4.7). Such measurements would simultaneously constrain the ionization and thermal state of the IGM (Figures 4.5-4.6), perhaps most notably providing strong evidence for the beginning of the EoR at  $z \sim 12$ .
- (2) Our fiducial realization of the signal is inconsistent with star-formation in halos with virial temperatures below  $\sim 10^{3.5}$  K at the  $2\text{-}\sigma$  level for the most pessimistic signal extraction scenario we consider. Such constraints are enabled in large part by a broad-band measurement of the signal, since  $T_{\min}$  affects all three turning points in the  $\sim 40 - 120$  MHz interval (Figures 4.1, 4.2, and 4.7).
- (3) In the simplest case, in which all model parameters are assumed to be constant in time, we can provide limits on both the escape fraction and the stellar IMF, primarily ruling out scenarios in which UV photons originate in extreme environments with very top-heavy IMFs or very high escape fractions (Figure 4.8).
- (4) Our constraints on X-ray sources are comparable to those achieved at  $z \lesssim 4$  via stacking and the cosmic X-ray background, though at  $z \sim 20$  to which the aforementioned techniques are insensitive (Figure 4.9). In the absence of independent information, this constraint requires an assumption about the star formation efficiency and X-ray SED of galaxies.
- (5) With only a subset of the turning points, constraints on our reference model are considerably worse

(Figures 4.10 and 4.11). The lowest frequency features (turning points B and C) hold the most power to constrain  $T_{\min}$ , which will make it difficult to constrain  $T_{\min}$  and  $\xi_{\text{ion}}$  with observations confined to the highest frequencies. Isolated detection of the absorption feature is the most valuable single-point measurement, as it leads to confidence contours which close over the prior space, except in the case of  $\xi_{\text{ion}}$ .

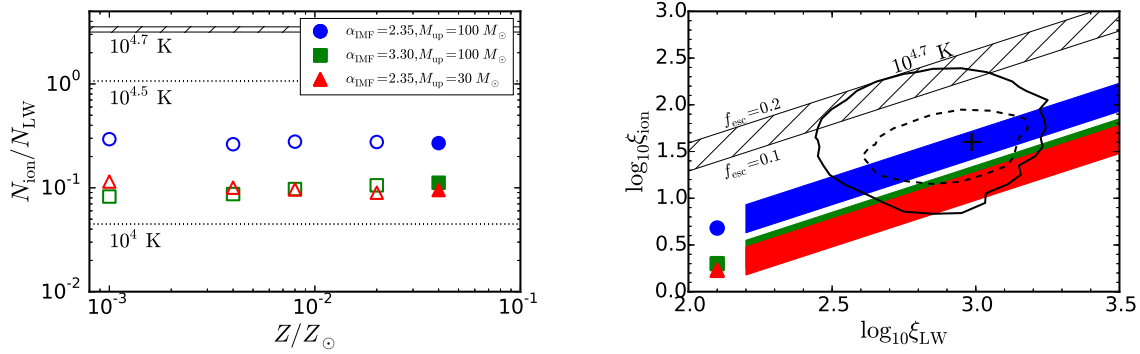


Figure 4.8 *Left*: Ratio of yields in the ionizing ( $h\nu > 13.6$  eV) and LW ( $10.2 \leq h\nu/\text{eV} \leq 13.6$ ) bands per stellar baryon as a function of metallicity and stellar IMF. Symbols represent model SEDs generated with STARBURST99 (those shown in Figures 1, 3, and 5 of Leitherer et al., 1999), while the horizontal lines show the values one obtains for pure blackbodies at 10,000, 30,000, and 50,000 K from bottom to top. The filled symbols are investigated in more detail in the right panel. *Right*: Constraints on the stellar population and the escape fraction of ionizing radiation. The solid contour is the  $2\text{-}\sigma$  constraint on our reference model, i.e., identical to the green area of panel (e) in Figure 4.7, while dashed contours correspond to turning point constraints from EM2 (see Table 4.1), which has a tighter constraint on the emission maximum (turning point D). The blue, green, and red bands have the same value of  $N_{\text{ion}}/N_{\text{LW}}$  as the filled plot symbols in the left-hand panel, while the cross-hatched band instead adopts a pure 50,000 K blackbody spectrum for the stellar population. The width of each band corresponds to a factor of 2 change in the escape fraction,  $0.1 \leq f_{\text{esc}} \leq 0.2$ .

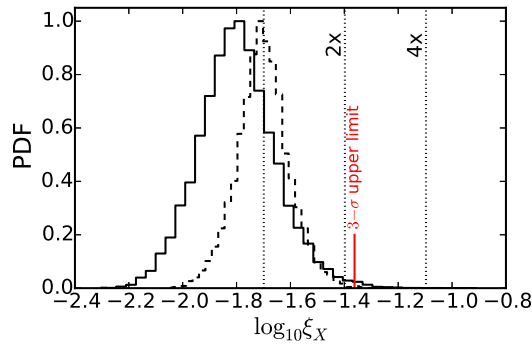


Figure 4.9 Constraints on sources of X-rays. The solid and dashed histograms are identical to the black and green PDFs shown in panel (i) of Figure 4.7, respectively, while dotted vertical lines denote values representative of  $2x$  and  $4x$  enhancements to the  $L_X$ -SFR relation, holding the star-formation efficiency constant at  $f_* = 0.1$ . For reference, we show the  $3\text{-}\sigma$  upper limit from extraction EM2 in red. Even if  $f_* = 0.01$ , we limit  $f_X < 20$ .

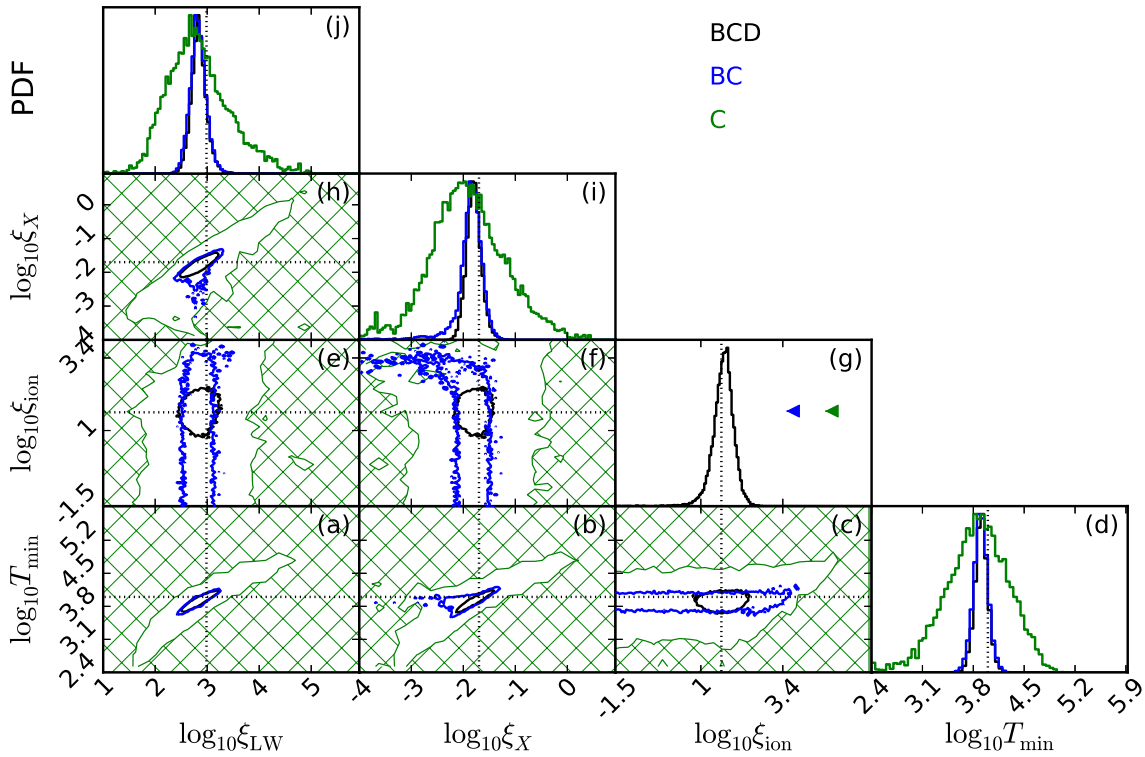


Figure 4.10 Constraints on the 4-parameter model, assuming the emission maximum is not detected. Solid black contours are the 95% confidence intervals of our reference fit to all three features. Blue contours are 95% confidence regions obtained when only turning points B and C are used in the fit, while the green hatched regions show areas of parameter space excluded at 95% confidence if only turning point C is used in the fit. When only upper or lower limits are available, we denote them with arrows in the marginalized 1-D PDFs.

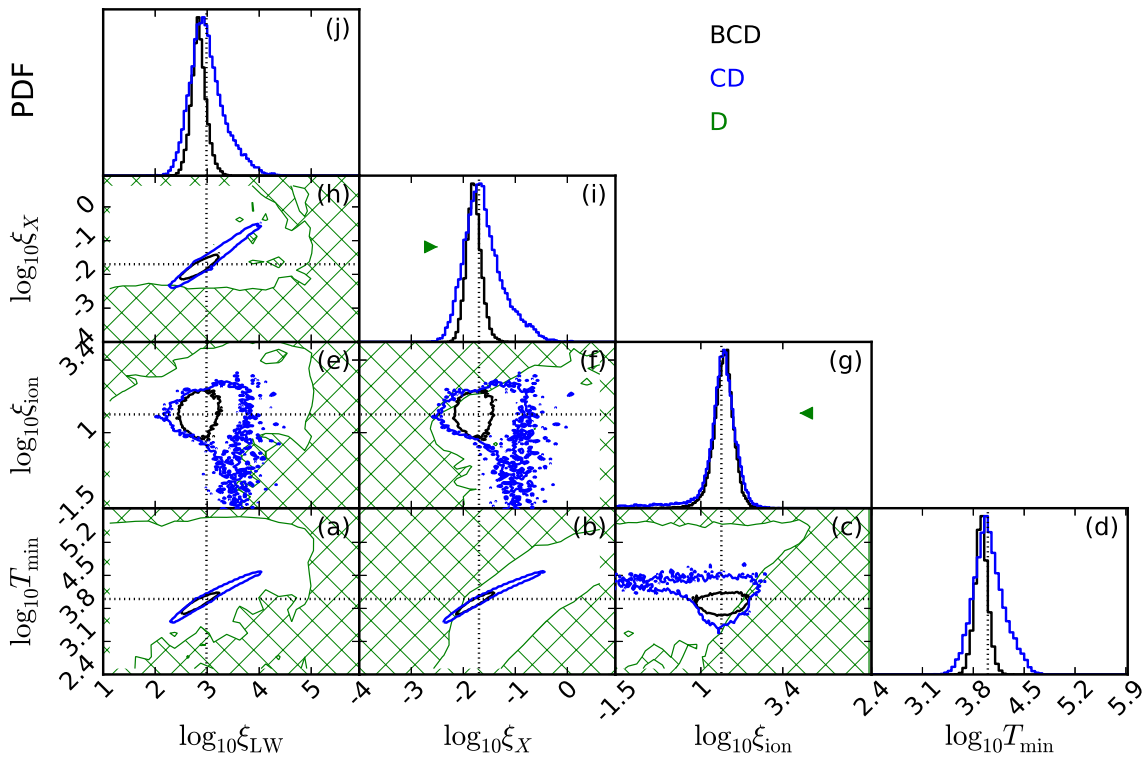


Figure 4.11 Constraints on the 4-parameter model, assuming turning point B is not detected. Solid black contours are the 95% confidence intervals of our reference fit to all three features. Blue contours are 95% confidence regions obtained when only turning points C and D are used in the fit, while the green hatched regions show areas of parameter space excluded at 95% confidence if only turning point D used in the fit. When only upper or lower limits are available, we denote them with arrows in the marginalized 1-D PDFs.

## Chapter 5

### Signatures of Accreting Black Holes at Redshifted 21-cm Wavelengths

Reproduced with permission of the RAS.

Reference:

“Decoding the X-ray Properties of Pre-Reionization Era Sources”

Mirocha, J. 2014, MNRAS, 443, 1211

#### 5.1 Context

Evolution in the X-ray luminosity – star formation rate ( $L_X$ -SFR) relation could provide the first evidence of a top-heavy stellar initial mass function in the early universe, as the abundance of high-mass stars and binary systems are both expected to increase with decreasing metallicity. The sky-averaged (global) 21-cm signal has the potential to test this prediction via constraints on the thermal history of the intergalactic medium, since X-rays can most easily escape galaxies and heat gas on large scales. A significant complication in the interpretation of upcoming 21-cm measurements is the unknown spectrum of accreting black holes (BHs) at high- $z$ , which depends on the mass of accreting objects and poorly constrained processes such as how accretion disk photons are processed by the disk atmosphere and host galaxy interstellar medium. Using a novel approach to solving the cosmological radiative transfer equation (RTE), we show that reasonable changes in the characteristic BH mass affects the amplitude of the 21-cm signal’s minimum at the  $\sim 10 - 20$  mK level — comparable to errors induced by commonly used approximations to the RTE — while modifications to the intrinsic disk spectrum due to Compton scattering (bound-free absorption) can shift the position of the minimum of the global signal by  $\Delta z \approx 0.5$  ( $\Delta z \approx 2$ ), and modify its amplitude by

up to  $\approx 10$  mK ( $\approx 50$  mK) for a given accretion history. Such deviations are larger than the uncertainties expected of current global 21-cm signal extraction algorithms, and could easily be confused with evolution in the  $L_X$ -SFR relation.

## 5.2 Introduction

In this work, we focus on the minimum of the global 21-cm signal and how its position could be used to probe the properties of accreting BHs in the early universe. The 21-cm minimum is well known as an indicator of heating (e.g., Furlanetto, 2006, Pritchard and Furlanetto, 2007, Mirabel et al., 2011), and from its position one can obtain model-independent limits on the instantaneous heating rate density and cumulative heating in the IGM over time (Mirocha et al., 2013). The 21-cm maximum is also a probe of the IGM thermal history (e.g., Ripamonti et al., 2008), though because it likely overlaps with the early stages of reionization, one must obtain an independent measurement on the ionization history in order to constrain the IGM temperature and heating rate density (Mirocha et al., 2013). In either case, extracting the properties of the heat sources themselves from the 21-cm signal is fraught with uncertainty since the number density of X-ray sources and their individual luminosities cannot be constrained independently by volume-averaged measures like the global 21-cm signal.

Despite such degeneracies among model parameters, accurate enough measurements could still rule out vast expanses of a currently wide-open parameter space. What remains could be visualized as a two-dimensional posterior probability distribution that characterizes the likelihood that any given pair of model parameters is correct, having marginalized over uncertainties in all additional parameters. Two likely axes in such analyses include (1) the characteristic mass (or virial temperature) of star-forming haloes and (2) the X-ray luminosity per unit star formation. However, a third, and often ignored axis that will manifest itself in such posterior probability spaces is the spectral energy distribution (SED) of X-ray sources. The reason for this expectation is simple: soft X-ray sources will heat the IGM more efficiently than hard X-ray sources (at fixed total X-ray luminosity) due to the strong frequency dependence of the bound-free absorption cross section ( $\sigma \propto \nu^{-3}$  approximately).

High-mass X-ray binaries (HMXBs) are often assumed to be the dominant source of X-rays in models

of high- $z$  galaxies. This choice is motivated by X-ray observations of nearby star-forming galaxies (see review by Fabbiano, 2006), as well as theoretical models of stellar evolution, which predict the formation of more massive stellar remnants and more binaries in metal-poor environments (e.g., Belczynski et al., 2008, Linden et al., 2010, Mapelli et al., 2010). Indeed, observations of star-forming galaxies are consistent with a boost in high-mass X-ray binary populations (per unit SFR) in galaxies out to  $z \sim 4 - 6$  (Basu-Zych et al., 2013, Kaaret, 2014), as is the unresolved fraction of the cosmic X-ray background (Dijkstra et al., 2012). Though direct constraints on the  $z \gtrsim 4$  population are weak, local analogs of high- $z$  galaxies exhibit a factor of  $\sim 10$  enhancement in the normalization of the X-ray luminosity function (XLF) in metal-poor galaxies relative to galaxies with  $\sim$  solar metallicity (e.g. Kaaret et al., 2011, Prestwich et al., 2013, Brorby et al., 2014).

Even if HMXBs are the dominant sources of X-rays in the early universe, there are various remaining uncertainties that may affect the global 21-cm signal and inferences drawn from the position of its minimum. Our focus is on modifications of the 21-cm signal brought about by variation in the characteristic mass of accreting objects and the reprocessing of their intrinsic emission spectrum by intervening material. Theoretical investigations of this sort can provide vital information to upcoming 21-cm experiments that seek to detect the absorption trough, such as the Dark Ages Radio Explorer (DARE; Burns et al., 2012), the Large Aperature Experiment to Detect the Dark Ages (LEDA; Greenhill and Bernardi, 2012), and the SCI-HI experiment (Voytek et al., 2014). For instance, how accurately must the 21-cm absorption trough be measured in order to distinguish models for the first X-ray sources?

The challenge for such studies is solving the cosmological radiative transfer equation (RTE) in a way that 1) accurately couples the radiation field from sources to the thermal and ionization state of the IGM, and 2) does so quickly enough that a large volume of parameter space may be surveyed. Recent studies have taken the first steps toward this goal by identifying SEDs likely to be representative of high- $z$  sources (e.g., Power et al., 2013). Some have applied semi-numeric schemes to predict how these SEDs contribute to the ionizing background (Power et al., 2013, Fragos et al., 2013), while others have studied the influence of realistic X-ray SEDs on the sky-averaged 21-cm signal and the 21-cm power spectrum (Ripamonti et al., 2008, Fialkov et al., 2014). Our focus is complementary: rather than calculating the ionizing background

strength or 21-cm signal that arise using “best guess” inputs for the SED of X-ray sources, we quantify how reasonable deviations from best guess SEDs can complicate inferences drawn from the signal.

The outline of this paper is as follows. In Section 2, we introduce our framework for cosmological radiative transfer and the global 21-cm signal. In Section 3, we describe our implementation of the Haardt and Madau (1996) method for discretizing the RTE and test its capabilities. In Section 4, we use this scheme to investigate the impact of SED variations on the global 21-cm signal. Discussion and conclusions are in Sections 5 and 6, respectively. We adopt WMAP7+BAO+SNIa cosmological parameters ( $\Omega_{\Lambda,0} = 0.728$ ,  $\Omega_{b,0} = 0.044$ ,  $H_0 = 70.2 \text{ km s}^{-1} \text{ Mpc}^{-1}$ ,  $\sigma_8 = 0.807$ ,  $n = 0.96$ ) throughout (Komatsu et al., 2011).

### 5.3 Theoretical Framework

As in Furlanetto (2006), we divide the IGM into two components: 1) the “bulk IGM,” which is mostly neutral and thus capable of producing a 21-cm signature, and 2) HII regions, which are fully ionized and thus dark at redshifted 21-cm wavelengths. This approach is expected to break down in the late stages of reionization when the distinction between HII regions and the “neutral” IGM becomes less clear. However, our focus in this paper is on the pre-reionization era so we expect this formalism to be reasonably accurate.

There are three key steps one must take in order to generate a synthetic global 21-cm signal within this framework. Starting from a model for the volume-averaged emissivity of astrophysical sources, which we denote as  $\epsilon_v(z)$  or  $\hat{\epsilon}_v(z)$ , further subdivided into a bolometric luminosity density (as a function of redshift) and SED (could also evolve with redshift in general), one must

- (1) Determine the mean radiation background pervading the space between galaxies (the so-called “metagalactic” radiation background), including the effects of geometrical dilution, redshifting, and bound-free absorption by neutral gas in the IGM. We denote this angle-averaged background radiation intensity as  $J_v$  or  $\hat{J}_v$ .
- (2) Once the background intensity is in hand, compute the ionization rate density,  $\Gamma_{\text{HI}}$ , and heating rate density,  $\epsilon_X$ , in the bulk IGM.
- (3) Given the ionization and heating rate densities, we can then solve for the rate of change in the

ionized fraction,  $x_e$ , and temperature,  $T_K$ , of the bulk IGM gas. The rate of change in the volume filling fraction of HII regions,  $x_i$ , is related more simply to the rate of baryonic collapse in haloes above a fixed virial temperature,  $T_{\min}$ , at the redshift of interest.

Once the thermal and ionization state of the IGM and the background intensity at the Ly- $\alpha$  resonance are known, a 21-cm signal can be computed. In this section, we will go through each of these steps in turn.

### 5.3.1 Astrophysical Models

We assume throughout that the volume-averaged emissivity is proportional to the rate of collapse,  $\hat{\epsilon}_v(z) \propto df_{\text{coll}}/dt$ , where

$$f_{\text{coll}} = \rho_m^{-1}(z) \int_{m_{\min}}^{\infty} mn(m)dm \quad (5.1)$$

is the fraction of gas in collapsed haloes more massive than  $m_{\min}$ . Here,  $\rho_m(z)$  is the mean co-moving mass density of the universe and  $n(m)dm$  is the co-moving number density of haloes with masses in the range  $(m, m+dm)$ . We compute  $n(m)$  using the `hmf-calc` code (Murray et al., 2013a), which depends on the *Code for Anisotropies in the Microwave Background* (CAMB; Lewis et al., 2000). We choose a fixed minimum virial temperature  $T_{\min} \geq 10^4$  K corresponding to the atomic cooling threshold (Eq. 26; Barkana and Loeb, 2001), which imposes redshift evolution in  $m_{\min}$ .

Our model for the emissivity is then

$$\epsilon_v(z) = \bar{\rho}_b^0 c_i f_i \frac{df_{\text{coll}}}{dt} I_v, \quad (5.2)$$

where  $\bar{\rho}_b^0$  is the mean baryon density today,  $c_i$  is a physically (or observationally) motivated normalization factor that converts baryonic collapse into energy output in some emission band  $i$  (e.g., Ly- $\alpha$ , soft UV, X-ray), while  $f_i$  is a free parameter introduced to signify uncertainty in how  $c_i$  evolves with redshift. The parameter  $I_v$  represents the SED of astrophysical sources, and is normalized such that  $\int I_v d\nu = 1$ . We postpone a more detailed discussion of our choices for  $c_i$ ,  $I_v$ , and what we mean by ‘‘astrophysical sources’’ to Section 5.5.

### 5.3.2 Cosmological Radiative Transfer

Given the volume-averaged emissivity,  $\epsilon_{\nu}$ , the next step in computing the global 21-cm signal is to obtain the angle-averaged background intensity,  $J_{\nu}$ . To do so, one must solve the cosmological RTE,

$$\left( \frac{\partial}{\partial t} - \nu H(z) \frac{\partial}{\partial \nu} \right) J_{\nu}(z) + 3H(z)J_{\nu}(z) = -c\alpha_{\nu}J_{\nu}(z) + \frac{c}{4\pi}\epsilon_{\nu}(z)(1+z)^3 \quad (5.3)$$

where  $H$  is the Hubble parameter, which we take to be  $H(z) \approx H_0\Omega_{m,0}(1+z)^{3/2}$  as is appropriate in the high- $z$  matter-dominated universe, and  $c$  is the speed of light. This equation treats the IGM as an isotropic source and sink of radiation, parameterized by the co-moving volume emissivity,  $\epsilon_{\nu}$  (here in units of  $\text{erg s}^{-1} \text{Hz}^{-1} \text{cMpc}^{-3}$ , where “cMpc” is short for “co-moving Mpc”), and the absorption coefficient,  $\alpha_{\nu}$ , which is related to the optical depth via  $d\tau_{\nu} = \alpha_{\nu}ds$ , where  $ds$  is a path length. The solution is cleanly expressed if we write the flux and emissivity in units of photon number (which we denote with “hats,” i.e.,  $[\hat{J}_{\nu}] = \text{s}^{-1} \text{cm}^{-2} \text{Hz}^{-1} \text{sr}^{-1}$  and  $[\hat{\epsilon}_{\nu}] = \text{s}^{-1} \text{Hz}^{-1} \text{cMpc}^{-3}$ ),

$$\hat{J}_{\nu}(z) = \frac{c}{4\pi}(1+z)^2 \int_z^{z_f} \frac{\hat{\epsilon}_{\nu'}(z')}{H(z')} e^{-\bar{\tau}_{\nu}} dz'. \quad (5.4)$$

The “first light redshift” when astrophysical sources first turn on is denoted by  $z_f$ , while the emission frequency,  $\nu'$ , of a photon emitted at redshift  $z'$  and observed at frequency  $\nu$  and redshift  $z$  is

$$\nu' = \nu \left( \frac{1+z'}{1+z} \right). \quad (5.5)$$

The optical depth is a sum over absorbing species,

$$\bar{\tau}_{\nu}(z, z') = \sum_j \int_z^{z'} n_j(z'') \sigma_{j,\nu''} \frac{dl}{dz''} dz'' \quad (5.6)$$

where  $dl/dz = c/H(z)/(1+z)$  is the proper cosmological line element, and  $\sigma_{j,\nu}$  is the bound-free absorption cross section of species  $j = \text{HI}, \text{HeI}, \text{HeII}$  with number density  $n_j$ . We use the fits of Verner and Ferland (1996) to compute  $\sigma_{j,\nu}$  unless stated otherwise, assume the ionized fraction of hydrogen and singly ionized helium are equal (i.e.,  $x_{\text{H II}} = x_{\text{He II}}$ ), and neglect HeII entirely (i.e.,  $x_{\text{He III}} = 0$ ). We will revisit this helium approximation in Section 5.6.

The Ly- $\alpha$  background intensity, which determines the strength of Wouthuysen-Field coupling (Wouthuysen, 1952, Field, 1958), is computed analogously via

$$\hat{J}_\alpha(z) = \frac{c}{4\pi} (1+z)^2 \sum_{n=2}^{n_{\max}} f_{\text{rec}}^{(n)} \int_z^{z_{\max}^{(n)}} \frac{\hat{\epsilon}_{\nu'}(z')}{H(z')} dz' \quad (5.7)$$

where  $f_{\text{rec}}^{(n)}$  is the ‘‘recycling fraction,’’ that is, the fraction of photons that redshift into a Ly- $n$  resonance that ultimately cascade through the Ly- $\alpha$  resonance (Pritchard and Furlanetto, 2006). We truncate the sum over Ly- $n$  levels at  $n_{\max} = 23$  as in Barkana and Loeb (2005b), and neglect absorption by intergalactic  $H_2$ . The upper bound of the definite integral,

$$1 + z_{\max}^{(n)} = (1+z) \frac{[1 - (n+1)^{-2}]}{1 - n^{-2}}, \quad (5.8)$$

is set by the horizon of Ly- $n$  photons – a photon redshifting through the Ly- $n$  resonance at  $z$  could only have been emitted at  $z' < z_{\max}^{(n)}$ , since emission at slightly higher redshift would mean the photon redshifted through the Ly( $n+1$ ) resonance.

Our code can be used to calculate the full ‘‘sawtooth’’ modulation of the soft UV background (Haiman et al., 1997) though we ignore such effects in this work given that our focus is on X-ray heating. Preservation of the background spectrum in the Lyman-Werner band and at even lower photon energies is crucial for studies of feedback, but because we have made no attempt to model  $H_2$  photo-dissociation or  $H^-$  photo-detachment, we neglect a detailed treatment of radiative transfer at energies below  $h\nu = 13.6$  eV and instead assume a flat UV spectrum between Ly- $\alpha$  and the Lyman-limit and ‘‘instantaneous’’ emission only, such that the Ly- $\alpha$  background at any redshift is proportional to the Ly- $\alpha$  emissivity,  $\hat{\epsilon}_\alpha$ , at that redshift. Similarly, the growth of HII regions is governed by the instantaneous ionizing photon luminosity, though more general solutions would self-consistently include a soft UV background that arises during the EoR due to rest-frame X-ray emission from much higher redshifts.

### 5.3.3 Ionization & Heating Rates

With the background radiation intensity,  $J_\nu$ , in hand, one can compute the ionization and heating this background causes in the bulk IGM. To calculate the ionization rate density, we integrate the background

intensity over frequency,

$$\Gamma_{\text{HI}}(z) = 4\pi n_{\text{H}}(z) \int_{v_{\text{min}}}^{v_{\text{max}}} \widehat{J}_v \sigma_{v,\text{HI}} dv, \quad (5.9)$$

where  $n_{\text{H}} = \bar{n}_{\text{H}}^0 (1+z)^3$  and  $\bar{n}_{\text{H}}^0$  is the number density of hydrogen atoms today. The ionization rate in the bulk IGM due to fast secondary electrons (e.g., Shull and van Steenberg, 1985, Furlanetto and Johnson Stoever, 2010) is computed similarly,

$$\gamma_{\text{HI}}(z) = 4\pi \sum_j n_j \int_{v_{\text{min}}}^{v_{\text{max}}} f_{\text{ion}} \widehat{J}_v \sigma_{v,j}(hv - hv_j) \frac{dv}{hv}, \quad (5.10)$$

and analogously, the heating rate density,

$$\epsilon_X(z) = 4\pi \sum_j n_j \int_{v_{\text{min}}}^{v_{\text{max}}} f_{\text{heat}} \widehat{J}_v \sigma_{v,j}(hv - hv_j) dv, \quad (5.11)$$

where  $hv_j$  is the ionization threshold energy for species  $j$ , with number density  $n_j$ , and  $v_{\text{min}}$  and  $v_{\text{max}}$  are the minimum and maximum frequency at which sources emit, respectively.  $f_{\text{ion}}$  and  $f_{\text{heat}}$  are the fractions of photo-electron energy deposited as further hydrogen ionization and heat, respectively, which we compute using the tables of Furlanetto and Johnson Stoever (2010) unless otherwise stated.

### 5.3.4 Global 21-cm Signal

Finally, given the ionization and heating rates,  $\Gamma_{\text{HI}}$ ,  $\gamma_{\text{HI}}$ , and  $\epsilon_X$ , we evolve the ionized fraction in the bulk IGM via

$$\frac{dx_e}{dt} = (\Gamma_{\text{HI}} + \gamma_{\text{HI}})(1 - x_e) - \alpha_{\text{B}} n_e x_e \quad (5.12)$$

and the volume filling factor of HII regions,  $x_i$ , via

$$\frac{dx_i}{dt} = f_* f_{\text{esc}} N_{\text{ion}} \bar{n}_{\text{b}}^0 \frac{df_{\text{coll}}}{dt} (1 - x_e) - \alpha_{\text{A}} C(z) n_e x_i \quad (5.13)$$

where  $\bar{n}_{\text{b}}^0$  is the baryon number density today,  $\alpha_{\text{A}}$  and  $\alpha_{\text{B}}$  are the case-A and case-B recombination coefficients, respectively,  $n_e = n_{\text{H II}} + n_{\text{He II}}$  is the proper number density of electrons,  $f_*$  is the star-formation efficiency,  $f_{\text{esc}}$  the fraction of ionizing photons that escape their host galaxies,  $N_{\text{ion}}$  the number of ionizing photons emitted per baryon in star formation, and  $C(z)$  is the clumping factor. We average the ionization state of the bulk IGM and the volume filling factor of HII regions to determine the mean ionized fraction,

i.e.,  $\bar{x}_i = x_i + (1 - x_i)x_e$ , which dictates the IGM optical depth (Eq. 5.6). We take  $C(z) = \text{constant} = 1$  for simplicity, as our focus is on the IGM thermal history, though our results are relatively insensitive to this choice as we terminate our calculations once the 21-cm signal reaches its emission peak, at which time the IGM is typically only  $\sim 10 - 20\%$  ionized.

The kinetic temperature of the bulk IGM is evolved via

$$\frac{3}{2} \frac{d}{dt} \left( \frac{k_B T_k n_{\text{tot}}}{\mu} \right) = \epsilon_X + \epsilon_{\text{comp}} - C \quad (5.14)$$

where  $\epsilon_{\text{comp}}$  is Compton heating rate density and  $C$  represents all cooling processes, which we take to include Hubble cooling, collisional ionization cooling, recombination cooling, and collisional excitation cooling using the formulae provided by Fukugita and Kawasaki (1994). Equations 5.12-6.5 are solved using the radiative transfer code<sup>1</sup> described in Mirocha et al. (2012).

Given  $T_K$ ,  $x_i$ ,  $x_e$ , and  $\hat{J}_\alpha$ , we can compute the sky-averaged 21-cm signal via the Equations presented in Chapter 1 and Appendix A.

## 5.4 The Code

The first step in our procedure for computing the global 21-cm signal – determining the background radiation intensity – is the most difficult. This step is often treated approximately, by truncating the integration limits in Equations 5.4 (for  $J_\nu$ ) and 5.11 (for  $\epsilon_X$ ) (e.g., Mesinger et al., 2011), or neglected entirely (e.g., Furlanetto, 2006) in the interest of speed. In what follows, we will show that doing so can lead to large errors in the global 21-cm signal, but more importantly, such approaches preclude detailed studies of SED effects.

Other recent works guide the reader through Equations 5.4 and 5.11, but give few details about how the equations are solved numerically (e.g., Pritchard and Furlanetto, 2007, Santos et al., 2010, Tanaka et al., 2012). Brute-force solutions to Equation 5.11 are accurate but extremely expensive, while seemingly innocuous discretization schemes introduced for speed can induce errors in the global 21-cm comparable in magnitude to several physical effects we consider in Section 5.5. The goal of this Section is to forestall con-

---

<sup>1</sup> <https://bitbucket.org/mirochaj/rt1d>

fusion about our methods, and to examine the computational expense of solving Equation 5.11 accurately.

#### 5.4.1 Discretizing the Radiative Transfer Equation

Obtaining precise solutions to Equation (5.4) is difficult because the integrand is expensive to calculate, mostly due to the optical depth term, which is itself an integral function (Equation 5.6). One approach that limits the number of times the integrand in Equation (5.4) must be evaluated is to discretize in redshift and frequency, and tabulate the optical depth *a-priori*. Care must be taken, however, as under-sampling the optical depth can lead to large errors in the background radiation intensity. This technique also requires one to assume an ionization history *a-priori*,  $\bar{x}_i(z)$ , which we take to be  $\bar{x}_i(z) = \text{constant} = 0$  over the redshift interval  $10 \leq z \leq 40$ . We defer a detailed discussion of this assumption to Section 5.6.

The consequences of under-sampling the optical depth are shown in Figure 5.1, which shows the X-ray background spectrum at  $z = 20$  for a population of  $10 M_\odot$  BHs with multi-color disk (MCD) spectra (Mitsuda et al., 1984) and our default set of parameters, which will be described in more detail in Section 5.5 (summarized in Table 5.1). Soft X-rays are absorbed over small redshift intervals – in some cases over intervals smaller than those sampled in the optical depth table – which leads to overestimates of the soft X-ray background intensity. Overestimating the soft X-ray background intensity can lead to significant errors in the resulting heating since soft X-rays are most readily absorbed by the IGM (recall  $\sigma_v \propto v^{-3}$  approximately). For a redshift grid with points linearly spaced by an amount  $\Delta z = \{0.4, 0.2, 0.1, 0.05\}$ , the errors in  $J_\nu$  as shown in Figure 5.1 correspond to relative errors in the heating rate density,  $\epsilon_X$ , of  $\{1.1, 0.44, 0.15, 0.04\}$ . Errors in  $\epsilon_X$  due to frequency sampling (128 used points here) are negligible (relative error  $< 10^{-4}$ ).

To prevent the errors in  $\epsilon_X$  associated with under-sampling  $\bar{\tau}_\nu$ , we must understand how far X-rays of various energies travel before being absorbed. We estimate a characteristic differential redshift element over which photons are absorbed by assuming a fully neutral medium, and approximate bound-free photoionization cross-sections ( $\sigma \propto v^{-3}$ ), in which case the optical depth (Eq. 5.6) can be written analytically

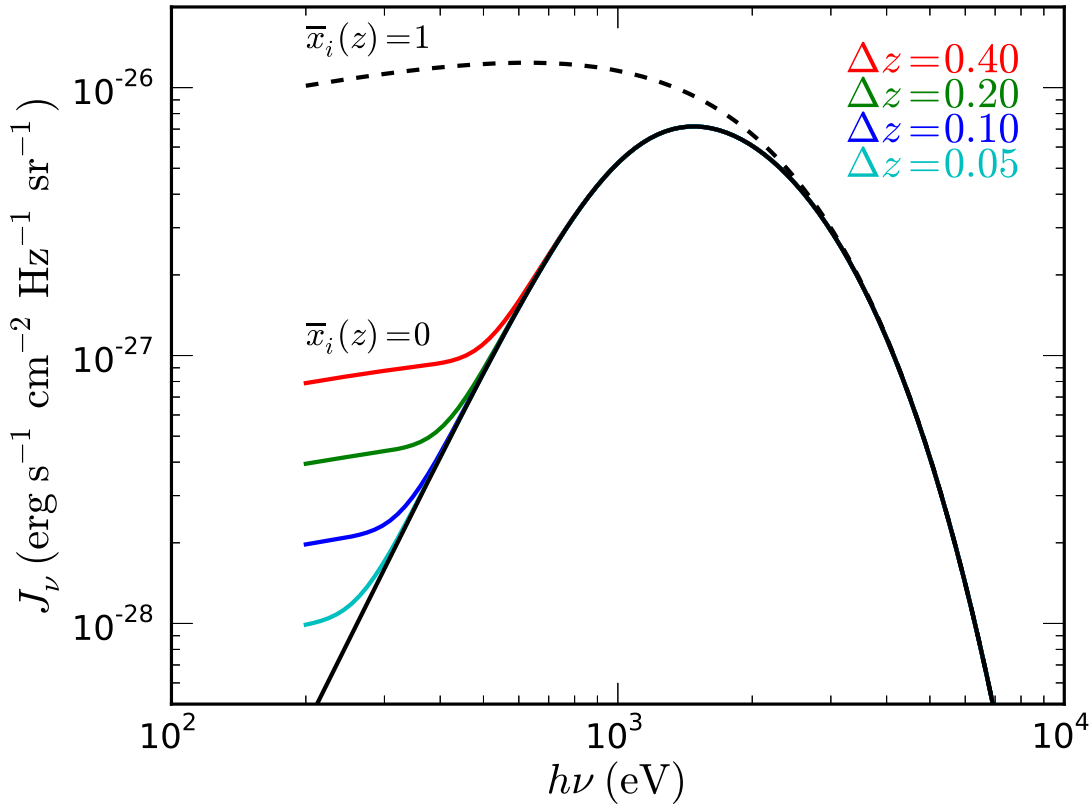


Figure 5.1 X-ray background intensity,  $J_\nu$ , at  $z = 20$  assuming a population of  $10 M_\odot$  BHs. The IGM optical depth,  $\bar{\tau}_\nu$ , is sampled at 128 logarithmically spaced frequencies between 0.2 and 30 keV, and linearly in redshift by  $\Delta z = 0.4$  (red), 0.2 (green), 0.1 (blue), and 0.05 (cyan). Poor redshift resolution always leads to overestimates of the background intensity at soft X-ray energies ( $h\nu \lesssim 0.5$  keV) since the integrand is a rapidly evolving function of redshift. The solid black line is the full numerical solution obtained by integrating Equation 5.4 with a Gaussian quadrature technique, and the dashed black line is the same calculation assuming the optically thin  $\bar{x}_i(z) = \text{constant} = 1$  limit as opposed to  $\bar{x}_i(z) = \text{constant} = 0$ . In order to prevent errors in  $J_\nu$  at all energies  $h\nu \geq 0.2$  keV, the redshift dimensions of  $\bar{\tau}_\nu$  must be sampled at better than  $\Delta z = 0.05$  resolution.

as

$$\bar{\tau}_\nu(z, z') \simeq \left(\frac{\mu}{\nu}\right)^3 (1+z)^{3/2} \left[1 - \left(\frac{1+z}{1+z'}\right)^{3/2}\right], \quad (5.15)$$

where

$$\mu^3 \equiv \frac{2}{3} \frac{\bar{n}_\text{H}^0 \sigma_0 c}{H_0 \sqrt{\Omega_{m,0}}} (\nu_\text{HI}^3 + y \nu_\text{HeI}^3). \quad (5.16)$$

Here,  $\sigma_0$  is the cross-section at the hydrogen ionization threshold,  $h\nu_\text{HI}$  and  $h\nu_\text{HeI}$  are the ionization threshold energies for hydrogen and helium, respectively,  $y$  is the primordial helium abundance by number,  $H_0$  the Hubble parameter today, and  $\Omega_{m,0}$  the matter density relative to the critical density today.

The characteristic energy  $h\mu \simeq 366.5$  eV may be more familiar as it relates to the mean-free paths of photons in a uniform medium relative to the Hubble length, which we refer to as ‘‘Hubble photons,’’ with energy  $h\nu_\text{Hub}$ .

$$\begin{aligned} h\nu_\text{Hub} &\simeq h\mu \left[\frac{3}{2}\right]^{1/3} (1-x_i)^{1/3} (1+z)^{1/2} \\ &\simeq 1.5(1-x_i)^{1/3} \left(\frac{1+z}{10}\right)^{1/2} \text{ keV}. \end{aligned} \quad (5.17)$$

The characteristic differential redshift element of interest (which we refer to as the ‘‘bound-free horizon,’’ and denote  $\Delta z_{bf}$ ) can be derived by setting  $\tau_\nu(z, z') = 1$  and taking  $z' = z + \Delta z_{bf}$  in Equation 5.15. The result is

$$\Delta z_{bf} \simeq (1+z) \left\{ \left[ 1 - \left( \frac{\nu/\mu}{\sqrt{1+z}} \right)^3 \right]^{-2/3} - 1 \right\}. \quad (5.18)$$

That is, a photon with energy  $h\nu$  observed at redshift  $z$  has experienced an optical depth of 1 since its emission at redshift  $z + \Delta z_{bf}$  and energy  $h\nu[1 + \Delta z_{bf}/(1+z)]$ . Over the interval  $10 \lesssim z \lesssim 40$ , this works out to be  $0.1 \lesssim \Delta z_{bf} \lesssim 0.2$  assuming a photon with frequency  $\nu = \mu$ .

In order to accurately compute the flux (and thus heating), one must resolve this interval with at least a few points, which explains the convergence in Figure 5.1 once  $\Delta z \leq 0.1$  for  $h\nu \lesssim 350$  eV. We discretize logarithmically in redshift (for reasons that will become clear momentarily) following the procedure outlined in Appendix C of Haardt and Madau (1996), first defining

$$x \equiv 1+z, \quad (5.19)$$

which allows us to set up a logarithmic grid in  $x$ -space such that

$$R \equiv \frac{x_{l+1}}{x_l} = \text{constant} \quad (5.20)$$

where  $l = 0, 1, 2, \dots, n_z - 1$ . The corresponding grid in photon energy space is

$$h\nu_n = h\nu_{\min} R^{n-1}, \quad (5.21)$$

where  $h\nu_{\min}$  is the minimum photon energy we consider, and  $n = 1, 2, \dots, n_\nu$ . The number of frequency bins,  $n_\nu$ , can be determined iteratively in order to guarantee coverage out to some maximum emission energy,  $h\nu_{\max}$ .

The emission frequency,  $\nu_{n'}$  of a photon observed at frequency  $h\nu_n$  and redshift  $z_l$ , emitted at redshift  $z_m$  is then (i.e. a discretized form of Eq. 5.5)

$$\nu_{n'} = \nu_n \left( \frac{1 + z_m}{1 + z_l} \right) \quad (5.22)$$

meaning  $\nu_{n'}$  can be found in our frequency grid at index  $n' = n + m - l$ .

The advantage of this approach still may not be immediately obvious, but consider breaking the integral of Equation 5.4 into two pieces, an integral from  $z_l$  to  $z_{l+1}$ , and an integral from  $z_{l+1}$  to  $z_{n_z-1}$ . In this case, Equation 5.4 simplifies to

$$\hat{J}_{\nu_n}(z_l) = \frac{c}{4\pi} (1 + z_l)^2 \int_{z_l}^{z_{l+1}} \frac{\hat{\epsilon}_{\nu_{n'}}(z')}{H(z')} e^{-\bar{\tau}_{\nu_n}(z_l, z')} dz' + \left( \frac{1 + z_l}{1 + z_{l+1}} \right)^2 \hat{J}_{\nu_{n+1}}(z_{l+1}) e^{-\bar{\tau}_{\nu_n}(z_l, z_{l+1})}. \quad (5.23)$$

The first term accounts for “new” flux due to the integrated emission of sources at  $z_l \leq z \leq z_{l+1}$ , while the second term is the flux due to emission from all  $z > z_{l+1}$ , i.e., the background intensity at  $z_{l+1}$  corrected for geometrical dilution and attenuation between  $z_l$  and  $z_{l+1}$ .

Equation 5.23 tells us that by discretizing logarithmically in redshift and iterating from high redshift to low redshift we can keep a “running total” on the background intensity. In fact, we must never explicitly consider the case of  $m \neq l + 1$ , meaning Equation 5.22 is simply  $\nu_{n'} = R\nu_n = \nu_{n+1}$ . The computational cost of this algorithm is independent of redshift, since the flux at  $z_l$  only ever depends on quantities at  $z_l$  and  $z_{l+1}$ . Such is not the case for a brute-force integration of Equation 5.4, in which case the redshift interval increases with time. The logarithmic approach also limits memory consumption, since we need not tabulate the flux

or optical depth in 3-D — we only ever need to know the optical depth between redshifts  $z_l$  and  $z_{l+1}$  — in addition to the fact that we can discard the flux at  $z_{l+2}$ ,  $J_\nu(z_{l+2})$ , once we reach  $z_l$ . A linear discretization scheme would require 3-D optical depth tables with  $n_\nu n_z^2$  elements, which translates to tens of Gigabytes of memory for the requisite redshift resolution (to be discussed in the next subsection).

Finally, linear discretization schemes prevent one from keeping a “running total” on the background intensity, since the observed flux at redshift  $z_l$  and frequency  $\nu_n$  cannot (in general) be traced back to rest frame emission from redshifts  $z_{l'}$  or frequencies  $\nu_{n'}$  within the original redshift and frequency grids (over  $l$  and  $n$ ). The computational cost of performing the integral in Equation 5.4 over all redshifts  $z' > z$  is prohibitive, as noted by previous authors (e.g., Mesinger et al., 2011).

#### 5.4.2 Accuracy & Expense

The accuracy of this approach is shown in Figure 5.2 as a function of the number of redshift bins in the optical depth lookup table,  $n_z$ . Errors in the heating rate density (top), and cumulative heating (middle),  $\Delta \int \epsilon_X dt$ , drop below 0.1% at all  $10 \leq z \leq 40$  once  $n_z \gtrsim 4000$ , at which time errors in the position of the 21-cm minimum (bottom) are accurate to  $\sim 0.01\%$ . Given this result, all calculations reported in Section 5.5 take  $n_z = 4000$ . For reference, errors of order 0.1% correspond to  $\sim 0.1$  mK errors in the amplitude of the 21-cm minimum in our reference model, which we will soon find is much smaller than the changes induced by physical effects.

Many previous studies avoided the expense of Equation 5.4 by assuming that a constant fraction of the X-ray luminosity density is deposited in the IGM as heat (e.g., Furlanetto, 2006). A physically-motivated approximation is to assume that photons with short mean free paths (e.g., those that experience  $\bar{\tau}_\nu \leq 1$ ) are absorbed and contribute to heating, and all others do not (e.g., Mesinger et al., 2011). This sort of “step attenuation” model was recently found to hold fairly well in the context of a fluctuating X-ray background, albeit for a single set of model parameters (Mesinger and Furlanetto, 2009).

An analogous estimate for the heating caused by a uniform radiation background assumes that photons with mean free paths shorter than a Hubble length are absorbed, and all others are not. We define  $\xi_X$  as

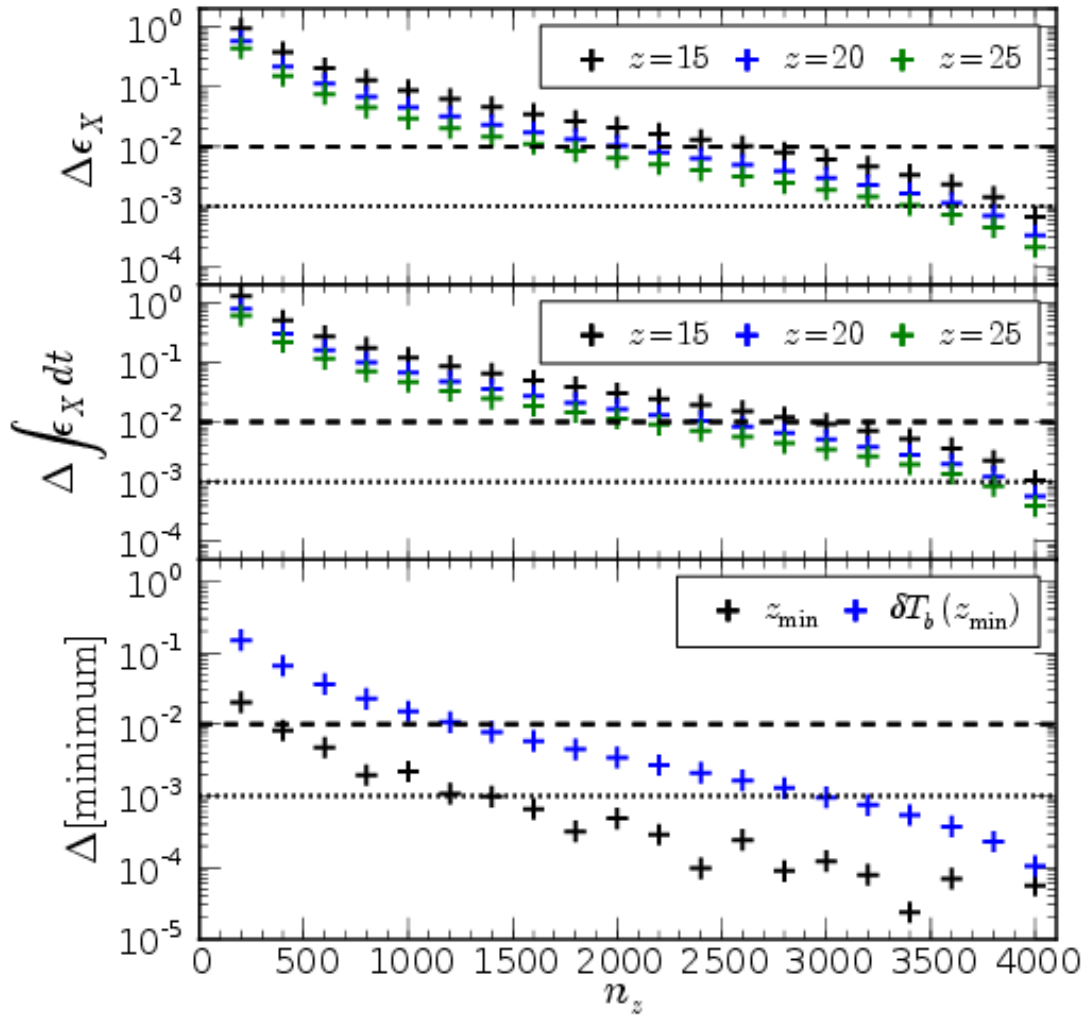


Figure 5.2 Accuracy of presented algorithm. *Top*: Relative error in the heating rate density,  $\epsilon_X$ , as a function of the number of redshift points,  $n_z$ , used to sample  $\bar{\tau}_\nu$ , as compared to a brute-force solution to Equation 5.11 using a double Gaussian quadrature integration scheme. *Middle*: Relative error in the cumulative heating as a function of  $n_z$ . *Bottom*: Relative error in the position of the 21-cm minimum, in redshift (black crosses) and amplitude (blue crosses). Dotted and dashed lines indicate 0.1% and 1% errors, respectively.

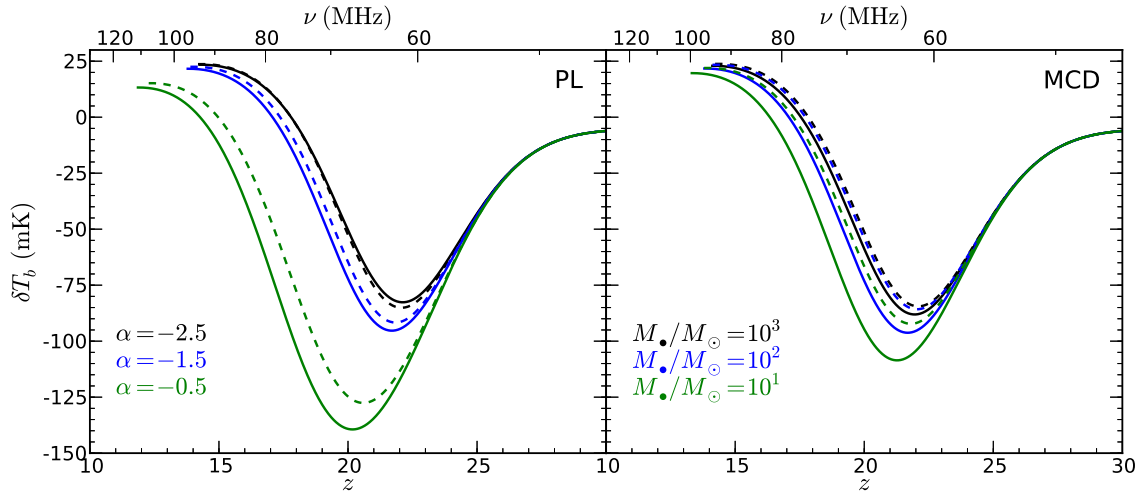


Figure 5.3 Testing the approximation of Equations 5.24 and 5.25. Dashed lines represent the approximate solutions, while solid lines represent the full solution for the global 21-cm signal using the procedure outlined in Section 5.4. *Left:* X-ray sources are assumed to have power-law (PL) SEDs with spectral index  $\alpha$ , extending from 0.2 to 30 keV. *Right:* X-ray sources are assumed to have multi-color disk (MCD) SEDs (Mitsuda et al., 1984). All sources have been normalized to have the same luminosity density above 0.2 keV ( $3.4 \times 10^{40} \text{ erg s}^{-1} (M_{\odot} \text{ yr}^{-1})^{-1}$ ), and all calculations are terminated once the emission peak ( $12 \lesssim z \lesssim 14$ ) has been reached. For the hardest sources of X-rays considered (left:  $\alpha = -0.5$ , right:  $M_{\bullet} = 10 M_{\odot}$ ), the global 21-cm minimum is in error by up to  $\sim 15$  mK in amplitude and  $\Delta z \simeq 0.5$  in position when Equation 5.24 is used to compute  $\epsilon_X$ .

the fraction of the bolometric luminosity density that is absorbed locally, which is given by

$$\xi_X(z) \approx \int_{\nu_{\min}}^{\nu_{\text{Hub}}} I_\nu d\nu \left( \int_{\nu_{\min}}^{\nu_{\max}} I_\nu d\nu \right)^{-1}, \quad (5.24)$$

where  $h\nu_{\text{Hub}}$  is given by Equation 5.17. There are approximate analytic solutions to the above equation for power-law sources (would be exact if not for the upper integration limit,  $\nu_{\text{Hub}}$ ), though  $\xi_X$  must be computed numerically for the MCD spectra we consider. We take  $h\nu_{\min} = 200$  eV and  $h\nu_{\max} = 30$  keV for the duration of this paper. The heating rate density associated with a population of objects described by  $\xi_X$  and  $\mathcal{L}_{\text{bol}}$  is

$$\epsilon_X(z) = \xi_X(z) \mathcal{L}_{\text{bol}}(z) f_{\text{heat}} \quad (5.25)$$

where  $f_{\text{heat}}$  is the fraction of the absorbed energy that is deposited as heat. Because there is no explicit dependence on photon energy in this approximation, we use the fitting formulae of Shull and van Steenberg (1985) to compute  $f_{\text{heat}}$ .

The consequences of using Equations 5.24 and 5.25 for the global 21-cm signal are illustrated in Figure 5.3. Steep power-law sources can be modeled quite well (signal accurate to 1-2 mK) using Equations 5.24 and 5.25 since a large fraction of the X-ray emission occurs at low energies. In contrast, heating by sources with increasingly flat (decreasing spectral index  $\alpha$ ) spectra is poorly modeled by Equations 5.24 and 5.25, inducing errors in the global 21-cm signal of order  $\sim 5$  mK ( $\alpha = -1.5$ ) and  $\sim 15$  mK ( $\alpha = -0.5$ ). The same trend holds for heating dominated by sources with a MCD spectrum, in which case harder spectra correspond to less massive BHs. We will see in the next section that these errors are comparable to the differences brought about by real changes in the SED of X-ray sources.

## 5.5 Accreting Black Holes in the Early Universe

Using the algorithm presented in the previous section, we now investigate the effects of varying four parameters that govern the SED of an accreting BH: (1) the mass of the BH,  $M_\bullet$ , which determines the characteristic temperature of an optically thick geometrically thin disk (Shakura and Sunyaev, 1973), (2) the fraction of disk photons that are up-scattered (Shapiro et al., 1976) by a hot electron corona,  $f_{\text{sc}}$ , (3)

the power-law index<sup>2</sup> of the resulting emission,  $\alpha$ , (using the SIMPL model; Steiner et al., 2009), and (4) the column density of neutral hydrogen that lies between the accreting system and the IGM,  $N_{\text{HI}}$ . Because we assume  $x_{\text{H II}} = x_{\text{He II}}$ , the absorbing column density actually has an optical depth of  $\tau_{\text{v}} = N_{\text{HI}} \sigma_{\text{v,HI}} (1 + y \sigma_{\text{v,HeI}} / \sigma_{\text{v,HI}})$ , where  $y$  is the primordial helium abundance by number, and  $\sigma_{\text{v}}$  is the bound-free absorption cross section for HI and HeI. A subset of the spectral models we consider are shown in Figure 5.4. Note that more efficient Comptonization (i.e., increasing  $f_{\text{sc}}$ ) and strong neutral absorption (increased  $N_{\text{HI}}$ ) act to harden the intrinsic disk spectrum (top panel), while increasing the characteristic mass of accreting BHs acts to soften the spectrum (bottom panel).

To compute the X-ray heating as a function of redshift,  $\epsilon_X(z)$ , we scale our SED of choice to a co-moving (bolometric) luminosity density assuming that a constant fraction of gas collapsing onto halos accretes onto BHs, i.e.,

$$\dot{\rho}_{\bullet}(z) = f_{\bullet} \bar{\rho}_{\text{b}}^0 \frac{df_{\text{coll}}(T_{\text{min}})}{dt}. \quad (5.26)$$

Assuming Eddington-limited accretion, we obtain a co-moving bolometric “accretion luminosity density,”

$$\mathcal{L}_{\text{acc}} = 6.3 \times 10^{40} \times \left( \frac{0.9}{\xi_{\text{acc}}} \right) \left( \frac{\dot{\rho}_{\bullet}(z)}{10^{-6} M_{\odot} \text{ yr}^{-1} \text{ cMpc}^{-3}} \right) \text{ erg s}^{-1} \text{ cMpc}^{-3}, \quad (5.27)$$

where

$$\xi_{\text{acc}} = \frac{1 - \eta}{\eta} f_{\text{edd}} \quad (5.28)$$

and  $\eta$  and  $f_{\text{edd}}$  are the radiative efficiency and Eddington ratio, respectively. To be precise,  $f_{\text{edd}}$  represents the product of the Eddington ratio and duty cycle, i.e., what fraction of the time X-ray sources are actively accreting, which are completely degenerate. This parameterization is very similar to that of Mirabel et al. (2011), though we do not explicitly treat the binary fraction, and our expression refers to the bolometric luminosity density rather than the 2-10 keV luminosity density. Our model for the co-moving X-ray emissivity is then

$$\hat{\epsilon}_{\text{v}}(z) = \mathcal{L}_{\text{acc}}(z) \frac{I_{\text{v}}}{h\nu}, \quad (5.29)$$

---

<sup>2</sup> We define the spectral index as  $L_{\nu} \propto \nu^{\alpha}$ , where  $L_{\nu}$  is a specific luminosity proportional to the *energy* of a photon with frequency  $\nu$ , per logarithmic frequency interval  $d\nu$ .

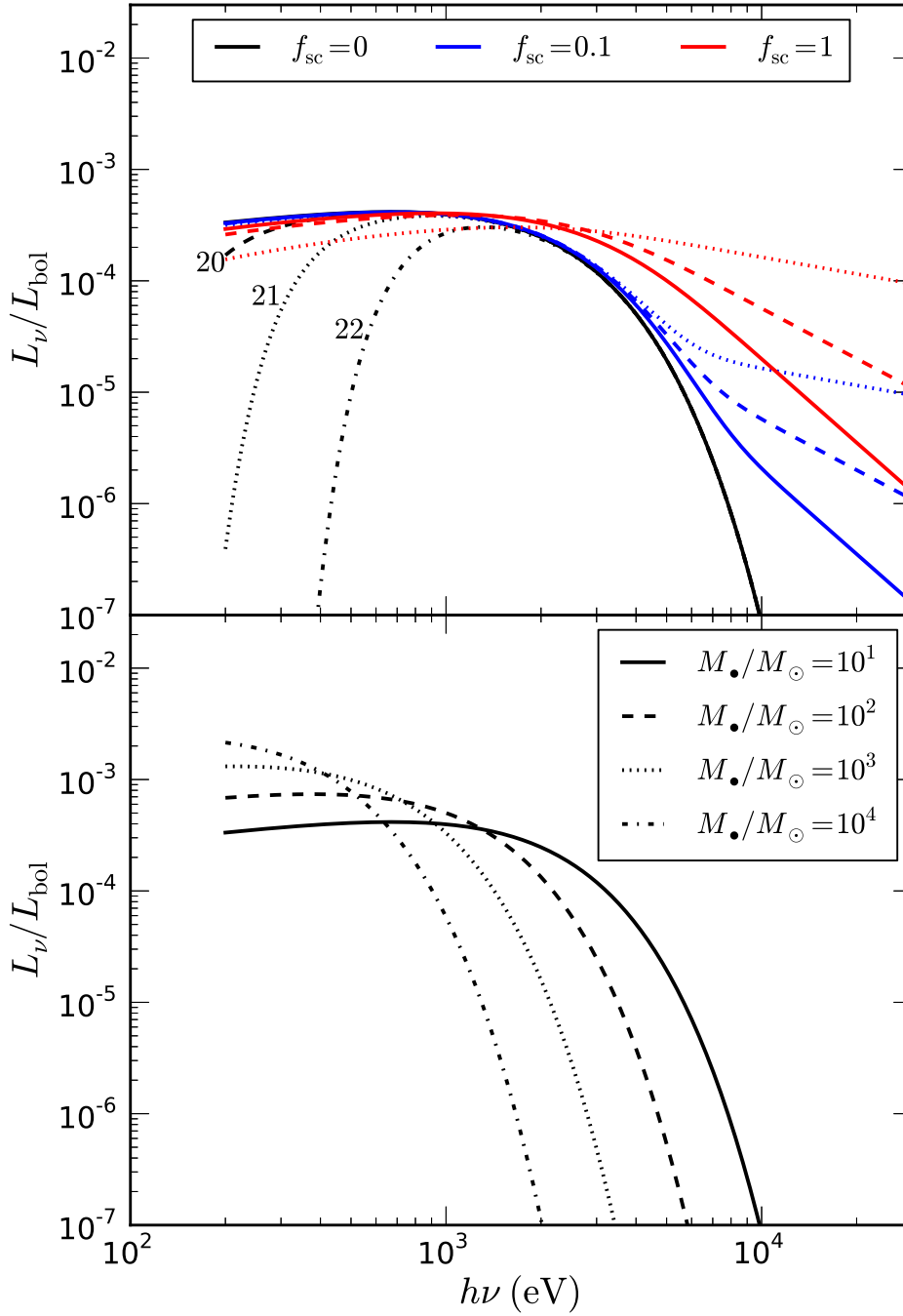


Figure 5.4 Subset of SEDs used in this work. *Top panel:* Assuming  $M_\bullet = 10 M_\odot$ , varying the fraction of disk photons scattered into the high energy power-law tail,  $f_{\text{sc}}$ , and the spectral index of the resulting high energy emission,  $\alpha$ , using the SIMPL model (Steiner et al., 2009). Solid, dashed, dotted, and dash-dotted black lines represent neutral absorption corresponding to  $N_{\text{H}1}/\text{cm}^{-2} = 0, 10^{20}, 10^{21},$  and  $10^{22}$ , respectively. Solid and dashed lines of different colors correspond to high energy emission with power-law indices of  $\alpha = -2.5$  and  $\alpha = -1.5$ , respectively, with the color indicating  $f_{\text{sc}}$  as shown in the legend. *Bottom panel:* Pure MCD SEDs for  $M_\bullet = 10 - 10^4 M_\odot$ , with no intrinsic absorption or Comptonization of the disk spectrum. The solid black line is our reference model, and is the same in both panels.

where  $I_\nu$  once again represents the SED of X-ray sources, and is normalized such that  $\int_0^\infty I_\nu d\nu = 1$ . Power-law sources must truncate the integration limits in this normalization integral so as to avoid divergence at low energies, though MCD models do not, since the soft X-ray portion of the spectrum is limited by the finite size of the accretion disk (which we take to be  $r_{\max} = 10^3 R_g$ , where  $R_g = GM_\bullet/c^2$ ).

It is common in the 21-cm literature to instead relate the co-moving X-ray luminosity density,  $L_X$ , to the star formation rate density,  $\dot{\rho}_*$ , as

$$L_X = c_X f_X \dot{\rho}_*(z), \quad (5.30)$$

where the normalization factor  $c_X$  is constrained by observations of nearby star forming galaxies (e.g., Grimm et al., 2003, Ranalli et al., 2003, Gilfanov et al., 2004), and  $f_X$  parameterizes our uncertainty in how the  $L_X - \text{SFR}$  relation evolves with redshift. The detection of a 21-cm signal consistent with  $f_X > 1$  could provide indirect evidence of a top-heavy stellar initial mass function (IMF) at high- $z$  since  $f_X$  encodes information about the abundance of high-mass stars and the binary fraction, both of which are expected to increase with decreasing metallicity.

However, assumptions about the SED of X-ray sources are built-in to the definition of  $f_X$ . The standard value of  $c_X = 3.4 \times 10^{40} \text{erg s}^{-1} (M_\odot \text{yr}^{-1})^{-1}$  (Furlanetto, 2006) is an extrapolation of the 2 – 10 keV  $L_X - \text{SFR}$  relation of Grimm et al. (2003), who found  $L_{2-10 \text{ keV}} = 6.7 \times 10^{39} \text{erg s}^{-1} (M_\odot \text{yr}^{-1})^{-1}$ , to all energies  $h\nu > 200 \text{ eV}$  assuming an  $\alpha = -1.5$  power-law spectrum. This means any inferences about the stellar IMF at high- $z$  drawn from constraints on  $f_X$  implicitly assume an  $\alpha = -1.5$  power-law spectrum at photon energies above 0.2 keV. Because our primary interest is in SED effects, we avoid the  $f_X$  parameterization and keep the normalization of the X-ray background (given by  $\dot{\rho}_\bullet/\xi_{\text{acc}}$ ) and its SED ( $I_\nu$ ) separate. We note that if one adopts a pure MCD spectrum (i.e.,  $f_{\text{sc}} = N_{\text{H I}} = 0$ ) for a  $10 M_\odot$  BH and set  $f_\bullet = 10^{-5}$  (as in our reference model), the normalization of Equation 5.27 corresponds to  $f_X \approx 2 \times 10^3$  assuming  $c_X = 2.61 \times 10^{39} \text{erg s}^{-1} (M_\odot \text{yr}^{-1})^{-1}$  (Mineo et al., 2012a). Despite this enhancement in the total X-ray luminosity density, our reference model produces an absorption trough at  $z \approx 22$  and  $\delta T_b \approx -100 \text{ mK}$ , similar to past work that assumed  $f_X = 1$ . This is a result of our choice for the reference spectrum, a multi-color disk, which is much harder than the  $\alpha = -1.5$  power law spectrum originally used to define  $f_X$ .

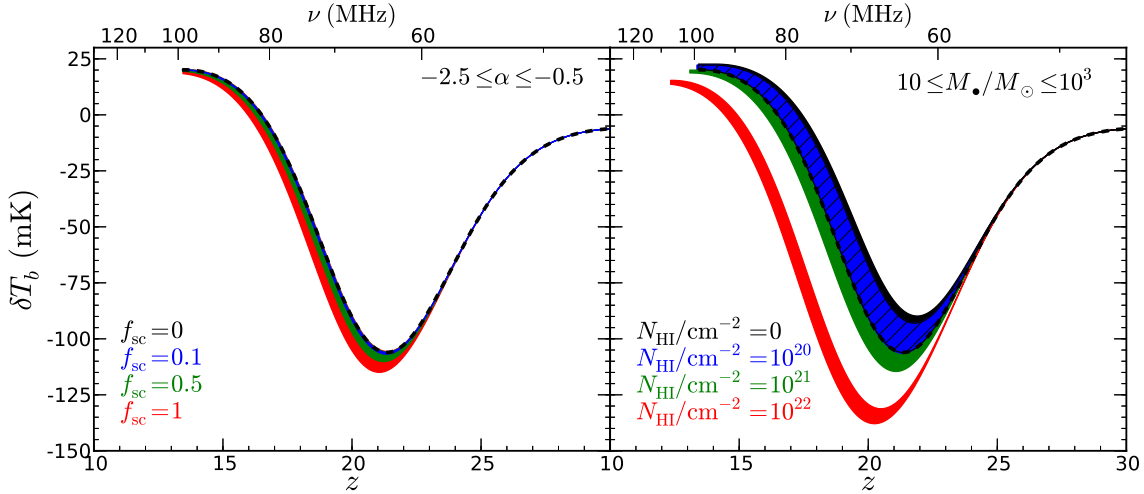


Figure 5.5 Evolution of the 21-cm brightness temperature for different BH SED models. *Left*: Effects of coronal physics, parameterized by the fraction of disk photons up-scattered by a hot electron corona,  $f_{\text{sc}}$ , and the resulting spectral index of up-scattered emission,  $\alpha$ , using the SIMPL Comptonization model of Steiner et al. (2009). The colors correspond to different values of  $f_{\text{sc}}$ , while the width of each band represents models with  $-2.5 \leq \alpha \leq -0.5$  (the upper edge of each band corresponds to the softest SED at fixed  $f_{\text{sc}}$ , in this case  $\alpha = -2.5$ ). *Right*: Effects of BH mass and neutral absorbing column. Colors correspond to  $N_{\text{HI}}$ , while the width of each band represents models with  $10 \leq M_{\bullet}/M_{\odot} \leq 10^3$  (the upper edge of each band corresponds to the softest SED at fixed  $N_{\text{HI}}$ , in this case  $M_{\bullet} = 10^3 M_{\odot}$ ). The dashed black line is our reference “pure MCD” model with  $M_{\bullet} = 10 M_{\odot}$ . The black and blue regions overlap considerably, indicating that absorbing columns of  $N_{\text{HI}} \gtrsim 10^{20} \text{ cm}^{-2}$  are required to harden the spectrum enough to modify the thermal history. Every realization of the signal here has the exact same ionization history, Ly- $\alpha$  background history, and BH accretion history. As in Figure 5.3, all calculations are terminated once the peak in emission is reached. Coronal physics influences the global 21-cm minimum at the  $\lesssim 10$  mK level, while  $M_{\bullet}$  is a 10-20 mK effect and  $N_{\text{HI}}$  is potentially a  $\sim 50$  mK effect.

Our main result is shown in Figure 5.5. The effects of the coronal physics parameters  $f_{\text{sc}}$  and  $\alpha$  are shown in the left panel, and only cause deviations from the reference model if  $f_{\text{sc}} > 0.1$  (for any  $-2.5 \leq \alpha \leq -0.5$ ). Increasing  $f_{\text{sc}}$  and decreasing  $\alpha$  act to harden the spectrum, leading to a delay in the onset of heating and thus deeper absorption feature. With a maximal value of  $f_{\text{sc}} = 1$  and hardest power-law SED of  $\alpha = -0.5$ , the absorption trough becomes deeper by  $\sim 10$  mK. In the right panel, we adopt  $f_{\text{sc}} = 0.1$  and  $\alpha = -1.5$ , and turn our attention to the characteristic mass of accreting BHs and the neutral absorbing column, varying each by a factor of 100, each of which has a more substantial impact individually on the 21-cm signal than  $f_{\text{sc}}$  and  $\alpha$ . The absorption trough varies in amplitude by up to  $\sim 50$  mK and in position by  $\Delta z \approx 2$  from the hardest SED ( $M_{\bullet} = 10 M_{\odot}$ ,  $N_{\text{H I}} = 10^{22} \text{ cm}^{-2}$ ) to softest SED ( $M_{\bullet} = 10^3 M_{\odot}$ ,  $N_{\text{H I}} = 0 \text{ cm}^{-2}$ ) we consider. The absorbing column only becomes important once  $N_{\text{H I}} \gtrsim 10^{20} \text{ cm}^{-2}$ .

Our study is by no means exhaustive. Table 5.1 lists parameters held constant for the calculations shown in Figure 5.5. Our choices for several parameters in Table 5.1 that directly influence the thermal history will be discussed in the next section. While several other parameters could be important in determining the locations of 21-cm features, for instance,  $N_{\text{ion}}$  is likely  $\gg 4000$  for Population III (PopIII) stars (e.g., Bromm et al., 2001, Schaerer, 2002, Tumlinson et al., 2003), we defer a more complete exploration of parameter space, and assessment of degeneracies between parameters, to future work.

## 5.6 Discussion

The findings of the previous section indicate that uncertainty in the SED of X-ray sources at high- $z$  could be a significant complication in the interpretation of upcoming 21-cm measurements. Details of Comptonization are a secondary effect in this study, though still at the level of measurement errors predicted by current signal extraction algorithms (likely  $\sim 10$  mK for the absorption trough; Harker et al., 2012). The characteristic mass of accreting BHs,  $M_{\bullet}$ , and the amount of absorption intrinsic to BH host galaxies, parameterized by a neutral hydrogen column density  $N_{\text{H I}}$ , influence the signal even more considerably. In this section, we examine these findings in the context of other recent studies and discuss how our methods and various assumptions could further influence our results.

Table 5.1. Parameter Space Explored

| Parameter        | Value      | Description   |
|------------------|------------|---|
| $hmf$            | PS         | Halo mass function  |
| $T_{\min}$       | $10^4$ K   | Min. virial temperature of star-forming haloes                  |
| $\mu$            | 0.61       | Mean molecular weight of collapsing gas                         |
| $f_*$            | $10^{-1}$  | Star formation efficiency                                       |
| $f_{\bullet}$    | $10^{-5}$  | Fraction of collapsing gas accreted onto BHs                    |
| $N_{LW}$         | 9690       | Photons per stellar baryon with $v_{\alpha} \leq v \leq v_{LL}$ |
| $N_{\text{ion}}$ | 4000       | Ionizing photons emitted per stellar baryon                     |
| $f_{\text{esc}}$ | 0.1        | Escape fraction   |
| $r_{\text{in}}$  | $6 R_g$    | Radius of inner edge of accretion disk                          |
| $r_{\text{max}}$ | $10^3 R_g$ | Max. radius of accretion disk                                   |
| $\eta$           | 0.1        | Radiative efficiency of accretion                               |
| $f_{\text{edd}}$ | 0.1        | Product of Eddington ratio and duty cycle                       |
| $h\nu_{\min}$    | 0.2 keV    | Softest photon considered                                       |
| $h\nu_{\max}$    | 30 keV     | Hardest photon considered                                       |

Note. — Parameters held constant in this work. Note that PS in the first row refers to the original analytic halo mass function derived by Press and Schechter (1974). Our reference model adopts this set of parameters and a pure MCD spectrum (i.e.,  $N_{\text{H1}} = f_{\text{sc}} = 0$ ) assuming a characteristic BH mass of  $M_{\bullet} = 10 M_{\odot}$ .

### 5.6.1 An Evolving IGM Optical Depth

Central to our approach to solving Equation 5.4 is the ability to tabulate the IGM optical depth (Eq. 5.6). This requires that we assume a model for the ionization history *a-priori*, even though the details of the X-ray background will in general influence the ionization history to some degree<sup>3</sup>. Because we focus primarily on 21-cm features expected to occur at  $z > 10$ , we assume  $\bar{x}_i = x_e = 0$  at all  $z > 10$  when generating  $\bar{\tau}_v(z, z')$ .

The effects of this approximation are shown in Figure 5.6, in which we examine how different ionization histories (and thus IGM opacities) affect the background flux,  $J_\nu$ . Because we assume a neutral IGM for all  $z \geq 10$ , we always underestimate the background flux, since an evolving IGM optical depth due to reionization of the IGM allows X-rays to travel further than they would in a neutral medium. The worst-case-scenario for this  $\bar{x}_i(z) = 0$  approximation occurs for very extended ionization histories (blue line in top panel of Figure 5.6), in which case the heating rate density at  $z = \{10, 12, 14\}$  is in error by factors of  $\{1.2, 0.5, 0.2\}$ . Because the 21-cm signal is likely insensitive to  $\epsilon_X$  once reionization begins<sup>4</sup>, we suspect this error is negligible in practice. As pointed out in Mirocha et al. (2013), the 21-cm emission feature can serve as a probe of  $\epsilon_X$  so long as independent constraints on the ionization history are in hand. In this case, we would simply tabulate  $\bar{\tau}_v$  using the observational constraints on  $\bar{x}_i(z)$ , and mitigate the errors shown in Figure 5.6. Our code could also be modified to compute the optical depth on-the-fly once  $\bar{x}_i$  exceeds a few percent, indicating the beginning of the EoR.

### 5.6.2 Neutral Absorption

Our choice of  $N_{\text{HI}}$  is consistent with the range of values adopted in the literature in recent years (e.g., Mesinger et al., 2013b), which are chosen to match constraints on neutral hydrogen absorption seen in high- $z$  gamma ray burst spectra (which can also be explained if reionization is patchy or not complete

<sup>3</sup> Evolution of the volume filling factor of HII regions,  $x_i$ , is the same in each model we consider because we have not varied the number of ionizing photons emitted per baryon of star formation,  $N_{\text{ion}}$ , or the star formation history, parameterized by the minimum virial temperature of star-forming haloes,  $T_{\text{min}}$ , and the star formation efficiency,  $f_*$ . X-rays are only allowed to ionize the bulk IGM in our formalism, whose ionized fraction is  $x_e \lesssim 0.1\%$  at all  $z \gtrsim 12$  in our models, meaning  $\bar{x}_i \approx x_i$ . The midpoint of reionization occurs at  $z \simeq 10.8$  in each model we consider.

<sup>4</sup> Though “cold reionization” scenarios have not been completely ruled out, recent work is inconsistent with a completely unheated  $z \approx 8$  IGM (Parsons et al., 2014).

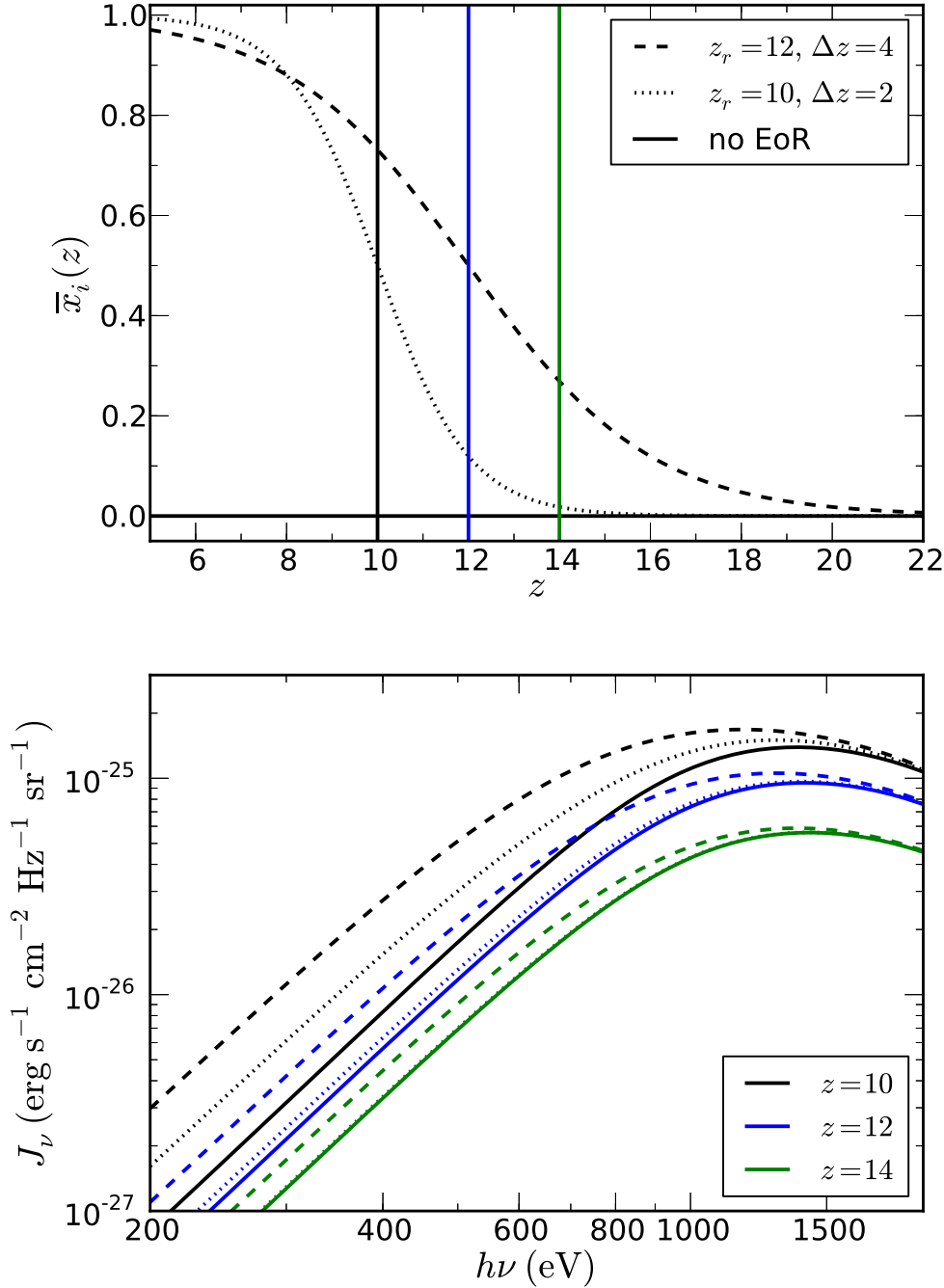


Figure 5.6 Consequences of the  $\bar{x}_i = \text{constant} = 0$  approximation on the background radiation field for our reference model (see Table 5.1). *Top*:  $\tanh$  ionization histories considered, i.e.,  $\bar{x}_i(z) \propto \tanh((z - z_r)/\Delta z)$ . *Bottom*: Angle-averaged background intensity,  $J_\nu$ , at  $z = 10, 12$  and  $14$  (black, blue, green) assuming a neutral IGM for all  $z$  (solid), compared to increasingly early and extended reionization scenarios (dotted and dashed). Errors in the background intensity due to the  $\bar{x}_i = \text{constant} = 0$  could be important at  $z \lesssim 14$ , assuming early and extended reionization scenarios (e.g.,  $z_r = 12, \Delta z = 4$ ), though by this time the global 21-cm signal is likely insensitive to the thermal history.

by  $z \approx 7$ ; Totani et al., 2006, Greiner et al., 2009). If we assume that the absorbing column is due to the host galaxy ISM, then it cannot be used solely to harden the X-ray spectrum – it must also attenuate soft UV photons from stars, and thus be related to the escape fraction of ionizing radiation,  $f_{\text{esc}}$ . In the most optimistic case of a PopIII galaxy (which we take to be a perfect blackbody of  $10^5$  K), an absorbing column of  $N_{\text{H1}} = 10^{18.5} \text{ cm}^{-2}$  corresponds to  $f_{\text{esc}} \simeq 0.01$ , meaning every non-zero column density we investigated in Figure 5.5 would lead to the attenuation of more than 99% of ionizing stellar radiation, thus inhibiting the progression of cosmic reionization considerably.

An alternative is to assume that the absorbing column is intrinsic to accreting systems, though work on galactic X-ray binaries casts doubt on such an assumption. Miller et al. (2009) monitored a series of photoelectric absorption edges during BH spectral state transitions, and found that while the soft X-ray spectrum varied considerably, the column densities inferred by the absorption edges remained roughly constant. This supports the idea that evolution in the soft X-ray spectrum of X-ray binaries arises due to evolution in the source spectrum, and that neutral absorption is dominated by the host galaxy ISM.

For large values of  $N_{\text{H1}}$ , reionization could still proceed if the distribution of neutral gas in (at least some) galaxies were highly anisotropic. Recent simulations by Gnedin et al. (2008) lend credence to this idea, displaying order-of-magnitude deviations in the escape fraction depending on the propagation direction of ionizing photons – with radiation escaping through the polar regions of disk galaxies preferentially. Wise and Cen (2009) performed a rigorous study of ionizing photon escape using simulations of both idealized and cosmological haloes, reaching similar conclusions extending to lower halo masses. The higher mass halos in the Wise and Cen (2009) simulation suite exhibited larger covering fractions of high column density gas (e.g., Figure 10), which could act to harden the spectrum of such galaxies, in addition to causing very anisotropic HII regions.

If there existed a population of miniquasars powered by intermediate mass BHs, and more massive BHs at high- $z$  occupy more massive haloes, then more massive haloes should have softer X-ray spectra (see Figure 5.4) and thus heat the IGM more efficiently. However, if they also exhibit larger covering fractions of high column density gas, the soft X-ray spectrum will be attenuated to some degree – perhaps enough to mimic an intrinsically harder source of X-rays. This effect may be reduced in galaxies hosting

an AGN, since X-rays partially ionize galactic gas and thus act to enhance the escape fraction of hydrogen- and helium- ionizing radiation (Benson et al., 2013). Ultimately the 21-cm signal only probes the volume-averaged emissivity, so if soft X-ray sources reside in high-mass haloes, they would have to be very bright to compensate for their rarity, and to contribute substantially to the heating of the IGM.

Lastly, it is worth mentioning that the hardness of the radiation field entering the “neutral” bulk IGM is not the same as that of the radiation field leaving the galaxy (whose edge is typically defined as its virial radius) since our model treats HII regions and the bulk IGM separately. As a result, there is an extra step between the intrinsic emission (that leaving the virial radius) and the IGM: of the photons that escape the virial radius, what fraction of them (as a function of frequency) contribute to the growth of the galactic HII region? The IGM penetrating radiation field is hardened as a result, and could become even harder and more anisotropic based on the presence or absence of large scale structure such as dense sheets and filaments<sup>5</sup>. Additionally, sources with harder spectra lead to more spatially extended ionization fronts, whose outskirts could be important sources of 21-cm emission (e.g., Venkatesan and Benson, 2011).

### 5.6.3 Accretion Physics

We have assumed throughout a radiative efficiency of  $\eta = 0.1$ , which is near the expected value for a thin disk around a non-spinning BH assuming the inner edge of the disk corresponds to the innermost stable circular orbit, i.e.  $r_{\text{in}} = r_{\text{isco}} = 6R_g$ . The radiative efficiency is very sensitive to BH spin, varying between  $0.05 \leq \eta \leq 0.4$  (Bardeen, 1970) from maximal retrograde spin (disk and BH angular momentum vectors are anti-parallel), to maximal prograde spin (disk and BH “rotate” in the same sense). While the spin of stellar mass BHs is expected to be more-or-less constant after their formation (King and Kolb, 1999), the spin distribution at high- $z$  is expected to be skewed towards large values of the spin parameter, leading to enhanced radiative efficiencies  $\eta > 0.1$  (Volonteri et al., 2005).

---

<sup>5</sup> In fact, the metagalactic background could be even harder than this, given that soft X-rays are absorbed on small scales and thus may not deserve to be included in a “global” radiation background. Madau et al. (2004) argued for  $E_{\text{min}} = 150$  eV since 150 eV photons have a mean-free path comparable to the mean separation between sources in their models, which formed in  $3.5\sigma$  density peaks at  $z \sim 24$ . However, for rare sources, a global radiation background treatment may be insufficient (e.g., Davies and Furlanetto, 2013). We chose  $E_{\text{min}} = 0.2$  keV to be consistent with other recent work on the 21-cm signal (e.g., Pritchard and Loeb, 2012), but clearly further study is required to determine reasonable values for this parameter. At least for large values of  $N_{\text{H}1}$ , the choice of  $E_{\text{min}}$  is irrelevant.

Our choice of  $f_{\text{edd}} = 0.1$  is much less physically motivated, being that it is difficult both to constrain observationally and predict theoretically. For X-ray binaries,  $f_{\text{edd}}$  should in general be considered not just what fraction of time the BH is actively accreting, but what fraction of the time it is in the high/soft state when the MCD model is appropriate. We ignore this for now as it is poorly constrained, but note that the emission during the high/soft state could dominate the heating even if more time is spent in the low/hard state simply because it is soft X-rays that dominate the heating.

While we don't explicitly attempt to model nuclear BHs, Equation 5.26 could be used to model their co-moving emissivity. Note, however, that this model is not necessarily self-consistent. We have imposed an accretion history via the parameters  $f_{\bullet}$  and  $T_{\text{min}}$ , though the Eddington luminosity density depends on the mass density of BHs. For extreme models (e.g., large values of  $f_{\bullet}$ ), the mass density of BHs required to sustain a given accretion luminosity density can exceed the mass density computed via integrating the accretion rate density over time. To render such scenarios self-consistent, one must require BH formation to cease or the ejection rate of BHs from galaxies to become significant (assuming ejected BHs no longer accrete), or both. The value of  $f_{\bullet}$  we adopt is small enough that we can neglect these complications for now, and postpone more detailed studies including nuclear BHs to future work.

#### 5.6.4 Choosing Representative Parameter Values

The results of recent population synthesis studies suggest that X-ray binaries are likely to be the dominant source of X-rays at high- $z$ . Power et al. (2013) modeled the evolution of a single stellar population that forms in an instantaneous burst, tracking massive stars evolving off the main sequence, and ultimately the X-ray binaries that form. Taking Cygnus X-1 as a spectral template, they compute the ionizing luminosity of the population with time (assuming a Kroupa initial mass function) and find that high-mass X-ray binaries dominate the instantaneous ionizing photon luminosity starting 20-30 Myr after the initial burst of star formation depending on the binary survival fraction. Fragos et al. (2013) performed a similar study, but instead started from the Millenium II simulation halo catalog and applied population synthesis models to obtain the evolution of the background X-ray spectrum and normalization from  $z \sim 20$  to present day. They find that X-ray binaries could potentially dominate the X-ray background over AGN (at least from 2-10 keV) at all

redshifts higher than  $z \sim 5$ .

Though our reference model effectively assumes that HMXBs dominate the X-ray background at high- $z$ , supernovae (Oh, 2001, Furlanetto and Loeb, 2004), accreting intermediate mass black holes, whether they be solitary “miniquasars” (e.g., Haiman and Loeb, 1998, Wyithe and Loeb, 2003, Kuhlen and Madau, 2005) or members of binaries, and thermal bremsstrahlung radiation from the hot interstellar medium of galaxies could be important X-ray sources as well (Mineo et al., 2012, Pacucci et al., 2014). In principle, our approach could couple detailed spectral models, composed of X-ray emission from a variety of sources, to the properties of the IGM with time, and investigate how the details of population synthesis models, for example, manifest themselves in the global 21-cm signal. Such studies would be particularly powerful if partnered with models of the 21-cm angular power spectrum, observations of which could help break SED-related degeneracies (Pritchard and Furlanetto, 2007, Mesinger et al., 2013b, Pacucci et al., 2014).

### 5.6.5 Helium Effects

The  $x_{\text{HI}} = x_{\text{HeI}}$  approximation we have made throughout is common in the literature, and has been validated to some extent by the close match in HI and HeI global ionization histories computed in Wyithe and Loeb (2003) and Friedrich et al. (2012), for example. However, recent studies of the ionization profiles around stars and quasars (e.g. Thomas and Zaroubi, 2008, Venkatesan and Benson, 2011) find that more X-ray luminous galaxies have larger HeII regions than HII regions. Given that the metagalactic radiation field we consider in this work is even harder than the quasar-like spectra considered in the aforementioned studies, the HI and HeI fractions in the bulk IGM may differ even more substantially than they do in the outskirts of HII/HeII regions near quasars.

We have neglected a self-consistent treatment of helium in this work, though more detailed calculations including helium could have a substantial impact on the ionization and thermal history. Ciardi et al. (2012) showed that radiative transfer simulations including helium, relative to their hydrogen-only counterparts, displayed a slight delay in the redshift of reionization, since a small fraction of energetic photons are absorbed by helium instead of hydrogen. The simulations including helium also exhibited an increase in the IGM temperature at  $z \lesssim 10$  due to helium photo-heating. At  $z \gtrsim 10$ , the volume-averaged temperature

in the hydrogen-only simulations was actually larger due to the larger volume of ionized gas. It is difficult to compare such results directly to our own, as our interest lies in the IGM temperature *outside* of ionized regions. Because of this complication, we defer a more detailed investigation of helium effects to future work.

## 5.7 Conclusions

Our conclusions can be summarized as follows:

- (1) Approximate solutions to the cosmological RTE overestimate the heating rate density in the bulk IGM, leading to artificially shallower absorption features in the global 21-cm signal, perhaps by  $\sim 15 - 20$  mK if sources with hard spectra dominate the X-ray background (Figure 5.3).
- (2) Brute-force solutions are computationally expensive, which limits parameter space searches considerably. The discretization scheme of Haardt and Madau (1996) is fast, though exquisite redshift sampling is required in order to accurately model X-ray heating (Figure 5.2).
- (3) More realistic X-ray spectra are harder than often used power-law treatments (Figure 5.4), and thus lead to deeper absorption features in the global 21-cm signal at fixed bolometric luminosity density. While the details of coronal physics can harden a “pure MCD” spectrum enough to modify the global 21-cm absorption feature at the  $\sim 10$  mK level (in the extreme case of  $f_{sc} = 1$  and  $\alpha = -0.5$ ), the characteristic mass of accreting BHs (amount of neutral absorption in galaxies) has an even more noticeable impact, shifting the absorption trough in amplitude by  $\sim 20$  ( $\sim 50$ ) mK and in redshift by  $\Delta z \approx 0.5$  ( $\Delta z \approx 2$ ) (Figure 5.5).
- (4) Care must be taken when using the local  $L_X - \text{SFR}$  relation to draw inferences about the high- $z$  stellar IMF, as assumptions about source SEDs are built-in to the often used normalization factor  $f_X$ . Even if the high- $z$  X-ray background is dominated by X-ray binaries, the parameters governing how significantly the intrinsic disk emission is processed influence the signal enormously, and could vary significantly from galaxy to galaxy.

## Chapter 6

### Optimized Multi-Frequency Spectra for Applications in Radiative Feedback and Cosmological Reionization

#### 6.1 Context

The recent implementation of radiative transfer algorithms in numerous hydrodynamics codes has led to a dramatic improvement in studies of feedback in various astrophysical environments. However, because of methodological limitations and computational expense, the spectra of radiation sources are generally sampled at only a few evenly-spaced discrete emission frequencies. Using one-dimensional radiative transfer calculations, we investigate the discrepancies in gas properties surrounding model stars and accreting black holes that arise solely due to spectral discretization. We find that even in the idealized case of a static and uniform density field, commonly used discretization schemes induce errors in the neutral fraction and temperature by factors of two to three on average, and by over an order of magnitude in certain column density regimes. The consequences are most severe for radiative feedback operating on large scales, dense clumps of gas, and media consisting of multiple chemical species. We have developed a method for optimally constructing discrete spectra, and show that for two test cases of interest, carefully chosen four-bin spectra can eliminate errors associated with frequency resolution to high precision. Applying these findings to a fully three-dimensional radiation-hydrodynamic simulation of the early universe, we find that the H II region around a primordial star is substantially altered in both size and morphology, corroborating the one-dimensional prediction that discrete spectral energy distributions can lead to sizable inaccuracies in the physical properties of a medium, and as a result, the subsequent evolution and observable signatures of objects embedded within it.

## 6.2 Introduction

Energy injection by radiative processes fundamentally changes the evolution of astrophysical systems, whether it be in the context of star formation, galaxy evolution, or the growth of super-massive black holes (SMBHs). For instance, ultraviolet photons from the universe's first stars (Population III (PopIII) stars; Abel et al., 2002) photo-dissociate the primary coolant ( $\text{H}_2$ ) that first enabled their formation. Very recent radiation-hydrodynamic calculations of PopIII stars find that PopIII star masses may be limited by proto-stellar radiative feedback, perhaps explaining the lack of evidence for exotic pair instability supernovae in the early universe (Hosokawa et al., 2011). Conventional metal line cooling driven star formation can be affected by radiative feedback as well. Krumholz (2006) showed that photo-heating around newly formed stars can strongly suppress fragmentation in surrounding proto-stellar clouds, while Dale et al. (2005) see both positive and negative feedback operating in radiation-hydrodynamic simulations of star cluster formation. Radiative feedback could also be a barrier to efficient black hole (BH) growth in the early universe (Alvarez et al., 2009), as X-rays from accreting BHs efficiently photo-heat surrounding gas, leading to smaller Bondi-Hoyle accretion rates (Bondi and Hoyle, 1944).

The mere presence of ionizing/dissociating photons ensures a change in the chemical and thermal state of a gas, though the magnitude of these changes hinges squarely on the number of photons propagating through the gas and their spectral energy distribution (SED). Holding the bolometric luminosity of a radiation source constant, even subtle changes in the SED can lead to noticeable differences in the properties of the surrounding medium. For example, adjusting the X-ray power-law index of a BH accretion spectrum results in ionization fronts which differ by factors of  $\approx 2-3$  in radius, and temperature profiles varying by  $10^2-10^3\text{K}$  on scales of several hundred kpc (Thomas and Zaroubi, 2008). Simply truncating the emission of identical X-ray SEDs at harder energies (0.4 keV rather than 0.2 keV) causes a drastic reduction in heating, ionized fractions, and  $\text{H}_2$  fractions surrounding 'miniquasars' at high redshift (Kuhlen and Madau, 2005).

Unfortunately, not all radiative transfer algorithms are able to represent radiation sources with continuous SEDs, or perhaps cannot afford the additional computational expense associated with the frequency dependence of the radiative transfer equation. The natural first step is to represent sources as monochromatic

emitters, choosing an emission frequency characteristic of the full SED. Some authors have improved upon the monochromatic treatment using ‘multi-group’ methods, which average SED properties and absorption cross-sections over one or more frequency bandpasses (Gnedin and Abel, 2001, Aubert and Teyssier, 2008), while others have sampled continuous SEDs at  $n_v$  frequencies, which are generally evenly spaced bins (in linear or log-space) between the hydrogen ionization threshold and an upper frequency cutoff. In either case, there is no clear method of deciding how many frequency-averaged bandpasses or discrete emission frequencies are required for a given problem, and though the standard multi-group treatment is physically motivated, it does not guarantee that the photo-ionization and photo-heating rates are adequately reproduced as a function of column density.

Frequency resolution has recently been studied in radiation-hydrodynamic settings by Wise and Abel (2011) and Whalen and Norman (2008). Wise and Abel (2011) find that for the expansion of an H II region around a  $10^5$  K blackbody source in a hydrogen-only medium, the density, temperature, velocity, and ionization profiles are well converged for  $n_v \geq 4$ . Use of a monochromatic spectrum for this problem introduces significant errors since all photons are absorbed at a characteristic column density, whereas multi-frequency treatments achieve some column density dependent behavior and can thus mimic the behavior of a truly continuous spectrum. Whalen and Norman (2008) studied the effects of frequency resolution in the setting of I-front instabilities, and did not achieve convergence until  $n_v \geq 80$  (logarithmically spaced between 13.6 and 90 eV).

The convergence for the test of Wise and Abel (2011) using only four frequency bins is reassuring, though the prospects for convergence are less clear if one were interested in the absorption processes of multiple chemical species, ionization and heating due to X-rays and their energetic secondary photo-electrons (Shull and van Steenberg, 1985, Furlanetto and Johnson Stoeber, 2010), or inhomogeneous media. Kramer and Haiman (2008, hereafter KH08) briefly compared monochromatic and continuous treatments of absorbed power-law X-ray sources in a study of ionization front thickness around high- $z$  quasars (the I-front thickness is a potentially powerful indirect probe of the ionizing spectrum of high- $z$  quasars). The hydrogen and helium I-front thickness is expected to grow over the lifetime of a quasar given the discrepancy in evolution timescales between the largest and smallest scales. At small radii, photo-ionization equilibrium

is reached quickly since ionizing photons are abundant, whereas geometrical dilution and attenuation of the initial radiation field slow ionization evolution considerably on large scales, effectively ‘stretching out’ the I-fronts of hydrogen and helium with time. A monochromatic representation of the quasar SED leads to a reduction in this effect, but also leads to severe errors in the overall ionization structure (see Figure 3 of KH08). These errors are of the same order of magnitude as those resulting from the neglect of physical effects, such as ionization via helium recombination photons (KH08, Figure 6), or ionization from secondary electrons (KH08, Figure 7). These effects are likely important in studies of radiative feedback from stars and active galactic nuclei (AGNs), and most certainly in efforts to simulate cosmological reionization. An effort must be made to ensure that the SEDs used in numerical simulations accurately reflect the properties of their continuous analogs, especially if it is spectrum-dependent effects in which we are most interested.

We will focus on the following questions in this paper. How significant are the errors in the temperature and ionization state of a medium that arise solely due to the discretization of SEDs? How many frequencies are required to minimize such errors, where must they be positioned in frequency-space, and how should their relative luminosities be apportioned? For what numerical methods is it possible to represent sources with continuous SEDs, or are there perhaps advantages in discretizing SEDs, even when it is not required by the algorithm of choice? Answers to these questions may lead to revised interpretations of previous studies which used discrete radiation fields, but more importantly, will reduce the guesswork involved in discretizing SEDs, and promote frequency resolution to the same status as spatial, temporal, and mass resolution, which are more easily selected on a problem-by-problem basis.

In Section 6.3 we will introduce the one-dimensional radiative transfer framework used to obtain the solutions presented in later sections. In Section 6.4, we quantitatively assess the accuracy with which multi-frequency calculations reproduce the ionization and heating profiles of continuous SEDs. Section 6.5 is devoted to introducing a technique for optimally selecting discrete SED templates, and Section 6.6 will present the results obtained with this method, including applications to one-dimensional and fully three-dimensional radiation-hydrodynamic calculations. Discussion and conclusions can be found in Sections 6.7 and 6.8, respectively. Validation of the radiative transfer code used for this work and further details regarding the optimization algorithm can be found in the Appendix.

### 6.3 Radiative Transfer Framework

One dimensional radiative transfer calculations around point sources have been used to model cosmological reionization (Fukugita and Kawasaki, 1994), the thickness of quasar ionization fronts (KH08), the time-evolution of ionization and heating around first stars, galaxies, and quasars (Thomas and Zaroubi, 2008, Venkatesan and Benson, 2011), and their associated observable signatures. Given that our focus is on frequency resolution, it would be unnecessary to perform calculations in a more complex setting than this, with additional unrelated physics. As a result, our one-dimensional methods strongly resemble those used by previous authors, though for completeness, we will reiterate the aspects of these methods most pertinent to the problem at hand.

In general, the chemical and thermal evolution of gas surrounding a radiation source is governed by a set of differential equations describing the number densities of all ions and the temperature of the gas. Assuming a medium consisting of hydrogen and helium only, we first solve for the abundances of each ion via

$$\frac{dn_{\text{H II}}}{dt} = (\Gamma_{\text{H I}} + \gamma_{\text{H I}} + \beta_{\text{H I}} n_e) n_{\text{H I}} - \alpha_{\text{H II}} n_e n_{\text{H II}} \quad (6.1)$$

$$\begin{aligned} \frac{dn_{\text{He I}}}{dt} &= (\Gamma_{\text{He I}} + \gamma_{\text{He I}} + \beta_{\text{He I}} n_e) n_{\text{He I}} + \alpha_{\text{He III}} n_e n_{\text{He III}} \\ &\quad - (\beta_{\text{He II}} + \alpha_{\text{He II}} + \xi_{\text{He II}}) n_e n_{\text{He II}} \end{aligned} \quad (6.2)$$

$$- (\Gamma_{\text{He II}} + \gamma_{\text{He II}}) n_{\text{He II}} \quad (6.3)$$

$$\frac{dn_{\text{He III}}}{dt} = (\Gamma_{\text{He II}} + \gamma_{\text{He II}} + \beta_{\text{He II}} n_e) n_{\text{He II}} - \alpha_{\text{He III}} n_e n_{\text{He III}}. \quad (6.4)$$

Each of these equations represents the balance between ionizations of species H I, He I, and He II, and recombinations of H II, He II, and He III. Associating the index  $i$  with absorbing species,  $i = \text{H I}, \text{He I}, \text{He II}$ , and the index  $i'$  with ions,  $i' = \text{H II}, \text{He II}, \text{He III}$ , we define  $\Gamma_i$  as the photo-ionization rate coefficient,  $\gamma_i$  as the secondary ionization rate coefficient,  $\alpha_{i'}$  ( $\xi_{i'}$ ) as the case-B (dielectric) recombination rate coefficients,  $\beta_i$  as the collisional ionization rate coefficients, and  $n_e = n_{\text{H II}} + n_{\text{He II}} + 2n_{\text{He III}}$  as the number density of electrons.

At each time step, we also solve for the temperature evolution,  $dT_k/dt$ , which is given by

$$\begin{aligned} \frac{3}{2} \frac{d}{dt} \left( \frac{k_B T_k n_{\text{tot}}}{\mu} \right) = & f_{\text{heat}} \sum_i n_i \mathcal{H}_i - \sum_i \zeta_i n_e n_i - \sum_{i'} \eta_{i'} n_e n_{i'} \\ & - \sum_i \psi_i n_e n_i - \omega_{\text{He II}} n_e n_{\text{He II}} \end{aligned} \quad (6.5)$$

where  $\mathcal{H}_i$  is the photo–electric heating rate coefficient (due to electrons previously bound to species  $i$ ),  $\omega_{\text{He II}}$  is the dielectric recombination cooling coefficient, and  $\zeta_i$ ,  $\eta_{i'}$ , and  $\psi_i$  are the collisional ionization, recombination, and collisional excitation cooling coefficients, respectively. The constants in Equation (6.5) are the total number density of baryons,  $n_{\text{tot}} = n_{\text{H}} + n_{\text{He}} + n_e$ , the mean molecular weight,  $\mu$ , Boltzmann’s constant,  $k_B$ , and the fraction of secondary electron energy deposited as heat,  $f_{\text{heat}}$ . We use the formulae in Appendix B of Fukugita and Kawasaki (1994) to compute the values of  $\alpha_i$ ,  $\beta_i$ ,  $\xi_i$ ,  $\zeta_i$ ,  $\eta_{i'}$ ,  $\psi_i$ , and  $\omega_{\text{He II}}$ .

The most critical aspect of propagating the radiation field in our one-dimensional simulations is computing the ionization ( $\Gamma_i$ ,  $\gamma_i$ ) and heating ( $\mathcal{H}_i$ ) rate coefficients accurately. In order to directly relate our results to fully three-dimensional radiative transfer calculations, we have chosen to adopt a photon-conserving (PC) algorithm nearly identical to those employed by several widely used codes, like *C<sup>2</sup>Ray* (Mellema et al., 2006, Friedrich et al., 2012), and *Enzo* (Wise and Abel, 2011). Our code is able to compute  $\Gamma_i$ ,  $\gamma_i$ , and  $\mathcal{H}_i$  in a non-photon-conserving (NPC) fashion as well, to enable comparison with previous one-dimensional work such as Thomas and Zaroubi (2008). The two formalisms are equivalent in the limit of very optically thin cells, a condition that can be met easily in one-dimensional calculations but is rarely computationally feasible in three dimensions. For NPC methods, if the optical depth of an individual cell is substantial, the number of ionizations in that cell will *not* equal the number of photons absorbed for that cell, i.e., photon number will not be conserved. This problem was remedied by Abel et al. (1999), who inferred the number of photo-ionizations of species  $i$  in a cell from the radiation incident upon it and its optical depth,

$$\Delta\tau_{i,\nu} = n_i \sigma_{i,\nu} \Delta r. \quad (6.6)$$

It is most straightforward to imagine our one-dimensional grid as a collection of concentric spherical shells, each having thickness  $\Delta r$  and volume  $V_{\text{sh}}(r) = 4\pi[(r + \Delta r)^3 - r^3]/3$ , where  $r$  is the distance between the origin and the inner interface of each shell. The ionization and heating rates can then be related to the

number of absorptions in any given shell (thus preserving photon number), as

$$\Gamma_i = A_i \int_{\nu_i}^{\infty} I_{\nu} e^{-\tau_{\nu}} (1 - e^{-\Delta\tau_{i,\nu}}) \frac{d\nu}{h\nu} \quad (6.7)$$

$$\gamma_{ij} = A_j \int_{\nu_j}^{\infty} \left( \frac{\nu - \nu_j}{\nu_i} \right) I_{\nu} e^{-\tau_{\nu}} (1 - e^{-\Delta\tau_{j,\nu}}) \frac{d\nu}{h\nu} \quad (6.8)$$

$$\mathcal{H}_i = A_i \int_{\nu_i}^{\infty} (\nu - \nu_i) I_{\nu} e^{-\tau_{\nu}} (1 - e^{-\Delta\tau_{i,\nu}}) \frac{d\nu}{\nu}, \quad (6.9)$$

where we have defined the normalization constant  $A_i \equiv L_{\text{bol}}/n_i V_{\text{sh}}(r)$ , and denote the ionization threshold energy for species  $i$  as  $h\nu_i$ .  $I_{\nu}$  represents the SED of radiation sources, and satisfies  $\int_{\nu} I_{\nu} d\nu = 1$ , such that  $L_{\text{bol}} I_{\nu} = L_{\nu}$ .

Equation (6.8) represents ionizations of species  $i$  due to fast secondary electrons from photoionizations of species  $j$ , which has number density  $n_j$ , and ionization threshold energy,  $h\nu_j$ .  $f_{\text{ion}}$  is the fraction of photo-electron energy deposited as ionizations of species  $i$ . In the remaining sections we only include the effects of secondary electrons when considering X-ray sources, which emit photons in the range  $10^2 \text{eV} < E < 10^4 \text{eV}$ . In this regime, the values of  $f_{\text{heat}}$  and  $f_{\text{ion}}$  computed via the formulae of Shull and van Steenberg (1985) are sufficiently accurate, but for radiation at lower energies where  $f_{\text{heat}}$  and  $f_{\text{ion}}$  have a stronger energy dependence, the fitting formulae of Ricotti et al. (2002) or the lookup tables of Furlanetto and Johnson Stoeber (2010) would be more appropriate. The total secondary ionization rate for a given species,  $\gamma_i$ , is the sum of ionizations due to the secondary electrons from all species,  $\gamma_i = f_{\text{ion}} \sum_j \gamma_{ij} n_j / n_i$ .

The optical depth,  $\tau_{\nu} = \tau_{\nu}(r)$ , in the above equations is the total optical depth at frequency  $\nu$  due to all absorbing species, i.e.,

$$\begin{aligned} \tau_{\nu}(r) &= \sum_i \int_0^r \sigma_{i,\nu} n_i(r') dr' \\ &= \sum_i \sigma_{i,\nu} N_i(r) \end{aligned} \quad (6.10)$$

where  $N_i$  is the column density of species  $i$  at distance  $r$  from the source. We calculate the bound-free absorption cross-sections using the fits of Verner and Ferland (1996) throughout.

The values of  $\Gamma_i$ ,  $\gamma_i$ , and  $\mathcal{H}_i$  are completely predetermined for a given radiation source, and as a result, can be tabulated as a function of column density to avoid evaluating the integrals in these expressions numerically ‘on-the-fly’ as a simulation runs (e.g., Mellema et al., 2006, Thomas and Zaroubi, 2008). Isolating

the frequency-dependent components of Equations (6.7)–(6.9), we can define the integrals

$$\Phi_i(\tau_\nu) \equiv \int_{\nu_i}^{\infty} I_\nu e^{-\tau_\nu} \frac{d\nu}{h\nu} \quad (6.11)$$

$$\Psi_i(\tau_\nu) \equiv \int_{\nu_i}^{\infty} I_\nu e^{-\tau_\nu} d\nu, \quad (6.12)$$

allowing us to re-express the rate coefficients as

$$\Gamma_i = A_i [\Phi_i(\tau_\nu) - \Phi_i(\tau'_{i,\nu})] \quad (6.13)$$

$$\gamma_{ij} = \frac{A_j}{h\nu_i} \{ \Psi_j(\tau_\nu) - \Psi_j(\tau'_{j,\nu}) - h\nu_j [\Phi_j(\tau_\nu) - \Phi_j(\tau'_{j,\nu})] \} \quad (6.14)$$

$$\mathcal{H}_i = A_i \{ \Psi_i(\tau_\nu) - \Psi_i(\tau'_{i,\nu}) - h\nu_i [\Phi_i(\tau_\nu) - \Phi_i(\tau'_{i,\nu})] \}, \quad (6.15)$$

where  $\tau'_{i,\nu} \equiv \tau_\nu + \Delta\tau_{i,\nu}$ . Later references to “continuous SEDs” signify use of this technique, where the integral values  $\Phi_i$  and  $\Psi_i$  are computed over a column density interval of interest a priori using a Gaussian quadrature technique, rather than on-the-fly via discrete summation.

Tabulating Equations (6.11) and (6.12) grants a significant speed-up computationally, but also forms the basis of our frequency resolution optimization strategy (Section 6.5). Note, however, that in general the dimensionality of these lookup tables is equal to the number of absorbing species (through  $\Delta\tau_{i,\nu}$ ), so the tables for simulations including hydrogen only are one dimensional, while those including hydrogen and helium are three dimensional. If we chose to adopt the secondary electron treatment of Ricotti et al. (2002) or Furlanetto and Johnson Stoeber (2010), our lookup tables would inherit an additional dimension, as the secondary ionization and heating factors  $f_{\text{ion}}$  and  $f_{\text{heat}}$  would depend both on photon energy and the hydrogen ionized fraction,  $x_{\text{H II}}$ . See Appendix E for a generalization of Equations 6.13-6.15 that includes energy-dependent secondary ionization and heating.

Equations (6.13)–(6.15) are completely general for PC algorithms, whether the source SEDs are discrete or continuous — the only difference being for discrete SEDs, the integrals in Equations (6.11) and (6.12) become sums over the number of discrete emission frequencies,  $n_\nu$ . In practice, computing  $\Gamma_i$ ,  $\gamma_i$ , and  $\mathcal{H}_i$  is more straightforward for sources with discrete SEDs, as we can simply count the number of ionizations caused by photons at each individual frequency, and convert this into the amount of excess electron kinetic energy available for further heating and ionization. When testing the accuracy of discrete solutions

in later sections we employ this method, where radiation is emitted at  $n_v$  frequencies, with each frequency  $\nu_n$  carrying a fraction  $I_n$  of the source's bolometric luminosity. The photoionization and heating coefficients can then be expressed as

$$\Gamma_{i,n} = \frac{A_i I_n}{h\nu_n} e^{-\tau_{\nu_n}} (1 - e^{-\Delta\tau_{i,\nu_n}}) \quad (6.16)$$

$$\gamma_{ij,n} = \Gamma_{j,\nu_n} (\nu_n - \nu_j) / \nu_i \quad (6.17)$$

$$\mathcal{H}_{i,n} = \Gamma_{i,\nu_n} h (\nu_n - \nu_i). \quad (6.18)$$

The total rate coefficients can be found by summing each of these expressions over all frequencies,  $n = 1, 2, 3, \dots, n_v$ . These equations are identical to Equations (6.13)–(6.15) for the discrete SED case, but are perhaps more intuitive.

For simplicity, our current treatment neglects a few physical processes that are cosmological in origin, or simply do not rely on the radiation field directly. These include cooling via free-free emission and hydrogen and helium ionization due to helium recombination photons (which depend on the gas kinetic temperature and electron density), and cosmological effects such as Hubble cooling, Compton cooling off cosmic microwave background (CMB) photons, and photo-ionization by Wien-tail CMB photons (which depend on kinetic temperature, redshift, and the Hubble parameter).

Two additional approximations are implicit in the remainder of this paper. They are (1) the infinite speed-of-light approximation and (2) the on-the-spot approximation (we use the case-B recombination coefficients in Equations (6.1)–(6.4)). The former approximation could be dubious for very bright sources in low-density media, while the latter is generally not a good assumption, as discussed at length in Cantalupo and Porciani (2011). As a result, the *absolute* accuracy of our solutions is not guaranteed in regimes where careful treatment of the speed of light and recombination photons is necessary, but this is acceptable since we only care about the *relative* differences among our solutions. The optimized SEDs of Section 6.6 will apply equally well to simulations including more ionization and/or heating/cooling processes, so long as they do not depend directly on the radiation field (e.g., ionization of H I and He I by helium recombination photons; Friedrich et al., 2012).

## 6.4 Assessing the Consequences of Discrete Radiation Fields

To quantify the differences between the ionization and temperature profiles around sources with continuous and discrete SEDs, we will simulate two test problems. First, the standard case of a  $10^5$  K blackbody in a hydrogen-only medium, and second, a power-law X-ray source in a medium consisting of both hydrogen and helium.

### 6.4.1 $10^5$ K Blackbody

The  $10^5$  K blackbody problem has been studied extensively (e.g., Test Problem 2 in the Radiative Transfer Comparison Project; Iliev et al., 2006, hereafter RT06) due to its simplicity, and perhaps also because the surface temperatures of PopIII stars are expected to be  $\sim 10^5$  K (Schaerer, 2002). We adopt nearly the identical setup as in RT06, i.e., a uniform hydrogen-only medium with number density  $n_{\text{H}} = 10^{-3} \text{ cm}^{-3}$ , initial ionized fraction  $x_{\text{H II}} = 1.2 \times 10^{-3}$ , initial temperature  $T_0 = 10^2$  K, and a  $10^5$  K blackbody with an ionizing photon luminosity of  $\dot{Q} = 5 \times 10^{48} \text{ s}^{-1}$ . The only difference between our simulations and RT06 is that we use a domain  $L_{\text{box}} = 10$  kpc in size, rather than  $L_{\text{box}} = 6.6$  kpc, to allow for a comparison of discrete and continuous solutions at slightly larger radii. We evolve the simulations for 500 Myr on a grid of 200 linearly spaced cells between  $0.1 < r/\text{kpc} < 10$ , ignoring the details of secondary ionization (i.e., all photo-electron energy is deposited as heat).

In Figure 6.1, we compare the ionization and temperature profiles around two  $10^5$  K ‘blackbody’ sources of constant ionizing photon luminosity  $\dot{Q} = 5 \times 10^{48} \text{ s}^{-1}$  — one a true blackbody emitter with a continuous SED spanning the range 13.6–100 eV (black lines), and the other with a monochromatic SED at  $h\nu_1 = 29.6$  eV, the average energy of ionizing photons for this source (red lines). We can see the same qualitative results that have been pointed out by previous authors, namely, that monochromatic sources of radiation fail to ionize (top panels) and heat (lower panels) gas at large radii as significantly as continuous sources, since all photons are absorbed near a single characteristic column density, representing the point where  $\tau_{\nu_1} \approx 1$ , i.e.,  $N_{\text{char}} \sim \sigma_{\nu_1}^{-1}$ . The relative error in the position of the ionization front,  $\Delta r_{\text{IF}}$ , where  $r_{\text{IF}} \equiv r(x_{\text{H I}} = x_{\text{H II}} = 0.5)$ , is 8% after 10 Myr, 10% after 100 Myr, and 11% after 500 Myr. In the optically

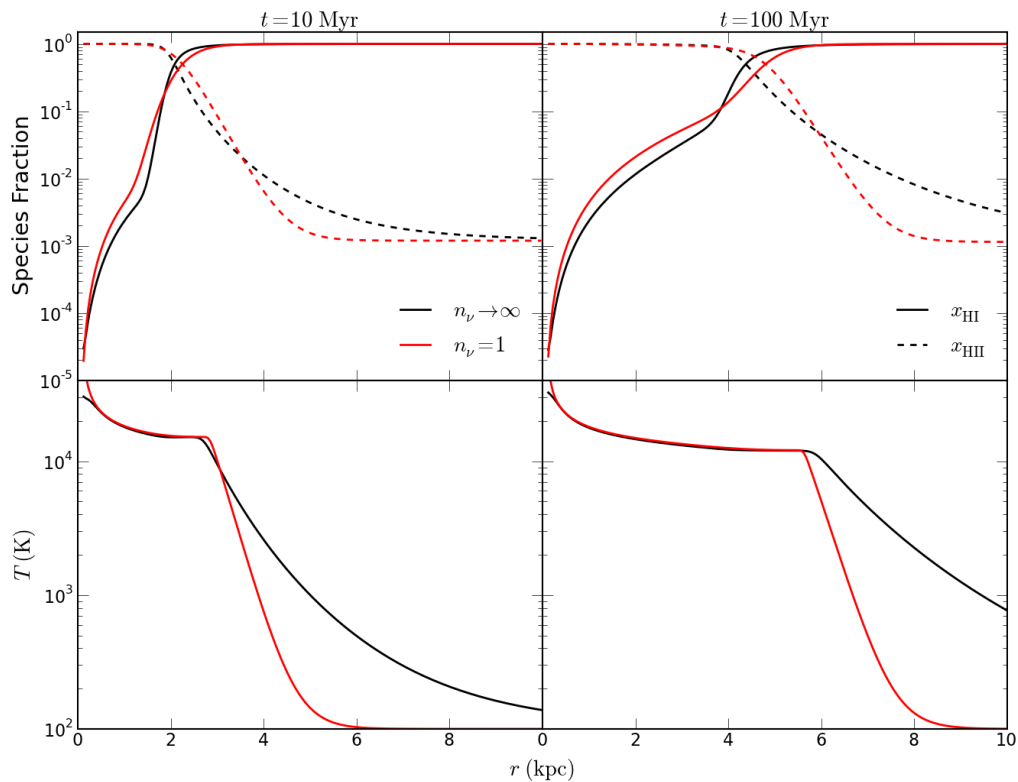


Figure 6.1 Comparison of ionization (top) and temperature (bottom) profiles around a  $10^5$  K blackbody source after 10 Myr (left) and 100 Myr (right) using continuous (black) and monochromatic (red) SEDs. Solid lines in the top panels correspond to the neutral fraction ( $x_{\text{HI}}$ ), while dashed lines correspond to the ionized fraction ( $x_{\text{HII}}$ ). We apply these line color and line style conventions for all radial profiles presented in this paper.

thin regime, the monochromatic spectrum overestimates ionization by factors of two to three on average and up to an order of magnitude at all times, though the latter effect is primarily because the neutral fraction is a steeply declining function with decreasing radius, and the I-fronts of the two solutions are offset. Outside the I-front, the situation is more interesting as the gas is mostly neutral. After 100 Myr of evolution, the ionized fraction outside the I-front is underestimated by a factor of two on average, and by as much as a factor of six.

The temperature evolution, shown in the bottom panels of Figure 6.1, is significantly more troubling. The monochromatic source captures the temperature well within the ionization front where the gas is in photoionization equilibrium, but quickly diverges from the continuous solution outside. Like the ionization profiles, discrepancies grow with time. After 10 Myr of evolution, the monochromatic source underestimates the temperature at large radii by a factor of two on average, and by a factor of seven at the point of greatest discrepancy. After 100 (500) Myr, the discrete solution underestimates the temperature by up to a factor of 17 (41).

If considering the heating and ionization around a single PopIII star, the errors induced by monochromatic treatments may not be cause for concern upon first inspection since PopIII stars are expected to live only a few Myr, and we can see that errors are less significant at early times. However, the intergalactic medium (IGM) is subject to the ionization and heating caused by all sources, whose cumulative impact will be substantial even though the ionization and heating caused by individual sources may be very small. Globally, then, the IGM is insensitive to individual stellar lifetimes, and instead evolves as it would if ionizing photons originated from a single, very luminous, very long lived object.

This manner of thinking has already materialized in the realm of large volume cosmological simulations, where ‘star particles’ are generally as luminous as one or more star clusters, and ‘galaxy particles’ behave in a way that is consistent with the integrated properties of an entire galactic stellar population (and perhaps active nucleus). Such approximations are necessary with limited spatial resolution, but more than adequate for studies of the IGM. Over time though, errors in gas properties due to poor frequency resolution will accrue, as it is the combined properties of all radiation sources which affect IGM properties, however short-lived each individual source may be.

### 6.4.2 Power-Law X-Ray Source

To address the effects of discrete SEDs in environments where multiple chemical species are important and large attenuating columns are possible, we now turn our attention to a power-law X-ray source embedded in a 1 Mpc domain consisting of hydrogen and helium, with a primordial helium abundance (by mass) of  $Y = 0.2477$ .

Our selection of parameters for this problem is motivated by studies of high-redshift quasars, and particularly their role in the epoch of reionization (e.g., Venkatesan et al., 2001). X-rays have long mean free paths, and as a result are capable of ionizing and heating gas on very large ( $\sim$ Mpc) scales. Large-scale heating is responsible for driving the high-redshift all-sky 21 cm signal toward emission, and inducing fluctuations in 21 cm power spectra on large angular scales (for a review of 21 cm cosmology, see Furlanetto (2006)). An early X-ray background may also be important in interpreting the optical depth to electron scattering of the CMB (e.g., Ricotti et al., 2005, Shull and Venkatesan, 2008).

While supernovae and/or X-ray binaries could be important sources of hard photons in the early universe, we assume the source of X-rays is persistent — an accreting SMBH with mass  $M_{\bullet} = 10^6 M_{\odot}$  and radiative efficiency of  $\epsilon_{\bullet} = 10\%$ , which leads to a bolometric luminosity of  $\mathcal{L}_{\text{bol}} = \epsilon_{\bullet} \mathcal{L}_{\text{edd}} \simeq 1.26 \times 10^{43} \text{ erg s}^{-1}$ . Here,  $\mathcal{L}_{\text{edd}} = 4\pi GM_{\bullet} m_p c / \sigma_T$  is the Eddington luminosity, where  $m_p$  is the proton mass and  $\sigma_T$  the Thomson cross-section. The mass (and thus luminosity) of the SMBH is allowed to grow as it accretes,

$$M_{\bullet}(t) = M_{\bullet}(0) \exp \left[ \frac{1 - \epsilon_{\bullet}}{\epsilon_{\bullet}} \left( \frac{t}{t_{\text{edd}}} \right) \right], \quad (6.19)$$

where  $t_{\text{edd}} = 0.45 \text{ Gyr}$  is the  $e$ -folding timescale for SMBH growth (an Eddington, or Salpeter time). The SED is taken to be a power law of the form

$$I_{\nu} \propto \left( \frac{h\nu}{\text{keV}} \right)^{1-\alpha}, \quad (6.20)$$

where  $\alpha$  is the spectral index. We adopt  $\alpha = 1.5$ , over the energy range  $10^2$ - $10^4 \text{ eV}$ . The surrounding medium has a constant mass density of  $\rho = 5.4 \times 10^{-28} \text{ g cm}^{-3}$  (cosmic mean at redshift  $z = 10$ ), initial ionized fractions  $x_{\text{H II}} = x_{\text{He II}} = 10^{-4}$ ,  $x_{\text{He III}} = 0$ , and initial temperature  $T_0 = 10^2 \text{ K}$ . The domain for this

problem is divided into 400 cells linearly spaced between  $0.01 < r/\text{Mpc} < 1$ , and is evolved for  $\epsilon_{\bullet} t_{\text{edd}} = 45$  Myr.

In Figure 6.2, we compare the hydrogen and helium ionization profiles for two X-ray sources having the same bolometric luminosity. One, a continuous power-law source as described above, and the other a monochromatic source of 0.5 keV photons (a fiducial monochromatic emission energy). The monochromatic source underestimates the radii of both the hydrogen and helium ionization fronts by a factor of  $\sim 2.3$ , and overestimates the hydrogen neutral fraction on average by a factor of three, and at most by a factor of 20 within the hydrogen I-front. The same general picture applies to helium, where errors in the neutral helium fraction are enormous since the He I-He II I-front is very sharp (as it was for hydrogen in the previous section), and  $x_{\text{He II}}$  and  $x_{\text{He III}}$  are in error by factors of 2–20 depending on radius.

Errors in the temperature profile are less extreme, as shown in Figure 6.3. On small scales, the monochromatic source captures the temperature quite well, but at large radii, the monochromatic source overestimates temperatures by a factor of two on average.

The disparity in the magnitude of ionization and temperature errors is a reflection of the strong frequency dependence of the bound–free absorption coefficients. Photo-ionization of hydrogen or helium by 0.5 keV photons is rare, but when it does occur, at least  $\sim 90\%$  of the original photon energy is left to be deposited mostly as heat, unless the free electron density is very low. Because the ionization of hydrogen and helium by the monochromatic source is very inaccurate, errors in the free electron density will substantially alter the amount of secondary electron energy deposited as heat, rather than further ionization.

The consequences of miscalculating ionization and heating could affect efforts to model and interpret current and future 21 cm measurements, since the primary 21 cm observable, the differential brightness temperature ( $\delta T_b$ ), depends on the hydrogen neutral fraction, UV radiation field, electron density, and the gas kinetic temperature ( $T_K$ ) (Furlanetto, 2006). Neglecting the presence of a Ly $\alpha$  background, the scaling

$$\delta T_b \propto T_K^{0.4} (1 + \delta) (1 + z)^{-1/2} \times \begin{cases} x_{\text{H I}} n_e & , n_e \gg n_{\text{H I}} \\ x_{\text{H I}}^2 & , n_e \ll n_{\text{H I}} \end{cases} \quad (6.21)$$

holds approximately in regimes where  $T_{\text{CMB}} \ll T_K \lesssim 10^4$  K.

In the immediate vicinity of radiation sources where gas is entirely ionized,  $\delta T_b \rightarrow 0$  due to the leading

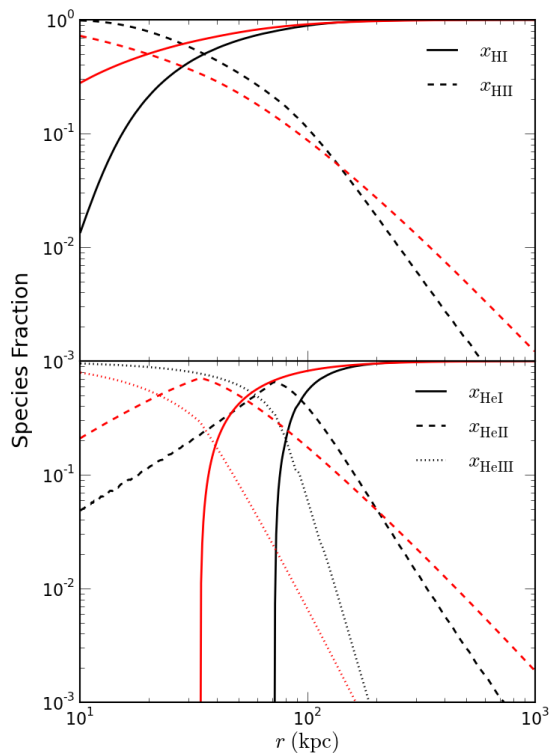


Figure 6.2 Comparison of hydrogen (top) and helium (bottom) ionization profiles around an  $\alpha = 1.5$  power-law X-ray source after 45 Myr using continuous (black) and monochromatic (red) SEDs.

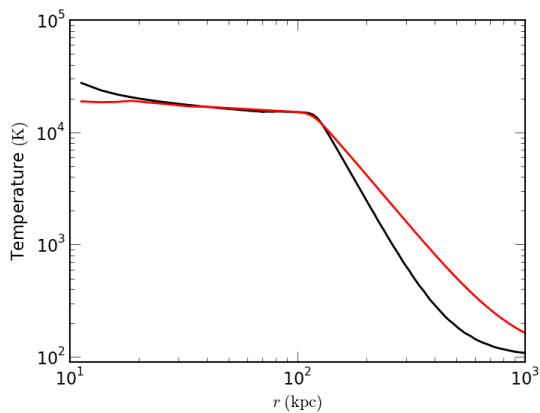


Figure 6.3 Comparison of temperature profiles around an  $\alpha = 1.5$  power-law X-ray source after 45 Myr using continuous (black) and monochromatic (red) SEDs.

$x_{\text{H I}}$  term, but at large radii where the ionizing flux is weaker, the  $\delta T_b$  signatures of stars and quasars could vary significantly solely due to miscalculations of  $x_{\text{H I}}$ ,  $n_e$ , and  $T_K$ . The above scalings have especially strong consequences for gas within a few Mpc of strong X-ray sources, where hydrogen is weakly ionized, temperatures are of order  $10^2$ - $10^3$  K, and the free electron density is enhanced due to efficient ionization of helium by the hard radiation field. In the earliest stages of reionization where  $T_K < T_{\text{CMB}}(z)$  and the Ly- $\alpha$  background is important, errors in  $x_{\text{H I}}$ ,  $n_e$ , and  $T_K$  will lead to errors in  $\delta T_b$  as well, though in a less straightforward way, since the spin temperature,  $T_S$ , must be computed carefully.

## 6.5 Optimization Strategy

To avoid errors of the sort described in the previous section, we have developed a technique for optimally constructing discrete SEDs that preserves the ionization and heating properties of their continuous counterparts. Although ray-tracing algorithms are capable of tabulating the relevant ionization and heating quantities (Equations (6.11) and (6.12)), few codes have taken advantage of this, and have instead cast monochromatic rays (e.g., state of the art reionization simulations with  $n_\nu = 5$ ; Trac et al., 2008). Monte Carlo codes (e.g., CRASH; Maselli et al., 2003) have been used to simulate reionization with  $n_\nu \geq 20$  multi-frequency photon packets (Ciardi et al., 2012), though such a large number of frequencies may be computationally debilitating for some algorithms, or unnecessary depending on the problem of interest.

Even when the algorithm of choice is compatible with propagating continuous radiation fields via tabulation of Equations (6.11) and (6.12), it may not be computationally advantageous. The overhead alone can in fact be substantial, particularly in the case of source-dependent SEDs — for example, the SED of a stellar population as a function of age, or BH accretion spectra that vary with mass or luminosity. Such situations would require a separate lookup table for Equations (6.11) and (6.12) at each age/mass/luminosity of interest for a given radiation source. In addition, there are algorithms for which propagating continuous radiation fields in large volumes become completely intractable, yet large volumes are a necessity for the science questions of interest (e.g., reionization). For more discussion on these issues, see Section 6.7.

As introduced in Section 6.3, our optimization strategy relies on the fact that the SED of a radiation source appears only in the quantities  $\Phi_i$  and  $\Psi_i$  (see Equations (6.11) and (6.12)). If we can construct a

discrete SED that reproduces the values of  $\Phi_i$  and  $\Psi_i$  to a high degree of accuracy over a column density interval of interest, then the discrete radiation field is indistinguishable from its continuous counterpart, and we have successfully preserved the true radiative properties of the source.

For sources with discrete SEDs, Equations (6.11) and (6.12) become

$$\Phi'_i(\tau_{\nu_n}) \equiv \sum_{n=1}^{n_\nu} \frac{I_n}{h\nu_n} e^{-\tau_{\nu_n}} \quad (6.22)$$

$$\Psi'_i(\tau_{\nu_n}) \equiv \sum_{n=1}^{n_\nu} I_n e^{-\tau_{\nu_n}}, \quad (6.23)$$

where we have used primes to indicate that these quantities are computed by direct summation over  $n = 1, 2, \dots, n_\nu$  frequencies, rather than by a continuous integral.

Ensuring that  $\Phi_i = \Phi'_i$  and  $\Psi_i = \Psi'_i$  is a minimization problem of dimensionality  $2n_\nu$ , since each additional frequency bin lends two degrees of freedom — its frequency ( $\nu_n$ ), and the fraction of the bolometric luminosity assigned to that frequency ( $I_n$ ). Our goal is to minimize the difference between continuous and discrete solutions, i.e.,

$$\begin{aligned} \Phi_i - \Phi'_i &= 0 \\ \Psi_i - \Psi'_i &= 0. \end{aligned} \quad (6.24)$$

These functions span several orders of magnitude over a broad range in column density, making it more practical to seek solutions to

$$\begin{aligned} \log\left(\frac{\Phi_i}{\Phi'_i}\right) &= 0 \\ \log\left(\frac{\Psi_i}{\Psi'_i}\right) &= 0 \end{aligned} \quad (6.25)$$

which place equal emphasis on all column densities. Preserving the high column density behavior of  $\Phi_i$  and  $\Psi_i$  is especially important for very luminous sources and/or environments with dense clumps in the immediate vicinity of the source, since the actual photoionization and heating rates are a combination of  $\Phi_i$ ,  $\Psi_i$ , and the normalization factor  $A_i \propto L_{\text{bol}}/r^2$ .

For a given  $n_\nu$  and source SED, we solve Equation (6.25) using the optimization technique Simulated Annealing (Kirkpatrick et al., 1983, Černý, 1985), which traverses our  $2n_\nu$  dimensional parameter space in

search of the frequency–normalization pairs  $(\nu_n, I_n)$  that best reproduce the values of  $\Phi_i$  and  $\Psi_i$ . We leave a more detailed description of the algorithm and our implementation of it to the Appendix.

## 6.6 Results

### 6.6.1 Optimal Discrete SEDs

We have obtained optimal SEDs for a  $10^5$  K blackbody emitting in the range 13.6-100 eV, and an  $\alpha = 1.5$  power-law X-ray source with emission spanning the interval  $10^2$ - $10^4$  eV. In each case, we set the upper column density limit for our optimization to be the column density of a fully neutral medium, i.e.,  $N_{\text{H I}}^{\text{max}} = n_{\text{H}} L_{\text{box}}$  and  $N_{\text{He I}}^{\text{max}} = n_{\text{He}} L_{\text{box}}$ , where we use  $L_{\text{box}}$  to denote the size of the domain, as in RT06. For the  $10^5$  K blackbody simulations, this works out to be  $N_{\text{H I}}^{\text{max}} = 3.1 \times 10^{19} \text{ cm}^{-2}$ , and for the power-law X-ray simulations,  $N_{\text{H I}}^{\text{max}} \simeq \times 10^{22} \text{ cm}^{-2}$  and  $N_{\text{He I}}^{\text{max}} \simeq \times 10^{21} \text{ cm}^{-2}$ . For cosmological simulations with periodic boundary conditions, the upper column density limits would need to be chosen based on a maximum length scale of interest, or for radiative feedback focused simulations, by the column density of the densest objects of interest (damped Ly $\alpha$  systems, for example). Such choices are already made in ray-tracing calculations to limit computational expense. Generally, rays are terminated once the emission has been attenuated by a large factor.

The only situation in which we do not evaluate the full cost function is  $n_{\nu} = 1$ , where we instead optimize for the optically thin regime alone (i.e., only the first term of Equation G.2), where  $\Phi_i$  and  $\Psi_i$  are  $\sim$  constant with column density. In this case, the optimal solutions are simply those that preserve the bolometric luminosity of the source and the total number of ionizing photons, and can be verified analytically (Equations (6.11) and (6.12)). For the case of a hydrogen and helium medium, we have found that neglecting He II opacities mitigates the computational cost of the computation while resulting in no appreciable changes in our optimal SEDs and thus negligible changes in  $\Phi'$  and  $\Psi'$ . The main results are summarized in Figures 6.6 and 6.7 and Tables 6.1 and 6.2, all results derived from  $K = 2 \times 10^4$  and  $K = 10^4$  Monte-Carlo trials, for the  $10^5$  K blackbody and  $\alpha = 1.5$  power-law source, respectively.

From Tables 6.1 and 6.2, it is clear that the optimal emission frequencies for both sources are not

Table 6.1. Optimal SEDs for  $10^5$  K Blackbody Sources

| $n_{\nu}$ | $n = 1$       | $n = 2$       | $n = 3$       | $n = 4$       |
|-----------|---------------|---------------|---------------|---------------|
| 1         | (29.61, 0.89) | ...           | ...           | ...           |
| 2         | (27.93, 0.68) | (62.04, 0.21) | ...           | ...           |
| 3         | (20.58, 0.39) | (40.75, 0.39) | (69.23, 0.11) | ...           |
| 4         | (17.98, 0.23) | (31.15, 0.36) | (49.09, 0.24) | (76.98, 0.06) |

Note. — Each entry is the  $(h\nu_n, I_n)$  pair for bin  $n$ . Energies are in units of eV, and normalizations are expressed as fraction of the bolometric luminosity.

Table 6.2. Optimal SEDs for  $\alpha = 1.5$  Power-Law X-ray Sources

| $n_{\nu}$ | $n = 1$        | $n = 2$        | $n = 3$        | $n = 4$        |
|-----------|----------------|----------------|----------------|----------------|
| 1         | (999.98, 1.00) | ...            | ...            | ...            |
| 2         | (255.87, 0.17) | (2553.6, 0.83) | ...            | ...            |
| 3         | (171.93, 0.08) | (518.22, 0.14) | (3098.5, 0.78) | ...            |
| 4         | (146.11, 0.05) | (307.30, 0.07) | (704.56, 0.14) | (3564.2, 0.73) |

Note. — Same as Table 6.1 but for an  $\alpha = 1.5$  power-law X-ray source.

evenly spaced above the hydrogen or helium ionization thresholds, either in linear or log-space. In each case, the addition of a new frequency bin leads to a decrease in both the emission frequency and normalization of all other bins. This signifies (1) the efficacy with which high energy photons photoionize and photoheat gas at large column densities (a regime inaccessible to lower energy photons which become optically thick at small columns), and (2) the increase in excess electron kinetic energy available for further ionization and heating with increasing photon energy. The former effect is most important for the blackbody source, which we can see in Figure 6.4. Not surprisingly, it is the lowest energy photons ( $h\nu_1 = 17.98$  eV) in the  $n_\nu = 4$  spectrum that are responsible for the ionization (through  $\Phi$ ) in the optically thin regime, while successively higher frequency bins become the primary agents of ionization as we move to higher column densities. The same trend does not hold completely in Figure 6.4b, as in this case it is the second and third energy bins that provide the bulk of the heating (through  $\Psi$ ) at low column densities.

For the X-ray source, the second effect dominates, as the optical depth at any column density is small for most photons considered ( $10^2 < h\nu < 10^4$  eV) over the entire domain. As shown in Figure 6.5, the photons responsible for the majority of the heating (through  $\Psi$ ) over all column densities are those in the highest energy bin, the same photons which are the least effective at ionization. The trends and errors of Figure 6.5 are the same for  $\Phi_i$  and  $\Psi$  as a function of helium column density.

In Figures 6.6 and 6.7, we show the probability distribution functions (PDFs) for the position and normalization of the optimal SED frequency bins obtained (drawn from Tables 6.1 and 6.2). Solutions are less tightly constrained as  $n_\nu$  is increased, as evidenced by a broadening in the distributions of frequency and normalization for each bin. This behavior is expected, given that each new bin contributes to the magnitude of  $\Phi$  and  $\Psi$  in some region of column density space previously occupied by one or more other frequencies.

Holding  $I_n$  constant, a decrease in  $\nu_n$  will cause a negative vertical shift in the contribution of bin  $n$  to the magnitude of  $\Phi$ , for example, but will simultaneously add power at larger column densities, since the turnover point for bin  $n$  occurs at  $N_{\text{char}} \sim \sigma_{\nu_n}^{-1}$ , and  $\sigma_{\nu_n} \sim \nu^{-3}$ . To avoid an increase in  $f$ , the power lost at small column densities has to be compensated for, either by a decrease in  $\nu_{n-1}$ , or an increase in  $I_{n-1}$ , where  $n-1$  denotes the bin with frequency  $\nu_{n-1} < \nu_n$ . As a result, there are degeneracies between all bins, and the magnitude of the degeneracy is greatest for bins positioned closest in frequency-space. In order to tighten

the PDFs for each optimal frequency bin, one or more terms would need to be added to  $f$ , in order to assign preference to one set of bins over another. For our purposes, any SED that minimizes  $f$  is just as good as any other, but additional terms in the cost function are certainly justifiable in the case of a ray-tracing calculation, where higher emission frequencies increase the computational cost of a calculation since their mean free paths are long. Adding a term to  $f$  that scales with  $\nu_n$  would encourage optimal SEDs with the smallest emission frequencies possible, for example.

Optimization for  $n_v > 4$  is certainly possible, though unnecessary in our case. At a given frequency, the transition from optically thin  $\tau = 0$  to optically thick ( $\tau \gtrsim 1$ ) in the functions  $\Phi$  and  $\Psi$  occurs over an order of magnitude in column density (by definition, see Equation (6.10)). For both SEDs we have investigated, the column density regime of interest spans fewer than four orders of magnitude, motivating our choice of  $1 \leq n_v \leq 4$ . We have performed optimizations with  $n_v > 4$ , but the addition of each additional bin when  $n_v > \log_{10}(N_{\max}/N_{\min})$  reduces the error between  $\Phi$  and  $\Phi'$ , and  $\Psi$  and  $\Psi'$  much less significantly than additional bins when  $n_v \leq \log_{10}(N_{\max}/N_{\min})$ . For a given  $n_v$ , increasing  $N_{\max}$  will simply increase  $\max|\Phi - \Phi'|$  and  $\max|\Psi - \Psi'|$ .

### 6.6.2 Confirmation with One-dimensional Calculations

To verify the solutions of the previous section, we ran simulations identical to those of Section 6.4 but with our optimal discrete SEDs. We compute  $\Gamma_i$ ,  $\gamma_i$ , and  $\mathcal{H}_i$  via Equations (6.16)–(6.18) “on-the-fly,” rather than generating lookup tables of  $\Phi_i$  and  $\Psi_i$ . As expected, accurate preservation of the quantities  $\Phi_i$  and  $\Psi_i$  over the column density ranges of interest renders ionization and temperature profiles around sources of discrete radiation indistinguishable from their continuous counterparts.

In Figure 6.8, we compare ionization and heating around a  $10^5$  K blackbody after 100 Myr of evolution as in Section 6.4, showing the solution obtained with our optimal monochromatic (red) and four-bin (blue) SEDs. The continuous and four-bin solutions are indistinguishable.

In Figure 6.9, we perform the same analysis for the  $\alpha = 1.5$  power-law simulations. Our optimal four-bin SED reproduces the hydrogen and helium ionization profiles (and thus electron density) and temperature of a continuous SED to high precision. The most noticeable errors are in the hydrogen neutral fraction within

the hydrogen ionization front, where errors between four-bin and continuous solutions are still only  $\sim 1\%$ . Errors in  $x_{\text{He III}}$  are negligible, justifying our neglect of  $N_{\text{He II}}$  in the optimization process.

It should be noted that our optimal monochromatic SED for the X-ray source performs even more poorly than the fiducial 0.5 keV SED. This signifies a general problem with monochromatic emission for any spectrum with a hard component. Whereas the monochromatic optimization ( $\tau_{\nu} = 0$ ) works quite well in the  $10^5$  K blackbody case since hydrogen absorbs UV photons readily, X-rays are not so readily absorbed by hydrogen and/or helium. As a result, the characteristic column density where most 1 keV photons are absorbed lies outside of our domain, leading to severe under-ionization (of all species) and under-heating. The reason the 0.5 keV SED works better is because its characteristic absorption column is smaller, lying within our domain. We have experimented with relaxing the optically thin requirement for monochromatic optimization, and find that it is equally difficult to preserve ionization and heating profiles with emission at a single frequency.

### 6.6.3 Three-dimensional Radiation-hydrodynamic Simulations with *Enzo*

To study the impact of spectral discretization in a more complex setting, we ran RT06 test problem 2 with hydrodynamics, as well as two fully three-dimensional cosmological radiation-hydrodynamic simulations similar to those of Abel et al. (2007) and Alvarez et al. (2009), both with the *Enzo* code (Bryan and Norman, 1997, O’Shea et al., 2004)<sup>1</sup>. All analysis was performed with *yt* (Turk et al., 2011).

The results of the RT06 radiation-hydrodynamic test problem are shown in Figure 6.10, where we compare the solutions obtained using the four-bin SED employed by Wise and Abel (2011) in addition to our own (Table 6.1). The solutions are indistinguishable, which is expected given the relatively small range of column density explored in this problem.

The cosmological simulations follow the formation of a  $100M_{\odot}$  PopIII star, its brief 2.7 Myr lifetime in which it emits  $1.2 \times 10^{50}$  ionizing photons per second, and the X-ray emission resulting from accretion onto a remnant BH assumed to form via direct collapse after stellar death (as in Alvarez et al. (2009)). The accretion rate, and thus luminosity assuming  $\epsilon_{\bullet} = 10\%$ , is the Bondi–Hoyle accretion rate of the cell in

<sup>1</sup> Revision f4a8b5f5e6c5, modified to form only one star and use optimal SEDs.

which the BH resides. The simulation volume is  $0.25 \text{ Mpc } h^{-1}$  on a side, with  $128^3$  particles and cells on the root grid. A single nested grid occupies the inner  $1/8$  of the volume at twice the root grid resolution, where eight additional levels of adaptive-mesh refinement are allowed, yielding a peak spatial resolution of  $0.23 \text{ pc } h^{-1}$ .

We run two simulations, each identical to the other except for the choice of discrete SED. Our ‘control’ simulation uses monochromatic SEDs — the PopIII star is a monochromatic source of  $E = 29.6 \text{ eV}$  photons, while the X-ray source emits at  $E = 2 \text{ keV}$ . The second simulation employs the optimal four-bin SEDs found in Tables 6.1 and 6.2.

As shown in Figure 6.11, the magnitude of the errors between monochromatic and  $n_{\nu} = 4$  solutions is even more significant in the cosmological problem than in the RT06 test problem, since the ionizing luminosity of the blackbody source considered is nearly two orders of magnitude larger ( $1.2 \times 10^{50}$  versus  $5 \times 10^{48} \text{ s}^{-1}$ ). For very luminous sources, even small errors in  $\Phi$  and  $\Psi$  will become noticeable as characteristic timescales for photoionization and heating are short.

During the BH phase of evolution, there are more ways for the monochromatic and multi-frequency solutions to differ aside from the SEDs being employed. The accretion luminosity depends on local gas properties, which will be different in each simulation due to errors accrued during the PopIII star’s lifetime. Properties of the broader medium will of course vary for the same reason, leading to changes in how far soft X-rays are able to propagate before being absorbed. Throughout the 100 Myr of evolution after the PopIII star’s death, the Bondi–Hoyle accretion rate and thus luminosity of the accreting BH is on average an order of magnitude smaller in the  $n_{\nu} = 4$  simulation than for the monochromatic case. Errors in ionization and temperature exceeding an order of magnitude persist throughout the BH phase as well. Rather than attempt to disentangle the BH phase induced errors from the preexisting errors, we simply emphasize that SED-induced errors will compound in feedback situations like this, since the initial conditions of each subsequent generation of objects will have been contaminated by errors associated with the previous one.

We cannot comment on the relative errors between monochromatic and multi-frequency treatments beyond the outermost column density contour, as our optimization extended only to  $N_{\text{HI}} = 3.1 \times 10^{19} \text{ cm}^{-2}$ . Future work focused on larger cosmological volumes, more luminous sources, and harder radiation fields

will need to construct optimal SEDs valid beyond  $N_{\text{H I}} = 10^{20} \text{ cm}^{-2}$ , at least.

## 6.7 Discussion

Algorithms developed for the purpose of studying point-source radiation (e.g., ray-tracing) are in principle capable of propagating continuous radiation fields, that is, tabulating Equations (6.11) and (6.12) and computing ionization and heating rates via Equations (6.13)–(6.15). The reason many have not taken this approach could be due to the additional computational overhead involved with using continuous SEDs — the quantities  $\Phi_i$  and  $\Psi_i$  must be tabulated over the complete column density interval of interest. This includes column densities of all absorbing species, each of which must extend from the smallest expected column (i.e., the column density of a “fully ionized” cell — we adopted a minimum species fraction of  $x_{\text{min}} = 10^{-5}$ ) up to the largest expected column (i.e., the column density of a fully neutral medium). The dimensionality of  $\Phi_i$  and  $\Psi_i$  can be increased even further if for example energy-dependent secondary electron treatments (e.g., Ricotti et al., 2002, Furlanetto and Johnson Stoever, 2010) or time-dependent SEDs are of interest.

For the simulations of Section 6.4.2, we generated three-dimensional lookup tables for  $\Phi_i$  and  $\Psi_i$  covering the column density range  $10^{11} < N_{\text{H I}} < 10^{21}$ , and  $10^{10} < N_{\text{He I}}, N_{\text{He II}} < 10^{20}$ , sampling  $N_{\text{H I}}$  at 200 points, and  $N_{\text{He I}}$  and  $N_{\text{He II}}$  with 100 points each, resulting in six three-dimensional tables, each consisting of  $2 \times 10^6$  elements. We found that poorer sampling (e.g., tables of dimension  $100 \times 50 \times 50$ ) leads to artificial “notches” in ionization and temperature profiles due to errors in the trilinear interpolation. In our case,  $\Phi_{\text{H I}} = \Phi_{\text{He I}} = \Phi_{\text{He II}}$  and  $\Psi_{\text{H I}} = \Psi_{\text{He I}} = \Psi_{\text{He II}}$  since all emission occurs above  $10^2 \text{ eV}$ , making the lower limit of integration for each quantity identical. In the general case, where emission extends all the way to the hydrogen ionization threshold, all six quantities would be unique. Generating these tables can take hundreds of CPU hours or more for a single SED depending on the number of column density elements. In addition, the radiative transfer solver requires additional modules to read in the lookup table, and perform interpolation four times per absorbing species per grid element (see Eqs (6.13)–(6.15)). For sources with discrete SEDs, one can simply compute the photo-ionization rate for each neutral species, from which point the secondary ionization and heating rate coefficients are obtained in a simple algebraic fashion (see Eqs (6.16)–(6.18)).

For high-resolution simulations focused on a single source of radiation (e.g., Kuhlen and Madau, 2005, Alvarez et al., 2009), the additional effort required to accommodate continuous radiation fields seems well worth it to ensure that the ionization and thermal state of the gas is captured accurately. However, in large-scale simulations of cosmic reionization, which may spawn hundreds of thousands or perhaps millions of radiating ‘star particles’ (depending on the simulation volume, resolution, etc.), ray-tracing methods are certainly not the most computationally advantageous algorithm. This is because the computational cost of a ray-tracing calculation scales with the number of radiation sources *and* the number of frequency bins in each source SED (though the former cost can be mitigated by merging nearby radiation sources; Trac and Cen, 2007, Okamoto et al., 2012). If photons with long mean free paths are of interest, the simulation will be even more expensive since rays must be followed to larger distances, i.e., more ray segments and iterations of the numerical solver are required. An appealing option is to instead use moment-based methods such as the Variable Eddington Tensor approach (e.g., Gnedin and Abel, 2001, Petkova and Springel, 2009), flux-limited diffusion (e.g., Reynolds et al., 2009), or other variations (González et al., 2007, Aubert and Teyssier, 2008, Finlator et al., 2009), as the computational cost of such algorithms is independent of the number of radiation sources and the mean free paths of photons, scaling only with the number of frequency bins in each source spectrum.

As discussed in Section 6.2, multi-group schemes common in the literature are an improvement over fiducial discrete SEDs, though it is not generally clear how many bandpasses are required for a given problem, or where they should lie in frequency space. Moreover, multi-group radiation suffers from the same problem as discrete polychromatic emission: photons at each frequency are absorbed near a characteristic column density,  $N_{\text{char}}$ . Computing new spectrum-weighted absorption cross-sections,  $\bar{\sigma}_n$ , for each frequency group merely shifts the location of  $N_{\text{char}}$ .

In principle, our minimization technique could be used to optimally select which bandpasses should be used for a multi-group algorithm, though in practice it would be much more computationally expensive. Rather than varying the location ( $\nu_n$ ) or normalization ( $I_n$ ) of frequency bin  $n$  on each Monte Carlo step, one would instead vary the position of bandpass edges, which would change the mean photon energy in each bandpass ( $h\bar{\nu}_n$ ) and spectrum-weighted cross section,  $\bar{\sigma}_n$  (e.g., Aubert and Teyssier, 2008). Because  $h\bar{\nu}_n$  and

$\bar{\sigma}_n$  are integral quantities, they would need to be computed numerically on each Monte-Carlo step, and thus hundreds of thousands of times for a single optimization. See Appendix F for a more detailed analysis of multi-group methods.

## 6.8 Conclusions

We have shown that the manner in which a discrete SED is constructed can induce substantial errors in simulation results, both in the ionization and temperature profiles around stars and quasars. But, these errors can be avoided to a large degree using only four discrete emission frequencies if source SEDs are designed via the methods of Section 6.5. Discrete SEDs constructed in a simple way (e.g., bins linearly spaced in frequency) will perform more poorly than optimally selected SEDs with the same number of bins, since it is the column density interval of interest that dictates the range of photon energies required, and the power to which each is assigned.

In general, discrete SED treatments fail to ionize and/or heat gas at large column densities, i.e., large physical scales or environments with dense clumps of gas. This has strong implications for simulations dedicated to understanding the magnitude and mode of radiative feedback on gas surrounding radiation sources. Current questions of this sort include whether or not radiation stimulates or suppresses further star formation in nearby proto-stellar clouds, and if radiative feedback can stifle the growth of SMBHs at high redshift.

As expected, extending our one-dimensional work to three-dimensions produces ionized regions around a first star and remnant BH that deviate significantly in ionized fraction, temperature, size, and morphology. Such findings have implications in radiative feedback, but also in studies of both hydrogen and helium reionization. Certainly miscalculations of the ionization state of gas surrounding galaxies in the early universe will lead to errors in the volume averaged neutral fraction, volume filling factor of ionized gas, and the optical depth of the CMB to electron scattering ( $\tau_e$ ). As we demonstrated in Section 6.4, such errors also introduce uncertainties in the interpretation of future 21 cm measurements, since the primary observable quantity ( $\delta T_b$ ) depends directly on the hydrogen neutral fraction, electron density, and gas kinetic temperature.

Our optimizations in this work are by no means comprehensive, having selected two commonly used radiation sources (UV blackbody and X-ray power law) as test cases to demonstrate the method. However, optimization for more complex spectra is straightforward, and any new optimizations run will be made publicly available by the authors. The minimization code and one-dimensional radiative transfer codes are both available upon request. We leave more detailed investigations of reionization and radiative feedback, including multiple radiation sources and multi-frequency radiation transport, to future work.

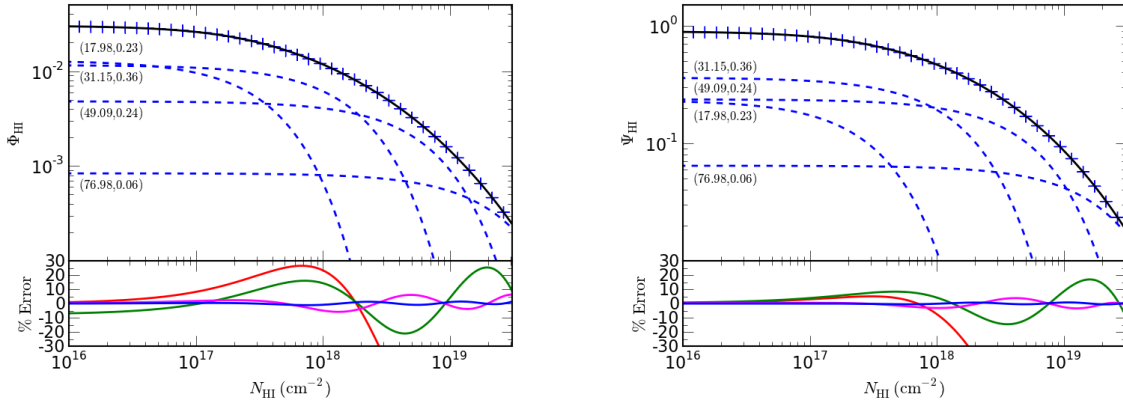


Figure 6.4 Top Panels: Comparison of  $\Phi_{\text{H I}}$  and  $\Phi'_{\text{H I}}$  (a) and  $\Psi_{\text{H I}}$  and  $\Psi'_{\text{H I}}$  (b) as a function of H I column density for a  $10^5$  K blackbody, showing the numerically computed continuous integral (solid black), best-fit composite four-bin discrete sum (blue crosses), and the contribution from each individual discrete frequency bin (dashed blue). Annotations represent the  $(h\nu_n, I_n)$  pairs for each frequency group, drawn from Table 6.1. Bottom Panels: Percent error between discrete and continuous solutions. The solid blue line is the error for the four-bin optimal solution, while the errors induced by three-, two-, and one-bin solutions are shown in magenta, green, and red, respectively.

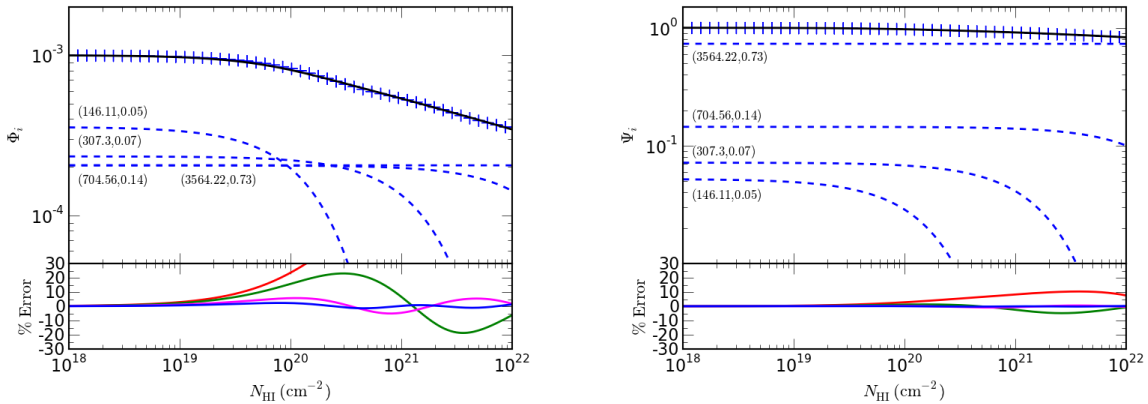


Figure 6.5 Same as Figure 6.4 but for an  $\alpha = 1.5$  power-law X-ray source.

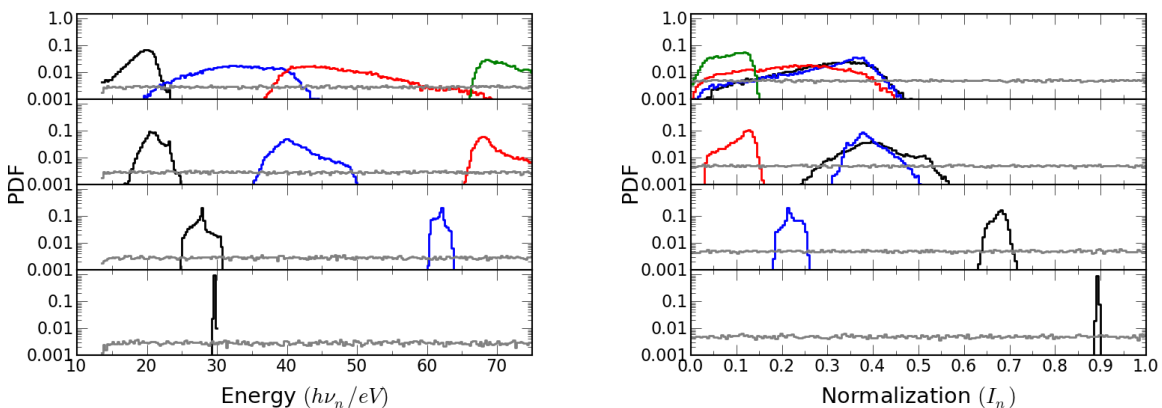


Figure 6.6 Emission energy (a) and normalization (b) probability distribution functions (PDFs) of optimized discrete  $10^5$  K blackbody spectrum using  $n_v = 1, 2, 3, 4$  (from bottom to top). In each panel, the gray histogram denotes the initial guesses for all Monte-Carlo trials, and the black, blue, red, and green histograms show the end point for the first, second, third, and fourth bins, respectively (ordered by increasing emission frequency).

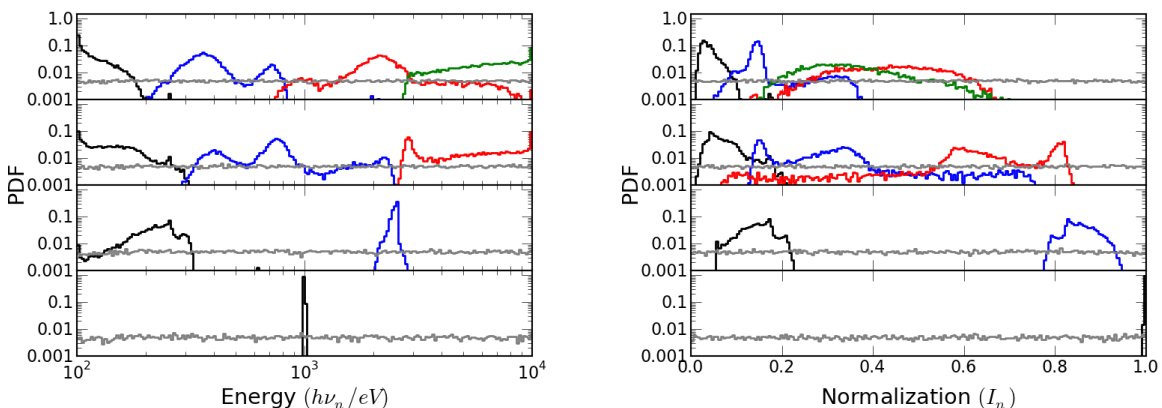


Figure 6.7 Same as Figure 6.6 but for an  $\alpha = 1.5$  power-law X-ray source.

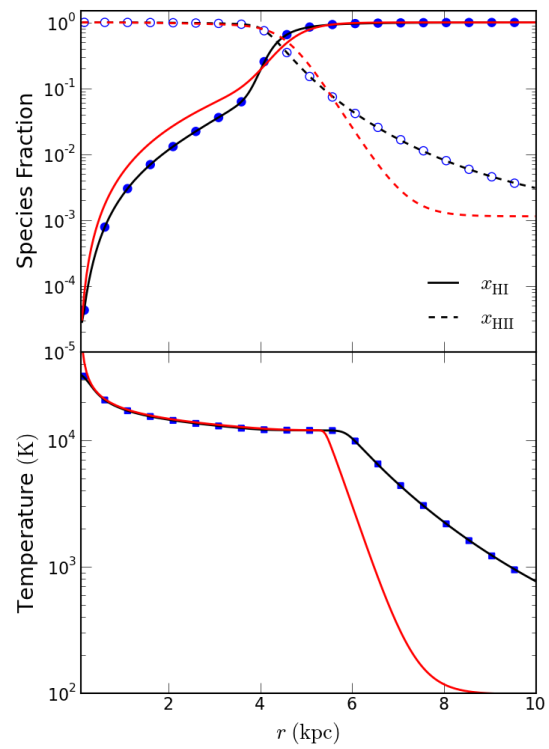


Figure 6.8 Comparison of ionization (top) and temperature (bottom) profiles around a  $10^5$  K blackbody source after 100 Myr showing the solutions obtained using continuous (black), monochromatic (red), and optimal four-bin discrete (blue circles/squares) SEDs.

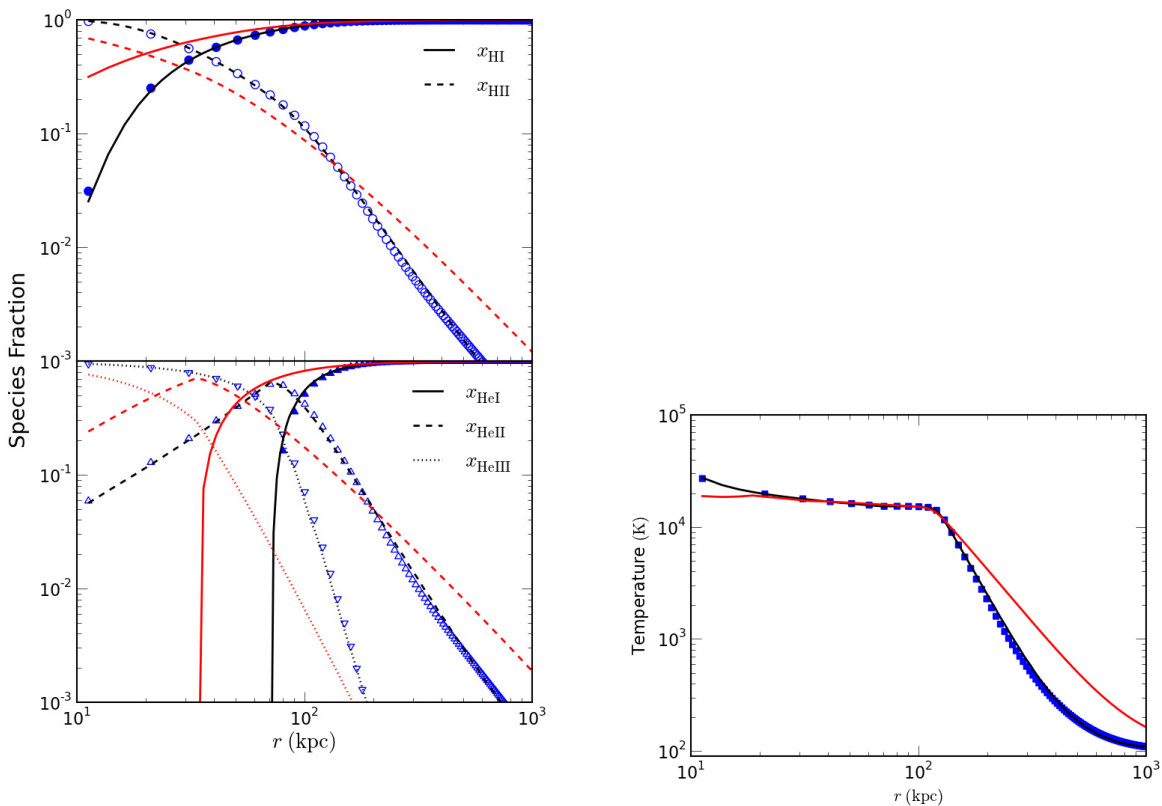


Figure 6.9 Comparison of hydrogen and helium ionization (a) and temperature profiles (b) around a power-law X-ray source after 50 Myr showing the solutions obtained using continuous (black) and optimal four-bin discrete (blue symbols) SEDs.

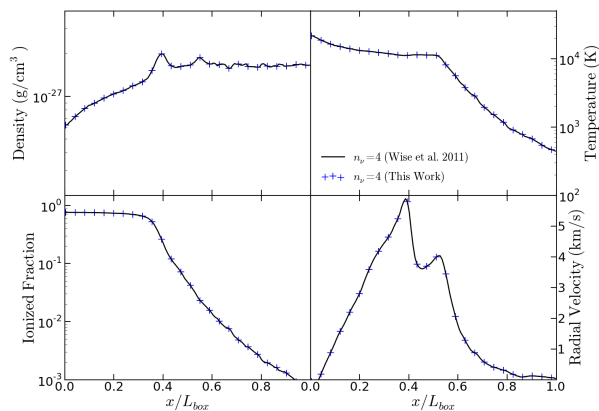


Figure 6.10 Comparison of the four-bin solutions of Wise and Abel (2011) (black) and our own (blue crosses) in a radiation-hydrodynamic simulation using the *Enzo* code. The setup is the same as in RT06 Test Problem 2, except hydrodynamics is included.

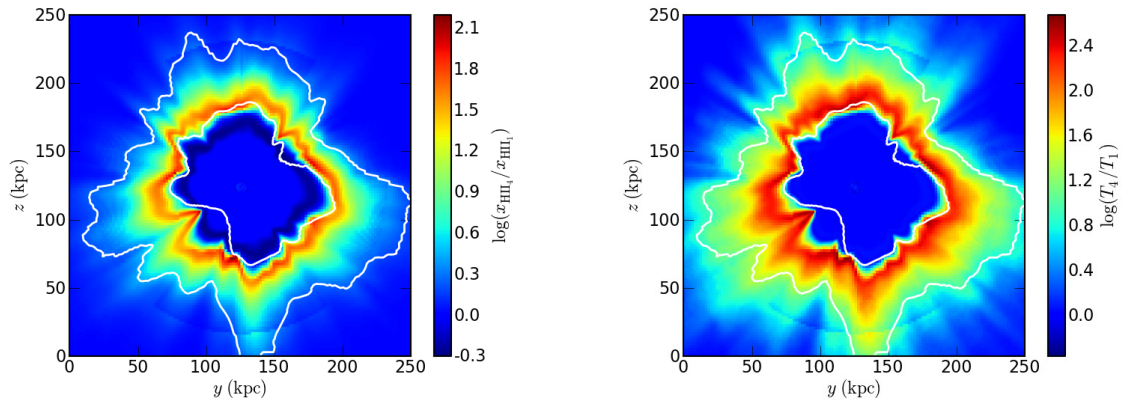


Figure 6.11 Ratio of slices of the ionized fraction (a) and temperature (b) obtained using our optimized  $n_{\nu} = 4$  blackbody SED ( $x_{\text{H II}_4}, T_4$ ) and the standard monochromatic SED ( $x_{\text{H II}_1}, T_1$ ). Both slices are 2.25 Myr after the formation of a Population III star. Contours (from center outwards) correspond to hydrogen column densities of  $N_{\text{H I}} = 2$  and  $4 \times 10^{19} \text{ cm}^{-2}$ .

## Chapter 7

### Conclusions and Future Work

The results presented in previous chapters have implications for observational campaigns as well as theoretical models. In this final chapter, I will summarize my findings in a broader context and where appropriate, include a discussion of future work that would address lingering issues or pave a new path forward.

Let us begin with perhaps the most pertinent results for global 21-cm experiments. For many years, the conventional thinking has been that global 21-cm experiments should seek observations in many independent sky regions (Shaver et al., 1999, Pritchard and Loeb, 2010, Harker et al., 2012) since the galactic foreground varies across the sky while the global 21-cm signal does not. There is a trade-off, however, between the angular resolution and sensitivity of an experiment. An experiment with high angular resolution can observe many independent regions of the sky but each with rather poor sensitivity (Liu et al., 2013). Alternatively, one may build an experiment with a very broad beam (Harker et al., 2012, Burns et al., 2012), which will be very sensitive but limited to a small number of independent pointings.

The findings of Chapter 3 (Harker et al., 2015) suggest that even experiments with very broad beams ( $\sim 50^\circ$  FWHM) need not observe more than a few sky regions. This is a result of incorporating more stringent priors on the global 21-cm signal than has been done in previous work. For example, though Harker et al. (2012) used a model that assumed the global 21-cm signal had three turning points and thus effectively imposed a prior on the allowed structure of the signal, the locations of these turning points were not restricted (in general) by this assumption. This in principle allowed turning point B to occur at  $\delta T_b > 0$ , turning point C to occur at depths only possible in a Universe that cools more rapidly than is allowed by the

Hubble expansion, and turning point D to occur in the “super-saturated” regime (see Figure 1.12). The latter cases, at least, are exceedingly unlikely, as they would require significant deviations from well-understood physics underlying models of the global 21-cm signal.

By instead employing the tanh model in fits to synthetic datasets, we were restricted to physically realistic histories. This automatically guarantees that the overall normalization of the global 21-cm signal is constrained quite well – a feat formerly accomplished by observing multiple independent sky regions. Indeed, integration time played more of a role than the number of sky areas viewed (Figure 3.8). It seems a proper time to determine the optimal observing strategy for pointed experiments (e.g., DARE; Burns et al., 2012).

Unfortunately, but unsurprisingly, use of a more physically-motivated model like the tanh did not solve every difficulty in the realm of signal extraction. Degeneracies between the global 21-cm signal and the foreground are exceptionally strong at frequencies  $\nu \gtrsim 100$  MHz where the signal is most spectrally smooth. One can still recover the turning point positions accurately by using more complex foreground models or truncating the band, but even then, the inferred properties of the *IGM* were biased relative to those of the input model. This suggests that the choice of parameterization of the signal may be a limiting factor in precision measurements of the global 21-cm signal, as the biases result from subtle mismatches in the shape of the physical model for the global 21-cm signal and its best-fit tanh representation. This would be a fantastic test for model selection algorithms: under what observing conditions can one derive evidence that one signal parameterization fits the data better than another, when both can adequately recover the turning points? Perhaps then it will be time to determine what new physical insights are to be had from constraints on the curvature of the turning points (i.e., an extension of the analytical models presented in Chapter 2).

Putting these issues aside for a moment, in Chapter 4 we investigated a “two-stage approach” to extracting information from the global 21-cm signal. First, one uses a fast (but approximate) model like the tanh to recover the turning point positions, and then follows up by fitting a more expensive but physically-motivated ARES model to those turning point positions. Earlier work suggested that the turning points were robust indicators of IGM properties (Chapter 2), so it was a natural next step to determine how well they

constrained a simple galaxy formation model. It turns out that in this case the detection of all three turning points is vital, as the timing of these features in large part encodes the characteristic mass of star-forming halos at high- $z$ , which we parameterize via the parameter  $T_{\min}$ . The emission maximum – turning point D – is least sensitive to  $T_{\min}$ , but is the only feature that encodes the ionizing efficiency of the first galaxies. In tandem with  $N_{\text{LW}}$ , it is then an essential constraint on the stellar IMF in high- $z$  galaxies (Figure 4.8).

It is unfortunate that the modest amplitude of the 21-cm emission signal and its spectral smoothness completely counteract the fact that the galactic foreground grows weaker toward higher frequencies. The detection of turning point D may be easier, if, for example, the true 21-cm emission signal is sharper than that of our typical models. If not, we are surely to benefit from the incorporation of current constraints as priors, e.g., measurements of  $\tau_e$  from CMB experiments like *Planck*. In addition, if the emission maximum of the global 21-cm signal occurs at  $z \lesssim 12$ , we could in principle leverage near-future constraints from *JWST* and ground-based interferometers like *PAPER*, provided we develop models that simultaneously track the galaxy population and their impact on the IGM.

Our initial parameter estimation exercise also used perhaps the simplest galaxy formation model that can capture all features of the global 21-cm signal. In reality, feedback is likely to be important, though it has been completely neglected in our model. One very realistic possibility is that  $T_{\min}$  evolves with time, most likely increasing with decreasing redshift due to negative feedback. Perhaps it starts out at a few hundred K at redshifts  $z \gtrsim 30$ , at which time  $\text{H}_2$  cooling in the first halos leads to the formation of massive PopIII stars. Once a substantial LW background emerges, however, the  $\text{H}_2$  cooling channel will be unavailable to most halos, which will then need to wait until atomic cooling becomes efficient (at  $T_{\min} \sim 10^4$  K). Large-scale heating may eventually drive  $T_{\min} \gtrsim 2 \times 10^5$  K (Gnedin, 2000). Allowing a time-variable  $T_{\min}$  is a natural extension of our physical models that may lead to interesting signatures. In fact, it might provide a physically-motivated way of modifying the shape of the signal, and thus be another interesting test for model selection algorithms.

To make the parameter estimation problem more computationally tractable, all global 21-cm models in Chapter 4 were generated neglecting detailed solutions to the radiative transfer equation. However, in Chapter 5, it was shown that detailed frequency-dependent solutions can lead to large variations in the

depth and timing of the 21-cm minimum – likely more than enough to be a complicating factor for first-generation experiments. Crude approximations to the RTE tend to overestimate the importance of heating, leading to artificially shallow 21-cm absorption troughs (perhaps by  $\sim 20$  mK). Coincidentally, adoption of SEDs appropriate to HMXBs (MCD spectra rather than power-laws) induce modulations of similar order ( $\sim 20 - 50$  mK), depending on the neutral gas content of high- $z$  galaxies and the masses of accreting BHs.

It was recently suggested that the 21-cm power spectrum may be a powerful degeneracy-breaking tool with regards to the degeneracy between the shape and amplitude of the X-ray background at high- $z$  (Pacucci et al., 2014). Generating these models, even with a semi-numeric code like 21CMFAST, is rather expensive computationally. Development of an even simpler approach would enable forecasting exercises analogous to those presented in Chapter 4 but for the 21-cm power spectrum. In addition, this capability would allow us to include measurements from ground-based interferometers as priors within our global 21-cm signal procedure. Measurements at  $z \sim 8.4 - 8.8$  with *PAPER* are already entering interesting regions of parameter space (Ali et al., 2015, Pober et al., 2015), so this would be fairly timely work.

This issue naturally ties into Chapter 6, where we showed that discretization of the radiation field near stars and BHs in numerical simulations can lead to sizable inaccuracies in the gas properties nearby. Though originally our motivation for this work was in to prepare for large-scale cosmological simulations of Reionization, the results certainly apply to models of the 21-cm power spectrum as well. For example, if the X-ray background is dominated by sources with soft spectra we should expect stronger fluctuations in the IGM temperature (and thus 21-cm background) on small scales since soft X-rays are absorbed more readily by the IGM than hard X-rays. Crude radiative transfer calculations could then artificially shift power to different characteristic scales and bias inferences of the 21-cm power spectrum. As a result, new power spectrum models should go through the trouble of taking frequency-dependent effects into account.

In closing, a productive path forward seems to be one that enables disparate measurements of the high- $z$  Universe to be interpreted within a common framework. Because 21-cm cosmology is still in its adolescence, even simple models are extremely valuable because they are inexpensive enough computationally to be used in forecasting exercises and in directly fitting near-future datasets. Eventually, of course, simple models will need to be tested and/or calibrated with more sophisticated calculations, ranging from semi-

numeric codes to 3-D radiation-hydrodynamic simulations. Given the enormous dynamic range and suite of physical solvers required to simulate the global 21-cm signal, an apples-to-apples comparison is likely still several years away. As a result, I will continue with developing more general semi-analytic models until the accuracy of the data exceeds that of my models.

## Bibliography

- T. Abel, M. L. Norman, and P. Madau. Photon-conserving Radiative Transfer around Point Sources in Multidimensional Numerical Cosmology. *ApJ*, 523:66–71, September 1999. doi: 10.1086/307739.
- T. Abel, G. L. Bryan, and M. L. Norman. The Formation of the First Star in the Universe. *Science*, 295: 93–98, January 2002. doi: 10.1126/science.295.5552.93.
- Tom Abel, John H Wise, and Greg L Bryan. The H II Region of a Primordial Star. *ApJ*, 659:L87, April 2007.
- Zaki S Ali, Aaron R Parsons, Haoxuan Zheng, Jonathan C Pober, Adrian Liu, James E Aguirre, Richard F Bradley, Gianni Bernardi, Chris L Carilli, Carina Cheng, David R DeBoer, Matthew R Dexter, Jasper Grobbelaar, Jasper Horrell, Daniel C Jacobs, Pat Klima, David H E MacMahon, Matthys Maree, David F Moore, Nima Razavi, Irina I Stefan, William P Walbrugh, and Andre Walker. PAPER-64 Constraints on Reionization: The 21cm Power Spectrum at  $z=8.4$ . [arXiv.org](https://arxiv.org/abs/1502.06016), page 6016, February 2015.
- Y. Ali-Haïmoud and C. M. Hirata. Ultrafast effective multilevel atom method for primordial hydrogen recombination. *PRD*, 82(6):063521, September 2010. doi: 10.1103/PhysRevD.82.063521.
- A. C. Allison and A. Dalgarno. Spin Change in Collisions of Hydrogen Atoms. *ApJ*, 158:423, October 1969. doi: 10.1086/150204.
- M. A. Alvarez, J. H. Wise, and T. Abel. Accretion onto the First Stellar-Mass Black Holes. *ApJL*, 701: L133–L137, August 2009. doi: 10.1088/0004-637X/701/2/L133.
- D. Aubert and R. Teyssier. A radiative transfer scheme for cosmological reionization based on a local Eddington tensor. *MNRAS*, 387:295–307, June 2008. doi: 10.1111/j.1365-2966.2008.13223.x.
- J E Baldwin. Searches for primordial pancakes. pages 333–339, 1986.
- Edward A Baltz, Nickolay Y Gnedin, and Joseph Silk. Spectral Features from the Reionization Epoch. *The Astrophysical Journal*, 493(1):L1–L4, January 1998.
- J. M. Bardeen. Kerr Metric Black Holes. *Nat*, 226:64–65, April 1970. doi: 10.1038/226064a0.
- Rennan Barkana and Abraham Loeb. In the beginning: the first sources of light and the reionization of the universe. *Physics Reports*, 349(2):125–238, 2001.
- Rennan Barkana and Abraham Loeb. Detecting the earliest galaxies through two new sources of 21 centimeter fluctuations. *ApJ*, 626(1):1, 2005a.

- Rennan Barkana and Abraham Loeb. Detecting the earliest galaxies through two new sources of 21 centimeter fluctuations. *ApJ*, 626(1):1, 2005b.
- Antara R Basu-Zych, Bret D Lehmer, Ann E Hornschemeier, Rychard J Bouwens, Tassos Fragos, Pascal A Oesch, Krzysztof Belczynski, W. N. Brandt, Vassiliki Kalogera, Bin Luo, Neal Miller, James R Mullaney, Panayiotis Tzanavaris, Yongquan Xue, and Andreas Zezas. THE X-RAY STAR FORMATION STORY AS TOLD BY LYMAN BREAK GALAXIES IN THE 4 Ms CDF-S. *ApJ*, 762(1):45, December 2013.
- Robert H Becker, Xiaohui Fan, Richard L White, Michael A Strauss, Vijay K Narayanan, Robert H Lupton, James E Gunn, James Annis, Neta A Bahcall, and J Brinkmann. Evidence for Reionization at  $z \sim 6$ : Detection of a Gunn-Peterson Trough in  $az = 6.28$  Quasar. *The Astronomical Journal*, 122(6):2850, 2001.
- M. C. Begelman, M. Volonteri, and M. J. Rees. Formation of supermassive black holes by direct collapse in pre-galactic haloes. *MNRAS*, 370:289–298, July 2006. doi: 10.1111/j.1365-2966.2006.10467.x.
- M. C. Begelman, E. M. Rossi, and P. J. Armitage. Quasi-stars: accreting black holes inside massive envelopes. *MNRAS*, 387:1649–1659, July 2008. doi: 10.1111/j.1365-2966.2008.13344.x.
- K. Belczynski, V. Kalogera, and T. Bulik. A Comprehensive Study of Binary Compact Objects as Gravitational Wave Sources: Evolutionary Channels, Rates, and Physical Properties. *ApJ*, 572:407–431, June 2002. doi: 10.1086/340304.
- Krzysztof Belczynski, Vassiliki Kalogera, Frederic A Rasio, Ronald E Taam, Andreas Zezas, Tomasz Bulik, Thomas J Maccarone, and Natalia Ivanova. Compact Object Modeling with the StarTrack Population Synthesis Code. *ApJS*, 174(1):223–260, January 2008.
- C L Bennett, D Larson, J L Weiland, N Jarosik, G Hinshaw, N Odegard, K M Smith, R S Hill, B Gold, M Halpern, E Komatsu, M R Nolte, L Page, D N Spergel, E Wollack, J Dunkley, A Kogut, M Limon, S S Meyer, G S Tucker, and E L Wright. Nine-Year Wilkinson Microwave Anisotropy Probe (WMAP) Observations: Final Maps and Results. preprint (astro-ph/12125225), December 2012.
- Andrew Benson, Aparna Venkatesan, and J Michael Shull. THE ESCAPE FRACTION OF IONIZING RADIATION FROM GALAXIES. *ApJ*, 770(1):76, May 2013.
- G. Bernardi, M. McQuinn, and L. J. Greenhill. Foreground Model and Antenna Calibration Errors in the Measurement of the Sky-averaged  $\lambda 21$  cm Signal at  $z \sim 20$ . *ApJ*, 799:90, January 2015. doi: 10.1088/0004-637X/799/1/90.
- H. Bondi and F. Hoyle. On the mechanism of accretion by stars. *MNRAS*, 104:273, 1944.
- R. J. Bouwens, G. D. Illingworth, P. A. Oesch, J. Caruana, B. Holwerda, R. Smit, and S. Wilkins. Reionization After Planck: The Derived Growth of the Cosmic Ionizing Emissivity Now Matches the Growth of the Galaxy UV Luminosity Density. *ApJ*, 811:140, October 2015. doi: 10.1088/0004-637X/811/2/140.
- J. D. Bowman and A. E. E. Rogers. A lower limit of  $\Delta z > 0.06$  for the duration of the reionization epoch. *Nat*, 468:796–798, December 2010. doi: 10.1038/nature09601.
- J. D. Bowman, I. Cairns, D. L. Kaplan, T. Murphy, D. Oberoi, L. Staveley-Smith, W. Arcus, D. G. Barnes, G. Bernardi, F. H. Briggs, S. Brown, J. D. Bunton, A. J. Burgasser, R. J. Cappallo, S. Chatterjee, B. E. Corey, A. Coster, A. Deshpande, L. deSouza, D. Emrich, P. Erickson, R. F. Goeke, B. M. Gaensler, L. J. Greenhill, L. Harvey-Smith, B. J. Hazelton, D. Herne, J. N. Hewitt, M. Johnston-Hollitt, J. C. Kasper,

- B. B. Kincaid, R. Koenig, E. Kratzenberg, C. J. Lonsdale, M. J. Lynch, L. D. Matthews, S. R. McWhirter, D. A. Mitchell, M. F. Morales, E. H. Morgan, S. M. Ord, J. Pathikulangara, T. Prabu, R. A. Remillard, T. Robishaw, A. E. E. Rogers, A. A. Roshi, J. E. Salah, R. J. Sault, N. U. Shankar, K. S. Srivani, J. B. Stevens, R. Subrahmanyam, S. J. Tingay, R. B. Wayth, M. Waterson, R. L. Webster, A. R. Whitney, A. J. Williams, C. L. Williams, and J. S. B. Wyithe. Science with the Murchison Widefield Array. Publications of the Astronomical Society of Australia, 30:e031, April 2013. doi: 10.1017/pas.2013.009.
- Michael Boylan-Kolchin, Daniel R Weisz, Benjamin D Johnson, James S Bullock, Charlie Conroy, and Alex Fitts. The Local Group as a time machine: studying the high-redshift Universe with nearby galaxies. arXiv.org, April 2015.
- V. Bromm, P. S. Coppi, and R. B. Larson. Forming the First Stars in the Universe: The Fragmentation of Primordial Gas. ApJL, 527:L5–L8, December 1999. doi: 10.1086/312385.
- Volker Bromm, Rolf P Kudritzki, and Abraham Loeb. Generic Spectrum and Ionization Efficiency of a Heavy Initial Mass Function for the First Stars. ApJ, 552(2):464–472, May 2001.
- Matthew Brorby, Philip Kaaret, and Andrea Prestwich. X-ray binary formation in low-metallicity blue compact dwarf galaxies. preprint (astro-ph/14043132), April 2014.
- G. L. Bryan and M. L. Norman. A Hybrid AMR Application for Cosmology and Astrophysics. preprint (astro-ph/9710187), October 1997.
- J. O. Burns, J. Lazio, S. Bale, J. Bowman, R. Bradley, C. Carilli, S. Furlanetto, G. Harker, A. Loeb, and J. Pritchard. Probing the first stars and black holes in the early Universe with the Dark Ages Radio Explorer (DARE). Advances in Space Research, 49:433–450, February 2012. doi: 10.1016/j.asr.2011.10.014.
- S. Cantalupo and C. Porciani. RADAMESH: cosmological radiative transfer for Adaptive Mesh Refinement simulations. MNRAS, 411:1678–1694, March 2011. doi: 10.1111/j.1365-2966.2010.17799.x.
- C. L. Carilli, S. Furlanetto, F. Briggs, M. Jarvis, S. Rawlings, and H. Falcke. Probing the dark ages with the Square Kilometer Array. New Astronomy Reviews, 48:1029–1038, December 2004. doi: 10.1016/j.newar.2004.09.046.
- V. Černý. Thermodynamical approach to the traveling salesman problem: An efficient simulation algorithm. Journal of Optimization Theory and Applications, 45(1):41–51, 1985. URL <http://www.springerlink.com/index/10.1007/BF00940812>.
- X. Chen and J. Miralda-Escudé. The Spin-Kinetic Temperature Coupling and the Heating Rate due to Ly $\alpha$  Scattering before Reionization: Predictions for 21 Centimeter Emission and Absorption. ApJ, 602:1–11, February 2004. doi: 10.1086/380829.
- Xuelei Chen, Xuelei Chen, Jordi Miralda-Escudé, and Jordi Miralda-Escudé. The 21 cm Signature of the First Stars. ApJ, 684(1):18–33, September 2008.
- J. Chluba and R. M. Thomas. Towards a complete treatment of the cosmological recombination problem. MNRAS, 412:748–764, April 2011. doi: 10.1111/j.1365-2966.2010.17940.x.
- T. R. Choudhury and A. Ferrara. Experimental constraints on self-consistent reionization models. MNRAS, 361:577–594, August 2005. doi: 10.1111/j.1365-2966.2005.09196.x.

- Leonid Chuzhoy, Marcelo A Alvarez, and Paul R Shapiro. Recognizing the First Radiation Sources through Their 21 cm Signature. *The Astrophysical Journal*, 648(1):L1–L4, August 2006.
- B Ciardi, R Salvaterra, and T Di Matteo. Ly $\alpha$  versus X-ray heating in the high- $z$  intergalactic medium. *MNRAS*, 401:2635, February 2010.
- B Ciardi, J S Bolton, and A Maselli. The effect of intergalactic helium on hydrogen reionization: implications for the sources of ionizing photons at  $z \geq 6$  - Ciardi - 2012 - Monthly Notices of the Royal Astronomical Society - Wiley Online Library. *MNRAS*, 2012.
- B. Ciardi, J. S. Bolton, A. Maselli, and L. Graziani. The effect of intergalactic helium on hydrogen reionization: implications for the sources of ionizing photons at  $z > 6$ . *MNRAS*, 423:558–574, June 2012. doi: 10.1111/j.1365-2966.2012.20902.x.
- Planck Collaboration, P A R Ade, N Aghanim, M Arnaud, M Ashdown, J Aumont, C Baccigalupi, A J Banday, R B Barreiro, J G Bartlett, N Bartolo, E Battaner, R Battye, K Benabed, A Benoit, A Benoit-Levy, J P Bernard, M Bersanelli, P Bielewicz, A Bonaldi, L Bonavera, J R Bond, J Borrill, F R Bouchet, F Boulanger, M Bucher, C Burigana, R C Butler, E Calabrese, J F Cardoso, A Catalano, A Challinor, A Chamballu, R R Chary, H C Chiang, J Chluba, P R Christensen, S Church, D L Clements, S Colombi, Colombo, L. P. L., C Combet, A Coulais, B P Crill, A Curto, F Cuttaia, L Danese, R D Davies, R J Davis, P de Bernardis, A de Rosa, G de Zotti, J Delabrouille, F X Desert, E Di Valentino, C Dickinson, J M Diego, K Dolag, H Dole, S Donzelli, O Dore, M Douspis, A Ducout, J Dunkley, X Dupac, G Efstathiou, F Elsner, T A Ensslin, H K Eriksen, M Farhang, J Fergusson, F Finelli, O Forni, M Frailis, A A Fraisse, E Franceschi, A Frejsel, S Galeotta, S Galli, K Ganga, C Gauthier, M Gerbino, T Ghosh, M Girard, Y Giraud-Heraud, E Giusarma, E Gjerlow, J Gonzalez-Nuevo, K M Gorski, S Gratton, A Gregorio, A Gruppuso, J E Gudmundsson, J Hamann, F K Hansen, D Hanson, D L Harrison, G Helou, S Henrot-Versille, C Hernandez-Monteagudo, D Herranz, S R Hildebrandt, E Hivon, M Hobson, W A Holmes, A Hornstrup, W Hovest, Z Huang, K M Huffenberger, G Hurier, A H Jaffe, T R Jaffe, W C Jones, M Juvela, E Keihanen, R Keskitalo, T S Kisner, R Kneissl, J Knoche, L Knox, M Kunz, H Kurki-Suonio, G Lagache, A Lahteenmaki, J M Lamarre, A Lasenby, M Lattanzi, C R Lawrence, J P Leahy, R Leonardi, J Lesgourgues, F Levrier, A Lewis, M Liguori, P B Lilje, M Linden-Vornle, M Lopez-Caniego, P M Lubin, J F Macias-Perez, G Maggio, D Maino, N Mandolesi, A Mangilli, A Marchini, P G Martin, M Martinelli, E Martinez-Gonzalez, S Masi, S Matarrese, P Mazzotta, P McGehee, P R Meinhold, A Melchiorri, J B Melin, L Mendes, A Mennella, M Migliaccio, M Millea, S Mitra, M A Miville-Deschenes, A Moneti, L Montier, G Morgante, D Mortlock, A Moss, D Munshi, J A Murphy, P Naselsky, F Nati, P Natoli, C B Netterfield, H U Norgaard-Nielsen, F Noviello, D Novikov, I Novikov, C A Oxborrow, F Paci, L Pagano, F Pajot, R Paladini, D Paoletti, B Partridge, F Pasian, G Patanchon, T J Pearson, O Perdereau, L Perotto, F Perrotta, V Pettorino, F Piacentini, M Piat, E Pierpaoli, D Pietrobon, S Plaszczynski, E Pointecouteau, G Polenta, L Popa, G W Pratt, G Prezeau, S Prunet, J L Puget, J P Rachen, W T Reach, R Rebolo, M Reinecke, M Remazeilles, C Renault, A Renzi, I Ristorcelli, G Rocha, C Rosset, M Rossetti, G Roudier, B Rouille d’Orfeuill, M Rowan-Robinson, J A Rubino-Martin, B Rusholme, N Said, V Salvatelli, L Salvati, M Sandri, D Santos, M Savelainen, G Savini, D Scott, M D Seiffert, P Serra, E P S Shellard, L D Spencer, M Spinelli, V Stolyarov, R Stompor, R Sudiwala, R Sunyaev, D Sutton, A S Suur-Uski, J F Sygnet, J A Tauber, L Terenzi, L Toffolatti, M Tomasi, M Tristram, T Trombetti, M Tucci, J Tuovinen, M Turler, G Umama, L Valenziano, J Valiviita, B Van Tent, P Vielva, F Villa, L A Wade, B D Wandelt, I K Wehus, M White, S D M White, A Wilkinson, D Yvon, A Zacchei, and A Zonca. Planck 2015 results. XIII. Cosmological parameters. [arXiv.org](https://arxiv.org/abs/1502.01589), page 1589, February 2015.

- J. E. Dale, I. A. Bonnell, C. J. Clarke, and M. R. Bate. Photoionizing feedback in star cluster formation. *MNRAS*, 358:291–304, March 2005. doi: 10.1111/j.1365-2966.2005.08806.x.
- A. Datta, R. Bradley, J. O. Burns, G. Harker, A. Komjathy, and T. J. W. Lazio. Effects Of The Ionosphere On Ground-Based Detection Of The Global 21 CM Signal From The Cosmic Dawn And The Dark Ages. *ArXiv e-prints*, September 2014.
- F. B. Davies and S. R. Furlanetto. The Effect of Fluctuations on the Helium-Ionizing Background. *ArXiv e-prints*, September 2012.
- F B Davies and S R Furlanetto. The effect of fluctuations on the helium-ionizing background. *MNRAS*, November 2013.
- Anglica de Oliveira-Costa, Max Tegmark, B M Gaensler, Justin Jonas, T L Landecker, and Patricia Reich. A model of diffuse Galactic radio emission from 10 MHz to 100 GHz. *MNRAS*, 388(1):247–260, July 2008.
- M. Dijkstra, M. Gilfanov, A. Loeb, and R. Sunyaev. Constraints on the redshift evolution of the  $L_X$ -SFR relation from the cosmic X-ray backgrounds. *MNRAS*, 421:213–223, March 2012. doi: 10.1111/j.1365-2966.2011.20292.x.
- Mark Dijkstra, Zoltán Haiman, and Abraham Loeb. A Limit from the X-Ray Background on the Contribution of Quasars to Reionization. *ApJ*, 613(2):646, 2004.
- J. Dunkley, E. Komatsu, M. R. Nolta, D. N. Spergel, D. Larson, G. Hinshaw, L. Page, C. L. Bennett, B. Gold, N. Jarosik, J. L. Weiland, M. Halpern, R. S. Hill, A. Kogut, M. Limon, S. S. Meyer, G. S. Tucker, E. Wollack, and E. L. Wright. Five-Year Wilkinson Microwave Anisotropy Probe Observations: Likelihoods and Parameters from the WMAP Data. *ApJS*, 180:306–329, February 2009. doi: 10.1088/0067-0049/180/2/306.
- R. S. Ellis, R. J. McLure, J. S. Dunlop, B. E. Robertson, Y. Ono, M. A. Schenker, A. Koekemoer, R. A. A. Bowler, M. Ouchi, A. B. Rogers, E. Curtis-Lake, E. Schneider, S. Charlot, D. P. Stark, S. R. Furlanetto, and M. Cirasuolo. The Abundance of Star-forming Galaxies in the Redshift Range 8.5-12: New Results from the 2012 Hubble Ultra Deep Field Campaign. *ApJL*, 763:L7, January 2013. doi: 10.1088/2041-8205/763/1/L7.
- H. I. Ewen and E. M. Purcell. Observation of a Line in the Galactic Radio Spectrum: Radiation from Galactic Hydrogen at 1,420 Mc./sec. *Nat*, 168:356, September 1951. doi: 10.1038/168356a0.
- G Fabbiano. Populations of X-Ray Sources in Galaxies. *Annual Review of Astronomy and Astrophysics*, 44(1):323–366, September 2006.
- X. Fan, R. L. White, M. Davis, R. H. Becker, M. A. Strauss, Z. Haiman, D. P. Schneider, M. D. Gregg, J. E. Gunn, G. R. Knapp, R. H. Lupton, J. E. Anderson, Jr., S. F. Anderson, J. Annis, N. A. Bahcall, W. N. Boroski, R. J. Brunner, B. Chen, A. J. Connolly, I. Csabai, M. Doi, M. Fukugita, G. S. Hennessy, R. B. Hindsley, T. Ichikawa, Ž. Ivezić, J. Loveday, A. Meiksin, T. A. McKay, J. A. Munn, H. J. Newberg, R. Nichol, S. Okamura, J. R. Pier, M. Sekiguchi, K. Shimasaku, C. Stoughton, A. S. Szalay, G. P. Szokoly, A. R. Thakar, M. S. Vogeley, and D. G. York. The Discovery of a Luminous  $Z=5.80$  Quasar from the Sloan Digital Sky Survey. *AJ*, 120:1167–1174, September 2000. doi: 10.1086/301534.

- X. Fan, M. A. Strauss, R. H. Becker, R. L. White, J. E. Gunn, G. R. Knapp, G. T. Richards, D. P. Schneider, J. Brinkmann, and M. Fukugita. Constraining the Evolution of the Ionizing Background and the Epoch of Reionization with  $z \sim 6$  Quasars. II. A Sample of 19 Quasars. *AJ*, 132:117–136, July 2006. doi: 10.1086/504836.
- Xiaohui Fan. Evolution of high-redshift quasars. *New Astronomy Reviews*, 50:665, November 2006.
- F. Feroz, M. P. Hobson, and M. Bridges. MULTINEST: an efficient and robust Bayesian inference tool for cosmology and particle physics. *MNRAS*, 398:1601–1614, October 2009. doi: 10.1111/j.1365-2966.2009.14548.x.
- L. Ferrarese and D. Merritt. A Fundamental Relation between Supermassive Black Holes and Their Host Galaxies. *ApJL*, 539:L9–L12, August 2000. doi: 10.1086/312838.
- A. Fialkov, R. Barkana, and E. Visbal. The observable signature of late heating of the Universe during cosmic reionization. *Nat*, 506:197–199, February 2014. doi: 10.1038/nature12999.
- Anastasia Fialkov, Rennan Barkana, Dmitriy Tseliakhovich, and Christopher M Hirata. Impact of the relative motion between the dark matter and baryons on the first stars: semi-analytical modelling. *MNRAS*, 424(2):1335–1345, June 2012.
- G. B. Field. Excitation of the Hydrogen 21-CM Line. *Proceedings of the IRE*, 46:240–250, January 1958. doi: 10.1109/JRPROC.1958.286741.
- K. Finlator, F. Özel, and R. Davé. A new moment method for continuum radiative transfer in cosmological re-ionization. *MNRAS*, 393:1090–1106, March 2009. doi: 10.1111/j.1365-2966.2008.14190.x.
- D. Foreman-Mackey, D. W. Hogg, D. Lang, and J. Goodman. emcee: The MCMC Hammer. *PASP*, 125:306–312, March 2013. doi: 10.1086/670067.
- T Fragos, B D Lehmer, S Naoz, A Zezas, and A Basu-Zych. ENERGY FEEDBACK FROM X-RAY BINARIES IN THE EARLY UNIVERSE. *ApJ*, 776(2):L31, October 2013.
- Martina M Friedrich, Garrelt Mellema, Ilian T Iliev, and Paul R Shapiro. Radiative transfer of energetic photons: X-rays and helium ionization in C2-RAY. *Monthly Notices of the Royal Astronomical Society*, 421(3):2232–2250, April 2012.
- M Fukugita and M Kawasaki. Reionization during Hierarchical Clustering in a Universe Dominated by Cold Dark Matter. *MNRAS*, 269:563, August 1994.
- S. R. Furlanetto and M. R. Furlanetto. Spin-exchange rates in electron-hydrogen collisions. *MNRAS*, 374:547–555, January 2007. doi: 10.1111/j.1365-2966.2006.11169.x.
- S. R. Furlanetto and S. Johnson Stoeber. Secondary ionization and heating by fast electrons. *MNRAS*, 404:1869–1878, June 2010. doi: 10.1111/j.1365-2966.2010.16401.x.
- S R Furlanetto and J R Pritchard. The scattering of Lyman-series photons in the intergalactic medium. *Monthly Notices of the Royal Astronomical Society*, 372(3):1093–1103, November 2006.
- S. R. Furlanetto and J. R. Pritchard. The scattering of Lyman-series photons in the intergalactic medium. *MNRAS*, 372:1093–1103, November 2006. doi: 10.1111/j.1365-2966.2006.10899.x.

- Steven R Furlanetto. The global 21-centimeter background from high redshifts. *MNRAS*, 371(2):867–878, September 2006.
- Steven R Furlanetto and Michael R. Furlanetto. Spin exchange rates in proton-hydrogen collisions. *MNRAS*, 379(1):130–134, July 2007.
- Steven R Furlanetto and Abraham Loeb. LargeScale Structure Shocks at Low and High Redshifts. *ApJ*, 611(2):642–654, August 2004.
- Steven R Furlanetto, S Peng Oh, and Frank H Briggs. Cosmology at low frequencies: The 21 cm transition and the high-redshift Universe. *Physics Reports*, 433(4):181–301, October 2006a.
- Steven R Furlanetto, S Peng Oh, and Elena Pierpaoli. Effects of dark matter decay and annihilation on the high-redshift 21cm background. *Physical Review D*, 74(1):103502, November 2006b.
- K. Gebhardt, R. Bender, G. Bower, A. Dressler, S. M. Faber, A. V. Filippenko, R. Green, C. Grillmair, L. C. Ho, J. Kormendy, T. R. Lauer, J. Magorrian, J. Pinkney, D. Richstone, and S. Tremaine. A Relationship between Nuclear Black Hole Mass and Galaxy Velocity Dispersion. *ApJL*, 539:L13–L16, August 2000. doi: 10.1086/312840.
- M. Gilfanov, H.-J. Grimm, and R. Sunyaev.  $L_X$ -SFR relation in star-forming galaxies. *MNRAS*, 347:L57–L60, January 2004. doi: 10.1111/j.1365-2966.2004.07450.x.
- N. Y. Gnedin. Effect of Reionization on Structure Formation in the Universe. *ApJ*, 542:535–541, October 2000. doi: 10.1086/317042.
- N. Y. Gnedin and P. A. Shaver. Redshifted 21 Centimeter Emission from the Pre-Reionization Era. I. Mean Signal and Linear Fluctuations. *ApJ*, 608:611–621, June 2004. doi: 10.1086/420735.
- N Y Gnedin, A V Kravtsov, and H W Chen. Escape of Ionizing Radiation from High-Redshift Galaxies - Abstract - The Astrophysical Journal - IOPscience. *ApJ*, 2008.
- Nickolay Y. Gnedin and Tom Abel. Multi-dimensional cosmological radiative transfer with a variable eddington tensor formalism. *New Astronomy*, 6(7):437 – 455, 2001. ISSN 1384-1076. doi: 10.1016/S1384-1076(01)00068-9. URL <http://www.sciencedirect.com/science/article/pii/S1384107601000689>.
- Nickolay Y Gnedin and Jeremiah P Ostriker. Reionization of the Universe and the Early Production of Metals. *The Astrophysical Journal*, 486(2):581–598, September 1997.
- M. González, E. Audit, and P. Huynh. HERACLES: a three-dimensional radiation hydrodynamics code. *A&A*, 464:429–435, March 2007. doi: 10.1051/0004-6361:20065486.
- Jonathan Goodman and Jonathan Weare. Ensemble samplers with affine invariance. *Commun. Appl. Math. Comput. Sci.*, 5:65–80, 2010. doi: 10.2140/camcos.2010.5.65.
- K. M. Górski, E. Hivon, A. J. Banday, B. D. Wandelt, F. K. Hansen, M. Reinecke, and M. Bartelmann. HEALPix: A Framework for High-Resolution Discretization and Fast Analysis of Data Distributed on the Sphere. *ApJ*, 622:759–771, April 2005. doi: 10.1086/427976.
- L J Greenhill and G Bernardi. HI Epoch of Reionization Arrays. [preprint \(astro-ph/12011700\)](#), January 2012.

- Bradley Greig and Andrei Mesinger. 21CMMC: An MCMC analysis tool enabling astrophysical parameter studies of the cosmic 21cm signal. [arXiv.org](https://arxiv.org/abs/1501.00007), January 2015.
- J. Greiner, T. Krhler, J. P. U. Fynbo, A. Rossi, R. Schwarz, S. Klose, S. Savaglio, N. R. Tanvir, and McBreen. GRB 080913 at Redshift 6.7. *ApJ*, 693:1610–1620, March 2009. doi: 10.1088/0004-637X/693/2/1610.
- H.-J. Grimm, M. Gilfanov, and R. Sunyaev. High-mass X-ray binaries as a star formation rate indicator in distant galaxies. *MNRAS*, 339:793–809, March 2003. doi: 10.1046/j.1365-8711.2003.06224.x.
- F. Haardt and P. Madau. Radiative Transfer in a Clumpy Universe. II. The Ultraviolet Extragalactic Background. *ApJ*, 461:20, April 1996. doi: 10.1086/177035.
- Z. Haiman, A. A. Thoul, and A. Loeb. Cosmological Formation of Low-Mass Objects. *ApJ*, 464:523, June 1996. doi: 10.1086/177343.
- Z Haiman, M J Rees, and A Loeb. Destruction of Molecular Hydrogen during Cosmological Reionization. *ApJ*, 1997.
- Z. Haiman, T. Abel, and M. J. Rees. The Radiative Feedback of the First Cosmological Objects. *ApJ*, 534: 11–24, May 2000. doi: 10.1086/308723.
- Zoltán Haiman and Abraham Loeb. Observational Signatures of the First Quasars. *ApJ*, 503:505, August 1998.
- W. J. Handley, M. P. Hobson, and A. N. Lasenby. POLYCHORD: nested sampling for cosmology. *MNRAS*, 450:L61–L65, June 2015. doi: 10.1093/mnras/slv047.
- G. Harker, S. Zaroubi, G. Bernardi, M. A. Brentjens, A. G. de Bruyn, B. Ciardi, V. Jelić, L. V. E. Koopmans, P. Labropoulos, G. Mellema, A. Offringa, V. N. Pandey, A. H. Pawlik, J. Schaye, R. M. Thomas, and S. Yatawatta. Power spectrum extraction for redshifted 21-cm Epoch of Reionization experiments: the LOFAR case. *MNRAS*, 405:2492–2504, July 2010. doi: 10.1111/j.1365-2966.2010.16628.x.
- G J A Harker. Selection between foreground models for global 21-cm experiments. *MNRASL*, 449(1): L21–L25, February 2015a.
- G J A Harker. Selection between foreground models for global 21-cm experiments. *MNRASL*, 449(1): L21–L25, February 2015b.
- G. J. A. Harker, J. R. Pritchard, J. O. Burns, and J. D. Bowman. An MCMC approach to extracting the global 21-cm signal during the cosmic dawn from sky-averaged radio observations. *MNRAS*, 419:1070–1084, January 2012. doi: 10.1111/j.1365-2966.2011.19766.x.
- G. J. A. Harker, J. Mirocha, J. O. Burns, and J. R. Pritchard. Parametrizations of the global 21-cm signal and parameter estimation from single-dipole experiments. [astro-ph/1510.00271](https://arxiv.org/abs/1510.00271), October 2015.
- C. G. T. Haslam, C. J. Salter, H. Stoffel, and W. E. Wilson. A 408 MHz all-sky continuum survey. II - The atlas of contour maps. *Astronomy and Astrophysics Supplement Series*, 47:1, January 1982.
- C. M. Hirata and K. Sigurdson. The spin-resolved atomic velocity distribution and 21-cm line profile of dark-age gas. *MNRAS*, 375:1241–1264, March 2007. doi: 10.1111/j.1365-2966.2006.11321.x.
- Christopher M Hirata. Wouthuysen-Field coupling strength and application to high-redshift 21-cm radiation. *MNRAS*, 367(1):259–274, March 2006.

- C J Hogan and M J Rees. Spectral appearance of non-uniform gas at high  $z$ . Monthly Notices of the Royal Astronomical Society, 188(4):791–798, September 1979.
- T. Hosokawa, K. Omukai, N. Yoshida, and H. W. Yorke. Protostellar Feedback Halts the Growth of the First Stars in the Universe. Science, 334:1250–, December 2011. doi: 10.1126/science.1207433.
- J. A. Hummel, A. Stacy, M. Jeon, A. Oliveri, and V. Bromm. The first stars: formation under X-ray feedback. MNRAS, 453:4136–4147, November 2015. doi: 10.1093/mnras/stv1902.
- I. T. Iliev, B. Ciardi, M. A. Alvarez, A. Maselli, A. Ferrara, N. Y. Gnedin, G. Mellema, T. Nakamoto, M. L. Norman, A. O. Razoumov, E.-J. Rijkhorst, J. Ritzerveld, P. R. Shapiro, H. Susa, M. Umemura, and D. J. Whalen. Cosmological radiative transfer codes comparison project - I. The static density field tests. MNRAS, 371:1057–1086, September 2006. doi: 10.1111/j.1365-2966.2006.10775.x.
- M. Jeon, A. H. Pawlik, V. Bromm, and M. Milosavljević. Radiative feedback from high-mass X-ray binaries on the formation of the first galaxies and early reionization. MNRAS, 440:3778–3796, June 2014. doi: 10.1093/mnras/stu444.
- S. Jester and H. Falcke. Science with a lunar low-frequency array: From the dark ages of the Universe to nearby exoplanets. New Astronomy Reviews, 53:1–26, May 2009. doi: 10.1016/j.newar.2009.02.001.
- J. L. Johnson. Population III star clusters in the reionized Universe. MNRAS, 404:1425–1436, May 2010. doi: 10.1111/j.1365-2966.2010.16351.x.
- J. L. Johnson, D. J. Whalen, C. L. Fryer, and H. Li. The Growth of the Stellar Seeds of Supermassive Black Holes. ApJ, 750:66, May 2012. doi: 10.1088/0004-637X/750/1/66.
- P Kaaret. X-ray luminous binaries, metallicity, and the early Universe. MNRASL, February 2014.
- Philip Kaaret, Joseph Schmitt, and Mark Gorski. X-Rays from Blue Compact Dwarf Galaxies. ApJ, 741(1): 10, November 2011.
- A. R. King and U. Kolb. The evolution of black hole mass and angular momentum. MNRAS, 305:654–660, May 1999. doi: 10.1046/j.1365-8711.1999.02482.x.
- S. Kirkpatrick, C. D. Gelatt, and M. P. Vecchi. Optimization by Simulated Annealing. Science, 220:671–680, May 1983. doi: 10.1126/science.220.4598.671.
- T. Kitayama, N. Yoshida, H. Susa, and M. Umemura. The Structure and Evolution of Early Cosmological H II Regions. ApJ, 613:631–645, October 2004. doi: 10.1086/423313.
- E. Komatsu, K. M. Smith, J. Dunkley, C. L. Bennett, B. Gold, G. Hinshaw, N. Jarosik, D. Larson, M. R. Nolta, L. Page, D. N. Spergel, M. Halpern, R. S. Hill, A. Kogut, M. Limon, S. S. Meyer, N. Odegard, G. S. Tucker, J. L. Weiland, E. Wollack, and E. L. Wright. Seven-year Wilkinson Microwave Anisotropy Probe (WMAP) Observations: Cosmological Interpretation. ApJS, 192:18, February 2011. doi: 10.1088/0067-0049/192/2/18.
- R H Kramer and Z Haiman. The thickness of high-redshift quasar ionization fronts as a constraint on the ionizing spectral energy distribution. MNRAS, 385(3):1561–1575, April 2008.
- M. R. Krumholz. Radiation Feedback and Fragmentation in Massive Protostellar Cores. ApJL, 641:L45–L48, April 2006. doi: 10.1086/503771.

- M. Kuhlen and P. Madau. The first miniquasar. *MNRAS*, 363:1069–1082, November 2005. doi: 10.1111/j.1365-2966.2005.09522.x.
- D. Larson, J. Dunkley, G. Hinshaw, E. Komatsu, M. R.olta, C. L. Bennett, B. Gold, M. Halpern, R. S. Hill, N. Jarosik, A. Kogut, M. Limon, S. S. Meyer, N. Odegard, L. Page, K. M. Smith, D. N. Spergel, G. S. Tucker, J. L. Weiland, E. Wollack, and E. L. Wright. Seven-year Wilkinson Microwave Anisotropy Probe (WMAP) Observations: Power Spectra and WMAP-derived Parameters. *ApJS*, 192:16, February 2011. doi: 10.1088/0067-0049/192/2/16.
- T. J. W. Lazio, R. J. MacDowall, J. O. Burns, D. L. Jones, K. W. Weiler, L. Demaio, A. Cohen, N. Paravastu Dalal, E. Polisensky, K. Stewart, S. Bale, N. Gopalswamy, M. Kaiser, and J. Kasper. The Radio Observatory on the Lunar Surface for Solar studies. *Advances in Space Research*, 48:1942–1957, December 2011. doi: 10.1016/j.asr.2011.07.006.
- C. Leitherer, D. Schaerer, J. D. Goldader, R. M. G. Delgado, C. Robert, D. F. Kune, D. F. de Mello, D. Devost, and T. M. Heckman. Starburst99: Synthesis Models for Galaxies with Active Star Formation. *ApJS*, 123:3–40, July 1999. doi: 10.1086/313233.
- C. Leitherer, S. Ekström, G. Meynet, D. Schaerer, K. B. Agienko, and E. M. Levesque. The Effects of Stellar Rotation. II. A Comprehensive Set of Starburst99 Models. *ApJS*, 212:14, May 2014. doi: 10.1088/0067-0049/212/1/14.
- S Lepp and J M Shull. Molecules in the early universe. *ApJ*, 280:465–469, May 1984.
- A. Lewis, A. Challinor, and A. Lasenby. Efficient Computation of Cosmic Microwave Background Anisotropies in Closed Friedmann-Robertson-Walker Models. *ApJ*, 538:473–476, August 2000. doi: 10.1086/309179.
- A. Lidz, O. Zahn, M. McQuinn, M. Zaldarriaga, and L. Hernquist. Detecting the Rise and Fall of 21 cm Fluctuations with the Murchison Widefield Array. *ApJ*, 680:962–974, June 2008. doi: 10.1086/587618.
- T. Linden, V. Kalogera, J. F. Sepinsky, A. Prestwich, A. Zezas, and J. S. Gallagher. The Effect of Starburst Metallicity on Bright X-ray Binary Formation Pathways. *ApJ*, 725:1984–1994, December 2010. doi: 10.1088/0004-637X/725/2/1984.
- Adrian Liu, Jonathan R Pritchard, Max Tegmark, and Abraham Loeb. Global 21 cm signal experiments: A designer’s guide. *Physical Review D*, 87(4):043002, February 2013.
- P Madau, M J Rees, M Volonteri, F Haardt, and S P Oh. Early Reionization by Miniquasars. *ApJ*, 604(2):484–494, April 2004.
- Piero Madau, Avery Meiksin, and Martin J Rees. 21 Centimeter Tomography of the Intergalactic Medium at High Redshift. *ApJ*, 475:429, February 1997.
- Sangeeta Malhotra and James E Rhoads. The volume fraction of ionized intergalactic gas at redshift  $z=6.5$ . *ApJ*, 647(2):L95, 2006.
- M Mapelli, E Ripamonti, L Zampieri, M Colpi, and A Bressan. Ultra-luminous X-ray sources and remnants of massive metal-poor stars. *MNRAS*, 408(1):234–253, September 2010.
- A. Maselli, A. Ferrara, and B. Ciardi. CRASH: a radiative transfer scheme. *MNRAS*, 345:379–394, October 2003. doi: 10.1046/j.1365-8711.2003.06979.x.

- M. McQuinn and R. M. O’Leary. The Impact of the Supersonic Baryon-Dark Matter Velocity Difference on the  $z \sim 20$  21 cm Background. *ApJ*, 760:3, November 2012. doi: 10.1088/0004-637X/760/1/3.
- M McQuinn, L Hernquist, M Zaldarriaga, and S Dutta. Studying reionization with Ly emitters. *MNRAS*, 381(1):75–96, October 2007.
- Matthew Mcquinn. Constraints on X-ray emissions from the reionization era. *MNRAS*, 426(2):1349–1360, October 2012.
- Avery Meiksin and Martin White. Constraints on the ultraviolet metagalactic emissivity using the Ly $\alpha$  forest. *MNRAS*, 342(4):1205–1214, July 2003.
- G. Mellema, I. T. Iliev, M. A. Alvarez, and P. R. Shapiro. C<sup>2</sup>-ray: A new method for photon-conserving transport of ionizing radiation. *New Astronomy*, 11:374–395, March 2006. doi: 10.1016/j.newast.2005.09.004.
- G. Mellema, L. V. E. Koopmans, F. A. Abdalla, G. Bernardi, B. Ciardi, S. Daiboo, A. G. de Bruyn, K. K. Datta, H. Falcke, A. Ferrara, I. T. Iliev, F. Iocco, V. Jelić, H. Jensen, R. Joseph, P. Labropoulos, A. Meiksin, A. Mesinger, A. R. Offringa, V. N. Pandey, J. R. Pritchard, M. G. Santos, D. J. Schwarz, B. Semelin, H. Vedantham, S. Yatawatta, and S. Zaroubi. Reionization and the Cosmic Dawn with the Square Kilometre Array. *Experimental Astronomy*, April 2013. doi: 10.1007/s10686-013-9334-5.
- A. Mesinger, S. Furlanetto, and R. Cen. 21CMFAST: a fast, seminumerical simulation of the high-redshift 21-cm signal. *MNRAS*, 411:955–972, February 2011. doi: 10.1111/j.1365-2966.2010.17731.x.
- Andrei Mesinger and Steven Furlanetto. The inhomogeneous ionizing background following reionization. *MNRAS*, 400(3):1461–1471, December 2009.
- Andrei Mesinger and Steven R Furlanetto. Ly $\alpha$  emitters during the early stages of reionization. *MNRAS*, 386(4):1990–2002, June 2008.
- Andrei Mesinger, Andrea Ferrara, and David S Spiegel. Signatures of X-rays in the early Universe. *MNRAS*, 2013a.
- Andrei Mesinger, Andrea Ferrara, and David S Spiegel. Signatures of X-rays in the early Universe. *MNRAS*, 2013b.
- J M Miller, E M Cackett, and R C Reis. ON NEUTRAL ABSORPTION AND SPECTRAL EVOLUTION IN X-RAY BINARIES. *ApJ*, 707(1):L77–L81, November 2009.
- S. Mineo, M. Gilfanov, and R. Sunyaev. X-ray emission from star-forming galaxies - I. High-mass X-ray binaries. *MNRAS*, 419:2095–2115, January 2012a. doi: 10.1111/j.1365-2966.2011.19862.x.
- S. Mineo, M. Gilfanov, and R. Sunyaev. X-ray emission from star-forming galaxies - I. High-mass X-ray binaries. *MNRAS*, 419:2095–2115, January 2012b. doi: 10.1111/j.1365-2966.2011.19862.x.
- S Mineo, M Gilfanov, and R Sunyaev. X-ray emission from star-forming galaxies – II. Hot interstellar medium - Mineo - 2012 - *MNRAS*- Wiley Online Library. *MNRAS*, 2012.
- I. F. Mirabel, M. Dijkstra, P. Laurent, A. Loeb, and J. R. Pritchard. Stellar black holes at the dawn of the universe. *A&A*, 528:A149, April 2011. doi: 10.1051/0004-6361/201016357.

- J. Mirocha. Decoding the X-ray properties of pre-reionization era sources. *MNRAS*, 443:1211–1223, September 2014. doi: 10.1093/mnras/stu1193.
- J. Mirocha, S. Skory, J. O. Burns, and J. H. Wise. Optimized Multi-frequency Spectra for Applications in Radiative Feedback and Cosmological Reionization. *ApJ*, 756:94, September 2012. doi: 10.1088/0004-637X/756/1/94.
- J. Mirocha, G. J. A. Harker, and J. O. Burns. Interpreting the Global 21cm Signal from High Redshifts. I. Model-independent constraints. *ApJ*, 777:118, November 2013. doi: 10.1088/0004-637X/777/2/118.
- J. Mirocha, G. J. A. Harker, and J. O. Burns. Interpreting the Global 21-cm Signal from High Redshifts. II. Parameter Estimation for Models of Galaxy Formation. *ArXiv e-prints*, September 2015.
- K. Mitsuda, H. Inoue, K. Koyama, K. Makishima, M. Matsuoka, Y. Ogawara, K. Suzuki, Y. Tanaka, N. Shibazaki, and T. Hirano. Energy spectra of low-mass binary X-ray sources observed from TENMA. *PASJ*, 36:741–759, 1984.
- A. Morandi and R. Barkana. Studying cosmic reionization with observations of the global 21-cm signal. *MNRAS*, 424:2551–2561, August 2012. doi: 10.1111/j.1365-2966.2012.21240.x.
- D. J. Mortlock, S. J. Warren, B. P. Venemans, M. Patel, P. C. Hewett, R. G. McMahon, C. Simpson, T. Theuns, E. A. González-Solares, A. Adamson, S. Dye, N. C. Hambly, P. Hirst, M. J. Irwin, E. Kuiper, A. Lawrence, and H. J. A. Röttgering. A luminous quasar at a redshift of  $z = 7.085$ . *Nat*, 474:616–619, June 2011. doi: 10.1038/nature10159.
- C. A. Muller and J. H. Oort. Observation of a Line in the Galactic Radio Spectrum: The Interstellar Hydrogen Line at 1,420 Mc./sec., and an Estimate of Galactic Rotation. *Nat*, 168:357–358, September 1951. doi: 10.1038/168357a0.
- S. G. Murray, C. Power, and A. S. G. Robotham. HMFcalc: An online tool for calculating dark matter halo mass functions. *Astronomy and Computing*, 3:23–34, November 2013a. doi: 10.1016/j.ascom.2013.11.001.
- S. G. Murray, C. Power, and A. S. G. Robotham. HMFcalc: An online tool for calculating dark matter halo mass functions. *Astronomy and Computing*, 3:23–34, November 2013b. doi: 10.1016/j.ascom.2013.11.001.
- P. A. Oesch, R. J. Bouwens, G. D. Illingworth, V. Gonzalez, M. Trenti, P. G. van Dokkum, M. Franx, I. Labbé, C. M. Carollo, and D. Magee. The Bright End of the Ultraviolet Luminosity Function at  $z \sim 8$ : New Constraints from CANDELS Data in GOODS-South. *ApJ*, 759:135, November 2012. doi: 10.1088/0004-637X/759/2/135.
- P A Oesch, R J Bouwens, G D Illingworth, I Labbé, M Franx, P G Van Dokkum, M Trenti, M Stiavelli, V Gonzalez, and D Magee. PROBING THE DAWN OF GALAXIES AT  $z$  9-12: NEW CONSTRAINTS FROM HUDF12/XDF AND CANDELS DATA. *The Astrophysical Journal*, 773(1):75, July 2013.
- S Peng Oh. Reionization by Hard Photons. I. X-Rays from the First Star Clusters. *ApJ*, 553(2):499–512, June 2001.
- T. Okamoto, K. Yoshikawa, and M. Umemura. ARGOT: accelerated radiative transfer on grids using oct-tree. *MNRAS*, 419:2855–2866, February 2012. doi: 10.1111/j.1365-2966.2011.19927.x.

- J H Oort. Superclusters at large redshifts - Can protosuperclusters and the birth of 'pancakes' be observed? *Astronomy and Astrophysics* (ISSN 0004-6361), 139:211–214, October 1984.
- B. W. O'Shea, G. Bryan, J. Bordner, M. L. Norman, T. Abel, R. Harkness, and A. Kritsuk. Introducing Enzo, an AMR Cosmology Application. preprint (astro-ph/0403044), March 2004.
- B. W. O'Shea, J. H. Wise, H. Xu, and M. L. Norman. The Ultraviolet Luminosity Function of the Earliest Galaxies. *ArXiv e-prints*, March 2015.
- D.E. Osterbrock and G J Ferland. *Astrophysics of Gaseous Nebulae and Active Galactic Nuclei*. 2006.
- G. Paciga, J. G. Albert, K. Bandura, T.-C. Chang, Y. Gupta, C. Hirata, J. Odegova, U.-L. Pen, J. B. Peterson, J. Roy, J. R. Shaw, K. Sigurdson, and T. Voytek. A simulation-calibrated limit on the H I power spectrum from the GMRT Epoch of Reionization experiment. *MNRAS*, 433:639–647, July 2013. doi: 10.1093/mnras/stt753.
- F. Pacucci, A. Mesinger, S. Mineo, and A. Ferrara. The X-ray spectra of the first galaxies: 21cm signatures. eprint (astro-ph/14036125), March 2014.
- Aaron R Parsons, Donald C Backer, Griffin S Foster, Melvyn C H Wright, Richard F Bradley, Nicole E Gugliucci, Chaitali R Parashare, Erin E Benoit, James E Aguirre, Daniel C Jacobs, Chris L Carilli, David Herne, Mervyn J Lynch, Jason R Manley, and Daniel J Werthimer. THE PRECISION ARRAY FOR PROBING THE EPOCH OF RE-IONIZATION: EIGHT STATION RESULTS. *AJ*, 139(4):1468–1480, March 2010.
- Aaron R Parsons, Adrian Liu, James E Aguirre, Zaki S Ali, Richard F Bradley, Chris L Carilli, David R DeBoer, Matthew R Dexter, Nicole E Gugliucci, Daniel C Jacobs, Pat Klima, David H E MacMahon, Jason R Manley, David F Moore, Jonathan C Pober, Irina I Stefan, and William P Walbrugh. New Limits on 21cm EoR From PAPER-32 Consistent with an X-Ray Heated IGM at  $z=7.7$ . preprint (astro-ph/1304.4991), April 2013.
- Aaron R Parsons, Adrian Liu, James E Aguirre, Zaki S Ali, Richard F Bradley, Chris L Carilli, David R DeBoer, Matthew R Dexter, Nicole E Gugliucci, Daniel C Jacobs, Pat Klima, David H E MacMahon, Jason R Manley, David F Moore, Jonathan C Pober, Irina I Stefan, and William P Walbrugh. NEW LIMITS ON 21 cm EPOCH OF REIONIZATION FROM PAPER-32 CONSISTENT WITH AN X-RAY HEATED INTERGALACTIC MEDIUM AT  $z=7.7$ . *ApJ*, 788(2):106, May 2014.
- P. J. E. Peebles. *Principles of Physical Cosmology*. 1993.
- M. Petkova and V. Springel. An implementation of radiative transfer in the cosmological simulation code GADGET. *MNRAS*, 396:1383–1403, July 2009. doi: 10.1111/j.1365-2966.2009.14843.x.
- N. Petrovic and S. P. Oh. Systematic effects of foreground removal in 21-cm surveys of reionization. *MNRAS*, 413:2103–2120, May 2011. doi: 10.1111/j.1365-2966.2011.18276.x.
- Jonathan C Pober, Adrian Liu, Joshua S Dillon, James E Aguirre, Judd D Bowman, Richard F Bradley, Chris L Carilli, David R DeBoer, Jacqueline N Hewitt, Daniel C Jacobs, Matthew McQuinn, Miguel F Morales, Aaron R Parsons, Max Tegmark, and Dan J Werthimer. WHAT NEXT-GENERATION 21 cm POWER SPECTRUM MEASUREMENTS CAN TEACH US ABOUT THE EPOCH OF REIONIZATION. *The Astrophysical Journal*, 782(2):66, January 2014.

- Jonathan C Pober, Zaki S Ali, Aaron R Parsons, Matthew McQuinn, James E Aguirre, Gianni Bernardi, Richard F Bradley, Chris L Carilli, Carina Cheng, David R DeBoer, Matthew R Dexter, Steven R Furlanetto, Jasper Grobbelaar, Jasper Horrell, Daniel C Jacobs, Patricia J Klima, Saul A Kohn, Adrian Liu, David H E MacMahon, Matthys Maree, Andrei Mesinger, David F Moore, Nima Razavi-Ghods, Irina I Stefan, William P Walbrugh, Andre Walker, and Haoxuan Zheng. PAPER-64 Constraints On Reionization II: The Temperature Of The  $z=8.4$  Intergalactic Medium. [arXiv.org](https://arxiv.org/abs/1502.04501), page 45, February 2015.
- Chris Power, Gillian James, Celine Combet, and Graham Wynn. FEEDBACK FROM HIGH-MASS X-RAY BINARIES ON THE HIGH-REDSHIFT INTERGALACTIC MEDIUM: MODEL SPECTRA. *ApJ*, 764(1):76, January 2013.
- Morgan Presley, Adrian Liu, and Aaron Parsons. Measuring the Cosmological 21 cm Monopole with an Interferometer. [arXiv.org](https://arxiv.org/abs/1501.06333), page 1633, January 2015.
- W. H. Press, B. P. Flannery, S. A. Teukolsky, and W. T. Vetterling. Numerical recipes in c: the art of scientific computing. 1992.
- William H Press and Paul Schechter. Formation of Galaxies and Clusters of Galaxies by Self-Similar Gravitational Condensation. *ApJ*, 187:425, February 1974.
- A H Prestwich, Maria Tsantaki, A Zezas, F Jackson, T P Roberts, R Foltz, T Linden, and V Kalogera. ULTRA-LUMINOUS X-RAY SOURCES IN THE MOST METAL POOR GALAXIES. *ApJ*, 769(2):92, May 2013.
- J. R. Pritchard and A. Loeb. 21 cm cosmology in the 21st century. *Reports on Progress in Physics*, 75(8):086901, August 2012. doi: 10.1088/0034-4885/75/8/086901.
- Jonathan R Pritchard and Steven R Furlanetto. Descending from on high: Lyman-series cascades and spin-kinetic temperature coupling in the 21-cm line. *MNRAS*, 367(3):1057–1066, April 2006.
- Jonathan R Pritchard and Steven R Furlanetto. 21-cm fluctuations from inhomogeneous X-ray heating before reionization. *MNRAS*, 376(4):1680–1694, April 2007.
- Jonathan R Pritchard and Abraham Loeb. Constraining the unexplored period between the dark ages and reionization with observations of the global 21 cm signal. *Physical Review D*, 82(2):23006, July 2010.
- Jonathan R Pritchard, Abraham Loeb, and J Stuart B Wyithe. Constraining reionization using 21-cm observations in combination with CMB and Ly $\alpha$  forest data. *MNRAS*, 408(1):57–70, October 2010.
- Edward M Purcell and George B Field. Influence of Collisions upon Population of Hyperfine States in Hydrogen. *Astrophysical Journal*, 124:542, November 1956.
- P. Ranalli, A. Comastri, and G. Setti. The 2-10 keV luminosity as a Star Formation Rate indicator. *A&A*, 399:39–50, February 2003. doi: 10.1051/0004-6361:20021600.
- Daniel R Reynolds, John C Hayes, Pascal Paschos, and Michael L Norman. Self-consistent solution of cosmological radiation-hydrodynamics and chemical ionization. *Journal of Computational Physics*, 228(18):6833–6854, October 2009.
- Massimo Ricotti, Nickolay Y Gnedin, and J Michael Shull. The Fate of the First Galaxies. I. Self-consistent Cosmological Simulations with Radiative Transfer. *ApJ*, 575(1):33–48, August 2002.

- Massimo Ricotti, Jeremiah P Ostriker, and Nickolay Y Gnedin. X-ray pre-ionization powered by accretion on the first black holes - II. Cosmological simulations and observational signatures. *MNRAS*, 357:207, February 2005.
- E Ripamonti, M Mapelli, and S Zaroubi. Radiation from early black holes – I. Effects on the neutral intergalactic medium. *MNRAS*, 387(1):158–172, June 2008.
- B. E. Robertson, R. S. Ellis, S. R. Furlanetto, and J. S. Dunlop. Cosmic Reionization and Early Star-forming Galaxies: A Joint Analysis of New Constraints from Planck and the Hubble Space Telescope. *ApJL*, 802:L19, April 2015. doi: 10.1088/2041-8205/802/2/L19.
- Brant E Robertson, Steven R Furlanetto, Evan Schneider, Stéphane Charlot, Richard S Ellis, Daniel P Stark, Ross J McLure, James S Dunlop, Anton Koekemoer, Matthew A Schenker, Masami Ouchi, Yoshiaki Ono, Emma Curtis-Lake, Alexander B Rogers, Rebecca A A Bowler, and Michele Cirasuolo. NEW CONSTRAINTS ON COSMIC REIONIZATION FROM THE 2012 HUBBLE ULTRA DEEP FIELD CAMPAIGN. *ApJ*, 768(1):71, April 2013.
- E. Rollinde, E. Vangioni, D. Maurin, K. A. Olive, F. Daigne, J. Silk, and F. H. Vincent. Influence of Population III stars on cosmic chemical evolution. *MNRAS*, 398:1782–1792, October 2009. doi: 10.1111/j.1365-2966.2009.15259.x.
- S. Salvadori, R. Schneider, and A. Ferrara. Cosmic stellar relics in the Galactic halo. *MNRAS*, 381:647–662, October 2007. doi: 10.1111/j.1365-2966.2007.12133.x.
- M G Santos, L Ferramacho, M B Silva, A Amblard, and A Cooray. Fast large volume simulations of the 21-cm signal from the reionization and pre-reionization epochs. *MNRAS*, 406(4):2421–2432, August 2010.
- D. Schaerer. On the properties of massive Population III stars and metal-free stellar populations. *A&A*, 382:28–42, January 2002. doi: 10.1051/0004-6361:20011619.
- D Scott and M J Rees. The 21-cm line at high redshift: a diagnostic for the origin of large scale structure. *Monthly Notices of the Royal Astronomical Society*, 247:510, November 1990.
- S. Seager, D. D. Sasselov, and D. Scott. A New Calculation of the Recombination Epoch. *ApJL*, 523:L1–L5, September 1999. doi: 10.1086/312250.
- S. Seager, D. D. Sasselov, and D. Scott. How Exactly Did the Universe Become Neutral? *ApJS*, 128:407–430, June 2000. doi: 10.1086/313388.
- N. I. Shakura and R A Sunyaev. Black holes in binary systems. Observational appearance. *A&A*, 24:337–355, 1973.
- P. R. Shapiro, I. T. Iliev, and A. C. Raga. Photoevaporation of cosmological minihaloes during reionization. *MNRAS*, 348:753–782, March 2004. doi: 10.1111/j.1365-2966.2004.07364.x.
- S. L. Shapiro, A. P. Lightman, and D. M. Eardley. A two-temperature accretion disk model for Cygnus X-1 - Structure and spectrum. *ApJ*, 204:187–199, February 1976. doi: 10.1086/154162.
- P. A. Shaver, R. A. Windhorst, P. Madau, and A. G. de Bruyn. Can the reionization epoch be detected as a global signature in the cosmic background? *A&A*, 345:380–390, May 1999.

- Ravi K Sheth and Giuseppe Tormen. An excursion set model of hierarchical clustering: ellipsoidal collapse and the moving barrier. *Monthly Notices of the Royal Astronomical Society*, 329(1):61–75, January 2002.
- J. M. Shull and M. E. van Steenberg. X-ray secondary heating and ionization in quasar emission-line clouds. *ApJ*, 298:268–274, November 1985. doi: 10.1086/163605.
- J Michael Shull and Aparna Venkatesan. Constraints on FirstLight Ionizing Sources from Optical Depth of the Cosmic Microwave Background. *ApJ*, 685(1):1–7, September 2008.
- J. Michael Shull, Anthony Harness, Michele Trenti, and Britton D Smith. CRITICAL STAR FORMATION RATES FOR REIONIZATION: FULL REIONIZATION OCCURS AT REDSHIFT  $z \approx 7$ . *ApJ*, 747(2): 100, February 2012.
- K. Sigurdson and S. R. Furlanetto. Measuring the Primordial Deuterium Abundance during the Cosmic Dark Ages. *Physical Review Letters*, 97(9):091301, September 2006. doi: 10.1103/PhysRevLett.97.091301.
- B. D. Smith, J. H. Wise, B. W. O’Shea, M. L. Norman, and S. Khochfar. The first Population II stars formed in externally enriched mini-haloes. *MNRAS*, 452:2822–2836, September 2015. doi: 10.1093/mnras/stv1509.
- James F Steiner, Ramesh Narayan, Jeffrey E McClintock, and Ken Ebisawa. A Simple Comptonization Model. *PASP*, 121(885):1279–1290, November 2009.
- S. Alan Stern. The lunar atmosphere: History, status, current problems, and context. *Reviews of Geophysics*, 37(4):453–491, 1999. ISSN 1944-9208. doi: 10.1029/1999RG900005. URL <http://dx.doi.org/10.1029/1999RG900005>.
- R A Sunyaev and Ya B Zeldovich. Formation of Clusters of Galaxies; Protocluster Fragmentation and Intergalactic Gas Heating. *Astronomy and Astrophysics*, 20:189, August 1972.
- R A Sunyaev and Ya B Zeldovich. On the possibility of radioastronomical investigation of the birth of galaxies. *MNRAS*, 171:375–379, May 1975.
- G Swarup and R Subrahmanyan. Search for proto-clusters at meter wavelengths. pages 441–444, 1987.
- T. Tanaka, R. Perna, and Z. Haiman. X-ray emission from high-redshift miniquasars: self-regulating the population of massive black holes through global warming. *MNRAS*, 425:2974–2987, October 2012. doi: 10.1111/j.1365-2966.2012.21539.x.
- Max Tegmark, Joseph Silk, Martin J Rees, Alain Blanchard, Tom Abel, and Francesco Palla. How Small Were the First Cosmological Objects? *ApJ*, 474:1, 1997.
- Rajat M Thomas and Saleem Zaroubi. Time-evolution of ionization and heating around first stars and miniquasars. *MNRAS*, 384(3):1080–1096, March 2008.
- Michael W Topping and J Michael Shull. The Efficiency of Stellar Reionization: Effects of Rotation, Metallicity, and Initial Mass Function. *ApJ*, 800(2):97, February 2015.
- T. Totani, N. Kawai, G. Kosugi, K. Aoki, T. Yamada, M. Iye, K. Ohta, and T. Hattori. Implications for Cosmic Reionization from the Optical Afterglow Spectrum of the Gamma-Ray Burst 050904 at  $z = 6.3$ . *PASJ*, 58:485–498, June 2006. doi: 10.1093/pasj/58.3.485.

- H. Trac and R. Cen. Radiative Transfer Simulations of Cosmic Reionization. I. Methodology and Initial Results. *ApJ*, 671:1–13, December 2007. doi: 10.1086/522566.
- Hy Trac, Renyue Cen, and Abraham Loeb. Imprint of Inhomogeneous Hydrogen Reionization on the Temperature Distribution of the Intergalactic Medium. *ApJ*, 689:L81, December 2008.
- M Trenti, M Stiavelli, R J Bouwens, P Oesch, J M Shull, G D Illingworth, L D Bradley, and C M Carollo. THE GALAXY LUMINOSITY FUNCTION DURING THE REIONIZATION EPOCH. *ApJ*, 714(2): L202–L207, April 2010.
- D. Tseliakhovich and C. Hirata. Relative velocity of dark matter and baryonic fluids and the formation of the first structures. *PRD*, 82(8):083520, October 2010. doi: 10.1103/PhysRevD.82.083520.
- Jason Tumlinson and J Michael Shull. Zero-Metallicity Stars and the Effects of the First Stars on Reionization. *ApJ*, 528(2):L65–L68, January 2000.
- Jason Tumlinson, J Michael Shull, and Aparna Venkatesan. Cosmological Effects of the First Stars: Evolving Spectra of Population III. *ApJ*, 584(2):608–620, February 2003.
- M. J. Turk, T. Abel, and B. O’Shea. The Formation of Population III Binaries from Cosmological Initial Conditions. *Science*, 325:601–, July 2009. doi: 10.1126/science.1173540.
- M. J. Turk, B. D. Smith, J. S. Oishi, S. Skory, S. W. Skillman, T. Abel, and M. L. Norman. yt: A Multi-code Analysis Toolkit for Astrophysical Simulation Data. *ApJS*, 192:9, January 2011. doi: 10.1088/0067-0049/192/1/9.
- E. P. J. van den Heuvel. Endpoints of stellar evolution: The incidence of stellar mass black holes in the galaxy. pages 29–36, July 1992.
- M. P. van Haarlem, M. W. Wise, A. W. Gunst, G. Heald, J. P. McKean, J. W. T. Hessels, A. G. de Bruyn, R. Nijboer, J. Swinbank, R. Fallows, M. Brentjens, A. Nelles, R. Beck, H. Falcke, R. Fender, J. Hörandel, L. V. E. Koopmans, G. Mann, G. Miley, H. Röttgering, B. W. Stappers, R. A. M. J. Wijers, S. Zaroubi, M. van den Akker, A. Alexov, J. Anderson, K. Anderson, A. van Ardenne, M. Arts, A. Asgekar, I. M. Avruch, F. Batejat, L. Bähren, M. E. Bell, M. R. Bell, I. van Bemmelen, P. Bennema, M. J. Bentum, G. Bernardi, P. Best, L. Bîrzan, A. Bonafede, A.-J. Boonstra, R. Braun, J. Bregman, F. Breitling, R. H. van de Brink, J. Broderick, P. C. Broekema, W. N. Brouw, M. Brüggen, H. R. Butcher, W. van Cappellen, B. Ciardi, T. Coenen, J. Conway, A. Coolen, A. Corstanje, S. Damstra, O. Davies, A. T. Deller, R.-J. Dettmar, G. van Diepen, K. Dijkstra, P. Donker, A. Doorduyn, J. Dromer, M. Drost, A. van Duin, J. Eislöffel, J. van Enst, C. Ferrari, W. Frieswijk, H. Gankema, M. A. Garrett, F. de Gasperin, M. Gerbers, E. de Geus, J.-M. Grießmeier, T. Grit, P. Gruppen, J. P. Hamaker, T. Hassall, M. Hoefl, H. Holties, A. Horneffer, A. van der Horst, A. van Houwelingen, A. Huijgen, M. Iacobelli, H. Intema, N. Jackson, V. Jelic, A. de Jong, E. Juetten, D. Kant, A. Karastergiou, A. Koers, H. Kollen, V. I. Kondratiev, E. Kooistra, Y. Koopman, A. Koster, M. Kuniyoshi, M. Kramer, G. Kuper, P. Lambropoulos, C. Law, J. van Leeuwen, J. Lemaître, M. Loose, P. Maat, G. Macario, S. Markoff, J. Masters, D. McKay-Bukowski, H. Meijering, H. Meulman, M. Mevius, E. Middelberg, R. Millenaar, J. C. A. Miller-Jones, R. N. Mohan, J. D. Mol, J. Morawietz, R. Morganti, D. D. Mulcahy, E. Mulder, H. Munk, L. Nieuwenhuis, R. van Nieuwpoort, J. E. Noordam, M. Norden, A. Noutsos, A. R. Offringa, H. Olofsson, A. Omar, E. Orrú, R. Overeem, H. Paas, M. Pandey-Pommier, V. N. Pandey, R. Pizzo, A. Polatidis, D. Rafferty, S. Rawlings, W. Reich, J.-P. de Reijer, J. Reitsma, A. Renting, P. Riemers, E. Rol, J. W. Romein, J. Roosjen, M. Ruiter, A. Scaife, K. van der Schaaf, B. Scheers, P. Schellart, A. Schoenmakers, G. Schoonderbeek, M. Serylak,

- A. Shulevski, J. Sluman, O. Smirnov, C. Sobey, H. Spreeuw, M. Steinmetz, C. G. M. Sterks, H.-J. Stiepel, K. Stuurwold, M. Tagger, Y. Tang, C. Tasse, I. Thomas, S. Thoudam, M. C. Toribio, B. van der Tol, O. Usov, M. van Veelen, A.-J. van der Veen, S. ter Veen, J. P. W. Verbiest, R. Vermeulen, N. Vermaas, C. Vocks, C. Vogt, M. de Vos, E. van der Wal, R. van Weeren, H. Weggemans, P. Weltevrede, S. White, S. J. Wijnholds, T. Wilhelmsson, O. Wucknitz, S. Yatawatta, P. Zarka, A. Zensus, and J. van Zwieten. LOFAR: The LOw-Frequency ARray. [preprint \(astro-ph/13053550\)](#), May 2013.
- H K Vedantham, L V E Koopmans, A G de Bruyn, S J Wijnholds, B Ciardi, and M A Brentjens. Chromatic effects in the 21 cm global signal from the cosmic dawn. [preprint \(astro-ph/13062172\)](#), June 2013.
- Aparna Venkatesan and Andrew Benson. X-rays and hard ultraviolet radiation from the first galaxies: ionization bubbles and 21-cm observations. *MNRAS*, 417(3):2264–2275, September 2011.
- Aparna Venkatesan, Mark L Giroux, and J Michael Shull. Heating and Ionization of the Intergalactic Medium by an Early XRay Background. *ApJ*, 563(1):1–8, December 2001.
- D A Verner and G J Ferland. Atomic Data for Astrophysics. I. Radiative Recombination Rates for H-like, He-like, Li-like, and Na-like Ions over a Broad Range of Temperature. *ApJS*, 103:467, April 1996.
- M. Volonteri, P. Madau, E. Quataert, and M. J. Rees. The Distribution and Cosmic Evolution of Massive Black Hole Spins. *ApJ*, 620:69–77, February 2005. doi: 10.1086/426858.
- T. C. Voytek, A. Natarajan, J. M. Jáuregui García, J. B. Peterson, and O. López-Cruz. Probing the Dark Ages at  $z \sim 20$ : The SCI-HI 21 cm All-sky Spectrum Experiment. *ApJL*, 782:L9, February 2014. doi: 10.1088/2041-8205/782/1/L9.
- David H Weinberg, Jordi Miralda-Escudé, Lars Hernquist, and Neal Katz. A Lower Bound on the Cosmic Baryon Density. *The Astrophysical Journal*, 490(2):564–570, December 1997.
- Daniel R Weisz, Benjamin D Johnson, and Charlie Conroy. The Very Faint End of the UV Luminosity Function over Cosmic Time: Constraints from the Local Group Fossil Record. [arXiv.org](#), September 2014.
- D. J. Whalen, W. Even, C. C. Lovekin, C. L. Fryer, M. Stiavelli, P. W. A. Roming, J. Cooke, T. A. Pritchard, D. E. Holz, and C. Knight. Illuminating the Primeval Universe with Type II<sup>n</sup> Supernovae. *ApJ*, 768:195, May 2013a. doi: 10.1088/0004-637X/768/2/195.
- D. J. Whalen, C. L. Fryer, D. E. Holz, A. Heger, S. E. Woosley, M. Stiavelli, W. Even, and L. H. Frey. Seeing the First Supernovae at the Edge of the Universe with JWST. *ApJL*, 762:L6, January 2013b. doi: 10.1088/2041-8205/762/1/L6.
- Daniel Whalen and Michael L Norman. Ionization Front Instabilities in Primordial H II Regions. *ApJ*, 673:664, February 2008.
- J. H. Wise and T. Abel. ENZO+MORAY: radiation hydrodynamics adaptive mesh refinement simulations with adaptive ray tracing. *MNRAS*, 414:3458–3491, July 2011. doi: 10.1111/j.1365-2966.2011.18646.x.
- J. H. Wise, V. G. Demchenko, M. T. Halicek, M. L. Norman, M. J. Turk, T. Abel, and B. D. Smith. The birth of a galaxy - III. Propelling reionization with the faintest galaxies. *MNRAS*, 442:2560–2579, August 2014. doi: 10.1093/mnras/stu979.

- John H Wise and Renyue Cen. IONIZING PHOTON ESCAPE FRACTIONS FROM HIGH-REDSHIFT DWARF GALAXIES. *ApJ*, 693(1):984–999, March 2009.
- S. A. Wouthuysen. On the excitation mechanism of the 21-cm (radio-frequency) interstellar hydrogen emission line. *AJ*, 57:31–32, 1952. doi: 10.1086/106661.
- J Stuart B Wyithe and Abraham Loeb. Reionization of Hydrogen and Helium by Early Stars and Quasars. *ApJ*, 586(2):693–708, April 2003.
- Hidenobu Yajima and Sadegh Khochfar. Can the 21-cm signal probe Population III and II star formation? *MNRAS*, 448(1):654–665, March 2015.
- Erik Zackrisson, Claes-Erik Rydberg, Daniel Schaerer, Göran Östlin, and Manan Tuli. THE SPECTRAL EVOLUTION OF THE FIRST GALAXIES. I. JAMES WEBB SPACE TELESCOPE DETECTION LIMITS AND COLOR CRITERIA FOR POPULATION III GALAXIES. *ApJ*, 740(1):13, September 2011.
- Erik Zackrisson, Adi Zitrin, Michele Trenti, Claes-Erik Rydberg, Lucia Guaita, Daniel Schaerer, Tom Broadhurst, Göran Östlin, and Tina Ström. Detecting gravitationally lensed Population III galaxies with the Hubble Space Telescope and the James Webb Space Telescope. *MNRAS*, 427(3):2212–2223, November 2012.
- O. Zahn, A. Mesinger, M. McQuinn, H. Trac, R. Cen, and L. E. Hernquist. Comparison of reionization models: radiative transfer simulations and approximate, seminumeric models. *MNRAS*, 414:727–738, June 2011. doi: 10.1111/j.1365-2966.2011.18439.x.
- O. Zahn, C. L. Reichardt, L. Shaw, A. Lidz, K. A. Aird, B. A. Benson, L. E. Bleem, J. E. Carlstrom, C. L. Chang, H. M. Cho, T. M. Crawford, A. T. Crites, T. de Haan, M. A. Dobbs, O. Doré, J. Dudley, E. M. George, N. W. Halverson, G. P. Holder, W. L. Holzappel, S. Hoover, Z. Hou, J. D. Hrubes, M. Joy, R. Keisler, L. Knox, A. T. Lee, E. M. Leitch, M. Lueker, D. Luong-Van, J. J. McMahon, J. Mehl, S. S. Meyer, M. Millea, J. J. Mohr, T. E. Montroy, T. Natoli, S. Padin, T. Plagge, C. Pryke, J. E. Ruhl, K. K. Schaffer, E. Shirokoff, H. G. Spieler, Z. Staniszewski, A. A. Stark, K. Story, A. van Engelen, K. Vanderlinde, J. D. Vieira, and R. Williamson. Cosmic Microwave Background Constraints on the Duration and Timing of Reionization from the South Pole Telescope. *ApJ*, 756:65, September 2012. doi: 10.1088/0004-637X/756/1/65.
- W. Zheng, M. Postman, A. Zitrin, J. Moustakas, X. Shu, S. Jouvel, O. Høst, A. Molino, L. Bradley, D. Coe, L. A. Moustakas, M. Carrasco, H. Ford, N. Benítez, T. R. Lauer, S. Seitz, R. Bouwens, A. Koekemoer, E. Medezinski, M. Bartelmann, T. Broadhurst, M. Donahue, C. Grillo, L. Infante, S. W. Jha, D. D. Kelson, O. Lahav, D. Lemze, P. Melchior, M. Meneghetti, J. Merten, M. Nonino, S. Ogaz, P. Rosati, K. Umetsu, and A. van der Wel. A magnified young galaxy from about 500 million years after the Big Bang. *Nat*, 489:406–408, September 2012. doi: 10.1038/nature11446.
- B Zygelman. Hyperfine Transitions in Atomic Hydrogen. *ApJ*, 622:1356–1362, 2005.

## Appendix A

### The Differential Brightness Temperature

Derivation of Equation 4.8 follows naturally from the radiative transfer equation (RTE), which describes the change in the specific intensity or radiation at frequency  $\nu$  along a differential line element  $ds$ ,

$$\frac{dI_\nu}{ds} = j_\nu - \alpha_\nu I_\nu. \quad (\text{A.1})$$

Here,  $j_\nu$  is the “source term,” and the second quantity is the “sink term,” given by the product of the specific intensity and the absorption coefficient  $\alpha_\nu$ . This equation is intuitive: the change in the intensity along a ray is given by the difference between how many photons are injected and how many photons are absorbed.

Introducing the specific optical depth  $\tau_\nu$ ,

$$d\tau_\nu = \alpha_\nu ds \quad (\text{A.2})$$

and assuming a homogenous medium (in which  $j_\nu$  and  $\alpha_\nu$  are independent of  $s$ ), we arrive at a solution to Equation A.1 in only a few lines upon adopting the integrating factor  $\mu \equiv e^{\int \alpha_\nu ds}$ :

$$I_\nu(\tau_\nu) = I_\nu(0)e^{-\tau_\nu} + \frac{j_\nu}{\alpha_\nu}(1 - e^{-\tau_\nu}) \quad (\text{A.3})$$

This solution is generic for homogeneous media. However, in the context of the early universe (see Figure A.1), the background light source is the cosmic microwave background, i.e.,

$$I_\nu(0) \simeq \frac{2\nu^2}{c^2} k_B T_\gamma \quad (\text{A.4})$$

where we’ve adopted the Rayleigh-Jeans approximation,  $h\nu \ll k_B T_\gamma$ . As is usually the case,  $c$  is the speed of light,  $k_B$  is Boltzmann’s constant, and  $T_\gamma = T_{\gamma,0}(1+z)$  is the CMB temperature at redshift  $z$ , with the CMB temperature today given by  $T_{\gamma,0} = 2.725$  K.

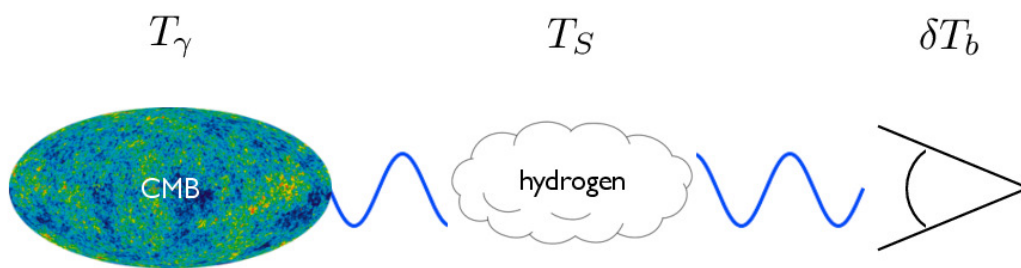


Figure A.1 Cartoon of the radiative transfer problem of the 21-cm signal.

Now, because we are radio astronomers, we will write the rest of the terms in Equation A.3 using the blackbody formula as well. Because we are merely using the Rayleigh-Jeans approximation for dimensional convenience, we will use the  $b$  subscript to indicate *brightness* temperatures, in contrast to the physically meaningful electron, or *kinetic* temperature,  $T_K$ . That is,

$$I_\nu(\tau_\nu) \equiv \frac{2\nu^2}{c^2} k_B T_b \quad (\text{A.5})$$

Similarly for the last term, whose brightness temperature we'll refer to with foresight as the “spin temperature,”  $T_S$ , such that Equation A.3 becomes

$$T_b = T_\gamma e^{-\tau_\nu} + T_S(1 - e^{-\tau_\nu}) \quad (\text{A.6})$$

Note that we are working in the frame of an HI cloud, meaning the redshift dependence of each temperature is implicit at this stage. A brightness temperature at redshift  $z$ ,  $T_b(z)$ , will correspond to an observed brightness temperature  $T_{b,0} = T_b(z)/(1+z)$ .

If we make the *ansatz* that  $\tau_\nu \ll 1$ , such that  $e^{-\tau_\nu} \approx 1 - \tau_\nu$  via a Taylor series expansion, then our solution simplifies further to

$$T_b \approx T_\gamma + (T_S - T_\gamma)\tau_\nu \quad (\text{A.7})$$

The observable signature of the 21-cm line at the Earth is simply  $T_{b,0} = T_b/(1+z)$ , which leaves

$$T_{b,0} \approx \frac{T_\gamma}{(1+z)} + \frac{T_S - T_\gamma}{(1+z)}\tau_\nu. \quad (\text{A.8})$$

The first term on the right-hand side is the CMB temperature today,  $T_{\gamma,0}$ , meaning the brightness temperature of an HI cloud relative to the CMB temperature is given by

$$\delta T_b \equiv T_{b,0} - T_{\gamma,0} \approx \frac{T_S - T_\gamma}{(1+z)}\tau_\nu. \quad (\text{A.9})$$

The quantity  $\delta T_b$  is the “differential brightness temperature” between HI and the CMB.

The optical depth depends on the cross-section for the 21-cm transition,

$$\sigma_{21} = \frac{3c^2 A_{21}}{8\pi\nu_{21}^2} \quad (\text{A.10})$$

integrated along a line of sight. A detailed solution, including redshift-space distortions, yields (e.g., Furlanetto et al., 2006a)

$$\tau_{\nu_0} \approx 0.0092(1 + \delta)(1 + z)^{3/2} \frac{x_{\text{H I}}}{T_S} \left[ \frac{H(z)/(1+z)}{dv_{\parallel}/dv_{\perp}} \right] \quad (\text{A.11})$$

Whether the signal is seen in emission or absorption against the CMB depends entirely on the spin temperature, which is determined by the strength of collisional and radiative coupling, characterized by the coefficients  $x_c$  and  $x_{\alpha}$ , respectively,

$$T_S^{-1} \approx \frac{T_{\gamma}^{-1} + x_c T_K^{-1} + x_{\alpha} T_{\alpha}^{-1}}{1 + x_c + x_{\alpha}}, \quad (\text{A.12})$$

where  $T_{\gamma} = T_{\gamma,0}(1+z)$  is the CMB temperature,  $T_K$  is the kinetic temperature, and  $T_{\alpha} \approx T_K$  is the UV color temperature.

In general, the collisional coupling is a sum over collision-partners,

$$x_c = \sum_i \frac{n_i \kappa_{10}^i T_*}{A_{10} T_{\gamma}}, \quad (\text{A.13})$$

where  $n_i$  is the number density of species  $i$ , and  $\kappa_{10}^i = \kappa_{10}^i(T_K)$  is the rate coefficient for spin de-excitation via collisions with species  $i$ . In a neutral gas, collisional coupling is dominated by hydrogen-hydrogen collisions (Allison and Dalgarno, 1969, Zygelman, 2005, Sigurdson and Furlanetto, 2006), though hydrogen-electron collisions can become important as the ionized fraction and temperature grow (Furlanetto and Furlanetto, 2007). We neglect collisional coupling due to all other species.<sup>1</sup>

The remaining coupling coefficient,  $x_{\alpha}$ , characterizes the strength of Wouthuysen-Field coupling (Wouthuysen, 1952, Field, 1958),

$$x_{\alpha} = \frac{S_{\alpha} \hat{J}_{\alpha}}{1 + z \bar{J}_{\alpha}}, \quad (\text{A.14})$$

where

$$\bar{J}_{\alpha} \equiv \frac{16\pi^2 T_* e^2 f_{\alpha}}{27 A_{10} T_{\gamma,0} m_e c}. \quad (\text{A.15})$$

<sup>1</sup> Furlanetto and Furlanetto (2007) investigated the effects of hydrogen-proton collisions on  $T_S$  and found that they could account for up to  $\sim 2\%$  of the collisional coupling at  $z \approx 20$ , and would dominate the coupling at  $z \approx 10$  in the absence of heat sources. However, an early Ly- $\alpha$  background is expected to couple  $T_S \rightarrow T_K$  prior to  $z = 20$ , and heating is expected prior  $z = 10$ , so protons are generally neglected in 21-cm calculations. Collisions with neutral helium atoms in the triplet state could also induce spin-exchange (Hirata and Sigurdson, 2007), though the cold high- $z$  IGM lacks the energy required to excite atoms to the triplet state. We also neglect hydrogen-deuterium collisions, whose rarity prevents any real effect on  $T_S$ , even though  $\kappa_{10}^{\text{HD}} > \kappa_{10}^{\text{HH}}$  at low temperatures (Sigurdson and Furlanetto, 2006). Lastly, we neglect velocity-dependent effects (Hirata and Sigurdson, 2007), which introduces an uncertainty of up to a few % in the mean signal.

$\hat{J}_\alpha$  is the angle-averaged intensity of Ly- $\alpha$  photons in units of  $\text{s}^{-1} \text{cm}^{-2} \text{Hz}^{-1} \text{sr}^{-1}$ ,  $S_\alpha$  is a correction factor that accounts for variations in the background intensity near line-center (Chen and Miralda-Escudé, 2004, Furlanetto and Pritchard, 2006, Hirata, 2006),  $m_e$  and  $e$  are the electron mass and charge, respectively,  $f_\alpha$  is the Ly- $\alpha$  oscillator strength, and  $A_{10}$  is the Einstein A coefficient for the 21-cm transition.

## Appendix B

### Non-Equilibrium Chemistry in a Gas of Primordial Composition

This appendix serves as a reference for the equations of non-equilibrium primordial (i.e., hydrogen & helium) chemistry, solutions to which are at the core of many results presented in this thesis.

Rate equations for hydrogen:

$$\begin{pmatrix} \dot{x}_{\text{H I}} \\ \dot{x}_{\text{H II}} \end{pmatrix} = \begin{bmatrix} -(\Gamma_{\text{HI}} + \gamma_{\text{HI,HI}} + \beta_{\text{H I}} n_e) & \alpha_{\text{H II}} n_e \\ \Gamma_{\text{HI}} + \gamma_{\text{HI}} + \beta_{\text{H I}} n_e & -\alpha_{\text{H II}} n_e \end{bmatrix} \begin{pmatrix} x_{\text{H I}} \\ x_{\text{H II}} \end{pmatrix}$$

Rate equations for helium

$$\begin{pmatrix} \dot{x}_{\text{He I}} \\ \dot{x}_{\text{He II}} \\ \dot{x}_{\text{He III}} \end{pmatrix} = \begin{bmatrix} -(\Gamma_{\text{HeI}} + \gamma_{\text{HeI}} + \beta_{\text{He I}} n_e) & +(\alpha_{\text{He II}} + \xi_{\text{HeII}}) n_e & 0 \\ \Gamma_{\text{HeI}} + \gamma_{\text{HeI}} + \beta_{\text{He I}} n_e & -(\Gamma_{\text{HeII}} + \gamma_{\text{HeII}}) - (\beta_{\text{He II}} + \alpha_{\text{He II}} + \xi_{\text{HeII}}) n_e & \alpha_{\text{He III}} n_e \\ 0 & \Gamma_{\text{HeII}} + \gamma_{\text{HeII}} + \beta_{\text{He II}} n_e & -\alpha_{\text{He III}} n_e \end{bmatrix} \begin{pmatrix} x_{\text{He I}} \\ x_{\text{He II}} \\ x_{\text{He III}} \end{pmatrix}$$

**Evolution of the (proper) electron number density:**

$$\dot{n}_e = \begin{bmatrix} n_{\text{H}}(\Gamma_{\text{HI}} + \gamma_{\text{HI}} + \beta_{\text{H I}} n_e) \\ -n_{\text{H}}\alpha_{\text{H II}} n_e \\ n_{\text{He}}(\Gamma_{\text{HeI}} + \gamma_{\text{HeI}} + \beta_{\text{He I}} n_e) \\ n_{\text{He}} \{ (\Gamma_{\text{HeII}} + \gamma_{\text{HeII}} + \beta_{\text{He II}} n_e) - (\alpha_{\text{He II}} + \xi_{\text{HeII}}) n_e \} \\ -n_{\text{He}}\alpha_{\text{He III}} n_e \end{bmatrix} \begin{pmatrix} x_{\text{H I}} & x_{\text{H II}} & x_{\text{He I}} & x_{\text{He II}} & x_{\text{He III}} \end{pmatrix}$$

| Term           | Description  |
|----------------|--|
| $\Gamma_i$     | Rate coefficient for photo-ionization of neutral species $i$   |
| $\gamma_{i,j}$ | Rate coefficient for collisional ionization of neutral species $i$ due to fast secondary electrons previously bound to species $j$ |
| $\beta_i$      | Rate coefficient for collisional ionization of neutral species $i$ due to thermal distribution of electrons                        |
| $\alpha_i$     | Rate coefficient for radiative recombination <i>into</i> species $i$   |

Table B.1 Description of terms in above equations.

### Evolution of the kinetic temperature:

Start with the first law of thermodynamics:

$$\frac{dU}{dt} = \frac{dQ}{dt} - P \frac{dV}{dt} \quad (\text{B.1})$$

For an ideal, monatomic gas, we can write

$$U = \frac{3}{2} nk_B T_K \quad (\text{B.2})$$

and

$$P = nk_B T_K \quad (\text{B.3})$$

Differentiating, we have

$$\frac{dU}{dt} = \frac{d}{dt} \left[ \frac{3}{2} nk_B T_K \right] = \frac{3}{2} k_B \left[ T_K \frac{dn}{dt} + n \frac{dT_K}{dt} \right] \quad (\text{B.4})$$

We'll take  $dQ/dt = \mathcal{H} - \Lambda$ , which means we've got

$$\frac{3}{2} k_B \left[ T_K \frac{dn}{dt} + n \frac{dT_K}{dt} \right] = (\mathcal{H} - \Lambda) - P \frac{dV}{dt} \quad (\text{B.5})$$

Solving for  $T_K$ , we've got

$$\frac{dT_K}{dt} = \frac{2(\mathcal{H} - \Lambda)}{3k_B n} - \frac{T_K}{n} \frac{dn}{dt} - \frac{2}{3} T_K \frac{dV}{dt} \quad (\text{B.6})$$

The last term vanishes if we're performing calculations on a static (physical) mesh, though in a cosmological volume element it will be non-zero.

## Appendix C

### Cosmological Radiative Transfer: Test Problem

In this section, we test our code with a double power-law form for the X-ray emissivity,  $\hat{\epsilon}_v(z) \propto (1+z)^{\beta} v^{\alpha-1}$ , noted by Meiksin and White (2003) to yield analytic solutions in two important limiting cases. In the optically-thin limit (e.g., the cosmologically-limited (CL) case of Meiksin and White, 2003, in which  $\bar{x}_i = 1$  at all redshifts), we find

$$\hat{J}_{v,CL}(z) = \frac{c}{4\pi} \frac{\hat{\epsilon}_v(z)}{H(z)} \frac{(1+z)^{9/2-(\alpha+\beta)}}{\alpha+\beta-3/2} \times \left[ (1+z_f)^{\alpha+\beta-3/2} - (1+z)^{\alpha+\beta-3/2} \right] \quad (\text{C.1})$$

In the Ly- $\alpha$  literature it is common to accommodate the alternative ‘‘absorption-limited’’(AL) case in which  $\bar{\tau}_v > 0$ , by defining the ‘‘attenuation length,’’  $r_0$ , as  $\exp[-\tau_v(z, z')] \equiv \exp[-l_H(z, z')/r_0]$ , where  $l_H$  is the proper distance between redshifts  $z$  and  $z'$ . Instead, we will adopt the neutral-medium approximation of Equation 5.18 (i.e.,  $\bar{x}_i = 0$ ), which permits the partially analytic solution

$$\hat{J}_{v,AL}(z) = \frac{c}{4\pi} \frac{\hat{\epsilon}_v(z)}{H(z)} (1+z)^{9/2-(\alpha+\beta)} \times \exp\left[-\left(\frac{\mu}{v}\right)^3 (1+z)^{3/2}\right] \mathcal{A}_v(\alpha, \beta, z, z_f) \quad (\text{C.2})$$

with

$$\mathcal{A}_v \equiv \int_{z'=z}^{z'=z_f} (1+z')^{\alpha+\beta-5/2} \exp\left[\left(\frac{\mu}{v}\right)^3 \frac{(1+z)^3}{(1+z')^{3/2}}\right] dz'. \quad (\text{C.3})$$

The function  $\mathcal{A}_v$  has analytic solutions (in the form of Exponential integrals) only for  $\alpha + \beta = 3n/2$  where  $n$  is a positive integer, which represents physically unrealistic scenarios.

The metagalactic spectral index in this case works out to be

$$\alpha_{MG} \equiv \frac{d \log J_v}{d \log v} = \alpha + 3 \left(\frac{\mu}{v}\right)^3 (1+z)^{3/2} \left[1 - \mathcal{B}_v(1+z)^{3/2}\right] \quad (\text{C.4})$$

where

$$\mathcal{B}_\nu = \mathcal{A}_\nu^{-1} \int_z^{z_f} (1+z')^{\alpha+\beta-4} \exp \left[ \left( \frac{\mu}{\nu} \right)^3 \frac{(1+z)^3}{(1+z')^{3/2}} \right] dz'. \quad (\text{C.5})$$

As  $\nu \rightarrow \infty$ , the second term vanishes, leaving the optically-thin limit,  $\alpha_{\text{MG}} = \alpha$ . As  $\nu \rightarrow 0$ ,  $\mathcal{B}_\nu \rightarrow 0$ , meaning  $\alpha_{\text{MG}} = \alpha + 3$ . The “break” in the cosmic X-ray background spectrum occurs when  $\alpha_{\text{MG}} = 0$ , corresponding to a photon energy of

$$h\nu_* = h\mu(1+z) \left\{ \frac{3}{\alpha} \left[ \mathcal{B}_{\nu_*} - (1+z)^{-3/2} \right] \right\}^{1/3} \quad (\text{C.6})$$

which must be solved iteratively. Solutions are presented in Figure C.1 for  $\alpha = -1.5$ ,  $\beta = -3$ ,  $\hat{\epsilon}_\nu(z_0) = 10^{-2}$  for  $z_0 = 10$ ,  $z_f = 15$ , and show good agreement between analytic and numerical solutions.

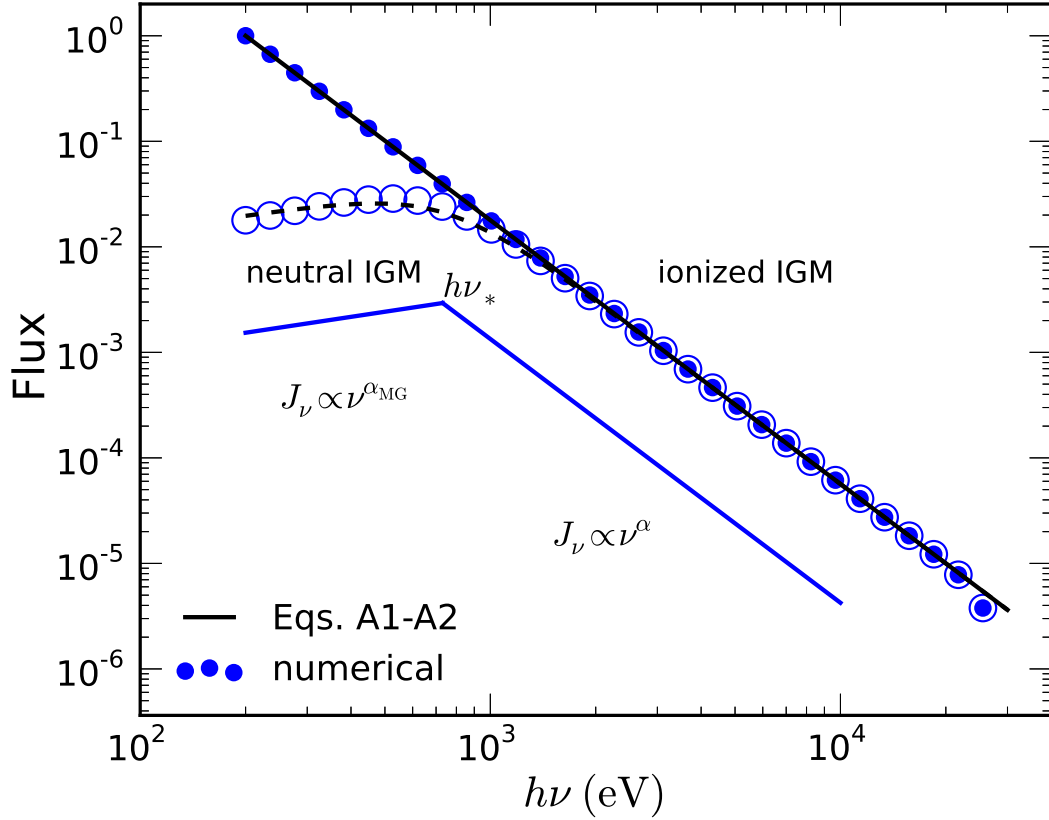


Figure C.1 Cosmic X-ray background spectrum at  $z = 20$  for  $\alpha = -1.5$  and  $\beta = -3$ . Normalization of the y-axis can be scaled arbitrarily depending on the normalization of the emissivity. The deviation at high energies is due to the fact that the analytic solution is not truncated by  $z_f$  or  $E_{\max}$ , meaning there are always higher energy photons redshifting to energies  $h\nu \leq h\nu_{\max}$ . The numerical solutions are computed with finite integration limits and truncated at  $E_{\max}$ , such that the emissivity at  $h\nu > h\nu_{\max}$  is zero, resulting in no flux at  $h\nu \geq h\nu_{\max}$ . Elsewhere, the agreement is very good, with discrepancies arising solely due to the use of approximate bound-free photo-ionization cross sections in the analytic solution.

## Appendix D

### 1-D Radiative Transfer: Test Problems

Our one-dimensional radiative transfer code solves Equations (6.1)–(6.5) using the implicit Euler method for integration and a Newton–Raphson technique for root finding. Each simulation is initialized on a grid of  $N_c$  cells between  $L_0$  and  $L_{\text{box}}$ , such that the finest resolution element is  $\Delta x = (L_{\text{box}} - L_0)/N_c$ , or simply  $\Delta x = 1/N_c$  in code units. Gas inside of the start radius,  $L_0$ , contributes no optical depth, and Equations (6.1)–(6.5) are not solved. For the purposes of this section, we chose to use  $N_c$  linearly spaced cells between  $L_0$  and  $L_{\text{box}}$ , though our code allows arbitrarily structured grids.

In order to track the propagation of ionization fronts accurately, we limit the time-step based on a maximum neutral fraction change as introduced in Shapiro et al. (2004),

$$\Delta t_i = \epsilon_{\text{ion}} \frac{n_i}{|dn_i/dt|}, \quad (\text{D.1})$$

where we include all absorbing species,  $i = \text{H I}, \text{He I}, \text{He II}$ , and set  $\Delta t = \min(\Delta t_i)$ . We additionally require that the time step increase by a factor of two at most, as in Wise and Abel (2011). For all simulations presented in this work, we have set  $\epsilon_{\text{ion}} = 0.05$ .

The primary solver implemented in our code assumes the speed-of-light is infinite. Such an algorithm is appealing for two main reasons, aside from the fact that it is a very good approximation for the problems presented in this work. First, treating the speed-of-light explicitly introduces additional computational overhead as “photon packages” must be launched from the radiation source at each time step and tracked until they exit the domain. In the earliest stages of I-front propagation, the time step can be very small (as required by Equation (D.1)), meaning the total number of photon packages,  $N_p$ , will be much larger than the

total number of grid cells,  $N_c$ . Whereas  $c = \infty$  treatments only require Equations (6.1)-(6.5) to be solved once per cell, finite speed-of-light treatments require this system of equations to be solved for each photon package. At later times, when  $N_p < N_c$ , solving the ion and heat equations is cheaper for finite speed-of-light treatments, though this offers no real advantage since the majority of the computational expense is at early times when I-front propagation is fastest. We have also included a finite  $c$  solver to accommodate a broader class of problems that may be of interest in future work.

The second advantage of assuming  $c = \infty$  is that it allows the code to be efficiently parallelized. If  $c = \infty$ , cells in the domain can be solved in arbitrary order by a single processor, or simultaneously by a network of processors, since the radiation incident on any cell is predetermined at the outset of each individual time step. Previous authors have ensured causality by solving cell  $k$  before cell  $k + 1$  at time  $t$  (where increasing  $k$  corresponds to increasing  $r$ ), but this is not in fact necessary — causality is ensured by the monotonicity of column density with distance. In other words, when  $c = \infty$ ,  $N_i$  does not change within any given time step, and so the column density (and thus radiative flux) to cell  $k$  is less than the column density (and flux) to cell  $k + 1$ , meaning the solution of Equations (6.1)-(6.5) in cell  $k + 1$  is completely independent of the properties of cell  $k$  at time  $t + \Delta t$ .

To demonstrate the functionality of the code, we repeat tests 1 and 2 from the Radiative Transfer Comparison Project (Iliev et al. (2006, hereafter referred to as RT06)) on a grid of 200 linearly spaced cells. Test 1 is the expansion of an H II region in a hydrogen-only, isothermal medium surrounding a monochromatic source of 13.6 eV photons. We adopt the same parameters used in RT06: constant temperature  $T = 10^4$  K, uniform hydrogen number density  $n_{\text{H}} = 10^{-3} \text{ cm}^{-3}$ , ionized fraction  $x_{\text{H II}} = 1.2 \times 10^{-3}$ , in a box  $L_{\text{box}} = 6.6$  kpc in size, and with photon luminosity  $\dot{Q} = 5 \times 10^{48} \text{ s}^{-1}$ . The classical analytic solution for the radius of an ionization front is

$$r_{\text{IF}}(t) = r_s(1 - e^{-t/t_{\text{rec}}})^{1/3}, \quad (\text{D.2})$$

where  $r_s$  is the Strömgen radius,

$$r_s = \left( \frac{3\dot{Q}}{4\pi\alpha_{\text{H II}}n_{\text{H}}^2} \right)^{1/3}, \quad (\text{D.3})$$

and the recombination time,  $t_{\text{rec}}$ , is defined as

$$t_{\text{rec}} \equiv \frac{1}{\alpha_{\text{H II}} n_{\text{H I}}}. \quad (\text{D.4})$$

This solution is approximate even in isothermal media, given that it assumes a constant neutral hydrogen density,  $n_{\text{H I}}$ . More accurate analytic solutions exist (Osterbrock and Ferland, 2006), and predict a departure from the classical solution at  $t/t_{\text{rec}} \simeq 1$ , which grows to a  $\sim 5\%$  difference by  $t/t_{\text{rec}} \simeq 4$ . Our numerical solution (see Figure D.1a) captures this behavior very well. In Figure D.1b, we show radial profiles of the ionized and neutral fractions at three stages of the I-front expansion, which are again in very good agreement with the calculations presented in RT06.

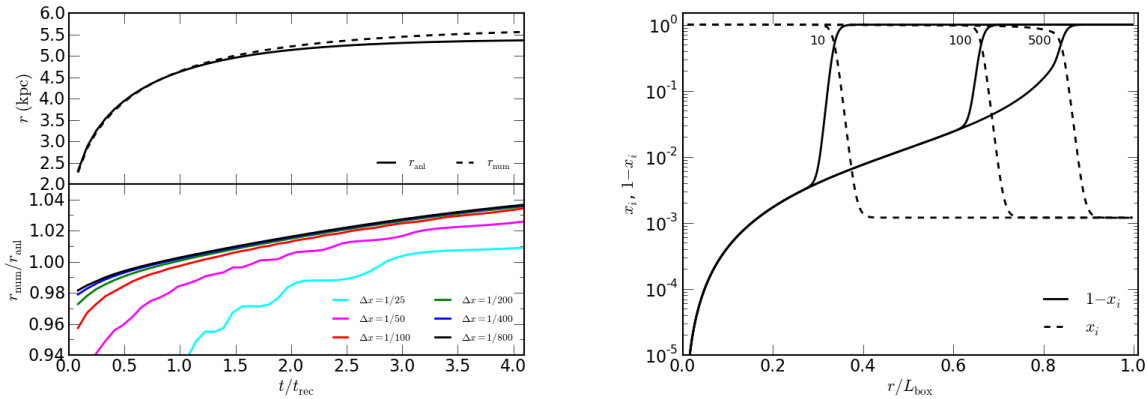


Figure D.1 Test 1: (a) Comparison of the numerical (dashed) and analytic (solid) solutions for the position of an expanding ionization front as a function of time in a hydrogen-only, isothermal medium (RT06 problem 1; top), and the ratio of the calculated and analytic solutions as a function of time and grid resolution (bottom). The numerical solution displayed in the top panel is from the highest resolution simulation (800 grid cells, i.e.,  $\Delta x = L_{\text{box}}/800$ ). (b) Radial profiles of the neutral (solid) and ionized (dashed) fractions at  $t = 10, 100,$  and  $500$  Myr.

Test 2 is the same as Test 1, except now the temperature is allowed to evolve according to Equation (6.5), and the monochromatic radiation source is replaced by a  $10^5$  K blackbody spectrum. Radial profiles of the neutral and ionized fractions and temperature can be seen in Figure D.2. Again, our numerical solutions are in very good agreement with previous work.

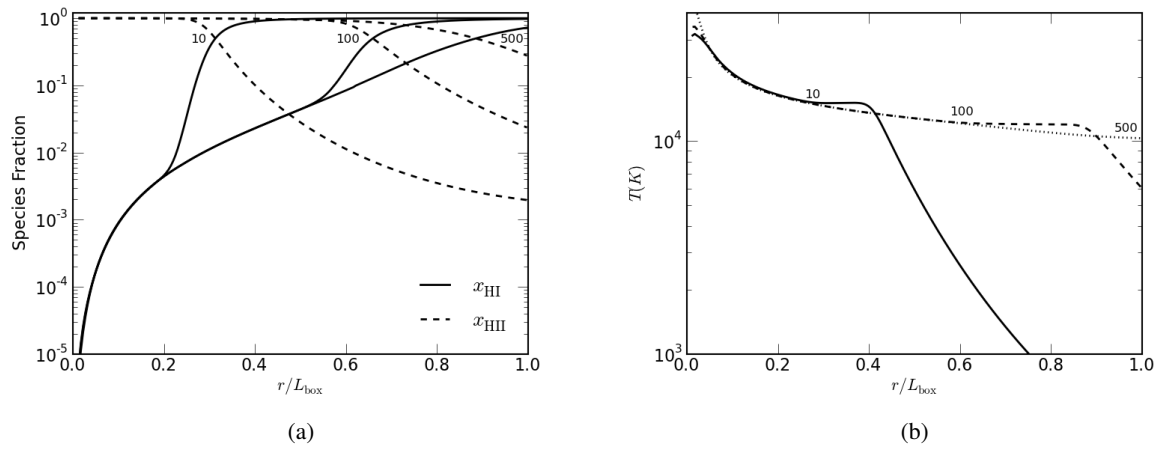


Figure D.2 Test 2: (a) Radial profiles of the neutral (solid) and ionized (dashed) fractions at  $t = 10, 100,$  and  $500$  Myr. (b) Radial profiles of the kinetic temperature at  $t = 10, 100,$  and  $500$  Myr (solid, dashed, and dotted lines, respectively).

## Appendix E

### Secondary Ionization & Heating

In the previous section (and in all of Mirocha et al. (2012)), we considered the asymptotic limit of Shull and van Steenberg (1985), in which the fractional energy deposition of secondary electrons as heat, ionization, and excitation depends only on the hydrogen ionized fraction. Ricotti et al. (2002) and Furlanetto and Johnson Stoeber (2010) updated this work, providing (respectively) empirical fits and lookup tables of deposition fraction as a function of both ionized fraction and electron energy. These effects are most important at  $E \lesssim 10^2$  eV.

To accommodate this model, we must redefine the quantities  $\Phi_i$  and  $\Psi_i$ . We will use a tilde to denote the new quantities related to secondary ionization,

$$\tilde{\Phi}_{ij} \equiv \int_{\nu_j}^{\infty} f_{ij,(\nu-\nu_j)}^{\text{ion}} I_{\nu} e^{-\tau_{\nu}} \frac{d\nu}{h\nu} \quad (\text{E.1})$$

$$\tilde{\Psi}_{ij} \equiv \int_{\nu_j}^{\infty} f_{ij,(\nu-\nu_j)}^{\text{ion}} I_{\nu} e^{-\tau_{\nu}} d\nu, \quad (\text{E.2})$$

and a hat to denote the new quantities related to photo-electric heating,

$$\hat{\Phi}_i \equiv \int_{\nu_i}^{\infty} f_{(i-\nu_i)}^{\text{heat}} I_{\nu} e^{-\tau_{\nu}} \frac{d\nu}{h\nu} \quad (\text{E.3})$$

$$\hat{\Psi}_i \equiv \int_{\nu_i}^{\infty} f_{(i-\nu_i)}^{\text{heat}} I_{\nu} e^{-\tau_{\nu}} d\nu. \quad (\text{E.4})$$

Now, our ionization and heating coefficients (formerly Eqs. 6.13-6.15) read

$$\Gamma_i = A_i [\Phi_i(\tau_{\nu}) - \Phi_i(\tau'_{i,\nu})] \quad (\text{E.5})$$

$$\gamma_{ij} = \frac{A_j}{h\nu_i} \left\{ \tilde{\Psi}_{ij}(\tau_{\nu}) - \tilde{\Psi}_{ij}(\tau'_{j,\nu}) - h\nu_j [\tilde{\Phi}_{ij}(\tau_{\nu}) - \tilde{\Phi}_{ij}(\tau'_{j,\nu})] \right\} \quad (\text{E.6})$$

$$\mathcal{H}_i = A_i \left\{ \hat{\Psi}_i(\tau_{\nu}) - \hat{\Psi}_i(\tau'_{i,\nu}) - h\nu_i [\hat{\Phi}_i(\tau_{\nu}) - \hat{\Phi}_i(\tau'_{i,\nu})] \right\}. \quad (\text{E.7})$$

## Appendix F

### Multi-Frequency vs. Multi-Group Transfer

#### F.1 ‘Multi-Group’ Methods

The standard method of discretizing spectra has been to calculate the mean photon emission energy in one or more bandpasses,

$$h\bar{\nu}_n \equiv \int_{\nu_n}^{\nu_{n+1}} I_\nu d\nu \left( \int_{\nu_n}^{\nu_{n+1}} \frac{I_\nu}{h\nu} d\nu \right)^{-1}, \quad (\text{F.1})$$

and define a new, spectrum-weighted bound-free absorption coefficient as

$$\bar{\sigma}_{i,n} \equiv \int_{\nu_n}^{\nu_{n+1}} \sigma_\nu \frac{I_\nu}{h\nu} d\nu \left( \int_{\nu_n}^{\nu_{n+1}} \frac{I_\nu}{h\nu} d\nu \right)^{-1}, \quad (\text{F.2})$$

where  $n = 0, 1, 2, \dots, n_\nu$ . Keep in mind that here, “spectrum-weighted” really means “weighted by photon number.”

For reference, if we assume a single (very large) bandpass, these equations reduce to:

$$h\bar{\nu}_i \equiv \int_{\nu_i}^{\infty} I_\nu d\nu \left( \int_{\nu_i}^{\infty} \frac{I_\nu}{h\nu} d\nu \right)^{-1}, \quad (\text{F.3})$$

and

$$\bar{\sigma}_i \equiv \int_{\nu_i}^{\infty} \sigma_{i,\nu} \frac{I_\nu}{h\nu} d\nu \left( \int_{\nu_i}^{\infty} \frac{I_\nu}{h\nu} d\nu \right)^{-1}. \quad (\text{F.4})$$

#### F.2 Analytic Limits

##### F.2.1 Perfectly Optically Thin

The simplest case is the perfectly optically thin limit (i.e.  $\tau_\nu = \Delta\tau_{i,\nu} = 0$ ), which is very uninteresting:

$$\Gamma_i = \mathcal{H}_i = \gamma_i = 0. \quad (\text{F.5})$$

Any other case with  $\Delta\tau_{i,v} = 0$  identically will be equally uninteresting.

### F.2.2 Optically Thin Cells, Arbitrary $\tau_v$

In this case,

$$\begin{aligned} (1 - e^{-\Delta\tau_{i,v}}) &\approx (1 - (1 - \Delta\tau_{i,v})) \\ &\approx \Delta\tau_{i,v} \\ &\approx \sigma_{i,v}N_i. \end{aligned} \tag{F.6}$$

With this approximation, and recalling  $A_i \equiv L_{\text{bol}}/n_iV_{\text{sh}}(r)$  (see §6.3), we have

$$\begin{aligned} \Gamma_i &= A_i \int_{v_i}^{\infty} I_v e^{-\tau_v} (1 - e^{-\Delta\tau_{i,v}}) \frac{dv}{h\nu} \\ &\approx \frac{L_{\text{bol}}}{n_iV_{\text{sh}}(r)} \int_{v_i}^{\infty} I_v e^{-\tau_v} \sigma_{i,v} N_i \frac{dv}{h\nu} \\ &\approx \frac{L_{\text{bol}}}{4\pi r^2} \int_{v_i}^{\infty} I_v e^{-\tau_v} \sigma_{i,v} \frac{dv}{h\nu}. \end{aligned} \tag{F.7}$$

Similarly,

$$\gamma_{ij} \approx \frac{L_{\text{bol}}}{4\pi r^2} \int_{v_j}^{\infty} \left( \frac{v - v_j}{v_i} \right) I_v e^{-\tau_v} \sigma_{j,v} \frac{dv}{h\nu} \tag{F.8}$$

$$\mathcal{H}_i \approx \frac{L_{\text{bol}}}{4\pi r^2} \int_{v_i}^{\infty} (v - v_i) I_v e^{-\tau_v} \sigma_{i,v} \frac{dv}{v}. \tag{F.9}$$

You may recognize the above equations as expressions for the rate coefficients in non-photon-conserving form. This isn't terribly useful, since we still have to do integrals (or use lookup tables) to compute the rate coefficients.

### F.2.3 Small Optical Depth

The only real analytic limit that exists occurs if  $0 < \tau_v \ll 1, 0 < \Delta\tau_{i,v} \ll 1$ , i.e. the limit where the optical depth between source and cell and the optical depth of the cells themselves is non-zero but small. In addition to Equation F.6, we have

$$e^{-\tau_v} \approx (1 - \tau_v). \tag{F.10}$$

We will now examine the ionization and heating rates for this limit in detail.

### F.2.3.1 Photo-Ionization Rate

Substituting the above approximation into Equation 6.7, we have

$$\begin{aligned}
 \Gamma_i &= A_i \int_{\nu_i}^{\infty} I_\nu e^{-\tau_\nu} (1 - e^{-\Delta\tau_{i,\nu}}) \frac{d\nu}{h\nu} \\
 &\approx A_i \int_{\nu_i}^{\infty} I_\nu (1 - \tau_\nu) \Delta\tau_{i,\nu} \frac{d\nu}{h\nu} \\
 &\approx A_i \left[ \int_{\nu_i}^{\infty} I_\nu (\Delta\tau_{i,\nu} - \tau_\nu \Delta\tau_{i,\nu}) \frac{d\nu}{h\nu} \right].
 \end{aligned} \tag{F.11}$$

Neglecting the second order term (where  $\Gamma_i \propto \tau_\nu \Delta\tau_{i,\nu}$ ), recalling  $A_i \equiv L_{\text{bol}}/n_i V_{\text{sh}}(r)$ , and the approximate value of  $\Delta\tau_{i,\nu}$  (Eq. F.6), we have

$$\Gamma_i \approx \frac{L_{\text{bol}}}{n_i V_{\text{sh}}(r)} \int_{\nu_i}^{\infty} I_\nu \sigma_{i,\nu} N_i(r) \frac{d\nu}{h\nu}. \tag{F.12}$$

Now, for  $r \gg \Delta r$ ,

$$V_{\text{sh}}(r) \approx 4\pi r^2 \Delta r, \tag{F.13}$$

but  $n_i \Delta r \equiv N_i$ , so

$$\Gamma_i \approx \frac{L_{\text{bol}}}{4\pi r^2} \int_{\nu_i}^{\infty} I_\nu \sigma_{i,\nu} \frac{d\nu}{h\nu}. \tag{F.14}$$

The integral in this expression also appears in the definition for a ‘‘spectrum-weighted’’ cross-section (Eq. F.4), allowing us to write

$$\Gamma_i \approx \frac{L_{\text{bol}}}{4\pi r^2} \bar{\sigma}_i \int_{\nu_i}^{\infty} \frac{I_\nu}{h\nu} d\nu, \tag{F.15}$$

and finally via Equation F.3,

$$\Gamma_i \approx \frac{L_{\text{bol}}}{4\pi r^2} \frac{\bar{\sigma}_i}{h\bar{\nu}_i} \int_{\nu_i}^{\infty} I_\nu d\nu. \tag{F.16}$$

This tells us that a ‘multi-group’ treatment which averages over one large bandpass will compute the photo-ionization rate accurately *so long as*  $\tau_\nu$  and  $\Delta\tau_{i,\nu}$  are very small.

### F.2.3.2 Photo-Heating Rate

Let's apply the same approximation,  $\Delta\tau_{i,v} \ll 1$ , to the heating rate coefficient.

$$\begin{aligned}
\mathcal{H}_i &= A_i \int_{\nu_i}^{\infty} (\nu - \nu_i) I_\nu e^{-\tau_\nu} (1 - e^{-\Delta\tau_{i,\nu}}) \frac{d\nu}{\nu} \\
&\approx \frac{\mathcal{L}_{\text{bol}}}{n_i V_{\text{sh}}(r)} \int_{\nu_i}^{\infty} (\nu - \nu_i) I_\nu \sigma_{i,\nu} N_i(r) \frac{d\nu}{\nu} \\
&\approx \frac{\mathcal{L}_{\text{bol}}}{4\pi r^2} \left[ \int_{\nu_i}^{\infty} \sigma_{i,\nu} I_\nu d\nu - h\nu_i \int_{\nu_i}^{\infty} \sigma_{i,\nu} I_\nu \frac{d\nu}{h\nu} \right]
\end{aligned} \tag{F.17}$$

Notice that the second term again contains the definition for a ‘‘spectrum-weighted’’ cross-section over one large bandpass. Substituting in Equations F.4 and F.3, we find

$$\begin{aligned}
\mathcal{H}_i &\approx \frac{\mathcal{L}_{\text{bol}}}{4\pi r^2} \left[ \int_{\nu_i}^{\infty} \sigma_{i,\nu} I_\nu d\nu - \bar{\sigma}_i h\nu_i \int_{\nu_i}^{\infty} \frac{I_\nu}{h\nu} d\nu \right] \\
&\approx \frac{\mathcal{L}_{\text{bol}}}{4\pi r^2} \left[ \int_{\nu_i}^{\infty} \sigma_{i,\nu} I_\nu d\nu - \bar{\sigma}_i \frac{h\nu_i}{h\bar{\nu}_i} \int_{\nu_i}^{\infty} I_\nu d\nu \right].
\end{aligned} \tag{F.18}$$

The second term is simply the photo-ionization rate (Eq. F.16), modulo a factor of  $h\nu_i$ , i.e.

$$\mathcal{H}_i \approx \frac{\mathcal{L}_{\text{bol}}}{4\pi r^2} \int_{\nu_i}^{\infty} \sigma_{i,\nu} I_\nu d\nu - h\nu_i \Gamma_i \tag{F.19}$$

The integral in the above expression is very similar to our expression for a ‘‘spectrum-weighted’’ cross-section, but now instead of weighting  $\sigma_{i,\nu}$  by the factor  $I_\nu/h\nu$  (which is proportional to photon number), it is weighted by  $I_\nu$  itself (which is proportional to photon energy). Now it should be a little bit more clear why I've been writing ‘‘spectrum-weighted’’ in quotes all this time – we really have *two* ‘‘spectrum-weighted’’ cross-sections to worry about, the second being

$$\tilde{\sigma}_i \equiv \int_{\nu_i}^{\infty} \sigma_{i,\nu} I_\nu d\nu \left( \int_{\nu_i}^{\infty} I_\nu d\nu \right)^{-1}. \tag{F.20}$$

With this definition, and using Equation F.16 to write the first term of Equation F.19 as a function of  $\Gamma_i$ , we have

$$\mathcal{H}_i \approx \Gamma_i h \left[ \bar{\nu}_i \left( \frac{\tilde{\sigma}_i}{\bar{\sigma}_i} \right) - \nu_i \right]. \tag{F.21}$$

But wait a second. If we were to run a simulation with monochromatic emission at frequency given by Equation F.3, we would compute the heating rate via

$$\mathcal{H}_i = \Gamma_i h (\bar{\nu}_i - \nu_i). \tag{F.22}$$

Setting Equations F.21 and F.22 equal, we have a condition under which  $\Gamma_i$  and  $\mathcal{H}_i$  will be simultaneously accurate when  $\Delta\tau_{i,v} \ll 1$ ,

$$\frac{\tilde{\sigma}_i}{\bar{\sigma}_i} = 1. \quad (\text{F.23})$$

For a  $10^5$  K blackbody spectrum,

$$\frac{\tilde{\sigma}_i}{\bar{\sigma}_i} \approx 0.7, \quad (\text{F.24})$$

which (partially) explains why monochromatic emission cannot simultaneously capture ionization and heating accurately, even when cells are optically thin. Remember too that so far we have assumed all photo-electron energy is deposited as heat.

So, in this limit, if we want to simultaneously capture ionization and heating, we should be computing the heating rate via Equation F.21, not Equation F.22.

### F.2.3.3 Secondary Ionization Rate

Finally, the secondary ionization rate (assuming asymptotic limit of Shull and van Steenberg (1985) - i.e. deposition fraction is energy independent)

$$\begin{aligned} \gamma_{ij} &= A_j \int_{v_j}^{\infty} \left( \frac{v - v_j}{v_i} \right) I_v e^{-\tau_v} (1 - e^{-\Delta\tau_{j,v}}) \frac{dv}{hv} \\ &\approx \frac{\mathcal{L}_{\text{bol}}}{n_j V_{\text{sh}}(r)} \int_{v_j}^{\infty} \left( \frac{v - v_j}{v_i} \right) I_v \sigma_{j,v} N_j \frac{dv}{hv} \\ &\approx \frac{\mathcal{L}_{\text{bol}}}{4\pi r^2} \left[ \frac{1}{hv_i} \int_{v_j}^{\infty} I_v \sigma_{j,v} dv - \frac{hv_j}{hv_i} \int_{v_j}^{\infty} I_v \sigma_{j,v} \frac{dv}{hv} \right]. \end{aligned} \quad (\text{F.25})$$

Substituting in our definitions for the spectrum weighted cross-sections (Equations F.4 and F.20), we have

$$\gamma_{ij} \approx \frac{\mathcal{L}_{\text{bol}}}{4\pi r^2} \left[ \frac{\tilde{\sigma}_j}{hv_i} \int_{v_j}^{\infty} I_v dv - \bar{\sigma}_j \left( \frac{hv_j}{hv_i} \right) \int_{v_j}^{\infty} \frac{I_v}{hv} dv \right], \quad (\text{F.26})$$

and the photo-ionization rate (Eq. F.16)

$$\gamma_{ij} \approx \Gamma_j \left( \frac{h\bar{v}_j}{hv_i} \right) \left( \frac{\tilde{\sigma}_j}{\bar{\sigma}_j} \right) - \frac{\mathcal{L}_{\text{bol}}}{4\pi r^2} \left( \frac{hv_j}{hv_i} \right) \bar{\sigma}_j \int_{v_j}^{\infty} \frac{I_v}{hv} dv. \quad (\text{F.27})$$

Lastly, we substitute the bandpass-averaged emission frequency (Eq. F.3) into the second term and find

$$\gamma_{ij} \approx \Gamma_j \left[ \left( \frac{h\bar{v}_j}{hv_i} \right) \left( \frac{\tilde{\sigma}_j}{\bar{\sigma}_j} \right) - \left( \frac{hv_j}{hv_i} \right) \right]. \quad (\text{F.28})$$

### F.2.4 General Case

The general case where  $\tau_v \gtrsim 1$ ,  $\Delta\tau_{i,v} \gtrsim 1$  has the opposite problem: we are stuck with Equations 6.13 and 6.15. Our task then is to find a set of  $n_v$  ( $I_n, h\nu_n$ ) pairs that minimizes the difference between  $\Phi$  and  $\Phi'_i$ , and  $\Psi$  and  $\Psi'_i$ , where

$$\Phi'_i(\tau_{v_n}) \equiv \sum_{n=1}^{n_v} \frac{I_n}{h\nu_n} e^{-\tau_{v_n}} \quad (\text{F.29})$$

$$\Psi'_i(\tau_{v_n}) \equiv \sum_{n=1}^{n_v} I_n e^{-\tau_{v_n}}. \quad (\text{F.30})$$

This requires numerical solutions, as discussed in Chapter 6.

## Appendix G

### Simulated Annealing

To solve Equation (6.25), we employ the Monte Carlo method of Simulated Annealing (Kirkpatrick et al., 1983, Černý, 1985). For a given source and  $n_v$ , we run  $K$  Monte-Carlo trials, each consisting of  $L$  steps, aimed at determining the optimal values of  $I_n$  and  $\nu_n$  for  $n_v$  frequency bins. We do not require the bolometric luminosity of sources to be conserved (i.e.,  $\sum_{n=1}^{n_v} I_n \neq 1$  is allowed), since some photons may traverse the entire one-dimensional “volume” without ionizing a single atom, or some fraction of the luminosity may be emitted below the hydrogen ionization threshold. Inclusion of such photons would be computational effort wasted in a fully three-dimensional ray-tracing calculation, for example, since their mean free paths are very long, and once absorbed they may contribute negligibly to ionization and heating.

Each random walk begins with randomly generated values of  $\nu_n$  distributed between the hydrogen ionization threshold and the maximum emission frequency in the spectrum, and randomly generated values of  $I_n$  that sum to unity. Subsequent steps vary the energy or normalization of (randomly chosen) frequency bin  $n$ . In order to steer each random walk towards the global minimum, we first evaluate the quantity

$$P = \exp[-(f_{k,l} - f_{k,l-1})/T_{SA}] \quad (\text{G.1})$$

where  $k = 0, 1, 2, \dots, K$  represents the current step in the current random walk,  $l$ , where  $l = 0, 1, 2, \dots, L$ , and  $f$  is the “cost function,” a measure of how good our current solution is. We adopt a cost function which is the sum of errors in  $\Phi_i$  and  $\Psi_i$  over the column density range of interest. For each species ( $i$ ), and each integral quantity ( $\Phi$ ,  $\Psi$ ), we add the maximum deviation from continuous and discrete solutions in the optically thin limit (first term in Equation (G.2)), the maximum deviation over the entire column density

range (second term in Equation (G.2)), and the average deviation over the entire column density range (final term in Equation (G.2)), all in dex, i.e.,

$$f_{k,l} = \sum_i \sum_{\Lambda=\Phi,\Psi} \left\{ \max \left[ \log \left( \frac{\Lambda_i}{\Lambda'_i(\mathbf{v}_{k,l}, I_{k,l})} \right)_{\tau=0} \right] + \max \left[ \log \left( \frac{\Lambda_i}{\Lambda'_i(\mathbf{v}_{k,l}, I_{k,l})} \right)_{\tau>0} \right] + \left\langle \log \left( \frac{\Lambda_i}{\Lambda'_i(\mathbf{v}_{k,l}, I_{k,l})} \right)_{\tau>0} \right\rangle \right\}. \quad (\text{G.2})$$

At each step in a given random walk, we also generate a random number,  $q \in [0, 1]$ , that will determine whether we keep our current guess,  $(\mathbf{v}_{k,l}, I_{k,l})$ , or revert to our previous guess,  $(\mathbf{v}_{k,l-1}, I_{k,l-1})$ . The condition for keeping our current guess is  $P \geq q$ .

The key aspect of this analysis is how we vary the control parameter  $T_{\text{SA}}$ , which is called the temperature in analogy with Boltzmann's equation (we add the subscript SA to distinguish the gas kinetic temperature from this unphysical Simulated Annealing temperature). Equation (G.1) tells us that regardless of the value of  $T_{\text{SA}}$ , if  $f_{k,l} < f_{k,l-1}$  (i.e., our most recent guess is better than the last), then  $P \geq 1$ , and we have a 100% chance of keeping our current guess. In other words, our method of controlling the  $T_{\text{SA}}$  only effects how we deal with bad guesses — decreasing the temperature means we become less tolerant of bad guesses. There are many ways of doing this (Press et al., 1992), but for simplicity we adopt the following technique. Every  $s/n_v$  steps per frequency bin, we take

$$T \rightarrow \lambda T, \quad (\text{G.3})$$

where  $\lambda$  is an experimentally determined quantity of order unity. For all results presented here, we have adopted  $\lambda = 0.98$ , and  $s/n_v = 10$ . We change the number of steps per random walk depending on the dimensionality,  $2n_v$ . We have found through experimentation that a good rule of thumb is  $L = 5000$  steps per trial,  $K$ , per frequency bin  $n_v$  for our choice of  $\lambda$  and  $s/n_v$ . These control parameters are fairly conservative — further experimentation with them may yield converged solutions for fewer trials,  $K$ , and steps,  $L$ .